

**Computer Controlled Surface Patterning to Produce Geometrically
Complex Cell Culture Substrates**

by

Matthew Alban Alexander Smith

Submitted in accordance with the requirements for the degree of Doctor of
Philosophy

The University of Leeds

School of Mechanical Engineering

March 2019

The candidate confirms that the work submitted is his/her own, except where work which has formed part of jointly-authored publications has been included. The contribution of the candidate and the other authors to this work has been explicitly indicated below. The candidate confirms that appropriate credit has been given within the thesis where reference has been made to the work of others. The work included in chapter four has been used in the following peer reviewed conference proceedings:

M A A Smith, N R Fry, R W Kay and R A Harris, "Digitally-driven Micro Surface Patterning by Hybrid Manufacturing" in Solid Freeform Fabrication Symposium 2018.

I was responsible for the technical content, the co-authors reviewed the paper and made suggestions on presentation.

The work included in chapter two has been used in:

N. J. Wilkinson, M. A. A. Smith, R. W. Kay, and R. A. Harris, "A review of aerosol jet printing—a non-traditional hybrid process for micro manufacturing," *The International Journal of Advanced Manufacturing Technology*, May 2019.

N Wilkinson and I were responsible for compiling the academic review. The other co-authors reviewed the paper and made suggestions on presentation.

The work included in chapters 2-6 has been used in a publication currently in internal review:

Matthew A A Smith, M Ibrahim Khot, Dr. Pirkko L Muhonen, Dr. Nicholas R Fry, Prof. Joanne Tipper, Prof. David G Jayne, Dr. Robert W Kay, and Prof. Russell A Harris, "A Digitally Driven Manufacturing Process for Adaptable Surface Patterning in *in vitro* Cell Models"

I was the responsible for majority of the technical engineering and biological content. M Ibrahim Khot advised on the cell culturing and biological assays used

throughout. Pirkko Muhonen cultured five of the eight cell types showcased in Figure 2A. Nicholas Fry helped with the illustration of Figure 1. In addition, all the co-authors reviewed the paper and made suggestions on presentation.

This copy has been supplied on the understanding that it is copyright material and that no quotation from the thesis may be published without proper acknowledgement.

The right of Matthew Smith to be identified as Author of this work has been asserted by Matthew Smith in accordance with the Copyright, Designs and Patents Act 1988.”

Acknowledgements

Firstly, I would like to thank my supervisors Russell Harris and Robert Kay for their support throughout the project, both at Loughborough University and at the University of Leeds. Russ you have constantly worked to ensure I kept focussed and driven to complete the project. Thank you for pushing me to aim higher. Rob thank you for your unwavering support and guidance throughout my academic studies, for the entirety of the time you have known me. Without your enthusiasm and support I would never have even started this PhD. Thank you for believing in me, giving me the chance to work with you for such a long time, and for your friendship.

I would also like to thank all members, past and present of the Future Manufacturing Research Group at the University of Leeds. Thank you also to my academic collaborators and members of other research institutions who have helped me in so many ways over the course of the project.

I would like to thank my PhD colleagues Jack Hinton, Nathan Wilkinson and Matt Shuttleworth for the exciting and thought provoking conversations at work, and the great time outside of it.

Special thanks must go to my family, Mum, Dad and Aidan who have always supported me throughout my life. Your constant support has given me the confidence to pursue all my dreams. Thank you all especially for proof reading my thesis and removing all the commas.

Finally, thank you to Faezeh Jahani for her patience and support throughout my whole project. You helped me to see the positives through some of the hardest parts of my life. I truly couldn't have done it without you.

This work was conducted in conjunction with the Engineering and Physical Sciences Research Council (EPSRC) grant EP/L02067X/2

Summary

In this thesis, a new technology and methodology is presented that can be applied to create the next generation of complex *in vitro* models for a range of high value applications.

Aerosol Jet printing is an emerging direct write technology. It can replace established fine feature patterning techniques with a digitally-driven, agile method. Aerosol Jet printing has advantages over other patterning technologies as it can deposit most liquids, solutions and suspensions in specific customisable designs on planar and non-planar surfaces. By automating the print process and establishing a range of enabling procedures, the technique was applied to pattern acellular structures in freeform patterns. These were used as culture substrates and shown to influence the growth and movement of cells in culture.

The fundamental engineering and validation of the apparatus is presented in this thesis. The design, development and testing of the automation system is reported, as well as the enabling procedures such as substrate production, alignment camera design, and control code generation. The automation system was experimentally proven to be capable of a minimum incremental movement of $<10\mu\text{m}$ and had a backlash of $25\mu\text{m}$ in the print region. The alignment camera is capable of distinguishing features as small as $5\mu\text{m}$. The control code generator was capable of producing high fidelity designs from mathematical equations or digital designs. These digital designs could be updated within hours, compared to a physical template which can take weeks to update if the production is outsourced.

To enable reliable micro-scale printing over long periods the material formulation and operating parameters are established. From an initial choice of three functional materials, an ink based around the conductive polymer poly(3,4-

ethylenedioxythiophene) polystyrene sulfonate (PEDOT:PSS) was used as the print feedstock. When using this functional material, pertinent operating parameters were investigated for their effect on the deposit geometry. Increasing the material flow rate through the machine or increasing the size of the nozzle orifice was found to enlarge the deposit, whereas increasing the scanning speed under the print head, or increasing the focusing sheath gas diminished the deposit. During a multivariable design of experiment with a 100 μm micron nozzle, the line cross sectional areas were measured between 6 and 10 μm^2 . The two most notable results were that the geometry is enlarged when the atomiser gas was increased, and diminished when the sheath gas was increased.

Finally, this thesis explores the ability for the deposited features to control the tethering and growth characteristics of cells in culture. The primary focus of the experiments was the HCT-116 colorectal cancer cell lines, which were encouraged to grow into the printed shapes including lines, dots, sharp angles, arcs, circles, and different pitched lines. Subsequently, the functionality of this method across eight different cell lines was proved. Baby Hamster Kidney, L929, primary Human Dermal Fibroblasts, HCT-116, RAW, C6, EA.hy 926, and HT-29 cells were all observed to preferentially tether to the deposited patterns and grow into shapes defined by them. The manner of the interaction was dependent on the cell type, however, a preferential response was seen across the full range of endothelial, fibroblast, neuronal and macrophage cells.

Finally, HCT-116 cells were patterned with high fidelity on curved surfaces, and with freeform patterns over areas larger than 2.5 mm^2 . These experiments proved the apparatus is a viable method to produce complex *in vitro* models used to replicate *in vivo* conditions in applications such as pre-clinical drug evaluation, tissue engineering and fundamental biological studies.

Table of Contents

Acknowledgements.....	v
Summary	vi
Table of Contents	viii
List of Tables	xiii
List of Figures	xiv
Chapter 1 Introduction and Motivation	1
1.1 Project Vision.....	4
1.2 Objectives.....	5
1.3 Challenges.....	6
1.4 Thesis Layout	8
Chapter 2 Literature Review	10
2.1 Principles of Aerosol Jet Printing	11
2.1.1 Atomisation	13
2.1.2 Transportation to the print head	18
2.1.3 Focusing and Deposition.....	19
2.1.4 Print Parameters	22
2.1.5 Substrate Wetting.....	24
2.1.6 Defects.....	26
2.1.7 Post Processing	29
2.2 Applications of Aerosol Jet Printing	30
2.2.1 Interconnects.....	32
2.2.2 Passive Electronic Components.....	36
2.2.3 Active Electronic Components	38
2.2.4 Actuators and Sensors.....	40

2.3	Non-traditional Applications of Aerosol Jet Printing	43
2.4	Competitor Technologies to Aerosol Jet Printing	46
2.4.1	Collimated Aerosol Beam Direct Write	46
2.4.2	Aerodynamic Lenses.....	47
2.4.3	Electro-Aerodynamic Jet Printing	49
2.4.4	Ultrasonic Horns.....	49
2.5	Cell Patterning Technologies	50
2.5.1	Mesoscale three dimensional technologies.....	50
2.5.2	Microscale surface patterning	51
2.5.3	Aerosol Jet Printing to Pattern Cell Cultures	52
2.6	Chapter Summary.....	53
Chapter 3	Methods and Materials	55
3.1.1	Substrate Manufacturing and Post Processing	55
3.1.2	Cleaning and Sterilisation Procedure.	56
3.1.3	Surface modification.....	57
3.1.4	Post processing.....	57
3.2	Analytical Techniques	57
3.2.1	Microscopy	58
3.2.2	White Light Interferometry	58
3.2.3	Scanning Electron Microscopy	59
3.2.4	Adhesion tape test.....	59
3.3	Biological Protocols	60
3.3.1	Cell culture Conditions	60
3.3.2	Patterning Experiment Procedure	61
3.3.3	Microscopy Protocol	61

3.3.4	Immunofluorescence Protocol.....	61
3.3.5	Preparation for SEM imaging	62
3.3.6	Live/Dead Assays	62
Chapter 4	Design, Fabrication and Testing of the Automation Apparatus	63
4.1	Design and Manufacture of the Automation Apparatus	64
4.1.1	Design and Implementation of Movement Axes	64
4.1.2	Printing Engine Configuration.....	73
4.1.3	Microscope Specification.....	73
4.1.4	Head Mount and Platform	75
4.1.5	Environment.....	76
4.2	Software and Control.....	76
4.2.1	Equation Driven G-code Generator.....	78
4.2.2	DXF Driven G-code Generator.....	81
4.3	Chapter Summary.....	88
Chapter 5	Validation of the Manufacturing Process.....	90
5.1	Initial Material Screening	92
5.1.1	Silane Based Functional Material.....	93
5.1.2	Poly(methyl methacrylate) Based Functional Material	98
5.2	PEDOT:PSS Ink Formulation Method.....	101
5.3	Material Longevity Assessment	108
5.4	Operational Window Testing for Printing PEDOT:PSS	110
5.4.1	Test Conditions	111
5.4.2	Changing Nozzle Exit Diameter	111
5.4.3	Changing Scanning Speed.....	112

5.4.4	Changing Z Stand-Off	114
5.4.5	Changing Focussing Ratio	115
5.4.6	Summary of Operational Window Testing	120
5.5	Two Level Multivariable Experimentation.....	121
5.6	Chapter Summary	128
Chapter 6 Application of Selectively Functionalised Substrates to Cell Culture		
130		
6.1	Compatibility with Cell Culture	132
6.1.1	Effect of Submerging PEDOT:PSS Features in Culture Medium	133
6.1.2	Cell Viability When Exposed to Printed Substrates	135
6.2	Basic Cell Patterning.....	136
6.2.1	Printed Lines	136
6.2.2	Dot Arrays	145
6.2.3	Sharp Corners.....	151
6.2.4	Circles	154
6.2.5	Pitch	157
6.2.6	Motility Testing	160
6.2.7	Summary of Capabilities for Engineered Cell Cultures.....	161
6.3	Polygons.....	162
6.4	Trials with Further Cell Types	163
6.4.1	Collaborative Work	169
6.4.2	Summary of Experiments with Further Cell Types	175
6.5	Complex Cell Culture Substrates.....	175
6.5.1	Non-planar Substrates	176
6.5.2	Freeform Patterning	178

6.6	Chapter Summary.....	186
Chapter 7	Conclusions.....	188
7.1	Future Work.....	192
7.1.1	Material development.....	192
7.1.2	Machine development.....	193
7.1.3	Increasing throughput.....	193
7.1.4	Co-culturing onto substrate.....	194
7.2	Pilot Studies.....	194
7.2.1	Printing into channels.....	194
7.2.2	Electrical integration of cell culture substrates.....	196
References	199
Appendix A:	White Light Data Processing.....	228
Appendix B:	Python Code to Generate Shapes from Equations.....	230
Appendix C:	Automated Machine Testing G-Code Script.....	236
Appendix D:	Time Stability Test Results.....	239
Appendix E:	Operational Window Testing Experimental Design.....	240
Appendix F:	Full Focussing Ratio Test Results.....	247
Appendix G:	Two Level Multivariable Experimentation Method.....	249
Appendix H:	Additional Images of Cells Responding to Printed Features.....	263

List of Tables

Table 1.1: Report overview summary	9
Table 2.1: Summary of useful PDMS properties	25
Table 2.2: Key techniques extracted from electronics applications literature	53
Table 3.1: Growth conditions for different cell lines.....	60
Table 4.1: Relevant EO-5012M specifications	73
Table 4.2: Circle and arc definitions in DXF files and G-code	84
Table 4.3: Example of an unsorted feature matrix	85
Table 5.1: Material concentrations limitations for PEDOT:PSS functional material	103
Table 5.2: Material formulation boundary conditions.....	104
Table 5.3: Deposit width and observations for PEDOT:PSS ink formulations.	106
Table 5.4: Atomiser Gas flow rate (sccm) with respect to each Sheath Gas and Focusing Ratio combination	116
Table 5.5: White light interferometry data for a focussing ratio of 1	116
Table 5.6: White light interferometry data for a focussing ratio of 0.5.	117
Table 5.7 White light interferometry data showing diminishing line geometry as atomiser gas was reduced.....	120
Table 5.8: Processing window for multivariable experimentation.....	122
Table 5.9: Hadamard matrix trials	123
Table 5.10: Mean data from the white light analysis for each trial.....	124
Table 5.11: Objective Criterion of Each Parameter	124
Table 5.12: Analysis of individual variables (rounded to 1dp).	125
Table 5.13: Analysis of two factor interactions (rounded to 1dp).	125
Table 5.14: Analysis of three and four factor interactions (rounded to 1dp)....	126
Table 5.15: Print parameters for PEDOT:PSS formulation 4	127

Table 6.1: Engineering Capabilities and Biological Observations for Designable cell cultures	162
--	-----

List of Figures

Figure 1.1: Comparison of the processing steps of photolithography, microcontact printing, and Direct Write [6]–[8].	2
Figure 2.1: AJP technology.	12
Figure 2.2: Ultrasonic atomisation principle [44]	14
Figure 2.3: Pneumatic atomisation principle.	15
Figure 2.4: A diagram of an impactor plate.	17
Figure 2.5: A virtual impactor schematic adapted from [49].	18
Figure 2.6: A cross section of the transportation tubing showing atomised functional material entrained in a gas sheath	19
Figure 2.7: Deposition head. Adapted from [53]. The diameter and properties of the emerging stream (and therefore the geometrical properties of the deposit) are controlled by several adjustable process parameters, discussed in the next section.	20
Figure 2.8: Tilted nozzle printing.	22
Figure 2.9: Factors affecting deposition. In addition, when using ultrasonic atomisation the atomiser current is a variable, when using the pneumatic atomiser the exhaust gas is a variable [46], [54], [57], [61]–[63]	24
Figure 2.10: Sylgard 184 Chemical Structure	26
Figure 2.11: Deposition of aerosolised material onto the substrate surface.	27
Figure 2.12: SEM analysis of a line showing the overspray to the sides of the printed features.	28
Figure 2.13 - Deposit examples (a) good, (b) pinching cause by substrate contamination, (c) pinching caused by insufficient material flow rate, (d)	

bulging cause by too high material flow rate, (e) overspray caused by high sheath gas [47].....	29
Figure 2.14: Representation of the categories of Aerosol Jet literature	31
Figure 2.15 Printed silver interconnects in a head-up display [93].....	32
Figure 2.16 Interconnection between stacked PCB components [87].....	33
Figure 2.17: Printed silver tracks (A) 20 μ m grid [50]and (B) 10 μ m tracks [75]..	34
Figure 2.18: Transfer process for flat conductive tracks adapted from [100]	35
Figure 2.19: Cracks in printed tracks after 10,000 cycles, the arrow highlights the crack [101].....	35
Figure 2.20: (A) Vertical antenna on a dielectric pillar (B) antenna microstructures [108]	37
Figure 2.21 All carbon based field effect transistor array on a flexible substrate [136]	39
Figure 2.22: Printed blue, green and red OLEDs [140].....	40
Figure 2.23: A printed strain gauge, printed on top of a polymer isolation layer [147]	41
Figure 2.24: Printed interdigitated capacitive sensor [150]	42
Figure 2.25: Dual atomiser arrangement [170], [171].....	44
Figure 2.26: SEM images (A) square grid pattern (B) 3D cone array structures [25]	45
Figure 2.27: SEM image of a three dimensional structure produced by AJP printing[178].....	46
Figure 2.28: Bioprinting overview [197].....	51
Figure 3.1: Cleaning procedure before printing.....	56
Figure 3.2: Example white light interferometry data (A) raw data (B) post processed data.....	58

Figure 3.3: (A) A horizontal section was taken from the data. (B) Example of profile data and an illustration of maximum height and width at half maximum.	59
Figure 4.1: Stepper motor control diagram	65
Figure 4.2: X and Y Axis timing belt.....	66
Figure 4.3: Dial indicator set up for measuring axes movements (A) side view showing the experimental set up (B) plan view of the experiment showing dial	68
Figure 4.4: Graph to show the measured deviation on approach to specific X axis positions from both directions.....	69
Figure 4.5: Graph to show the measured deviation on approach to specific Y axis positions from both directions.....	69
Figure 4.6: Calculated backlash at specific positions on the X and Y axis.....	70
Figure 4.7: Z axis timing belt.....	71
Figure 4.8: Z axis verification. (A) Stage is moved until the spacer just fits between the nozzle bracket and the stage plate. (B) The stage is moved down 20 mm and the movement is verified by the addition of a second calibrated spacer.	72
Figure 4.9: Z height deviation from the centre point.....	72
Figure 4.10: Images taken on the in-process camera (A) 50 μ m width line (B) 5 μ m width etched features.	75
Figure 4.11: Print head mounts and rotating stage	76
Figure 4.12: Overview of the equation driven G-code generator process.....	79
Figure 4.13: Complex curves generated through the equation-based G-code generator.....	81

Figure 4.14: (A) Designs are generated in a CAD software. (B) Designs can be instanced many times to scale up production rates (C) A DXF output file is generated.	82
Figure 4.15: Overview of the DXF driven G-code generator	83
Figure 4.16: Illustration of a multi-shape test DXF file, and snippets of code with the definition of a line, arc and circle highlighted.	83
Figure 4.17: Overview of the DXF driven G-code generator	84
Figure 4.18: (A) G-Code Generated with the unsorted matrix (B) G-code generated using the sorted algorithm. Red dashed lines are shuttered movements, blue and purple lines are print movements.	86
Figure 4.19: First step in the sorting algorithm, with the next closest co-ordinates highlighted in yellow. As it contains the next closest co-ordinate, row two of the unsorted array is copied to row zero of the sorted array.	87
Figure 4.20: Second step in the sorting algorithm with the next closest co-ordinate highlighted in yellow. As the next closest co-ordinate in the unsorted array is in columns 2 and 3 of row 1; the start and end co-ordinates are swapped, the direction marker (column 6) is changed, and the row is copied to the sorted array.	87
Figure 4.21: Third step in the sorting algorithm, with the next closest co-ordinates highlighted.	87
Figure 4.22: Overview of the AJP print engine integrated into a bespoke automated apparatus.	89
Figure 5.1: Summary of the validation testing in Chapter 4	90
Figure 5.2: Printed lines with two concentrations of APTES ink.	93
Figure 5.3: Printed APTES line.	94
Figure 5.4: Stable printed features using new processing parameters.	94

Figure 5.5: An overview example of the results of a typical test, showing the changing geometries at different processing parameters.....	95
Figure 5.6: The effect of increasing number of passes and increasing scanning speed.	96
Figure 5.7: Printed features when z stand-off is (A) 2mm (B) 3mm (C) 4mm. ..	96
Figure 5.8: Effect of atomiser gas on print geometry (A) 20 sccm (B) 10 sccm (C) 5 sccm.....	97
Figure 5.9: (A) The effect of track crossovers. (B) White light interferometry image showing the height change due to the cross over.	97
Figure 5.10: Comparison of Blocked and Unblocked nozzle when tested on the Aerosol Jet. The pressure response of blocked nozzles was clear as the pressure would increase at a faster rate and would not stabilise.	98
Figure 5.11: PMMA deposit printing at (A) sheath gas 20 sccm, atomiser gas 15 sccm (B) sheath gas 40 sccm, atomiser gas 30 sccm.....	99
Figure 5.12: A confluent PMMA line	100
Figure 5.13: Example prints with PMMA (A) reliable printing of lines (B) a printed pad of material (C) Freeform patterning demonstration.....	100
Figure 5.14: Material development method.....	104
Figure 5.15: Effect of material formulation on PEDOT:PSS prints.	105
Figure 5.16: Generalised material formulation strategy	107
Figure 5.17: Time stability images (A) 10 mins (B) 30 mins (C) 60 mins (D) 90 mins (E) 120 mins (F) 125 mins - atomiser pulsing.	109
Figure 5.18: Aerosol Jet failures are indicated by changes in pressure time graphs, in this case a rise in pressure due to the nozzle blocking.....	110
Figure 5.19: Effect of changing nozzle size on line width.....	112
Figure 5.20: Effect of changing scanning speed on line width	113

Figure 5.21: Graph to show effect of changing z stand off on line width	114
Figure 5.22: Effect of gas flow rate on (A) maximum height and (B) width at half maximum height.	119
Figure 5.23: Proposed Interactions for Material Deposition Rate.....	121
Figure 5.24: The WHM increases with a logarithmic fitting to the cross-sectional area	127
Figure 6.1: Summary of the application testing in Chapter 5	131
Figure 6.2: Chaotic nature of HCT-116 cell growth on an untreated polystyrene substrate after 48 hrs.	132
Figure 6.3: Degraded features detach from the surface during cell culturing. .	133
Figure 6.4 PEDOT:PSS F4 (A) Before ASTM Tape Adhesion Test (B) After ASTM Tape Adhesion Test.	134
Figure 6.5 PEDOT:PSS Formulation P4 +0.2%Vol GOPS (A) Before ASTM Tape Adhesion Test (B) After ASTM Tape Adhesion Test.	135
Figure 6.6: Live/dead Staining of colorectal cancer cells cultured onto a PEDOT:PSS coated substrate. blue = Live (Hoechst 33342) red/purple=le= Dead (Propidium Iodide). Note that there were no dead cells hence there is no red/purple colour.	136
Figure 6.7: (A) Definition of line widths and pitches (B) an example of a print.	136
Figure 6.8: White light interferometry measurement of a printed line after the addition of GOPS.	137
Figure 6.9: HCT-116 cell response to PEDOT:PSS features on glass after 48 hours.	137
Figure 6.10: Images of cell response after 24 hrs at different seeding densities (A) 6000 cells/sample (B) 10000 cells/sample.....	138

Figure 6.11: A response to printed features was observed after 8 hours of culture.	140
Figure 6.12: HCT-116 growth over 72 hours.....	140
Figure 6.13: 20X optical microscope image of HCT-116 growth after (A) 48 hours (B) 72 hours.	141
Figure 6.14: HCT-116 cells grow outside the printed features after 96 hours.	141
Figure 6.15: SEM image of cells tethering along a PEDOT:PSS printed line..	142
Figure 6.16: SEM image, taken at a 20 degree angle, showing a cell tethering to the overspray (left).	142
Figure 6.17: Immersion SEM images of cells (Left of both images) extending projections to attach to the deposited nanoparticles of PEDOT:PSS. (A) 10000X (B) 25000X.....	143
Figure 6.18: Cells during the cell splitting phase extend projections to tether to the PEDOT:PSS particles.	143
Figure 6.19: Cell tethering to single nanoparticles on an 'unpatterned' PDMS region.	144
Figure 6.20: (A) 40X image with transmitted light (B) DAPI nucleus staining (C) α -tubulin cytoskeleton staining (D) superimposed image as standard in biological assays.	145
Figure 6.21: Dots with 50 μ m WHM in an array are distinguishable at 100 μ m pitch. (A) White light data. (B) Cross sectional data showing the width at half maximum. (C) Cross sectional data with a pitch measurement.....	146
Figure 6.22: Dots with 20 μ m WHM in an array are distinguishable at 40 μ m pitch. (A) White light data. (B) Cross sectional data showing the width at half maximum. (C) Cross sectional data with a pitch measurement.....	147

Figure 6.23: (A) Sputtering interference causing features to amalgamate at 30 μ m pitch. (B) White light interferometry image showing bridging between dots of material..... 147

Figure 6.24 (A) Overview of an entire dot array with distinguishable features. (B) SEM image of the dot array..... 148

Figure 6.25: HCT-116 growth on three pitches of dot arrays after 24 hrs and 48 hrs. 149

Figure 6.26: HCT-116 growth on three of dot arrays after 48 hrs (A) 80 μ m pitch (B) 110 μ m pitch (C) 140 μ m pitch. 149

Figure 6.27: 20X magnification image of HCT-116 cell growth of an 80 μ m dot array. 150

Figure 6.28: 20X magnification image of HCT-116 cell growth on a 140 μ m dot array. 150

Figure 6.29: Cell growth is contained to the printed region even after 96 hours of growth. 151

Figure 6.30: White light interferometry of changing angles. (A) Printing with 40 μ m WHM. (B) Printing with 20 μ m WHM. 152

Figure 6.31: Acute angles exhibit a build-up of material at the vertex (A) 40 μ m WHM (B) 20 μ m WHM..... 152

Figure 6.32: Sharp angle printed on PDMS. (A) A 24 hrs HCT-116 cells tether only to the printed regions. (B) After 42 hrs the cells begin to divide and grow preferentially along the feature. (C) After 72 hrs the cells are confluent on the feature. 153

Figure 6.33: HCT-116 cells grow along around some sharp corners of different angles after 24 hours..... 153

Figure 6.34: White light interferometry of printed circles of decreasing diameter.	
(A) Printing with 40 μm WHM. (B) Printing with 20 μm WHM.....	154
Figure 6.35: (A) 200 μm diameter circle with a 40 μm WHM line (B) A cross sectional data can be used to measure the feature. (C) 100 μm diameter circle printed using a 20 μm WHM line (D) cross sectional assessment shows the distorted nature of the small feature due to different sized peaks.	155
Figure 6.36: (A) Right HCT-116 cells respond to print at 24 hours. (B) Growth after 96 hours.	156
Figure 6.37: HCT-116 cell response to PEDOT:PSS circles on PDMS substrates.	156
Figure 6.38: Cellular response to incomplete circle.	157
Figure 6.39: (A) 40 μm line pitch experiment (B) 20 μm line pitch experiment..	158
Figure 6.40: Selected points of the pitch experiment showing effect of decreasing pitch, printed with a 40 μm WHM line.....	158
Figure 6.41: Selected points of the pitch experiment showing effect of decreasing pitch, printed with a 20 μm WHM line.....	159
Figure 6.42 Typical response of HCT-116 cells to a pitch test over time.	160
Figure 6.43: White light interferometry scan of cell motility test, and a profile showing the increasing pitch.	160
Figure 6.44: Representative results of motility testing with HCT-116 cells, all images after 48 hrs of growth.....	161
Figure 6.45: IF imaging of the motility test culture.	161
Figure 6.46: HCT-116 cells respond exactly to simple printed shapes under suitable cell seeing densities. 1 st row, white light interferometry measurements. 2 nd row, transmitted light of cells responding to shapes. 3 rd row, DAPI staining of cell nuclei.	163

Figure 6.47: Combining tests made it viable to test new cell types in a much faster approach than previously possible	164
Figure 6.48: Different growth characteristics of (A) HCT-116 (B) HT-29 (C) EA.hy 926. All samples cultures on PS and imaged at 48 hrs.	165
Figure 6.49: Comparison of the growth of HT-29 and HCT features on PEDOT:PSS printed lines at different time points.	166
Figure 6.50: HCT-116, HT-29 and EA.hy 926 cell growth on 110um pitch dot array over time.....	167
Figure 6.51: Comparison of HCT-116, HT-29 and EA.hy 926 response to printed shapes after 48 hours.....	168
Figure 6.52: Sharp angle printed on PDMS. (A) After 24 hrs HT-29 Colonic rectal cancer cells tether only to the printed regions. (B) After 48 hrs the cells begin to divide and grow preferentially along the feature. (C) After 72 hrs the cells are confluent on the feature and grow outward forming a tumour.	168
Figure 6.53: Some EA.hy 926 cells respond by elongating along lines and curves.	169
Figure 6.54: L929 cellular response to PEDOT:PSS printed features on PDMS. Day 4 and Live/Dead (Day 7).	170
Figure 6.55: BHK cell line response to PEDOT:PSS printed features on PDMS. Days 4 and Live/Dead (Day 7).	171
Figure 6.56: C6 cell line response to PEDOT:PSS printed features on PDMS. Day 7 and Live/Dead (Day 7).	172
Figure 6.57: pHDF cell line response to PEDOT:PSS printed features on PDMS. Day 7 & Live/Dead.	173
Figure 6.58: RAW cell line response to PEDOT:PSS printed features on PDMS. Day 7& Live/Dead.	174

Figure 6.59: PC-12 non-adherent cell line is not patterned.....	175
Figure 6.60: Representation of the curved substrate with the printing region highlighted in red.....	176
Figure 6.61: Cells patterned and printed onto a curved surface with perspective. (A) a low magnification image imparts perspective on the curved surface. (B) higher magnification shows the cells adhering only to the PEDOT:PSS features.	177
Figure 6.62: Cellular response to features printed onto a 25mm radius curved surface.	177
Figure 6.63: (a) Cell response to printed lines on a double curved surface. (b) magnified image of the cells on a line, curved surface highlighted in red.	178
Figure 6.64: Printed University of Leeds logo demonstrating freeform capability. (A) Image next to a matchstick for scale. (B) White light interferometry data.	179
Figure 6.65: EA.hy 926 cells growing into a branching structure. Yellow lines outline the AJ printed feature.	180
Figure 6.66: Complex 'star' designs and cellular response over time.	181
Figure 6.67: (A) Cells adhere to a complex pattern made of dots after 24 hours. (B) After 72 hours the cells have grown to mirror the printed line of dots.	182
Figure 6.68: Large area images of stained cell cultures.	183
Figure 6.69: Large area merged image of cell nucleus and cell body staining.	184
Figure 6.70: Higher magnification image showing the cell density of two vertices of the star.	185
Figure 6.71: Immunofluorescence image of HCT-116 cells. Blue = cell nucleus, green = cell cytoskeleton.....	185

Figure 6.72: Large area control of cell growth. (A&C) White light interferometry image of complex patterns. (B&D) Image of cell nuclei to show cell response after 72 hours. Blue colour is DAPI stain of nucleus, Scale = 100µm..... 186

Figure 7.1: Final process overview 192

Figure 7.2: A high fidelity PDMS substrate is cast from the photolithography mould. 195

Figure 7.3: The process printed repeatably into 50µm wide channels. 195

Figure 7.4: (A) 20X magnification image of printed line in a 50µm wide channel. (B) PEDOT:PSS was printed into channels with 20 µm width. 196

Figure 7.5: PEDOT:PSS printing incorporated into an electrical circuit. (A) A printed interconnect. (B) A microcontact apparatus was manufactured to incorporate the printed designs. (C) The apparatus could be attached to power supplies and measurement apparatus..... 197

Figure 7.6: (A) PEDOT:PSS structures are stimulated by small electrical pulses, an LED light confirms when the pulsed current is on. (B) Plasma bonding a PDMS cylinder onto the glass results in a usable cell well. (C) Top view of the device, filled with DI water. 198

Abbreviations

AJP – Aerosol Jet Printing

APTES - (3-Aminopropyl)triethoxysilane

CAB-DW – Collimated Aerosol Beam Direct Write

CAD – Computer Aided Design

CNC – Computer Numeric Control

BHK – Baby Hamster Kidney

DI - Deionised

DXF – Design Exchange Format

DW – Direct Write

EAD - Electro-aerodynamic

FR – Focussing Ratio

GOPS - (3-Glycidyoxypropyl)trimethoxysilane

pHDF – Primary Human Dermal Fibroblast

OLEDs – Organic Light Emitting Diodes

PDMS - Poly(dimethylsiloxane)

PMMA - Poly(methyl methacrylate)

PWM – Pulse Width Modulation

UA – Ultrasonic Atomisation

WHM – Width at half maximum

Chapter 1 Introduction and Motivation

This thesis summarises the development of a new manufacturing process for *in vitro* cell culture substrates. *In vitro* cell culture is performed as an attempt to model *in vivo* environment. However, many routine cell culture assays are performed on flat featureless glass or plastic substrates, which are a poor model of the natural cell milieu. Flat, featureless substrates are unsuitable for many applications because in natural growth the cells do not grow in isolation. In natural growth cells experience interactions with multiple distinct cell types and extra cellular molecules, which provide structural and biochemical support. Further, the cells experience changing stimuli based on the stage of the growth cycle [1]. The key to producing realistic *in vitro* models is to depart from simplistic traditional artificial cell culturing substrates in which cells fail to recapitulate the environment and phenotype of the tissue of origin [2].

There is an increasing demand for the capability to create advanced *in vitro* cell models with greater complexity [3]. Advanced models will expand the range of physiological conditions that may be studied *in vitro*, particularly as an alternative to expensive and time consuming *in vivo* animal models [4]. The paradigm shift, away from using animal models, will also increase the rate of research by circumventing the need to adhere to animal safety and ethical regulations associated with animal testing. However, this drive toward more complex synthetic modelling at the micro scale cannot be met by traditional manufacturing processes. Engineers and biologists must collaborate to produce these complex cell culture substrates with suitable accuracy and speed to screen a range of interactions. There is a competitive advantage to manufacturing technologies that can be adapted to a range of scenarios.

Processes that deposit material directly onto a surface remove the need for a template and several intermediary steps associated with manufacturing at the microscale (Figure 1.1). The broad category of processes that deposit directly onto the substrate are known as ‘direct write’ (DW) processes [5], [6]. In DW processes material is dispensed directly from the print head onto the substrate. By translating the substrate underneath the deposition head traces of material are produced. The design of the deposited material is controlled by a digital script which contains the instructions for translating the substrate, and the controls required for other commands, such as on/off patterning [6]. By updating the digital script, the design can be changed without a fundamental change to the production process. The reduction in processing steps also reduces the possibility of error by reducing the number of data formats and parties involved in the manufacturing process. These new manufacturing capabilities will enable novel and desirable substrates to be produced. When used in biological studies, surface treatments at this micro level give the ability to model the cell environment. The increased capability compared to other processes can be used to study, model, and apply key biological phenomena.

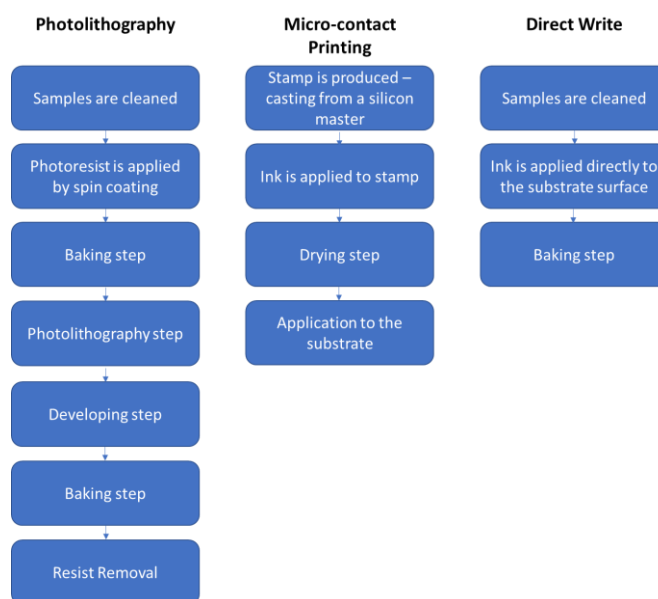


Figure 1.1: Comparison of the processing steps of photolithography, microcontact printing, and Direct Write [6]–[8].

DW processes are compatible with a wider range of substrates than template and stamp based processes, as the material is deposited directly onto the surface of the substrate. Notably textured surfaces, and non-planar surfaces can be patterned, and these are desirable in many high value fields such as tissue engineering, healthcare and aerospace [9]. Once applications have been proven in a laboratory environment, DW processes are suitable to scale up due to the small number of processing steps. For example, if several print heads are combined into a single machine the machine throughput increases, and can also incorporate several feedstock materials [10].

The materials that can be printed are limited only by the ability to transition the desired bulk material into a medium that is suitable to print with [11], [12]. Most DW processes require a feedstock of liquid material which is produced by dissolving, suspending of nanoparticles in a liquid (i.e. a colloid), or melting. This material stock contains a functional material suspended in solvents and may contain other additives. This material feedstock is called an 'ink', and this the properties of the ink is one of the fundamental drivers for most operational decisions [13].

A promising DW process that is compatible with a wide range of feedstock material viscosities is known as Aerosol Jet Printing (AJP). This process is unique in the family of commercialised DW systems as it transitions the liquid feedstock (containing the functional material) into an aerosolised state prior to deposition onto the substrate. This atomisation step can be achieved in different ways depending on the material characteristics of the feedstock. Low viscosity inks (1-5mPa·s) are atomised through ultrasonic energy, higher viscosity inks (5-500mPa·s) are atomised using a system based on pneumatic shearing. After transportation to the print head the aerosol is focussed and accelerated toward

the substrate where it is deposited. The focussing head produces a collimated jet of material, giving a working distance of 1-5mm [14]. Due to the unique atomisation and focussing steps AJP overcomes the limited compatible materials, and the difficulties in patterning non-flat substrates, and the significant lead-time and costs of turning around new pattern designs associated with other patterning techniques.

By developing the automation and enabling procedures for AJP, the time taken to deliver new cell culture substrates is reduced compared to traditional techniques. These can be tailored to model conditions as described by the biologists, enabling more realistic cell culturing to take place.

1.1 Project Vision

The machinery and procedures described in this report were developed to support the EPSRC funded project EP/L02067X/2. The vision of the project was to progress high value biological applications by the creation of bespoke apparatus and ancillary procedures. For example, these capabilities may be used to manufacture models for pre-clinical drug evaluation [15], tissue engineering [16], and fundamental biological studies [10]. In this thesis the apparatus and methods to produce high fidelity surface treatments were developed. These surface treatments were used as specialised cell culture substrates that encourage cells to grow into high fidelity complex features. The manufactured substrates had to enable new studies, but also be compatible with existing biological assays to ensure validity of the analysis.

The developed apparatus and methods produced surface treatments of biocompatible and cell adherent material onto non-cell adherent substrate, to influence biological response at the microscale. As it was a new automation apparatus the machine had to be characterised and the essential parameters for

controllable deposits identified. In addition to stable printing, the designs had to be updateable to meet changing biological needs. These were communicated from the biologists and implemented by the engineers. The manufacturing apparatus was to be capable of printing structures that combine the specificity and fidelity required for *in vitro* models with the speed of manufacture to incorporate these structures into routine testing. The machine was to have scale up in mind, and the potential for the production capability to apply these *in vitro* models to high value applications.

1.2 Objectives

The final developed platform was to have the ability to provide focussed surface treatment onto a range of substrates with micron-scale accuracy. This direct write process was then to be applied to specific biological testing, the requirements of which were driven by collaborative partners. The main objectives were:

- A comprehensive review of Aerosol Jet Printing.
- Design and production of a modular system capable of directed chemical treatment, including 3 axes of movement and alignment capabilities.
- A methodology to formulate new inks for Aerosol Jet Printing.
- A methodology for achieving controllable and designable deposition of any new ink introduced to the system, including identification of significant process inputs and responses.
- Ascertaining an operational window for reliable printing of lines with defined geometries of a single material.
- The use of such surface specific requirements to show a response from an identified cell groups.
- Printing of desirable structures, as directed by collaborative partners.

1.3 Challenges

The first and most significant challenge was the incorporation of the AJP process into an automated manufacturing apparatus. This was fundamental to producing micro-scale features that this project required. This challenge was tackled by thorough characterisation, validating that the stage was suitable for the application. Controlling the acceleration profiles and speeds was a factor in enabling reliable print results. A body of work defining and standardising the actuation meant that the automation apparatus was understood and the capabilities defined. These criteria were taken into consideration when designing the cell culture substrates.

Secondly, there are a range of factors that can affect the success of the printing with AJP, such as:

- Print material and substrate material interaction
- Control of the gas flow rate ratios
- The speed at which the substrate is moved under the head
- The distance between the print head and the substrate
- Environmental and drying conditions

In addition, inhomogeneous mixing and solvent evaporation of the material feedstock caused process variation. These challenges were addressed by using the literature to identify the key processing variables, and then defining the trends when altering processing conditions. Combined with reliable stage movement, this enabled definition of process parameters to enable consistent printing of micro-scale features.

Thirdly, some substrates were not suitable for printing on in their natural state. Improper matching of the surface energies had a deleterious effect on line quality

and caused defects such as bulging. In these cases, surface chemical alterations of the substrate to match the ink properties were essential to the project.

The fourth challenge was to analyse and define the printed features once they had been printed. A range of metrology equipment was used to measure the printed geometries including white light interferometry, optical microscopy, atomic force microscopy, and scanning electron microscopy. No standardised method of reporting the geometry of Aerosol Jet printed features exists, so a range of data was reported in line with the best practices from the literature.

The fifth challenge was to produce and update substrates to meet the requirements of internal biological testing. In Particular, the speed of turnaround was challenging to produce throughout the project. In addition, the stringent requirements of cleanliness and sterility and the changing designs from different collaborators had to be addressed. To speed up the production and alteration of designs a new program was developed in Python, which could take either equations or digital design data, and output machine control code. At the beginning of the project, the designs needed to be simple so that they could be coded manually, and complex requirements took between 2 to 3 days of development. By the end of the project, new designs could be output within an hour and the complexity of the design was not a factor in the length of time it took to develop. In addition, scaling and batch production increased the throughput of printed substrates. The biological testing was performed in a different laboratory to the manufacturing, and therefore a cleaning and sterilisation procedure was developed for the manufactured parts. After sterilisation procedure the parts were sealed and taken for biological testing.

Finally, using the printed substrates in a biological application required both the substrate manufacturing and existing biological methods to be adapted. Many

trials were required to define these new protocols and ensure that the cell consistently reacted to the printed features. In addition, the requirements of the biological testing meant that tight sterilisation and transportation procedures had to be defined.

1.4 Thesis Layout

The background and motivation for the work is described above in Chapter 1.

Chapter 2 presents an overview of Direct Write and Hybridisation. It then gives a detailed review of AJP technology, and its key applications. Finally, the current state of the technology for applying direct write processes to pattern cell cultures is discussed.

Chapter 3 Defined the methods for blank substrate production, surface alterations and post processing. Then, the method for key analytical techniques and biological protocols are described.

Chapter 4 discusses the core principles of AJP technology, the mechanical design and fabrication of the automation apparatus from componentry, and the development of the ancillary procedures and the hybridisation of the technologies that enabled the production of the cell culture substrates. This chapter also defines the methods to produce the machine control code and the printed substrates.

Chapter 5 explores the experimentation required to define new printing inks and presents the formulation for a stable printing ink. The characterisation identified significant parameters of the bespoke automation apparatus. The parameters and their interactions are assessed through the experimentation. The incorporation of non-planar substrates and electrical stimulation of the substrates is shown.

Chapter 6 presents stable printing conditions for lines of several geometries. Printed substrates are proved to be non-toxic and the cells are viable. Limitations in terms of manufacturing capability, and the response of cell cultures are defined. Outside these limitations, cells respond exactly to the printed features, even over large areas and complex designs. By incorporating many tests onto a single substrate, the rate of testing was increased. Nine cell lines were assessed, and the method was proven with all eight adherent cell lines. A range of functional tests are presented which pave the way for new understanding in these biological systems.

Chapter 7 concludes the thesis and suggests relevant avenues for future research.

Table 1.1: Report overview summary

Chapter	Subject	Contents
1	Introduction	Motivation. Vision. Challenges.
2	Literature Review	Overview of Direct Write, and Hybridisation. Review of applications of Aerosol Jet Printing. Overview of alternative Aerosol Based Direct Write technologies Overview Applying Direct Write to cell culture.
3	Methods	Overview of substrate production, analytical techniques and biological protocols.
4	Machine Development and Characterisation	Mechanical design and fabrication of apparatus. Aerosol Jet Printing integration. Machine code generation.
5	Process Specification	Print material development. Experiments to determine operational conditions Printing onto non-flat substrates. Compatibility with electrical stimulation.
6	Applying Technology	Printing geometrical features. Use as cell culture substrates. Compatibility with multiple cell types. Cell culturing on non-flat substrates. Demonstration of high fidelity cell patterning
7	Conclusions	Concluding remarks. Recommendations of further work.

Chapter 2 Literature Review

This chapter provides an overview of the Aerosol Jet Printing (AJP) process by identifying its place in the wider direct write (DW) field, summarising the underlying principles, and reviewing the applications of the technology. The competitor technologies to AJP are discussed, as is the application of DW to cell culture.

DW technologies cover those which selectively deposit a range of materials to produce freeform patterns without the requirement for any tooling or masks [6]. The development of DW technologies was accelerated by the U.S. Defence Advanced Research Projects Agency funded 'Mesoscale Integrated Conformal Electronics' project, which aimed to develop manufacturing processes capable of depositing a diverse range of materials onto virtually any substrate [17]. Notable technologies developed from this project are Matrix-Assisted Pulsed Laser Evaporation Direct Write – often abbreviated to MAPLE-DW [18], nScript [19], 3De [17], Direct Write Thermal Spraying [20], and Maskless Mesoscale Materials Deposition (M³D, now rebranded as Aerosol Jet printing) [21]. The AJP process was devised and patented by Optomec Inc (USA), who now sell the apparatus directly and through distributors internationally. Due to the nature of the project the primary use for many of the DW technologies was, and continues to be, the production of electrical circuitry [22]. DW technology is increasingly used in other applications that require the deposition of functional [23], [24] or structural inks [25], [26] directly onto a substrate.

DW techniques compete with more traditional template and mask based processes for surface modification [27]. Surface features are routinely produced using a range of template driven techniques including photolithography and soft lithography.[8], [28]–[32] However, these processes have restrictions which

include limited compatible materials, significant lead-time and cost of turning around new pattern designs, the geometrical complexity of achievable patterns, and the difficulties in patterning non-flat substrates. A major contribution of DW is that by removing the templates it enables higher orders of patterning complexity while providing currently unobtainable degrees of flexibility and responsiveness to design changes. In addition, throughput is increased as many ancillary procedures associated with template driven manufacturing, such as spin coating and mask alignment, are not required [2].

Within the DW technologies, the new AJP process is attractive, as it can print any material that can be transitioned from the liquid/suspension state to an aerosol state [33]. Therefore, it can print most liquids, solutions and suspensions in specific customisable patterns [34]. AJP can be automated, requires few processing steps and has a large and flexible stand-off distance compared to other DW technologies [35]. This means it is compatible with a wide range of substrate shapes, such as steps and curves. As the material is only printed where required, the material usage is lower than some other manufacturing techniques [36]. Through changing process parameters or rastering, AJP is used to produce fine features (between 10-100 μ m) [37] but can also produce films [38].

2.1 Principles of Aerosol Jet Printing

AJP is based around the aerodynamic focussing of an aerosol containing the functional material. There are three key stages to the process:

1. The atomising stage: where the aerosol is generated from a liquid feedstock of functional material.
2. The transportation and refinement stage: where the aerosol is transported from the atomising chamber to the focussing head. This stage may include a flow refinement component to filter the particle sizes and flow rates.

3. The focussing stage: where the aerosol is focussed and accelerated toward the substrate.

An overview of the printing process is shown in Figure 2.1. A liquid sample containing the functional material is atomized within a sealed container (1). Then, an inert gas is used to increase the pressure in the atomizer chamber and a mixed stream of nitrogen and aerosol is produced (2). This is transported to the deposition head, via flow refinement stages when appropriate, with the gas acting as a sheath around the aerosol (3). A further annular sheath of inert gas is introduced in the print head, which focuses and accelerates the aerosol (4) and the resulting high velocity jet is deposited onto the substrate (5). To produce a pattern the stage is moved in up to 5 axes (6), On/off patterning is achieved by interrupting the jet with a mechanical shutter (7). The key novel and proprietary element of AJP is the approach used to focus and deposit the aerosol [39].

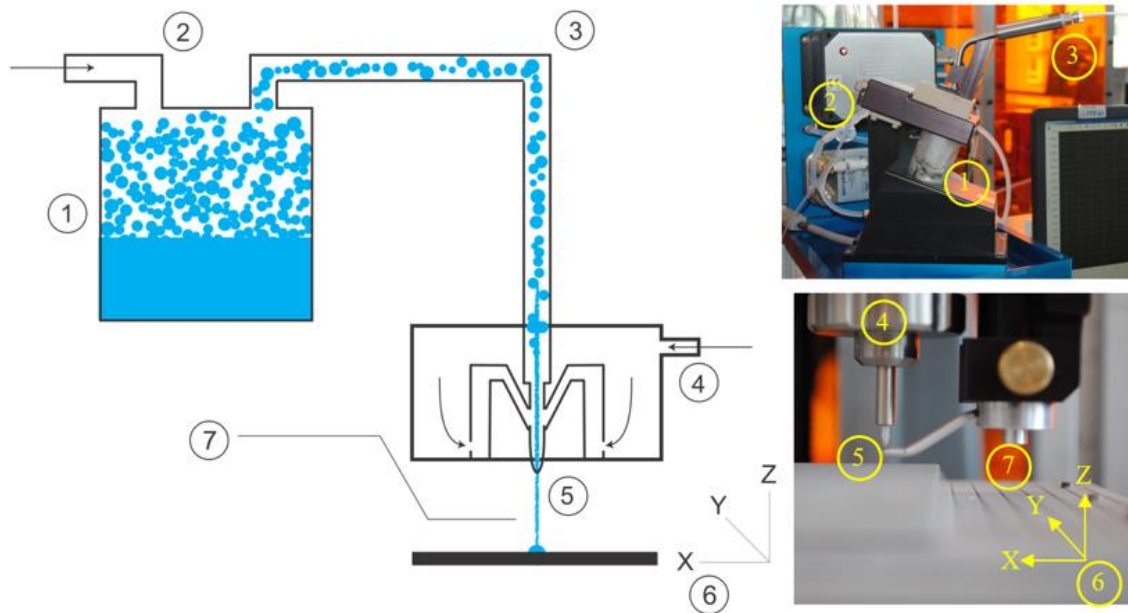


Figure 2.1: AJP technology.

Characteristics of the deposit are a function of the nozzle size, material-substrate wetting, and process parameters. Using AJP large working distances of between 1 to 5mm can be realised, and this enables printing on irregular surfaces [40].

Printing is generally done in air at atmospheric pressure with equipment running at or near ambient temperatures. As with all micro-manufacturing processes environmental controls improve the reliability of the process [41].

2.1.1 Atomisation

The process of depositing aerosol particles requires a monodisperse aerosol with uniform properties over long periods of time to be produced in the atomisation container, if exceptional print quality comparable to photolithography is to be achieved [14]. There are two choices of atomisation method. The principle of both methods is to seal a small sample of functional material into a chamber and atomise it using either focussed ultrasonic energy or pneumatic shearing of the fluid in a Collinson type atomiser.

A factor that is controlled in both methods is the atomisation temperature. When most materials are atomised, there is a reduction in temperature as the liquid is dispersed. Therefore, the atomisation step causes a reduction of temperature within the atomisation chamber, which increases the material viscosity, in turn affecting the print characteristics. An arbitrary standard is to attempt to hold the temperature at 30°C. However, this can be altered to suit the material and user preference [42], [43]. In both methods a dense aerosol with droplet sizes between 1 and 5 μm is produced [34]. However, the volume of aerosol and particle size distribution varies, making the two methods suitable for different applications.

2.1.1.1 Ultrasonic Atomisation

Ultrasonic atomisation (UA) techniques produce a monodisperse aerosol when compared to the Collinson atomiser. The Optomec ultrasonic atomiser can nebulise a range of materials with a droplet size between 1 and 5 μm . It has a viscosity limit of around 10 mPa-s. At viscosities higher than this an aerosol will not be produced [33].

A diagram explaining the UA process is shown in Figure 2.2. An ultrasonic transducer is oscillated using a high frequency alternating current (1). Then, the energy is propagated through an intermediary liquid layer to the material which is suspended in a small bottle over the transducer (2). A capillary wave is formed on the material surface. Constructive interference causes increased local shear, which in turn causes small particles to be ejected from the bulk producing an aerosol (3). Finally, a positive pressure is applied to the atomisation chamber which pushes the aerosol out toward the deposition head (4).

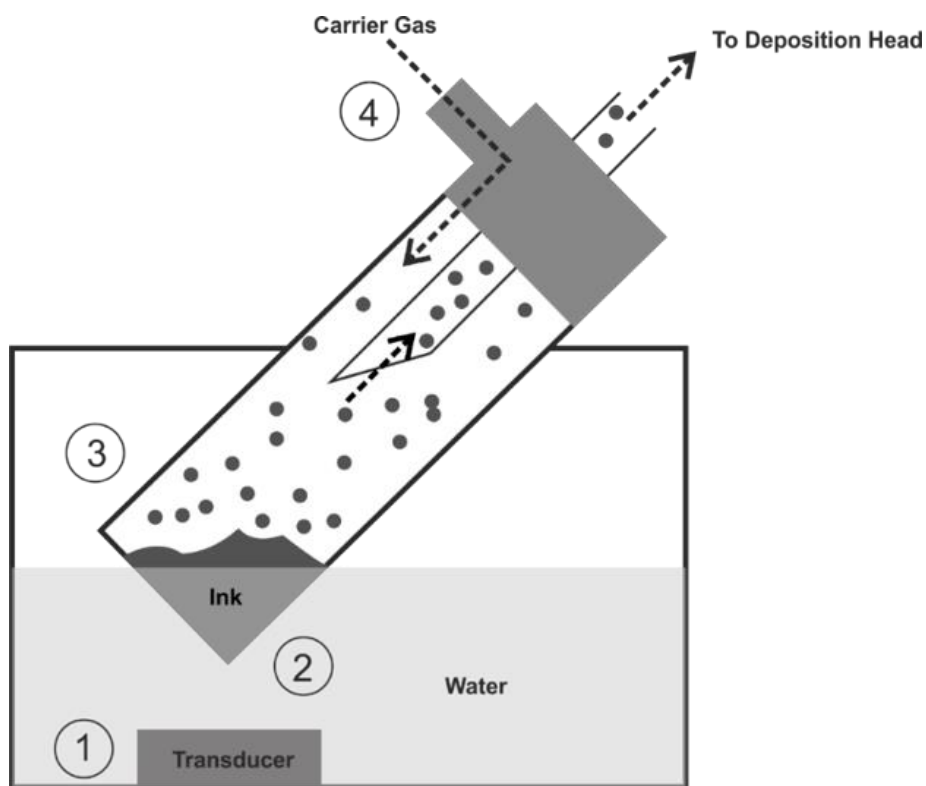


Figure 2.2: Ultrasonic atomisation principle [44]

UA devices suffer from long term changes in atomisation, exacerbated by the small (2ml) material reservoir. Factors such as ink drying, where the solvent is evaporated into the atmosphere, and ink curing can substantially alter the properties of the material over time.

For pure liquids, liquid solutions and colloids that contain small solid particles UA is the preferred atomisation method. UA may damage larger molecules such as polymer chains and living tissue due to high localised energy build up that causes

aerosol generation [45]. Particles larger than 50nm may not be picked up by the UA process, due to the small diameter of the Aerosol droplets that are formed. When ultrasonic atomisation is used an additional variable is the current supplied to the atomiser. Increases in current result in an increase in ultrasonic energy transfer to the material resulting in smaller average particle size of the aerosol [46].

2.1.1.2 Pneumatic Atomisation

The second type of atomising apparatus is based on a Collision type atomiser and is explained in Figure 2.3. The reduced static pressure due to the flow of compressed gas draws liquid material up the tube (1). The material is sheared by the gas producing droplets (2). Larger droplets ($>5\mu\text{m}$) impact the sidewall and are returned to the reservoir (3), droplets smaller than this remain as an aerosol and are exhausted from the atomiser (4).

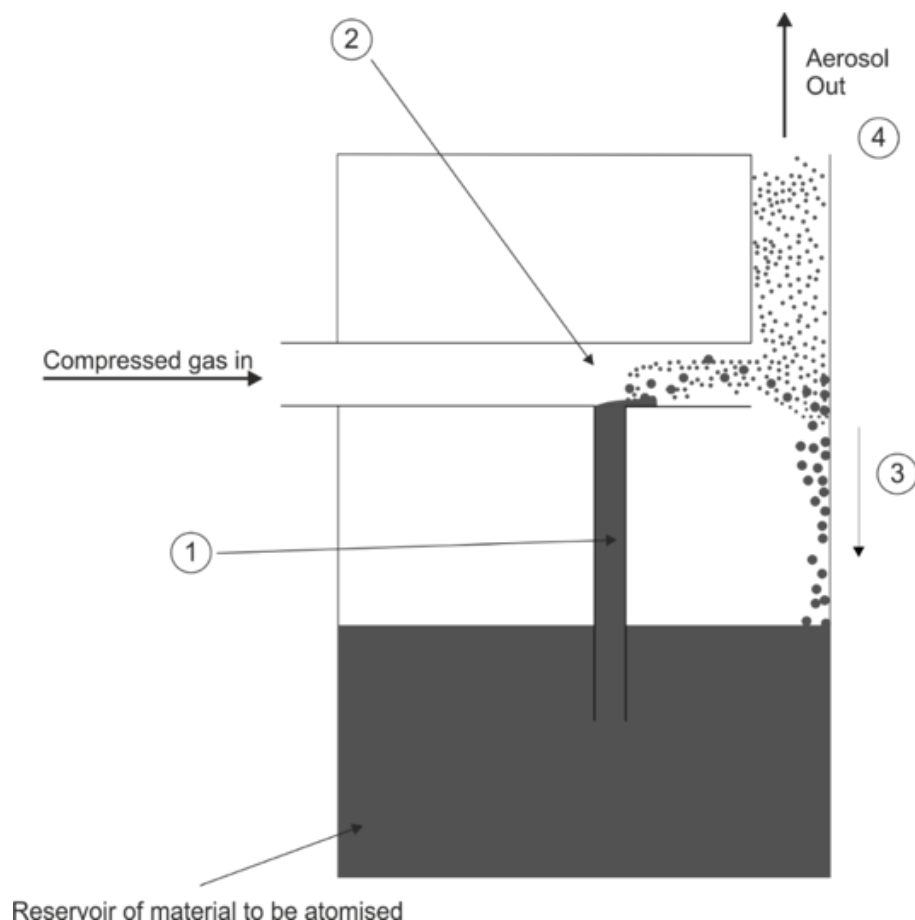


Figure 2.3: Pneumatic atomisation principle.

Pneumatic atomisation is compatible with materials that have a viscosity up to 1000mPa-s. Although the capacity of the reservoir is between 80 to 100ml, the higher gas flows mean that the solvent evaporation can still affect the material. The shearing of the material surface produces an aerosol with a wide range of particle sizes [47]. In addition, the volume of material produced can overload the print process at the focussing stage, resulting in blockages. To reduce the range of particle sizes and volume of material an auxiliary filtering step is required.

2.1.1.3 The Virtual Impactor

When printing with the pneumatic atomiser It is important to refine the flow due to the droplet size range, and volume of aerosol produced. This step removes material and filters the aerosol to ensure that only droplets within a printable range reach the print head. Due to the high gas flows rates (>1000SCCM in some applications [48]) present during the atomisation process there is also an excess material contained within the flow. To tune the particle size and reduce the total mass flow rate a device known as a virtual impactor is used.

To describe a virtual impactor, it is first useful to understand a related device, and Impactor. In aerosol science, an impactor is a device that can separate a single aerosol stream in to two streams depending on the inertia of the suspended droplets. Figure 2.4 is an illustration of an impactor plate. Collimated flow approaches a static plate (1). The flow of gas is interrupted and forced to flow outward to conserve momentum, smaller particles can change direction (2). Larger particles with a higher momentum do not change direction and impact with the plate (3). The flow then contains only small particles (4). In AJP it is the larger particles which are desired, as printing with these has advantages such as reduced overspray (discussed in Section 2.1.3). However, in an impactor the larger particles are accumulated on the plate and cannot be used.

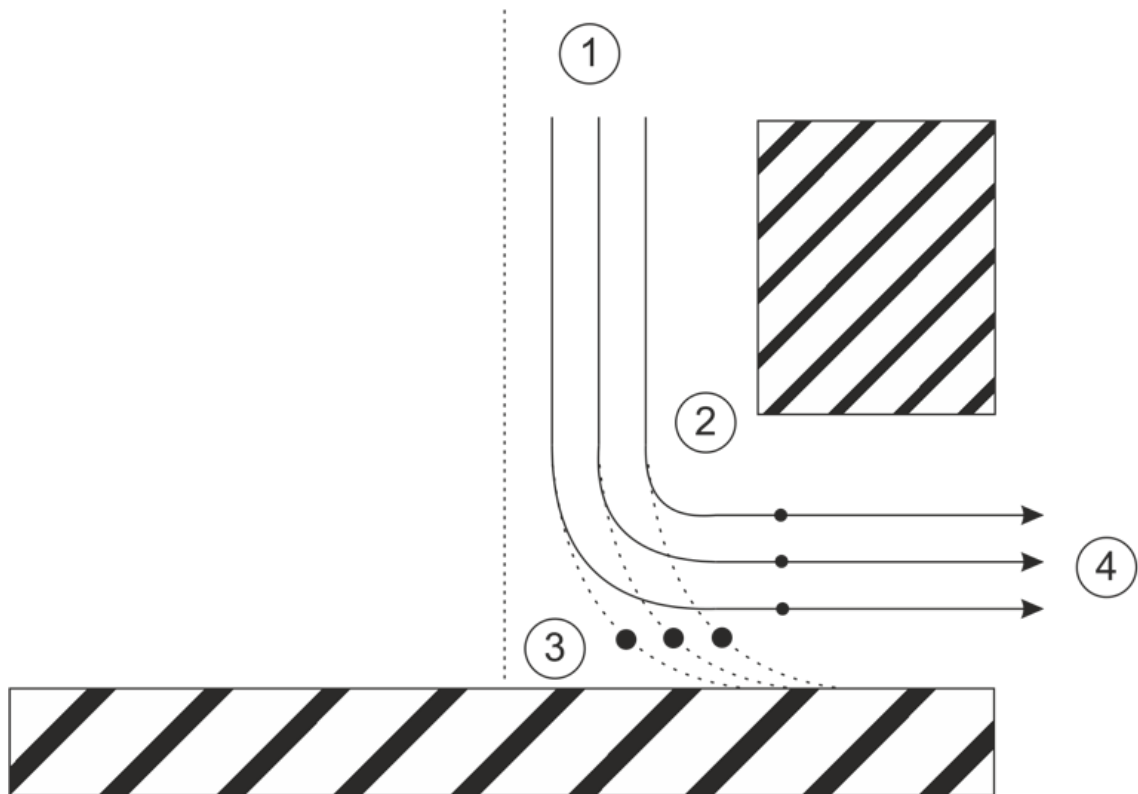


Figure 2.4: A diagram of an impactor plate.

The virtual impactor achieves the same effect as an impactor, however in place of a physical plate, it uses a region of stagnated flow achieved by a step increase in the diameter of the tube (Figure 2.5). Most of the small particles do not have enough inertia to overcome this stagnation and are carried outwards by the major flow. In the AJP process these are not required and are vented through a filter to the atmosphere. The minor flow containing the larger particles that were able to overcome the stagnated air continues to the deposition head. The particle size cut-off is not sharp and as a result some smaller particles ($<5\mu\text{m}$) are contained within the minor flow [9].

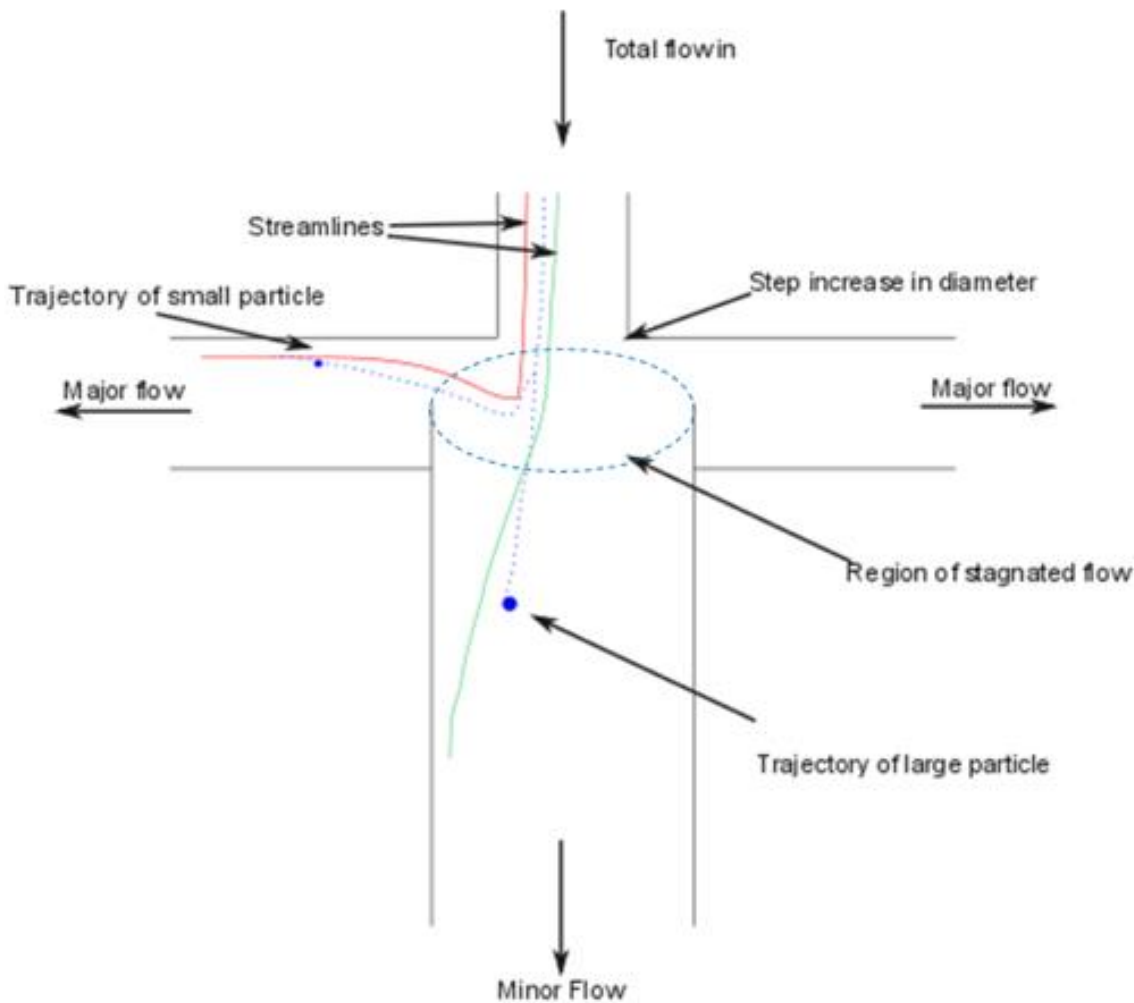


Figure 2.5: A virtual impactor schematic adapted from [49]

2.1.2 Transportation to the print head

No matter which atomisation technique is used, the aerosol is entrained within a gas stream and transported to the deposition head. Nitrogen is generally used as it is a cheap and inert gas [45]. The sheath gas forms a boundary layer around the aerosol that prevents the majority of the particles in the aerosol stream from contacting the tubing (Figure 2.6) [9]. The degree to which the gas acts as a sheath is proportional to the volume flow rate of the sheath gas [14]. However, it is inevitable that some material contacts the tubing during the transportation. To minimise the effects of this, polyethylene tubing should be used where an aqueous solvent is predominant and PTFE tubing used when an organic solvent is used. By choosing the tube material based on the solvent, any material that

contacts the tube wets to the surface, reducing its impact. The tube length should be minimised, and any radii maximised to reduce the head loss during the transportation. The aerosol stream can be heated during transportation to alter or evaporate the pre-cursor solvents, additives or particle suspending medium [9], [44].

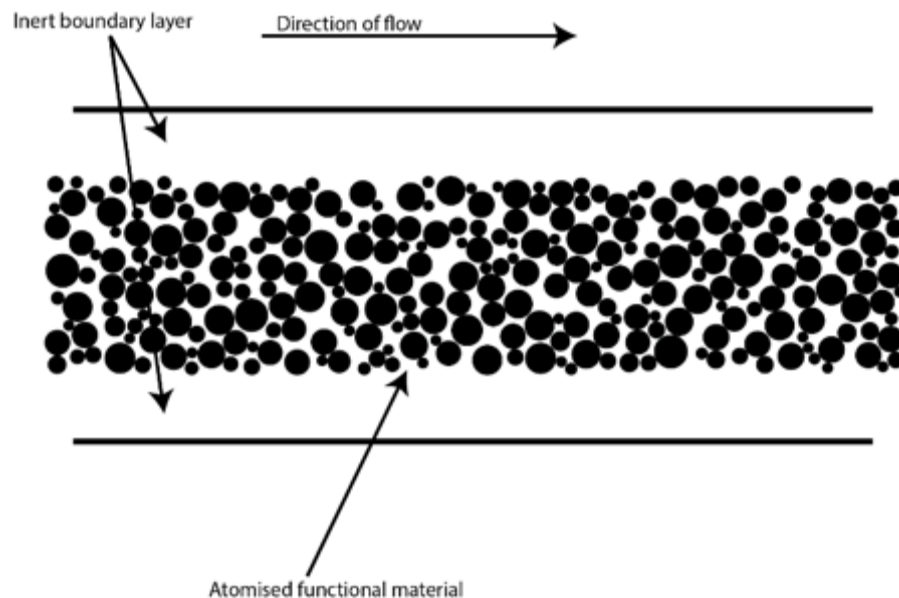


Figure 2.6: A cross section of the transportation tubing showing atomised functional material entrained in a gas sheath

2.1.3 Focusing and Deposition

The concept of dynamic focussing has been used in biological analysis for many years. Crosland-Taylor's reports on the focusing of wide columns of particles by injecting them into a stream of fast slow fluid moving in the same direction [50]. In the AJP process, the aerosol stream is aerodynamically focussed and accelerated in the deposition head as illustrated in Figure 2.7. An annular, co-axial sheath is formed between the aerosol stream and the sheath gas stream. This collimates the aerosol stream to a degree. The co-axial stream exits the flow head through a nozzle directed at the substrate. The sheath gas prevents contact of the aerosol stream with the nozzle or orifice walls. This reduces instances of clogging [44]. Hoey *et al.* contend that the stream isn't completely collimated [51]. The converging nozzle focuses the particles within the stream further. This is

because of inertial effects where the particles obtain a radially inward motion. This is retained downstream of the nozzle even as the carrier gas diverges radially outwards [52]. This means that there is a common focal point downstream from the nozzle exit, but also that particles diverge outwards past this point. Consequently, precise control of tip to substrate working distance is required. Figure 2.7 shows a diagram of the deposition head. The aerosol stream (1) and inert sheath gas (2) enter the deposition head. The Sheath gas flows co-axially with the aerosol flow creating an aerodynamic lens (3). The aerosol then exits the nozzle orifice and is printed (4).

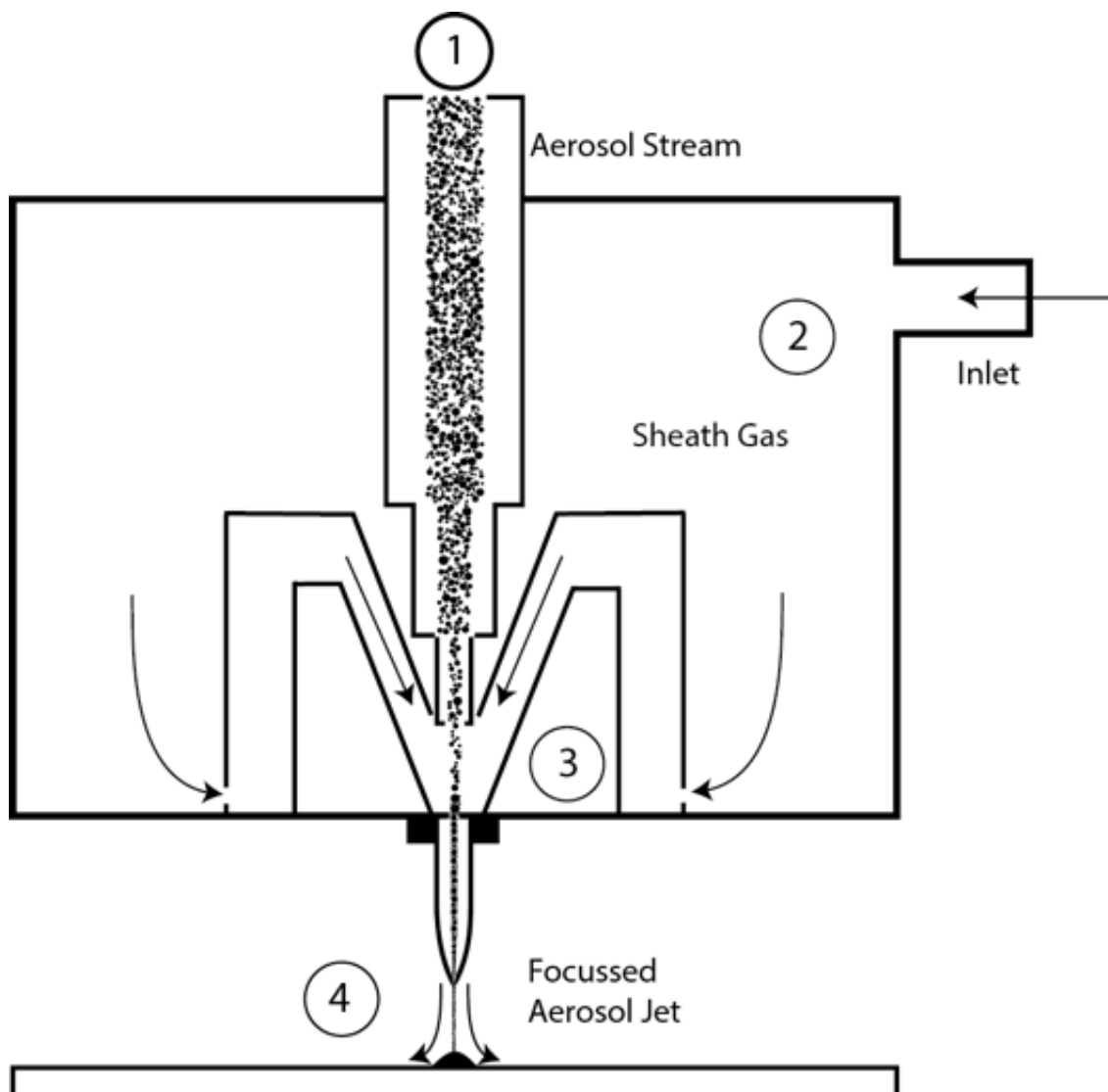


Figure 2.7: Deposition head. Adapted from [53]. The diameter and properties of the emerging stream (and therefore the geometrical properties of the deposit) are controlled by several adjustable process parameters, discussed in the next section.

The standard print head is capable of focussing an aerosol stream to as small as one tenth the diameter of the nozzle orifice [41]. The size of the orifice opening affects the range of line geometries that can be printed. In general, smaller nozzles print smaller thinner lines than larger nozzles. Within the limits imposed by nozzle size selection, the width of a printed line is controlled by the sheath gas flow rate and the flow rate of material from the atomising apparatus. From a practical point of view larger nozzles are harder to block and are easier to clean, meaning that larger nozzles should be preferred if wider lines are non-critical.

The jet is deposited continuously and a line is formed by moving the substrate in the XY axes, with some machines capable of movement in up to three further axes (Z $\theta\phi$). The speed at which the substrate is moved under the beam is an additional variable that influences the properties and quality of the lines. Thicker lines are produced by slow translation speeds, and increasing the speed generally results in a thinner line [54].

On/off Patterning is achieved by use of an external mechanical shutter located between the nozzle and the substrate. The shutter interrupts the continuous flow whilst the substrate is translated or rotated to the next prescribed position. The aerosol is collimated when the Z stand-off is between 2 to 5mm. There is a focal point where the beam is the thinnest and the position of this depends on the Stokes number of the flow. The stand-off height can be varied between 2 and 3mm without a significant change in diameter allowing printing on non-planar surfaces [44], [55]. Some configurations also allow the nozzle to be tilted, facilitating printing on a vertical surface, illustrated in Figure 2.8 [55]. The design freedom this enables has been showcased by Optomec with a video on their website printing a circuit board onto an golf ball and an egg shell [56].

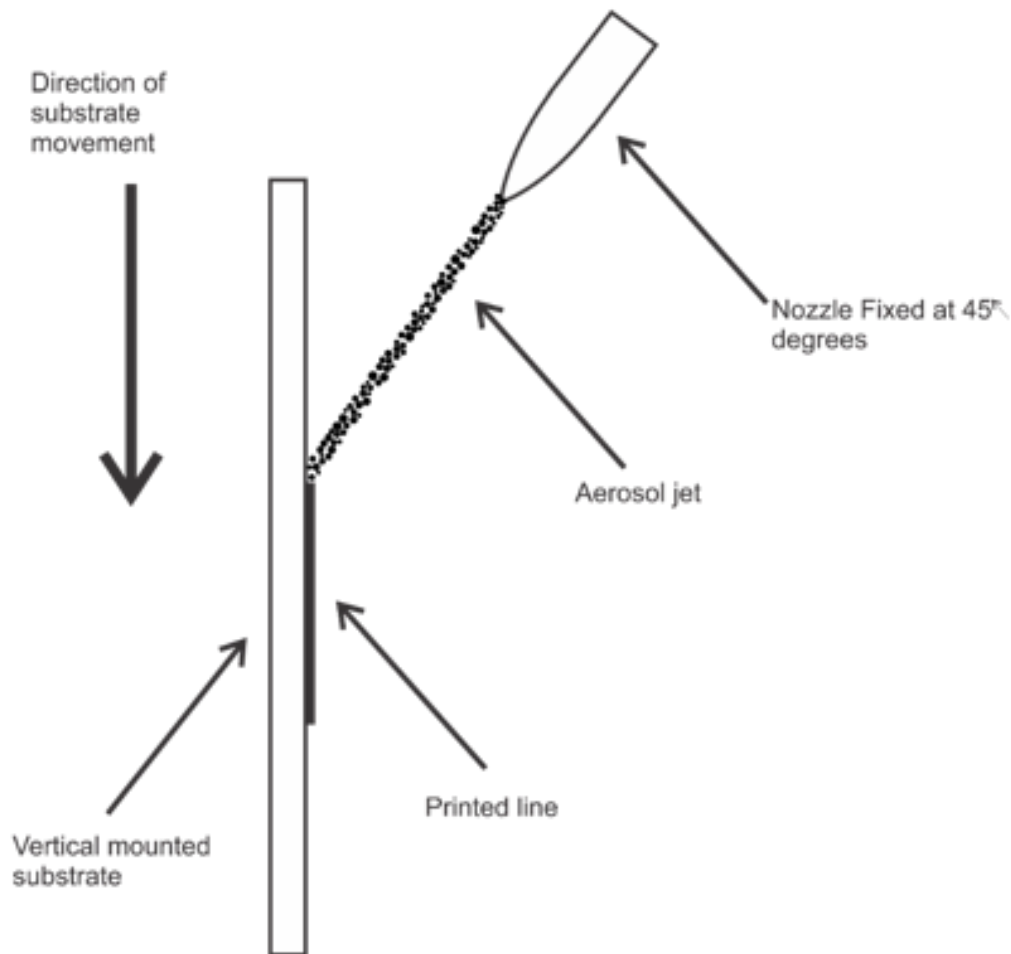


Figure 2.8: Tilted nozzle printing

Ideally a 3-dimensional measurement of the deposit is taken, analysing the cross sectional area, maximum height and width at half maximum height (WHM) [53]. If 3-dimensional measurements are not available lines are characterised by their width under an optical microscope.

2.1.4 Print Parameters

The physical line width of the deposit depends on several parameters and can approach single micrometre figures under optimal conditions. Goth *et al.* were the first research group to publish a study on factors to be considered when optimising the deposit characteristics for a silver nanoparticle ink. The adjustable process parameters pertinent to both atomisation methods are the carrier gas

flow rate, sheath gas flow rate, nozzle diameter, working distance, stage speed, and stage temperature [57].

Optomec assign the sheath gas as the variable responsible for line width [58].

Mahajan *et al.* [53] contend that to control the width, the key variable is the focussing ratio (FR) defined as:

$$\text{focusing ratio (FR)} = \frac{\text{sheath gas flow rate}}{\text{carrier gas flow rate}} \quad (2.1)$$

By modifying focussing ratio, flow conditions and stage speed, lines can be deposited ranging in width from 10 μm to 300 μm in a single pass [59]. To create trace geometries wider than a single line, multiple traces can be applied with a slight overlap or with infill patterns similar to other direct write processes [60].

There are several other papers which contain small sections on the factors that can affect printing. When using ultrasonic atomisation additional parameters are the atomisation frequency and temperature of the atomisation chamber. Pneumatic atomisation must also consider the exhaust gas flow rate. These parameters affect the size range of the printed particles so can be tuned to improve print quality [61]. Printing must consider the compatibility of the surface energy of the substrate and the majority solvent. A mismatch in the adjacent surface energies can have a dramatic and deleterious effect on overall print quality [59]. Design properties can also have an influence on the print quality. The number of layers, design layout, and cornering radii are all important factors to consider when producing a pattern [46]. A summary of all the factors that affect the deposition discussed in the literature is presented in Figure 2.9.

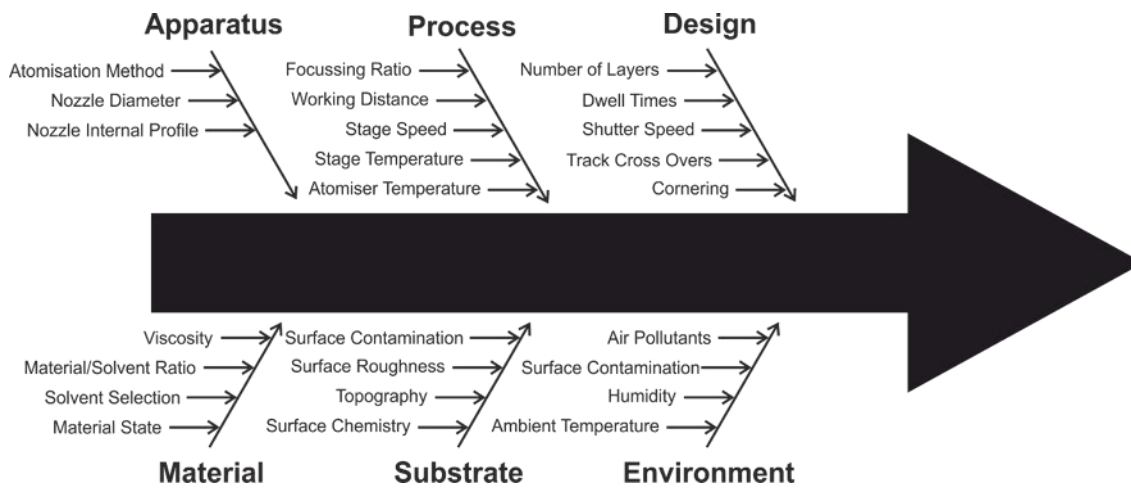


Figure 2.9: Factors affecting deposition. In addition, when using ultrasonic atomisation the atomiser current is a variable, when using the pneumatic atomiser the exhaust gas is a variable [46], [54], [57], [61]–[63]

2.1.5 Substrate Wetting

A key processing requirement which is highlighted in the studies and can be universally applied is the substrate wetting characteristics. Ink spreading on the substrate affects the geometry of the deposit. Vunnam *et al.* specifically investigate the effects of air plasma and self-assembled monolayer treatments on the adhesion of printed silver ink on an indium tin oxide substrate. They highlight that controlling the surface energy can influence ink spreading on the solid substrate. Other factors that influenced the geometry were the ink solvent selection and sheath gas flow rate [65]. Many other surface treatments exist to alter the surface energies, which could be applied to different manufacturing requirements [66].

2.1.5.1 PDMS as a Printing Substrate

PDMS is primarily an engineering material which is becoming more prevalent as a cell culture substrate. PDMS is gaining popularity as a cell culture substrate, as it is non-cytotoxic, biocompatible, and easy to process [67]. A range of advantages for cell culture are summarised in Table 2.1 **Error! Reference source not found..**

Table 2.1: Summary of useful PDMS properties

Area	Property	Advantage for use as a cell culture substrate.
Physical	0.25MPa shear modulus and 0.5-1MPa Young's modulus, characteristic of a stiff elastomer [68][69].	Can be released from moulds with ease. Sub-micrometre scale features can be produced through cast moulding [70]. Can be reversibly deformed. Conforms to complex topological surfaces
	Optical transparency from deep UV to near IR	Compatible with optical detection techniques that are widespread in biological assays
Surface chemistry	Hydrophobicity – but can be treated to become hydrophilic using well developed techniques	Hydrophobic surfaces can be used as cell repulsive zones to direct growth. Hydrophilic surfaces are compatible with the printing method.
Bulk chemistry	Chemical inertia	Does not react with many solvents. Able to be cleaned.
	Non-permeable to water	Will not swell when submerged
Accessibility	Non-toxic	Able to support cell culture
	Widespread availability	Available to many laboratories allowing direct comparison of results
	Low capital and manufacturing costs	Accessible to many scientists.

The chemical nature of PDMS is a polymer back bone based on a repeating unit of a dimethylsiloxane group, shown in Figure 2.10 **Error! Reference source not found.** In the literature, the term 'PDMS' usually refers to the most commonly used variant, commercially available silicone from Dow Corning. This variant is 'Sylgard 184' and is specified as having greater than 60% by weight dimethyl-vinyl terminated molecular structure. Sylgard 184 is favoured as it contains no filling additives and is seen as a 'pure' PDMS based material. Other commercially available PDMS based materials are also used for microfluidic devices and differ

in the terminal groups or filler material used. These changes may affect the chemical interaction or limit the topographical alterations of the devices.

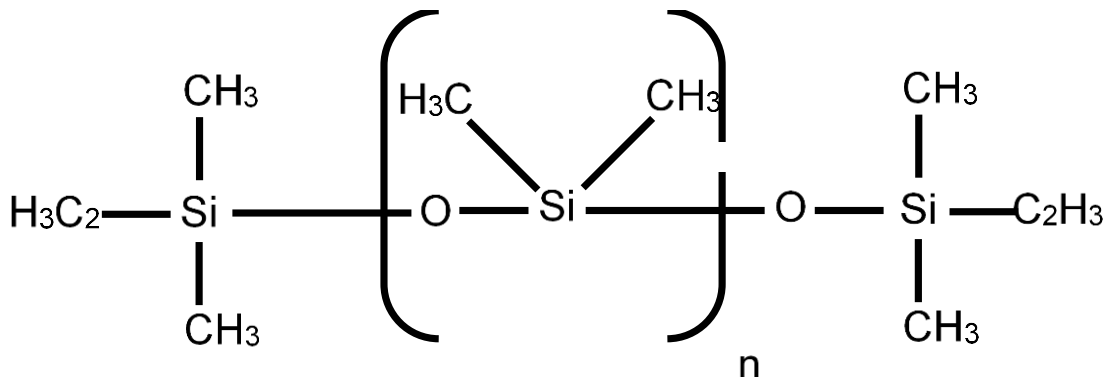


Figure 2.10: Sylgard 184 Chemical Structure

There are some challenges with surface patterning PDMS that are inherent to its chemical nature. The low modulus of Sylgard 184 can result in unstable features if the aspect ratio (defined as the ratio of width to height) is outside a certain range. This collapse can be due to gravity, adhesion, or capillary forces. Therefore, any topographical features on the surface are limited by their achievable aspect ratio [71], [72].

The methyl/vinyl terminal group of PDMS is inherently hydrophobic, and reacts non-specifically with other hydrophobic substances, such as drugs or proteins used regularly in biomedical research [73]. The PDMS surface has also been shown to leach un-cross linked particles into solutions [74].

Surface chemical alterations result in only temporary hydrophilicity. After a few hours (as short as 2) the surface begins to revert to a hydrophobic state, and eventually returns to its original hydrophobic state. The phenomenon is described frequently and is termed 'hydrophobic recovery' [75], [76].

2.1.6 Defects

Satellite deposits are common issues in jetting processes and AJP is no exception. Satellite deposits are described as additional, unwanted deposits

formed either during the ejection of material from the nozzle, or due to 'bounce' as the jetted droplets hit the surface [77].

A similar but distinct defect which is unique to this process is known as overspray or sputtering. Figure 2.11 illustrates the aerosol exiting the print head. Hoey *et al.* investigated the overspray phenomenon and concluded that deposits outside the main region are not due to droplet bounce. Rather, on impact with the substrate, the sheath gas must change direction to maintain its momentum, in a similar scenario to the impactor plates described previously. Whilst most of the aerosol is deposited in the focal spot, overspray is caused by smaller droplets ($<0.1\mu\text{m}$) that do not have enough momentum to overcome the sheath gas. These droplets are carried outwards by the sheath gas and are deposited outside the intended focal point. The distance between the nozzle exit orifice and the top of the substrate is known as the z stand-off. The overspray is worsened if the z stand off is not within the tight focal spot of the aerosol beam [78], [79].

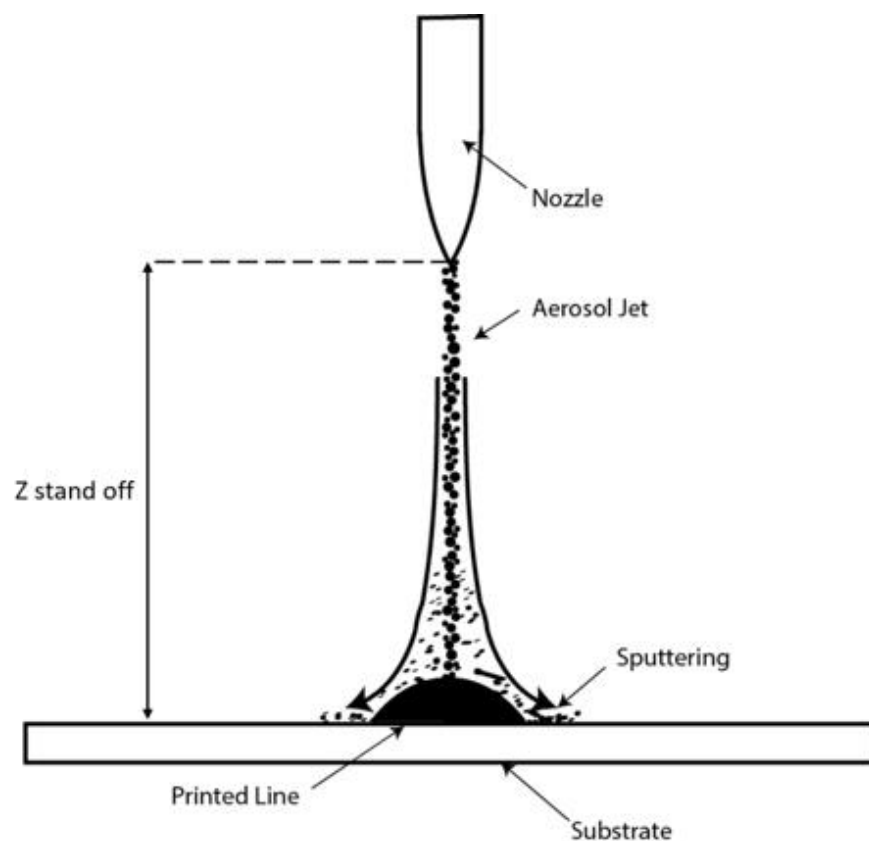


Figure 2.11: Deposition of aerosolised material onto the substrate surface.

Figure 2.12 is a scanning electron microscope (SEM) analysis of an example printed line between the yellow lines a confluent deposit was printed, however at both edges of the print there are regions of smaller particles which can be observed with a high contrast compared to the underlying substrate (overspray).

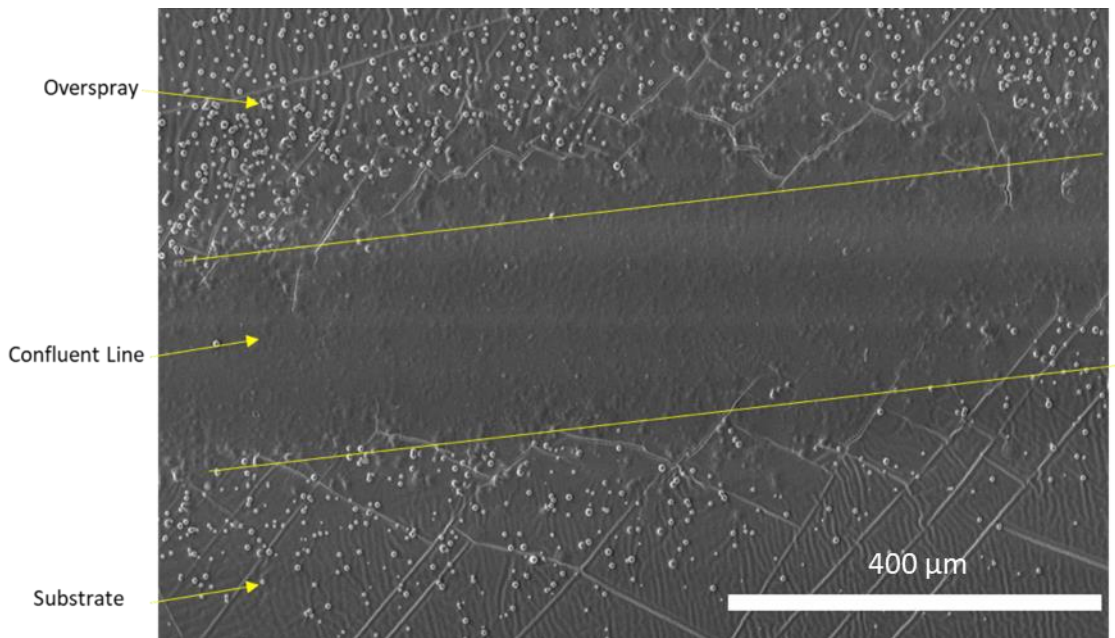


Figure 2.12: SEM analysis of a line showing the overspray to the sides of the printed features.

Several tactics have been identified to overcome satellites and overspray including: increasing material viscosity, use of a co-solvent [42], reducing the stand-off distance, depositing into channels [79], and adjustment of the process parameters to affect the volume of deposited material [55], [80].

Other defects that can affect line quality, shown in Figure 2.13, include line pinching and bulging, associated with the improper interaction of sheath, atomiser and substrate scanning speed, wetting interaction between the material and substrate, or substrate cleanliness. The optimal parameters such as sheath gas pressure, atomising pressure and exhaust pressure may differ based upon the viscosity of the ink, particle size and the solvent used [55].

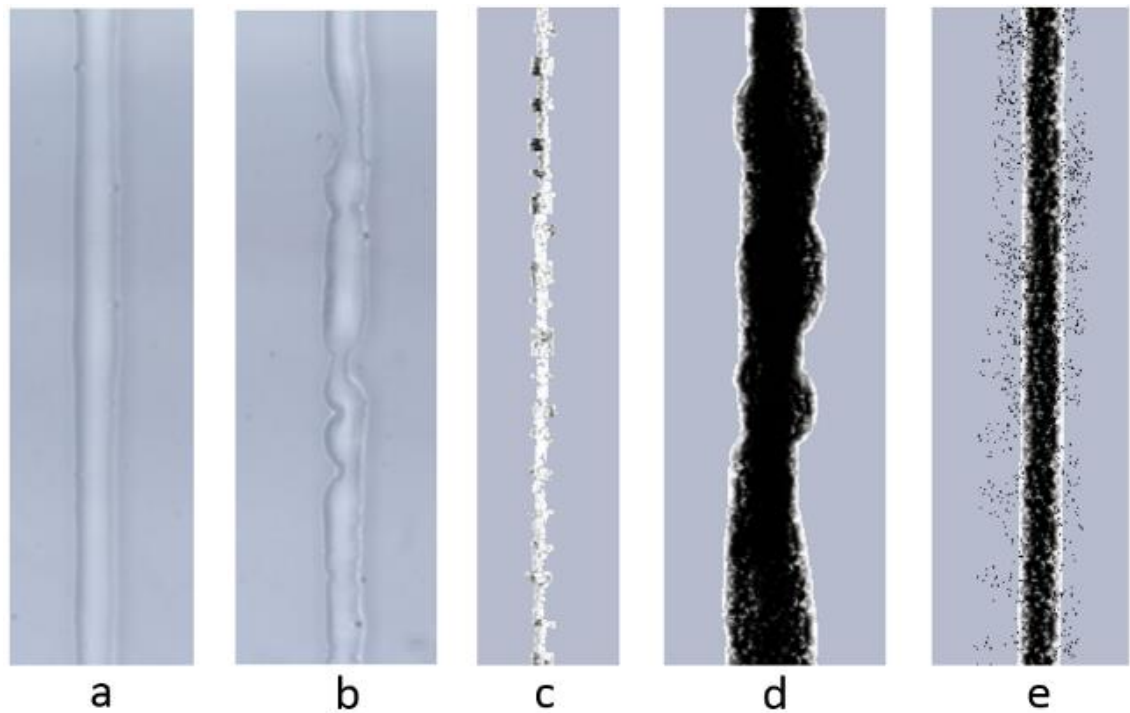


Figure 2.13 - Deposit examples (a) good, (b) pinching cause by substrate contamination, (c) pinching caused by insufficient material flow rate, (d) bulging cause by too high material flow rate, (e) overspray caused by high sheath gas [47].

In general width measurements should exclude any defects and characterise only the functional part of the line. When material flow rate is very low a complete line may not be produced at all. The aerosol stream can be heated to alter properties or evaporate the solvents and additives or the particle suspending medium.

2.1.7 Post Processing

Post deposition processing may be required to give structures with the desired electrical and mechanical properties. This requires additional cost and time and can limit the ability to print on some substrates. The specifics of these treatments depend upon the chemical nature of the precursor, the potential for interdiffusion between the layers, the stability of the substrate and the engineering requirement of the final targeted product [79]. When the ink is deposited onto the substrate some, but not all, of the solvent evaporates. After deposition a drying or sintering phase is common to drive off remaining solvents and solidify nanoparticle deposits into a single line [55]. Thermal sintering is an important post processing step when printing with nanoparticle inks. It is used to densify the printed features

by heating, without the phase change to liquid [81], [82]. AJP discussion of sintering is usually around the sintering of metal nanoparticles, but the principles can be applied to any nanoparticle inks. This is achieved either by bulk heating the build platform or putting the substrate into an oven. For temperature sensitive substrates, some configurations have a laser post processing capability built in to locally dry and sinter the deposit without affecting the surrounding substrate [83]. Other local sintering options include *in situ* line sintering through electrical sintering [82], and selective exposure to a xenon light source [84]. These approaches have been shown to enable the sintering of silver nanoparticle tracks on a thermally sensitive polycarbonate substrate with limited substrate damage, increasing conductivity by a factor of 100 whilst maintaining flexibility [85]. In addition, by depositing larger features, the requirement for sintering has been bypassed and a nanoparticle deposit used in an electrical circuit [86].

Higher sintering temperatures can speed up the process, however thermal sintering has presented issues with interconnect cracking due to differences in the coefficient of thermal expansion between the ink and substrate [57]. Further to this, multi-layered (>10) printed silver tracks peel during sintering as a result of residual stresses [87]. The sintering temperature can also influence the granular structure of the deposit [88].

2.2 Applications of Aerosol Jet Printing

A range of applications have been identified for AJP both as a standalone technology and as a constituent part of a hybrid system. AJP was developed primarily to print electronic materials on non-planar substrates, and much of the literature is focussed on these applications. Figure 2.14 is a summary of the applications-based studies reviewed in this thesis. Looking at the number of studies in each category, it is evident that biological applications are

underrepresented in the literature. Indeed, if the overarching category of 'electronics' was used (in place of all the categories highlighted in shades of blue) 92% of the reviewed studies would be contained within that category. This highlights both an opportunity to develop the technology and methods for biological applications, and the lack of precedent for such projects.

However, some of the information contained within the electronics papers is useful, aspects such as materials formulation, initial printing parameters, and the techniques used to optimise machine performance can be extracted for use in this thesis.

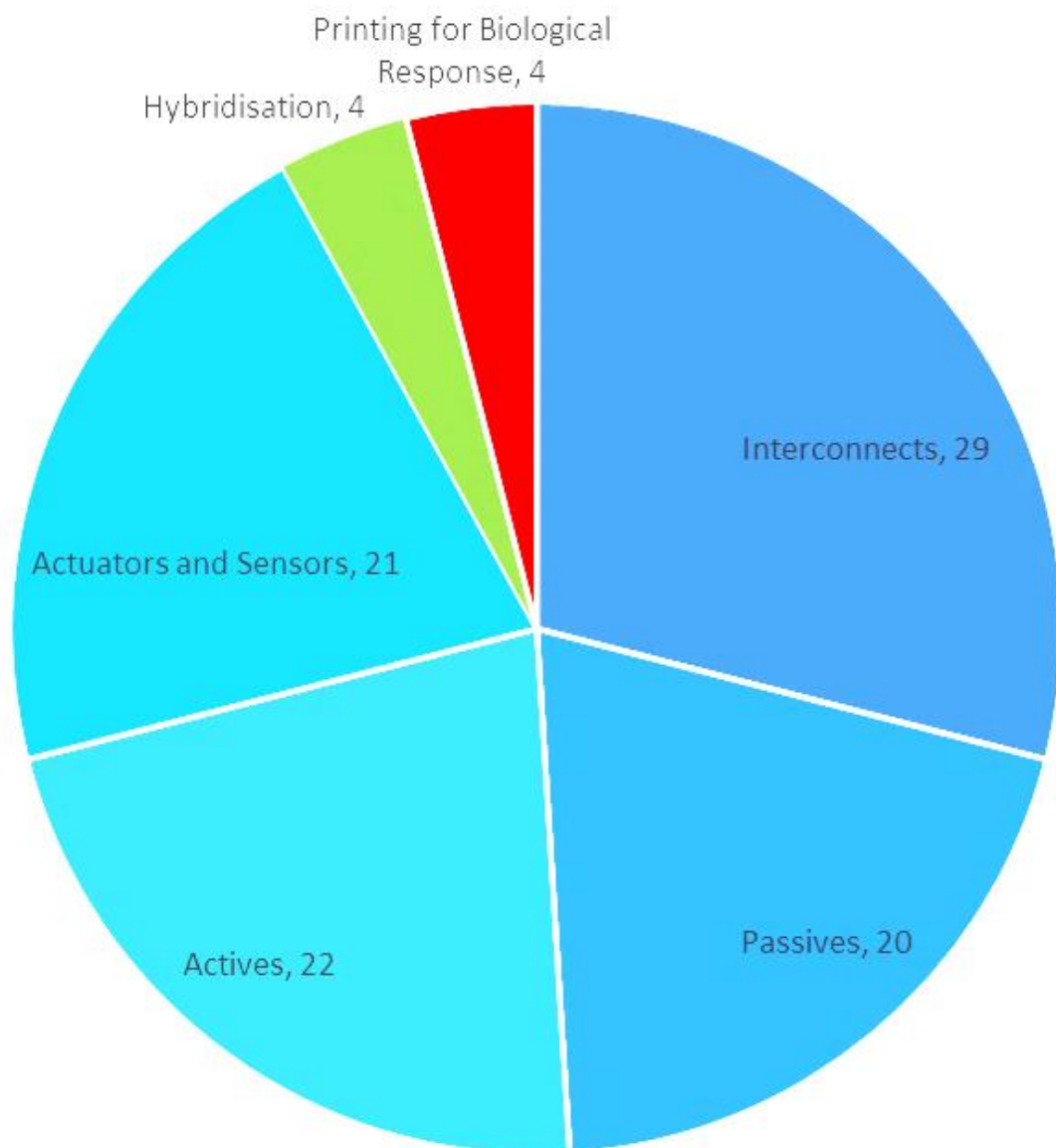


Figure 2.14: Representation of the categories of Aerosol Jet literature

2.2.1 Interconnects

AJP has been shown to print conductive deposits to connect two or more electronic components, termed interconnects. The simplicity of interconnects has made them the primary structure for the evaluation of new conductive materials for AJP.

Silver nanoparticle ink is the most commonly used and best characterised AJP material. When printing with metal nanoparticle inks, oxidation of the material is a key issue due to the large surface area of the nanoparticles. This limits the applicability of reactive materials such as copper [89]. Silver is therefore a useful ink as it can be deposited and sintered in an oven without oxidising, even in nanoparticle form [90]. Silver and copper nanoparticles have uses outside of interconnects, a relevant application being used as an antimicrobial coating [91], however the application to *in vitro* models is limited by toxicology concerns of the nanoparticle materials [92].

From a process standpoint the studies described in this section highlight some key abilities of the apparatus. The ability to print micro scale functional structures with AJP was proven by printing 35 μ m interconnects between LEDs in a transparent heads-up display (Figure 2.15) [93].

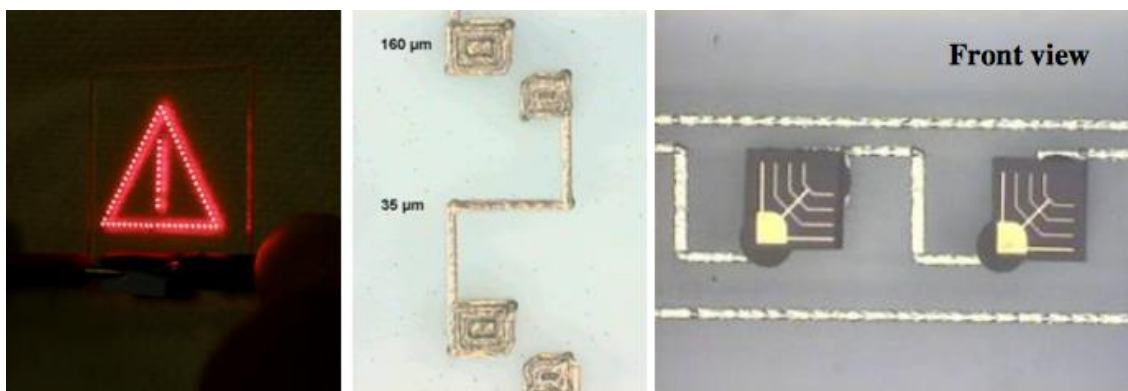


Figure 2.15 Printed silver interconnects in a head-up display [93]

The interaction of AJP printed structures with existing topography was shown by printing over conformal geometries to produce multi-layer circuits for electronic

packaging. Vertical interconnects were printed into voids in trapezoidal and reverse-trapezoid substrate geometries (Figure 2.16) [87], [94]. In addition printed silver ink has been used in a wire bonding application [95], and by using ultrasonic energy to sinter the tracks, printed silver was joined to componentry and other circuitry on both glass and polythalamide substrates [96]. Printed silver ink has also been used to produce contact pads for micro electromechanical systems [97].

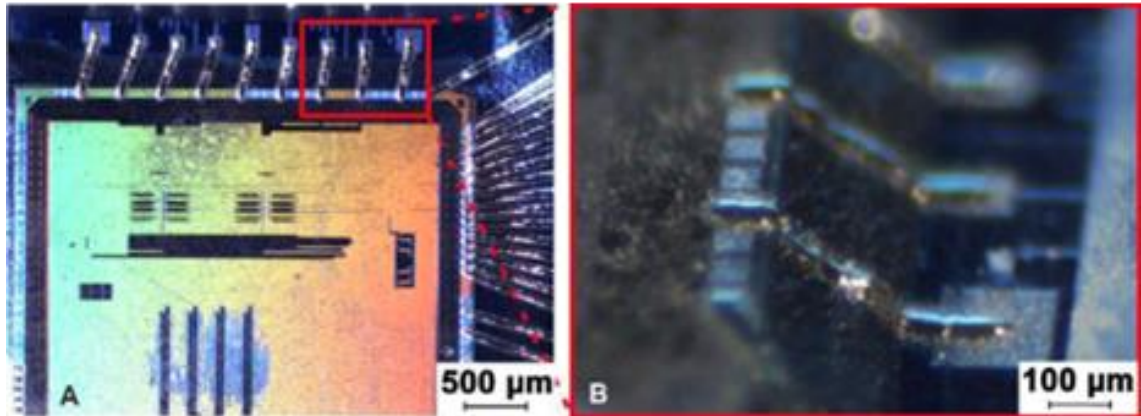
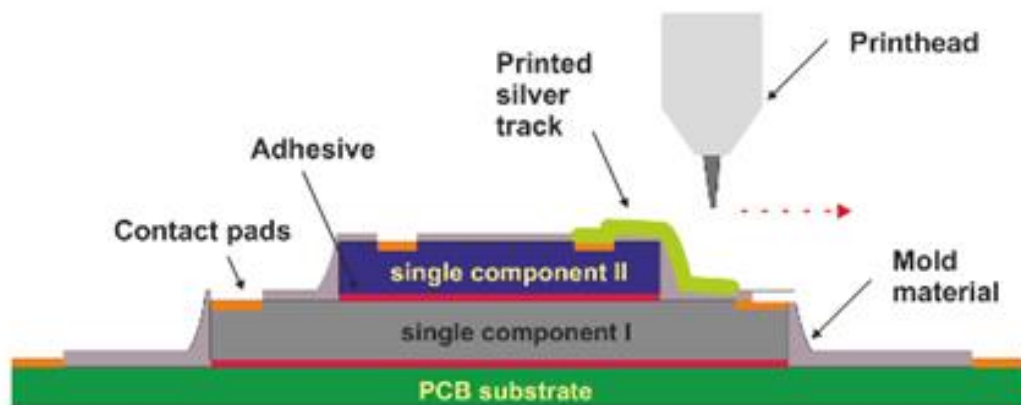


Figure 2.16 Interconnection between stacked PCB components [87]

The reliable microscale printing afforded by AJP is especially well suited for fine pitch electronics applications [40]. For example, decreasing the width of printed features resulted in improved device performance in the current collection grid of an inverted, ITO-free solar cell [54]. A more comprehensive study on the optimisation of high resolution ($20\mu\text{m}$), high aspect ratio silver lines (0.1) was also performed [53]. The finest reported printed conductive metallic lines have a width

of $10\mu\text{m}$, measured by optical microscopy, and were printed with a silver nanoparticle ink [64]. These studies prove the ability of the apparatus to produce fine pitch high aspect ratio structures. Fine pitch structures such as these are analogous to surface treatments used to guide cell movement in *in vitro* models [27].

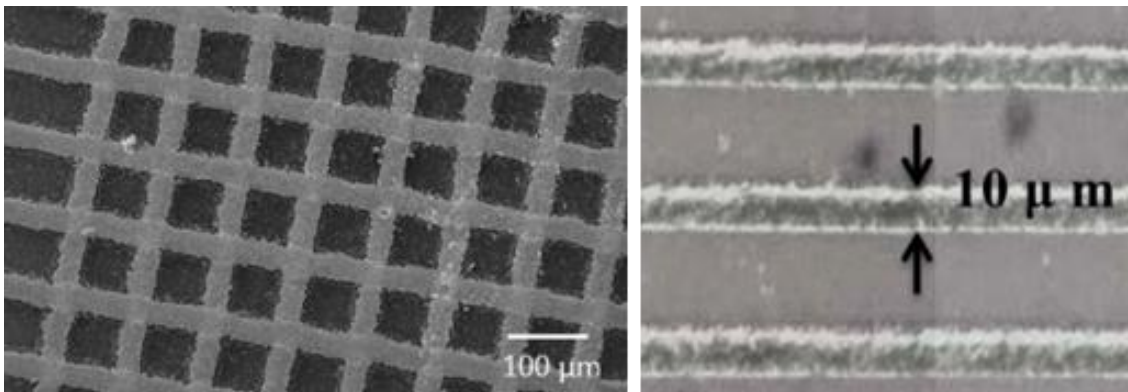


Figure 2.17: Printed silver tracks (A) $20\mu\text{m}$ grid [50] and (B) $10\mu\text{m}$ tracks [75]

A novel transfer process has been developed to embed sintered silver lines in a temperature sensitive substrate (Figure 2.18). The nanoparticles are first printed on to a low energy substrate that can withstand the thermal sintering cycle. After sintering a second substrate is cast on top, left to cure, and then peeled. The printed interconnects release from the initial, low energy substrate and are embedded in the final temperature sensitive substrate. Therefore, the final substrate is not exposed to high temperatures. This print-transfer-peel technique has also been applied to flexible substrates [98]. A common material used in biological studies is polystyrene, a temperature sensitive thermos plastic [99]. Methods such as these may facilitate thermal treatments onto substrates for biological applications.

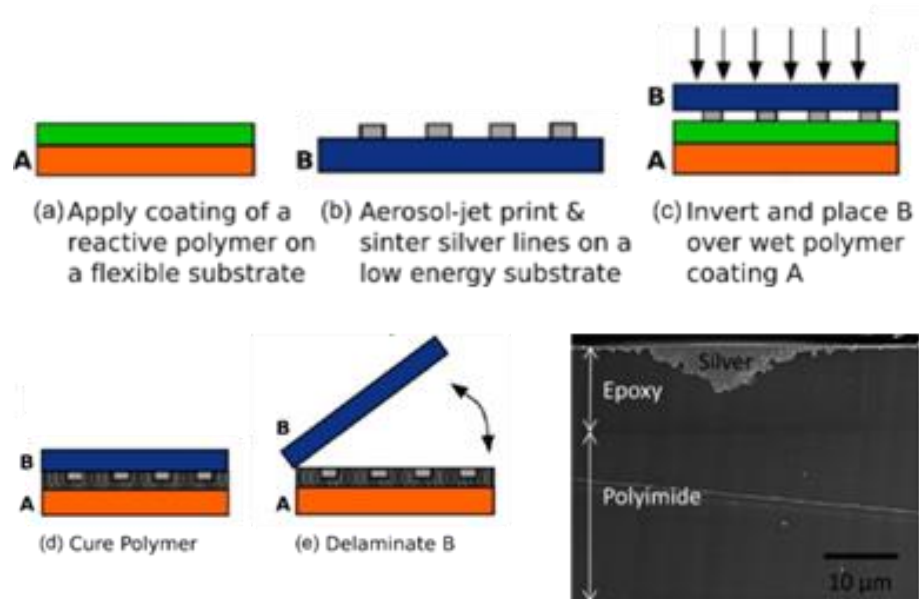


Figure 2.18: Transfer process for flat conductive tracks adapted from [100]

2.2.1.1 Flexible Substrates

AJP has also been used to print electronics on flexible substrates. A common issue with printed interconnects is this bending endurance of features [101] [102]. Flexible materials such as PDMS are used in lab-on-a-chip and microfluidics applications, however these are not normally submitted to the same bending cycles as flexible electronics applications [73], [103], [104].

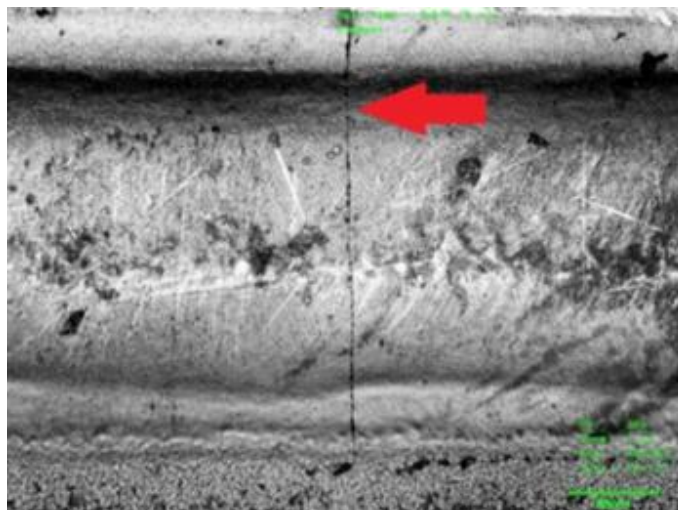


Figure 2.19: Cracks in printed tracks after 10,000 cycles, the arrow highlights the crack [101]

2.2.2 Passive Electronic Components

Passive electronic components do not increase the net power of the circuit, and the output is not controlled by another signal. Examples of passive components have been printed by AJP are resistors [43], capacitors [105], [106] and inductors [107]. Their relative simplicity makes them an achievable application if a conductive material can be printed reliably. Printing passive electronic components reduces their space claim and allows greater integration of electronic circuitry with fewer processing steps. Notably, the ability to print onto non-planar surfaces and steps surpasses all other technology in this area. This treatment of non-planar surfaces is also useful in microfluidics applications. It is challenging to pattern non-planar substrates with template based methods such as photolithography and soft lithography [32], [69].

For example, when printing an antenna structure, AJP has been used to produce both the 3D shape from the dielectric, and the functional antenna geometry [55]. The structure was printed using a UV curable dielectric to build a 3D 'pillar' onto a substrate, before functionalisation using a silver nanoparticle ink. Changing the orientation of the print head (by tilting it 45 degrees) enabled printing up a vertical wall [108]. Similar techniques have been used to produce radio frequency identification tags [109], scaled mobile phone handset antennas [110], other radio frequency antennas [111], modulated transmission lines [112], and three-dimensional coplanar waveguides [113]. Other wideband radio and microwave frequency components such as a four stage Wilkinson combiner/divider have been described [114], [115], as have terahertz band filters [116] and notch filters [117]. This vast range of applications showcase the flexible nature of the technology, and techniques such as printing on non-planar geometry and up

vertical walls may find use in biological fields such as multilayer microfluidics which currently require complex alignment mechanisms [118].

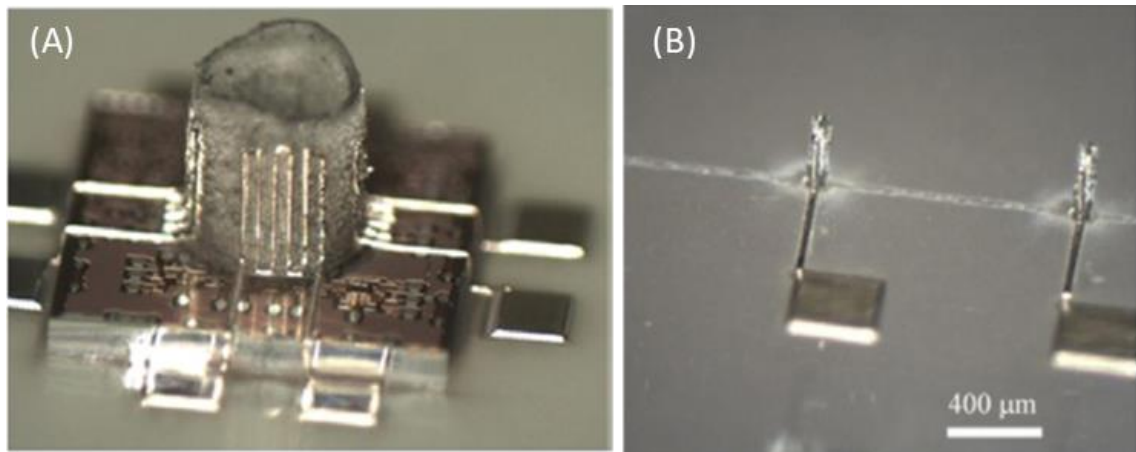


Figure 2.20: (A) Vertical antenna on a dielectric pillar (B) antenna microstructures [108]

2.2.2.1 Secondary Processing of Aerosol Jet Printed Features

Aerosol jet printed features have been used indirectly as a precursor step for another manufacturing process. For example, AJP has been used to deposit nanoparticles as a seed layer for secondary light-induced-plating on glass and silicone substrates for the front side metallisation of solar cells [44], [119]. This two-step process produced high quality electrical and mechanical contact with the silicon solar cell. The printed nanoparticles defined the positions of the interconnects, and the light-induced plating provided a higher conductivity finger for more efficient transfer of charge. The team at the Fraunhofer Institute for Solar Energy Systems have continued to develop the seed-plating process through investigation of scale-up potential [119] and material development [120], [121]. Indeed, many aspects of photovoltaic cells, including the electrodes, contacts and functional organic photovoltaics can be produced by AJP [122]. These are beneficial as their small size reduces shadowing on the cell [123]. In addition, AJP has been identified for its ability to print films of material over large areas for light harvesting [124], [125]. It is not common to see the combination of in large area patterning over large areas (without rastering) with fine feature

printing a single manufacturing apparatus. Especially in biological applications large area surface treatments can be used to affect the culture, whilst fine features direct some specific cell growth characteristics. This can be applied in, for example, a neuromuscular junction where the neurons must be specifically guided into the muscle tissue [126].

An innovative patterning method was to spin coat a water soluble polymer onto the substrate then selectively depositing a fluoride solution by AJP. The reaction of the fluoride and polymer locally produces hydrofluoric acid which is used to etch the substrate. A post rinse in DI water rinses off the acidic polymer layer leaving a chemically etched substrate. This research was used in a photovoltaics application but could easily be adapted to provide topographical cues on cell culture substrates [127].

2.2.3 Active Electronic Components

Active electronic components either require power to work or can introduce net power into a circuit. Active electronic components tend to be multi-material structures which are more complex than electrodes or passives electronics.

Transistors are ubiquitous in modern electronic devices, which makes them a key component for producing functional printed electronic circuitry. As such, functional printed transistors have been repeatedly proven by multiple research groups, for a variety of applications [128]–[133]. A challenge for printed transistors is the development of a high capacitance dielectric ink to perform as the gate insulator in thin-film transistors. Accessible gate dielectric ink candidates have low-resistance to organic solvents, which makes them hard to use in printing inks for solution-based processes such as AJP. More chemically resistant dielectrics, such as polyvinyl phenol and polyimide, require curing temperatures

exceeding those of low cost thermoplastics materials that are often used as substrates [134].

AJP has been shown to print high value materials such as high purity single-walled carbon nanotubes. [129]. In the current research focussed on carbon nanotubes for AJP, the researchers primarily discuss the importance of solvent selection and dispersion of inks. Specifically for carbon nanotubes, a toluene and xylene co-solvent mix is used, but solvent selection is based on the compatibility with the functional material and substrate [135]. Once efficient dispersion techniques have been developed, the technology has been shown to be scalable [133].

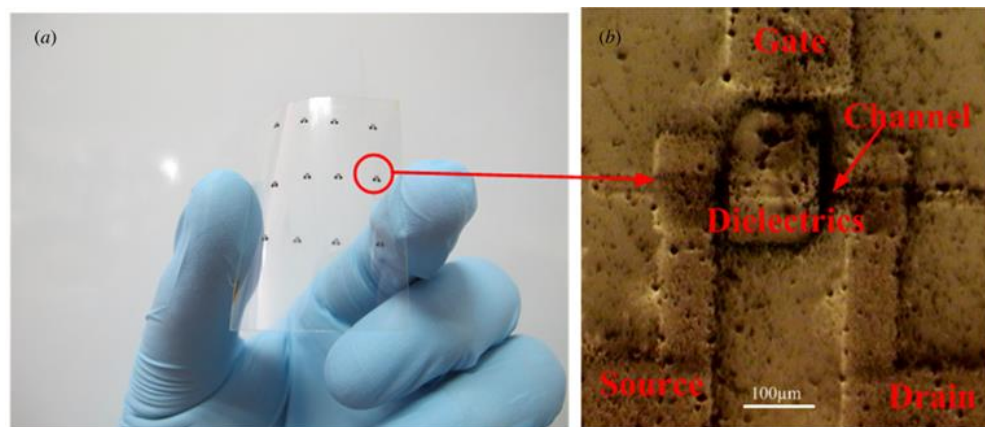


Figure 2.21 All carbon based field effect transistor array on a flexible substrate [136]

2.2.3.1 Functional Material Doping

To print materials with advanced functions some researchers dope a majority carrier component with a minority functional component. For example, ion-gels, a polymer matrix blended with ionic liquids, show promise as a key material in fully printed transistors [128]. Ion-gels are used in the gate insulator material in these transistors. A series of transistors in the form of a ring oscillator has been printed fully using AJP [137]–[139].

In some cases, the function can be altered without changing the processing conditions by changing the dopant. Figure 2.22 shows red, green and blue organic light emitting diodes (OLEDs) that have been manufactured using a

doped material. The colour can be controlled by dissolving a host particle into a solvent mix and adding various emitting dopants. As the majority component is unchanged, the AJP print parameters do not change when printing 30 μm features of each colour [140]–[142].

An analogous material used in biological applications are the cell laden polymer gel blends used in bioprinting [143]. For example, cell laden polymeric gels have been used in an extrusion based bioprinter to form three-dimensional structures [144]. In this case the majority component is the gel matrix, and the minority components would be the salts, proteins and cells themselves [144]–[146].

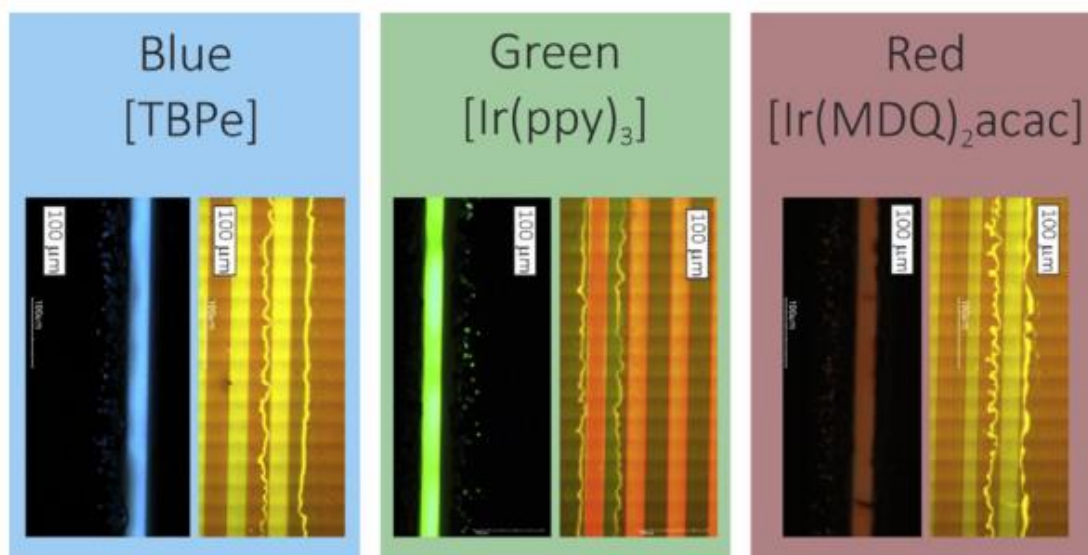


Figure 2.22: Printed blue, green and red OLEDs [140]

2.2.4 Actuators and Sensors

AJP has been shown as an effective technique in the manufacture of high resolution actuators and sensors on conformal substrates. AJP holds promise for the development of a multitude of sensing and actuation technologies as it enables fast turnaround time for new designs and deposition of a range of materials onto non-planar substrates. The range of compatible materials presents an opportunity to create complex devices in a single processing step. Fully printed sensors are good examples of multi-material structures.

Strain gauges are patterned conductive traces that change resistance in response to mechanical strain. Using the AJP process these components can be printed directly onto the surface of the component. To produce a strain gauge on a conductive surface a polymer isolation layer was printed before using a silver ink to produce the strain gauge geometry (Figure 2.23) [147]. A similar approach has been adopted by Zhao *et al.* to embed silver ink strain gauges in carbon-fibre composite devices without a significant change to the mechanical properties [148]. Their work suggests AJP is a promising approach for embedded sensors; further work is required to remove defects, optimise curing processes and investigate the interface between the sensor and carbon fibre prepreg [148]. Recently, a multi-material ceramic and metal strain sensor for high-temperature applications has been manufactured [149]. A similar approach to separate the functional component from the substrate surface has been used in cell culture applications. An initial layer of 'extra cellular matrix like' laminin was applied by electrospinning before a functional treatment was applied by ink jetting [10]. AJP surpasses this capability by enabling both steps in a single machine.

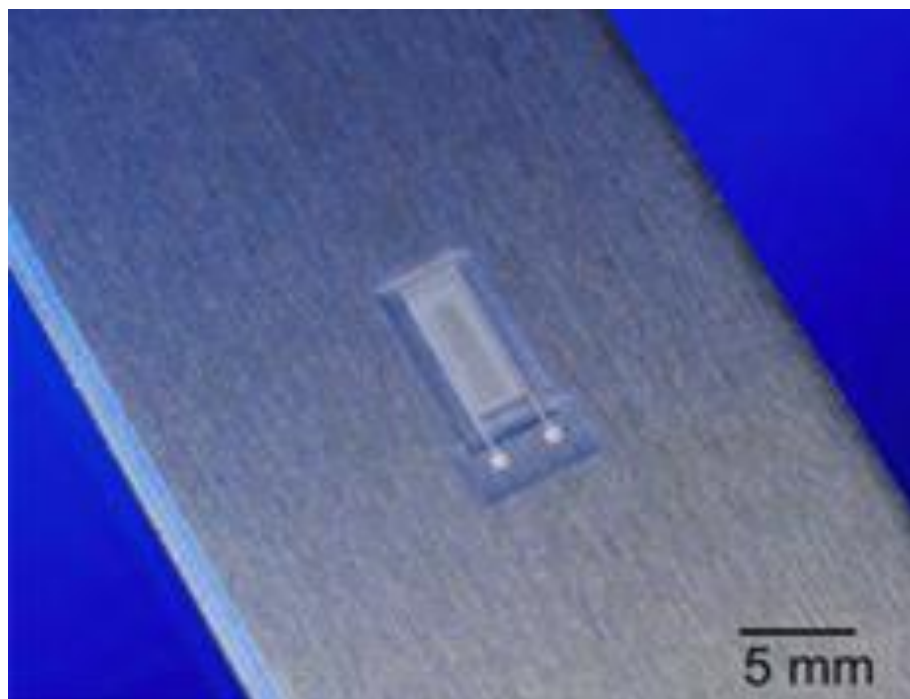


Figure 2.23: A printed strain gauge, printed on top of a polymer isolation layer [147]

An interdigitated capacitive touch sensor has been manufactured by printing silver nanoparticle ink onto a glass slide (Figure 2.24) [150]. These patterns can be printed onto non-planar and flexible substrates without a degradation in performance and exhibit similar performance to those produced by template based methods [151]. In a novel application, a printed interdigitated structure has been demonstrated to electrostatically adhere small molecules for use as a gripper in miniturised robotics [152].

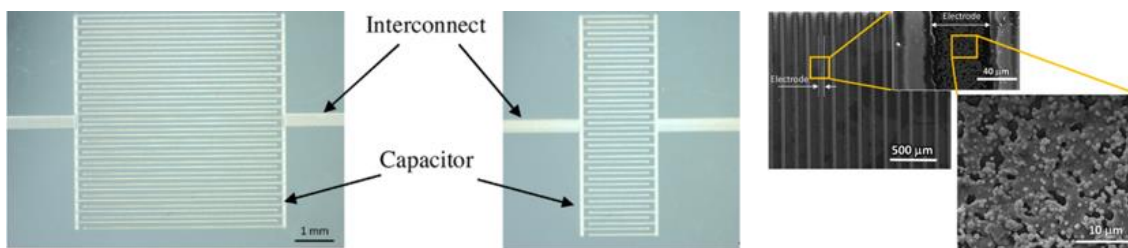


Figure 2.24: Printed interdigitated capacitive sensor [150]

Multilayer (>2) devices have been demonstrated in the form of chemical and photodetectors. The manufacture of low-cost, flexible paper based detectors using a combination of AJP and Ink Jet printing has been shown [153], [154]. PEDOT:PSS and P3HT:PCBM polymer blend layers were printed; the silver bottom electrode was deposited using inkjet printing; and the DNA biopolymer was drop-cast. A printed nanowire network of zinc octaethylporphyrin has been shown to have a high photosensitivity [155], and a cost efficient light sensor device was printed from a nanoparticle solution [156]. A similar multimaterial sensor was produced by combining Aerosol Jet and Ink Jet printing steps [157]. Quantum dots have been shown to be sensitive to deep UV light and have been printed onto several substrates [158]. The production of complex sensors shows the potential of AJP to be used in the manufacture of low-cost, flexible devices. Further, the ease at which AJP can be integrated with other processes to improve build times and functionality shows promise.

Multilayer dielectric elastomer actuators have been produced fully using AJP. These layered structures consist of a dielectric sandwiched between compliant electrodes. The layer-by-layer approach of AJP, combined with its ability to produce films, makes it a promising approach to produce actuators in a single processing step [159], [160].

Semi-conducting single walled carbon nanotubes have been shown to change their conductivity in response to the presence of hydrogen. Consequently, researchers have been developing systems that use this to produce low-cost hydrogen sensors. AJP has been shown as an effective way of creating uniform deposition onto pre-patterned substrates. This approach has led to the development of a functional hydrogen sensor [161], a nitrogen dioxide sensor [162], and a multi material structure capable of sensing hydrogen peroxide [163]. There is some progress in printing of ceramics for chemical detection [164], [165] and optical waveguides [166]–[169].

2.3 Non-traditional Applications of Aerosol Jet Printing

Whilst the primary application of AJP has been used for surface patterning, some researchers are beginning to explore its use in novel ways, such as multi-material printing, incorporation into hybrid machines, and the production of three dimensional structures. Aerosol Jet has been used to print two part materials by using a dual atomiser configuration (Figure 2.25), where multiple atomisation chambers are connected to a single print head. Each atomisation chamber contains a separate material and the sheath /atomiser/ exhaust gasses are controlled independently. A two part silicone elastomer has been printed using this method [170], [171]. In addition, the dual atomiser set up has been applied to print graduated regions in solid oxide fuel cells by printing a combination of

dense and porous layers. These layers encourage controllable chemical reactions to capture the useful energy. Thin electrolyte and cathode layers were deposited onto a standard anode substrate to form a functioning fuel cell [172]–[174].

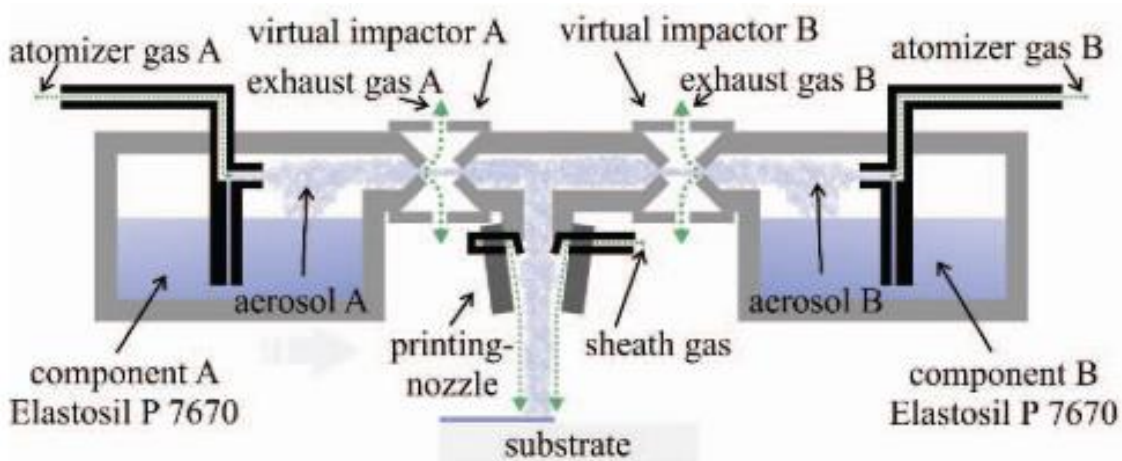


Figure 2.25: Dual atomiser arrangement [170], [171]

Hybrid processes refer to the combination of two or more synergistic manufacturing processes. The combination of these processes produces or enhances the end product in a way that could not be performed by a single process [175]. AJP has been incorporated as a part of a hybrid manufacturing chain to take advantage of its applicability to different materials and print regimes. For example, AJP has been used to deposit thin layers (5-35 μm) of UV curable inks onto non-planar surfaces that were subsequently cured through exposure to a UV laser. This hybrid approach combines the thin layer capabilities of AJP with the fine feature capabilities of laser based direct write to produce high resolution structures (Figure 2.26) [25], [26]. Although these studies were completed with polydimethylsiloxane, it is easy to see how this can be expanded to accommodate more exotic materials. The combination of AJP and laser based direct write may also present a pathway to multi-material stereolithography that is unachievable through the conventional vat based processes. By using independent print heads,

printing different UV curable material a model can be produced using multiple materials.

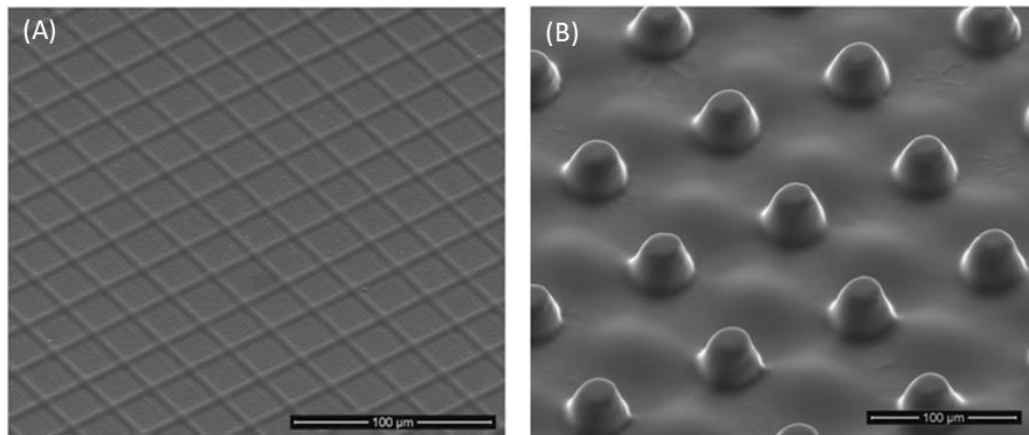


Figure 2.26: SEM images (A) square grid pattern (B) 3D cone array structures [25]

In addition, AJP has been explored as a functionalisation step in a hybrid- additive manufacturing process. The hybrid process was used to print functional structures and encapsulate them between the layers of the additive manufactured part. The researchers identified the ability to print metals, elastomers, and ceramics in a single process as a key parameter that differentiated the AJP process as a functionalisation step [176]. The AJP process has also been incorporated into a Stratasys extrusion based printer for a similar application [177]. Saleh *et al.* were the first to demonstrate the production of three dimensional structures using AJP. To do this they integrated the core technology into an environment heated between 90-110°C. This high environmental temperature resulted in fast solidification of the ink, enabling printing in three dimensions without the normal spreading and wetting associated with AJP. Whilst silver ink was used in this study, the authors contend that this work can be replicated by any nanoparticle ink [178]. Subsequent work has characterised the mechanical strength of these three dimensional structures and worked to apply them as electrodes in lithium ion batteries [179], [180].

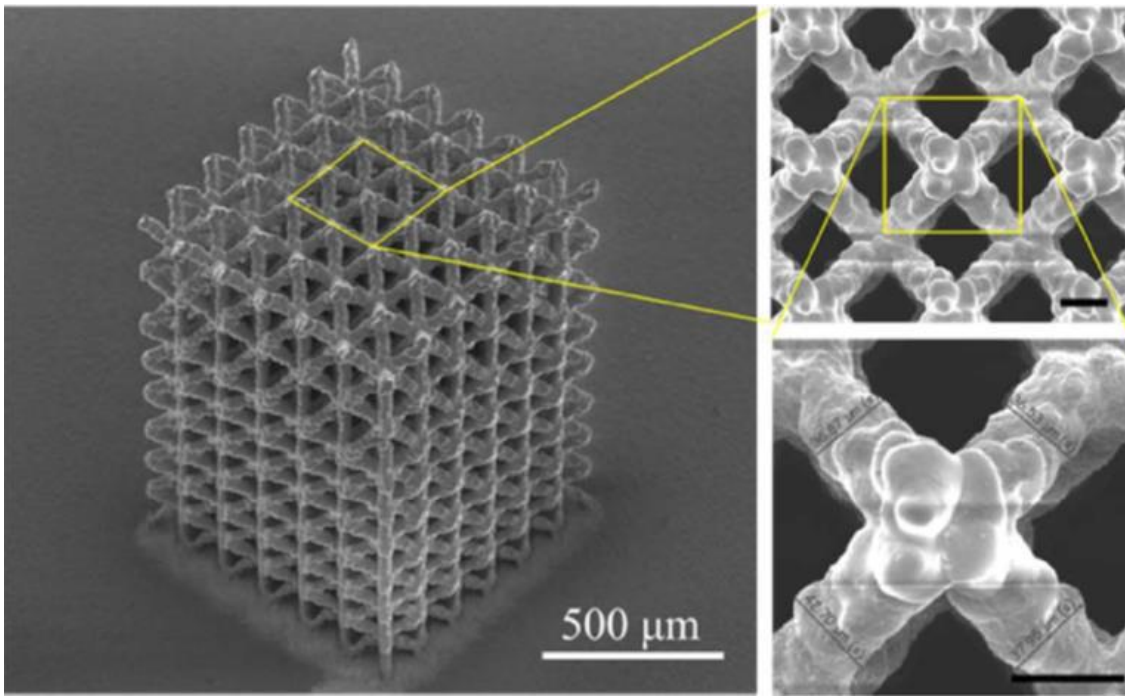


Figure 2.27: SEM image of a three dimensional structure produced by AJP printing[178]

2.4 Competitor Technologies to Aerosol Jet Printing

Other institutions are developing alternative aerosol based DW systems. These are based around new focussing techniques, atomisation techniques, or combinations of the two.

2.4.1 Collimated Aerosol Beam Direct Write

To further reduce the size of the printed features and overcome some defects a technology known as Collimated Aerosol Beam Direct Write (CAB-DW) was developed by the Centre for Nanoscale Science and Engineering at North Dakota State University. The reduction of the trace width is achieved through improved focussing of the aerosol beam, and is useful in applications such as fine pitch printed electronics [78]. The technology is capable, under the proper conditions, of reducing depositions to 5μm in width [14]. It was both theoretically and experimentally shown that when travelling through a converging long (1mm) capillary, high velocity (~100m/s) particles entrained in a fluid migrate toward the centre axis [181]. This is due to the Saffman force, the lift force associated with local shear. When an aerosol is contained within a tube this constrains the

aerosol to the centre line of the flow. Though smaller than the Stokes force, causes the flow of aerosol particles to migrate closer to the centreline of the nozzle. The AJP designers base their calculations on Stokes force alone. This is flawed as it assumes ideal and incompressible flow, and spherical particles which is not the case for this application [181].

During their study the theoretical calculations show that the Stokes force should always be considered and Saffman forces should be considered if the nozzle is greater than 10mm in length. The other forces are small by comparison as to be negligible. The underlying premise of the new approach is using a three-part, converging-diverging-converging nozzle to promote the focusing and collimation of the jet. By translating a substrate underneath this collimated flow, a pattern can be traced [182]. The nozzle is longer than normal AJ nozzles, meaning it is better termed a capillary. Particles of all sizes and initial positions were predicted to migrate toward the centre line and this was confirmed experimentally. The lines written using a CAB-DW system were approximately 1/3 the width of the AJP printed lines using otherwise identical processing conditions [182].

The dynamics of CAB-DW printing are similar to other processes where a careful balance is struck between stand-off distance, printing rate, surface wetting, solvent evaporation, and deposition temperature to realise a deposit of uniform composition and morphology [183].

2.4.2 Aerodynamic Lenses

Aerodynamic lenses are used to generate particle beams for aerosol characterisation. These aerodynamic lenses are a series of centre collimated orifices contained in tubes that create converging flow accelerations and diverging decelerations. Particles are separated from the carrier gas and are focussed to a tight beam due to their inertia. The exit nozzle is responsible for

accelerating the particles toward the substrate with a minimal divergence angle. The pressure limiting orifice controls the volumetric flow rate through the lens system and the exit nozzle defines the lens operating pressure. Particles that exit an aerodynamic assembly are accelerated in the low pressure environment required to maintain the focussing effect. The particles impact the substrate at a velocity of between 400 to 500m/s. An aerodynamic lens has been developed to obtain focussed, low divergence particle beams for long-distance transport inside a vacuum chamber. The aerosol stream is directed toward a substrate which can be translated to produce a direct write system [184].

Nano particle deposition using aerodynamic lenses has several potential advantages [185]:

- It requires neither sheath gas nor micro nozzles to achieve a 10 μ m resolution.
- Aerodynamic lenses consist of thin metal plates with orifices that are greater than 1mm in diameter, which can be manufactured by many well characterised techniques.
- An aerodynamic lens assembly can also be incorporated into a high vacuum system commonly used in micro-electronics fabrication and use the pressure drop from ambient to the chamber to deposit the material.

Qi *et al.* use aerodynamic focussing to deposit nanocrystal assemblies in controlled patterns. They use a silicon wafer substrate and achieve a scanning speed of 10 μ m/s. The line height was a maximum of 2.9 μ m and the WHM was 9.4 μ m. A triangular distribution was observed [185].

Girsheck *et al.* discuss the deposition of particles by hypersonic impaction. An aerodynamic lens is used to produce a focussed beam with a width of a few 10s of micrometres. The group state that the aerodynamic lens could be interfaced

between a particle synthesis reactor to produce a complete manufacturing system [186].

2.4.3 Electro-Aerodynamic Jet Printing

In electro-aerodynamic (EAD) jet printing aerodynamic force is coupled with electrostatic force to obtain a wide range of controlled pattern sizes. In the EAD jet printing method, electrically charged aerosol particles move through the inner cylinder of a co-axial nozzle where an external electric field is applied. A sheath air flow passes through the outer cylinder of the nozzle to prevent the particles from digressing from the aerosol stream. A Collinson type atomiser is used to create the aerosol which is then passed through a unipolar charging device. A stainless steel needle located at the centre of the charger is put under a high voltage to generate corona discharge at its sharp tip. This discharge ionises the particles. The particles then pass through an aerodynamic lens (Section 2.4.2). After the particles are ejected from the nozzle they are encased by the outer sheath of air and electrically forced to deposit on the surface.

Park *et al.* designed two co-axial nozzles to observe the effect of electrostatic force, particle size and air flow rate on particle trajectory and dot pattern size. They found a higher sheath air flow rate caused the aerosol stream to be focused. When the Stokes number was higher than one, the dominant focussing effect was the sheath flow rate rather than the applied voltage. However for Stokes numbers lower than one, the pattern size was affected by both the sheath airflow rate and the applied voltage [187].

2.4.4 Ultrasonic Horns

As an alternative atomisation step manufacturers such as Sono-Tek and Sonaer Ultrasonics [188], [189] have developed technology known as ultrasonic horns that are capable of creating aerosol particles with a Gaussian droplet size

distribution. Sono-tek has commercialised the technology and advertises the capability to produce lines with the width of 400µm.

2.5 Cell Patterning Technologies

Some research groups have exploited the abilities of surface patterning technologies for cell culture applications. Although the material selection, resolution, and flexibility in design and substrates is limited in comparison to AJP, site specific surface treatments produced by both mask based and mask less techniques have been produced. These cell culture substrates are used as models of *in vivo* tissue architecture and physiology for applications such as drug screening applications [190], engineering blood vessels [191], and controlling stem cell fate [192], and neuromuscular research [193]. It has been suggested that traditional 2D monolayer cell cultures are limited in application and more complex 3D models of disease are required for more effective and efficient pre-clinical evaluations [15].

2.5.1 Mesoscale three dimensional technologies

In methods commonly termed 'bioprinting', the cells are printed directly onto the substrate to form a mesoscale three dimensional shape. Bioprinting techniques include cell sheet technology [194], acoustic cell patterning [195], ink jet based techniques[196], and extrusion based systems [197]. Cells are usually contained within a hydrogel to reduce the shear forces associated with printing [194]. The shape of the growth is defined by the initial pattern shape. However, the processing parameters are specific to each cell culture and cultures suffer from poor cell viability after printing [198], and low resolutions [199].

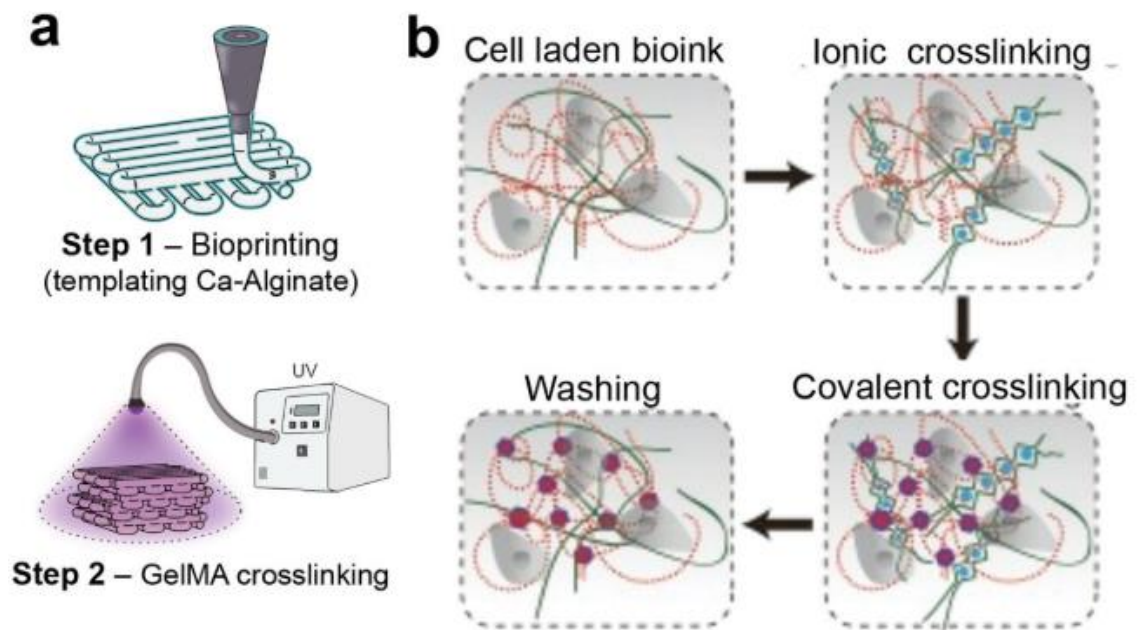


Figure 2.28: Bioprinting overview [197]

2.5.2 Microscale surface patterning

In microscale patterning cells are patterned on a smaller scale. Cells are either directly patterned (by containing them within the printed material), or an acellular structure is manufactured from suitable materials. This structure is then used as the underlying substrate for cell culture. Many techniques that are used in other surface patterning technologies have been used to pattern cells on this scale including photolithography, soft lithography (microcontact printing), and a suite of template less technologies such as Laser Induced Forward Transfer (also known as LIFT) [200], dip pen lithography [201], and ink jet printing.

The ability to pattern onto the substrate enables use of specialist materials such as nanofibrous substrates that mimic the important ‘extracellular matrix’ [10]. In these methods, it is the topographical and chemical cues of the printed material that are used to influence the spatiotemporal growth and movement of cells on solid substrates [202]. These cues can be manufactured of any compatible materials, and with smaller dimensions that are cannot be achieved by direct bioprinting [203]. However, each of these technologies has its limitations. For

example, soft lithography is inherently template based, and issues with the mask such as deformation of the template [204]. In LIFT printing, the cells cannot be finely patterned and instead their distribution must be statistically controlled, limiting resolution [194], and, in ink jetting low seeding densities are required to stop the nozzle from clogging during the printing process [194].

Due to these limitations, no single technology is suitable for freeform cell patterning in every scenario. Solutions that are being explored are to combine technologies into a single hybrid machine [175], and to investigate new micro-scale manufacturing technologies that enable greater flexibility in terms of materials and processing requirements.

2.5.3 Aerosol Jet Printing to Pattern Cell Cultures

AJP has been investigated as a flexible method to pattern cells. It has been applied as a bioprinter to print biological media directly. Using the pneumatic atomisation method, materials such as protein and DNA have been printed using AJP without denaturing the structure of the molecules. Using the pneumatic atomiser reduced the shear force on the proteins. Lines, dots and squares of various proteins were printed and the proteins were not denatured. The printing of proteins can be extended to active enzymes [45] and gels containing live cells [205], with feature sizes of approximately 100µm. Printing smaller sized features introduced significant shear forces which affected the viability of the cells.

Using printed acellular structures, MG-63 cells have been directed to grow into lines [206]. In addition, de Silva *et al.* have proved the ability to both positively (LLCPK1 and NIH3T3 cells grow on in straight lines) and negatively (NIH 3T3 cells avoid the printed features) control cell growth by changing the print material. The design complexity of these features was limited to lines and grids, and the scale of the features was in still in the order of 100 µm [207].

2.6 Chapter Summary

Within the direct write processes, the relatively new AJP method is compatible with the widest range of functional materials. This is due to its unique and patented atomisation and focussing steps. AJP has primarily been explored in electronics manufacturing applications to date. Several techniques extracted from the literature are summarised in Table 2.2. These techniques have implications outside of electronics manufacturing and should be considered for all new applications of AJP.

Table 2.2: Key techniques extracted from electronics applications literature

Electronic Structure Printed	Key Techniques Identified
Interconnects	New material introduction
	Substrate wetting
	Thermal sintering
	Printing onto flexible substrates
Passive Electronic Components	Printing simple structures
	Secondary processing of features
Active Electronic Components	Printing complex structures
	Functional Material Doping
Actuators and Sensors	Printing complex structures
	Advanced material printing

The landscape of increasing complexity of *in vitro* cell culture models necessitates a new suite of digital manufacturing apparatus. The varied demands of these new applications require a flexible approach that can be updated to suit a range of manufacturing requirements, and to complement existing 2D and 3D techniques.

A major contribution of these new manufacturing apparatus and methodologies should be to enable printing at an order of magnitude smaller than current methods while providing currently unobtainable degrees of material flexibility and responsiveness to design changes. The practical implication of this is that not only can a greater variation of cell models be created and explored, but that different designs can be created in the matter of minutes as compared to typically 1 week+ for template-based methods, and at a fraction of the costs. This unlocks the both the range and viability of new forms of *in vitro* cell models. The current AJP literature for cell patterning primarily tackle only straight lines and grid patterns [45], [205]–[207].

By incorporating AJP into a new methodology, and using techniques and materials developed in the electronics production literature to rapidly advance the capabilities, printed cell culture substrates can be realised. The key to producing complex surface patterns is establishing a digitally-driven and computer-controlled manufacturing process that prints directly onto substrates before the culturing

Chapter 3 Methods and Materials

3.1.1 Substrate Manufacturing and Post Processing

Substrate selection can have a large effect on print quality, due to physical or chemical interactions between the substrate and the material discussed in Section 2.1.4. Improper wetting of the ink on the substrate can cause an incomplete line where the material dries into droplets on the surface. In applications where a solid line is needed this can cause a failure of the part. Both chemical interactions and surface roughness can affect the wetting of an ink on the substrate. Larger scale surface topography should also be considered, as although the aerosol stream is collimated to an extent, topographical changes are effectively a change in z stand-off which can affect line geometry.

3.1.1.1 Washed Glass

The surface of glass is naturally very flat due to the lapping step in its manufacturing. This flat surface can act as a good reference surface, making metrology processes used in this project easier to perform. Polymer substrates are not flat by comparison. Therefore, the primary use for glass substrates was in the engineering characterisation of the process.

The cell response to glass substrates, discussed in Section 6.2, made them unsuitable for use as a cell culture substrate.

3.1.1.2 PDMS Substrates

The specific manufacturing moulds used for the substrates was altered many times to fit new engineering requirements and biological assays. The PDMS was cast into different thicknesses and shapes to be suitable for a range of technologies such as white light interferometry, compound optical microscopy, compound tissue culture microscopy, fluorescence microscopy, and scanning electron microscopy. This range of substrate sizes did not affect the surface

patterning as due to the digital nature of the automation the code could be adapted. The effect of different substrate sizes on the cell culture was accounted for by using an initial cell density (cells/cm²) as an initial condition for the cell culture, rather than the number of cells only (Discussed in Section 6.2).

3.1.2 Cleaning and Sterilisation Procedure.

To remove contaminants and clean the substrate surface, all substrates for this experimentation were washed and prepared in house using the following method:

1. 10 mins ultrasonication in acetone
2. 5 mins ultrasonication in isopropyl alcohol
3. Rinsing with DI water or storage in DI water until use

This process is based on the solvent cleaning of wafers used in the University of Leeds clean room. Acetone is used first to remove any organic contaminants. However, the acetone solvent itself can leave a residue. This is removed by the second wash in isopropyl alcohol. If the substrate was to be used right away it was rinsed with Type 2 DI water (15 megaohms-cm). If the substrate was to be stored it was immersed in the same type DI water and sealed in a container until use to avoid further contamination.

Prior to use the substrates were dried under a nitrogen stream. If the surface required oxidation they were placed in an Inseto PE-25 plasma cleaner and treated for 60 seconds with oxygen plasma. The overall cleaning procedure is shown in **Error! Reference source not found..**

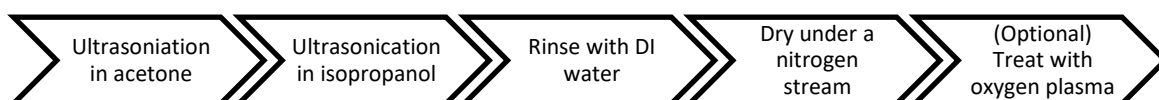


Figure 3.1: Cleaning procedure before printing

3.1.3 Surface modification

The hydrophobic nature of native PDMS causes issues with surface wetting of water based inks. To make PDMS surfaces suitable for use in this process the surface energy of the device must be increased to make it hydrophilic. One method of doing this is by a reaction to oxidise the surface. The aim of this oxidation is to covalently bond a hydroxyl group to the terminus with a substitution reaction with a methyl group [208]. This can be achieved using several methods, most commonly exposure to oxygen free radicals from oxygen plasma or corona discharge [73], [209]. When exposed to oxygen plasma, the PDMS is attacked by oxygen free radical molecules which result in the formation of silanol groups on its surface. During the research, the surface chemistry was altered to facilitate printing of water-based inks. This was achieved by treatment with an oxygen plasma prior to printing. An Inseto PE-25 plasma cleaner was set to 75W power and a vacuum of 175torr was pulled. The oxygen flow rate was set to 10cc/min. The samples were exposed to plasma for 60 seconds.

3.1.4 Post processing

After the printing process, the parts were baked for 30 mins at 150°C to drive off solvents. Then, parts were sterilised by immersing them in 70:30 ethanol:DI water to swell and burst any organic matter. The parts were then sealed in a pre-sterilised cell well container for transportation to the cell culture laboratory. This step is especially important to avoid bacterial infections in the cell culture, particularly in later tests when antibiotics were not used.

3.2 Analytical Techniques

The geometrical features of the printed deposits were checked for defects and dimensionally assessed using several analytical techniques.

3.2.1 Microscopy

Microscope images were taken using a calibrated Olympus BX53 Upright Microscope with either 4X, 10X or 20X objective lens and a 12.5 MP camera. Samples were illuminated using the in-line LED. Particulates were removed from the sample using a nitrogen stream. Under optical microscopy sample were assessed for their optical width and for the defects discussed in 2.1.5.

3.2.2 White Light Interferometry

This analysis was performed with a Bruker NP Flex White Light Interferometer, using a 20X objective and stitching 4 measurements per sample. The full method to process white light data is shown in Appendix A. After gathering the data, the tilt was digitally removed from the data results, and a data restore algorithm was run to fill in any blank pixels with the average value of those directly surrounding it. Where required the data was rotated and magnified. These steps flattened the results and set the scales to make them comparable. A sigma filter with a window size of three was passed over the data once to remove noise. An example of raw data input and the processed data set is shown in **Error! Reference source not found.**

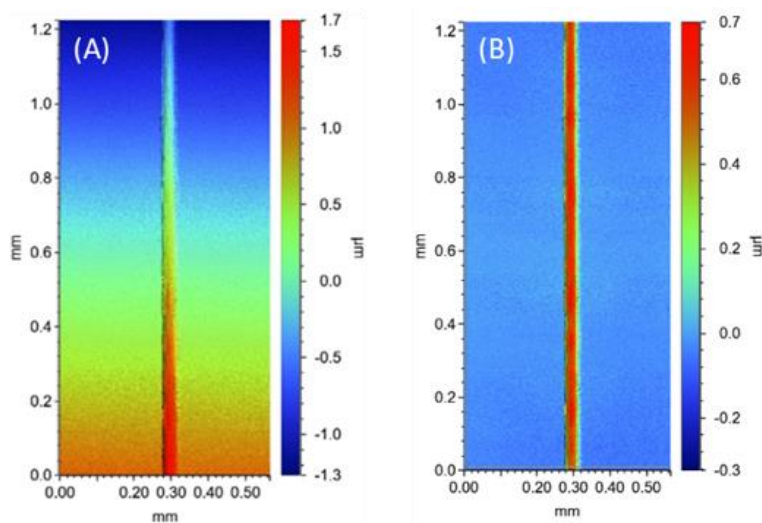


Figure 3.2: Example white light interferometry data (A) raw data (B) post processed data

Quantitative cross sectional data was extracted from the interferometer by assessing a single horizontal section for its height data. The maximum height was defined by the biggest measurement distance between the substrate surface and the peak of the inverted U profile. A measurement of width was then taken at half this maximum height value. Figure 3.3 shows the horizontal sectional data height data and defines the maximum height and width at half maximum.

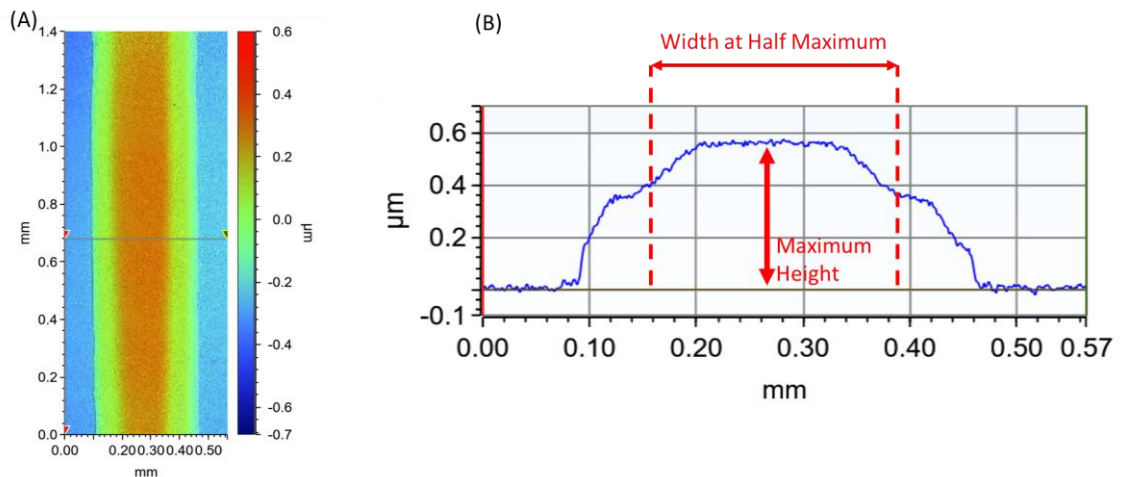


Figure 3.3: (A) A horizontal section was taken from the data. (B) Example of profile data and an illustration of maximum height and width at half maximum.

3.2.3 Scanning Electron Microscopy

A FEI Nova NanoSEM (Thermo Fisher Scientific) was used in low vacuum mode to image the samples at incident angles between 0 and 30 degrees. Prior to imaging on a scanning electron microscope, samples were sputter coated in a 4nm layer of conductive iridium to inhibit surface charging, reduce thermal build up and improve the image resolution. Ultra-high magnification images were taken using the immersion mode of scanning electron microscopy.

3.2.4 Adhesion tape test

Adhesion tape tests were performed according to the standard ASTM D3359 – 09 (Test method B) [210]. By rastering the fine printed features a pad of material was produced. A grid was scored into the pad using a razor blade. The pad was viewed under an optical microscope. Elcometer 99 pressure sensitive tape was

firmly pressed down onto the pad and left for 120 seconds before being sharply removed. The pad was then inspected underneath the microscope and material removal analysed in line with the standard.

3.3 Biological Protocols

The following biological protocols were used for the cultures discussed in Chapter 6.

3.3.1 Cell culture Conditions

The cell lines were maintained in T75 flasks (Thermofisher scientific). The cell cultures were maintained at 37°C / 5% CO₂ / 95% relative humidity. The cells were cultured in suitable growth medium and supplements as described in Table 3.1.

Table 3.1: Growth conditions for different cell lines

Cell line	Description	Medium	Supplements
RAW 264.7	Mouse macrophages	Dulbecco's Modified Eagle's Medium	10% Fetal Bovine Serum 2mM L-Glutamine 100 I.U./ml Penicillin 100 µg/ml Streptomycin ATPlite positive control: 5-10 µg/ml Camptothecin at Day 4
L929	Mouse fibroblasts	Dulbecco's Modified Eagle's Medium	
C6	Rat glial cells	Ham's F12	
PHDF	Primary human dermal fibroblasts	Dulbecco's Modified Eagle's Medium	
BHK	Baby hamster kidney cells	Glasgow's Minimal Essential Medium	
EA.hy 926	Human somatic cell hybrid	Dulbecco's Modified Eagle's Medium	10% Fetal Bovine Serum 1% Penicillin/Streptomycin
HT29	Human Colon Cancer	RPMI Media	
HCT116	Human Colon Cancer	RPMI Media	

On 90% confluency the cells were passaged. Spent media was removed from the culture flask and deposited into waste container containing Virkon solution. 5ml DPBS was added to briefly wash cells and remove any residual FCS. The cells were then incubated with 2ml of trypsin (0.05% vol/vol) and ethylenediaminetetraacetic acid (0.5% vol/vol) for 5 minutes. 8ml complete media was then deposited into flask. The total solution (10ml), was then transferred to a universal tube and centrifuged at 400g for 5 minutes to form a pellet of cells. The

media was removed by pouring into the waste pot. The pellet was then re-suspended in 10ml of fresh media. 1ml of the media containing cells was deposited into a T75 flask containing 9ml of fresh medium to maintain the culture for future experiments. The remaining 9ml of media containing cells was diluted to the appropriate cell concentration and used in patterning experiments.

3.3.2 Patterning Experiment Procedure

The PDMS substrates were sterilised in 70% ethanol for 10 minutes, and then dried in a sterile hood, prior to cell culturing. The patterning experiments were maintained at the conditions described in section 3.2.1

Cells were seeded at 7.5×10^4 cells per PDMS substrate and incubated for a specified time period before being analysed.

3.3.3 Microscopy Protocol

Images of the cell culture were taken at various magnifications with an EVOS FL microscope. There was no interference with the cell culture for routine microscopy analysis.

3.3.4 Immunofluorescence Protocol

The cells were fixed with 4% paraformaldehyde in phosphate buffered solution (PBS) for 15 minutes. Subsequently, they were blocked with 0.5% skimmed milk for 10 minutes at room temperature. Then, they were incubated with 100 μ L of a 1:200 solution of mouse monoclonal anti- α -tubulin antibody in PBS for 1 hour at room temperature. After washing, the substrates were incubated with 100 μ L of Alexafluor 488 goat anti-mouse antibody (1:300 with PBS).

To stain the cell nucleus 15 μ L of Hoechst 33342 (100 μ g/ml) in DPBS was added to each sample. The culture plates were covered and left for 15 minutes at room temperature before imaging.

Images were taken at 10X magnification with the EVOS FL microscope. The brightness and contrast of the images were enhanced with ImageJ, before combining the signals from the cytoskeleton and nucleus staining. Larger images were stitched together from several frames and mounted onto a black background.

3.3.5 Preparation for SEM imaging

Cells cultures were briefly washed with pre-warmed (DPBS) and fixed in 2.5% (v/v) glutaraldehyde for 20 minutes. Cells were then subjected to dehydration in increasing gradients of ethanol (25%, 40%, 60%, 80%, 90% and 100%). For imaging, samples were coated with 4nm of iridium and imaged using a FEI Nova NanoSEM (Thermo Fisher Scientific)

3.3.6 Live/Dead Assays

These experiments were conducted by collaborative partners. Live/Dead assays were conducted with the Live/Dead Cell Staining Kit II (PromoCell GmbH, Germany). Cells were stained according the manufacturers instruction. 1µl of 4mM Calcein solution and 2 ul of 2mM EthD-1 solution were mixed in 4 ml DPBS. Culture medium was removed and 300 ul of Calcein – EthD-1 solution was added to the wells. Samples were incubated in room temperature for 1 hour, and the dye solution was then replaced with DPBS. For imaging, the samples were placed on a microscope slide (upright) and covered with DPBS to avoid drying while imaging by using upright fluorescent microscope. The cells on the bottom of the wells were imaged by using inverted fluorescent microscope.

Chapter 4 Design, Fabrication and Testing of the Automation Apparatus

In Chapter 2 digitally driven technologies were identified as suitable systems to produce cell culture substrates that could be updated as a response to changing biological requirements without the cost or time implications of changing a physical mask. From these processes AJP was shown to be compatible with the widest range of functional printing materials, substrate materials, and substrate shapes due to its unique atomisation and focusing steps. This flexibility in materials and substrate shaping were identified as desirable for use in developing complex *in vitro* models. Using a flexible system such as this increased the range of applications, provided the core AJP technology ('print engine') could be integrated into a suitable automation apparatus.

In this chapter the core Aerosol Jet technology is incorporated into a programmable three axis system. To manipulate the substrate under the print head, a three-axis stage was controlled through a control code (G-Code) input to Mach3 CNC software. A key enabler of the technology was a script which produced the control code from an equation or digital design data. The process incorporates rotary stages and alignment apparatus capable of distinguishing features as small as 5 μ m. This enables the integration of substrates produced using other techniques, forming a hybrid process.

First, the mechanical and component design of the processes enabling the incorporation into a full manufacturing system is given. The machine axes, which enable manipulation of the substrate, were designed, assembled and tested. Next, the calculations for an substrate alignment camera, and integration of the print engine with the automation apparatus are shown.

In the second section, the methods to prepare the substrate blanks and the cleaning and sterilisation procedures are detailed. These processes were essential to use the printed cell culture substrates in the cell culturing laboratories. Finally, the generation of machine control code is explored. This section explains how Computer Numeric Control (CNC) apparatus control code can be written by hand for simple shapes, and how it is interpreted and used to control the apparatus. Then, new programs to generate machine control codes that produced complex shapes is described. The input data to the programs could be from either mathematical equations or design exchange format (DXF) designs. The capabilities of this complex control code generation differentiated this work from previous AJP cell patterning research by enabling higher orders of patterning complexity, flexibility and decreasing the time to implement design changes.

4.1 Design and Manufacture of the Automation Apparatus

The automation of the process was fundamental to the production of cell culture substrates. The primary objective of the manufacturing apparatus was the accurate and repeatable microscale movement capability. After the design and development of the apparatus, the system was tested. A secondary process consisting of an in-process alignment camera and rotating stage were also incorporated. The print engine was also integrated with ancillary components such as a gas supply, cooling system and a vacuum pump.

4.1.1 Design and Implementation of Movement Axes

The three-axis stage is powered using a single phase 30V DC power supply capable of producing the 25W required to run the three motors. The Pulse Width Modulation (PWM) signal was initiated from the computer using MACH3 software.

It is interpreted through the CNC control board, which sends switching signals to the three motor drivers. These drivers apply power to the motor coils in response to these switching signals, causing them to turn. Figure 4.1 illustrates how the stepper motor for each axis is controlled.

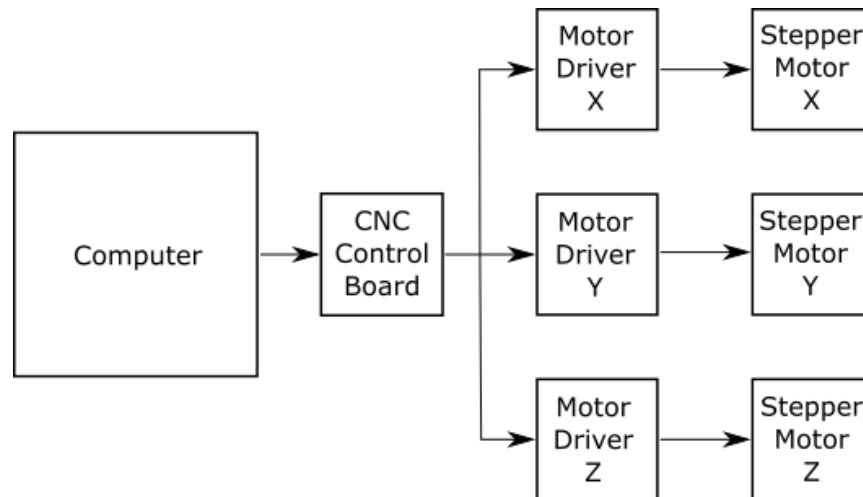


Figure 4.1: Stepper motor control diagram

4.1.1.1 X and Y Movement Axes

The components that were available to build the X and Y axis were specified in British units. Therefore, these units were used in this design section to ensure the precision of the design (by removing the possibility of rounding errors). However, for reporting the capabilities of the machine, SI units are used.

The X and Y axes design was identical. Both axes were driven using a stepper motor. The stepper motor was powered at 4.7V, 1.8A DC. The motor specification was 200 steps per rotation, therefore the rotation was 1.8 degrees per step.

To reduce the minimum rotation angle of the stepper motor the driver is set to microstep. Microstepping divides the movement of one full step (1.8° in this case) by overlapping currents in the stepper motor coils and changing the ratio of these currents. These overlapping currents can move the motor by less than one step, increasing the accuracy at a cost of motor torque. Microstepping is controlled by tuning the relationship between the PWM controller and the digital stepper drivers. The motors were tuned to 1/8 microstepping, as this is commonly taken as the

maximum level of microstepping for non-specialist stepper motors. 1/8 microstepping means that the minimum appreciable movement of the stepper motor axle is 0.225° ($1.8 \div 8$). Setting the pulses per revolution higher did not increase the accuracy of the motor movement by any appreciable amount but can improve smoothness of motion. As the application of stepper motors for a three axis stage without any machining requirement will not strain the stepper motors maximum torque, this was set to 25000 pulses per revolution – the maximum value.

The motors were fastened to a drive a 'trapezoidal XL' specification timing belt. A timing belt was used as it permits smaller gears than equivalents such as chains, reducing the space claim. Timing belts are also driven by teeth, rather than by friction as in a smooth belt, which reduces the slippage and ensures the driving and driven shafts remain synchronised. The required belt length, calculated from the geometry, was 8 inches. The method and geometry are found in Equation 3.1 and Figure 4.2.

$$\text{Belt length} = 0.828\pi + 1.655\pi + 2 \times \frac{2}{\cos(22.5)} \approx 8'' \quad (3.1)$$

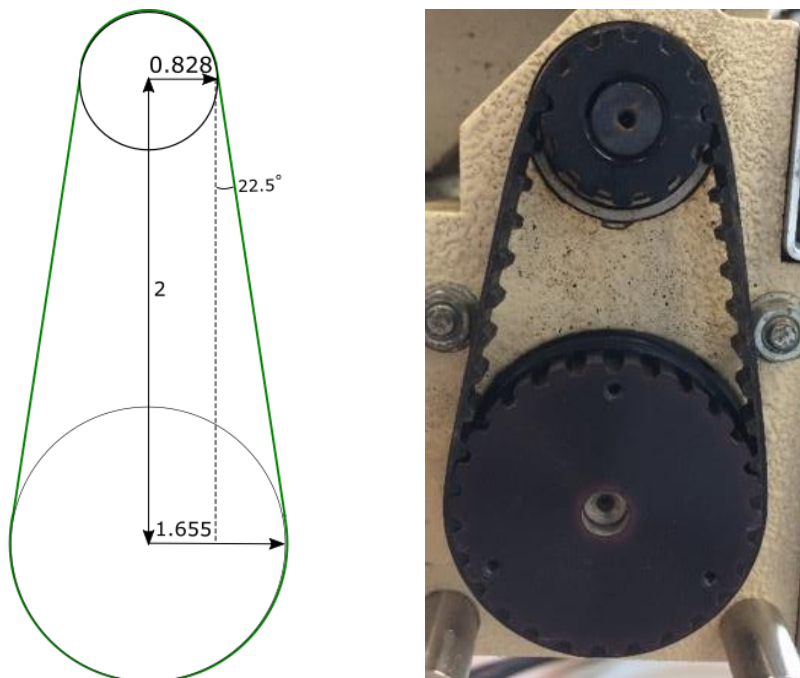


Figure 4.2: X and Y Axis timing belt

A polyurethane belt reinforced with steel fibres was used. A belt with a nylon coating on the tooth side was purchased. This nylon coating reduced the coefficient of friction and improve the engagement of the belt and pulley. 8-inch welded belts of the ‘trapezoidal XL’ specification have 40 teeth. The large pulley had 26 teeth and the small pulley had 13 giving a speed ratio of 2. The belt width was 0.25 inches, this width was enough to withstand the forces required to turn the lead screw. The large pulley was fixed to the stepper motor shaft. The small pulley drove the precision acme single start lead screw. The width of the screw was 3/8” with 10 threads per inch. The thread lead was therefore 0.1” [211].

The theoretical accuracy of the stage can then be calculated as the resultant movement of the stage due to one microstep. This accuracy value assumes a perfect system and does not consider factors such as backlash, inertia in the system, wear of the components, temperature effects or latency in the controls. It is not a guarantee of the minimum movement of the stage, however is useful for comparing designs. A 0.225° movement in the motor spindle equates to a 0.45° movement in the lead screw due to the gearing ratio. This equates to a theoretical accuracy of 3 µm for each axis as shown in Equation 3.2.

$$\begin{aligned} \textit{Theoretical Accuracy (mm)} &= 25.4 \times \textit{Leadscrew rotation} \times \frac{\textit{Thread lead}}{360} \quad (3.2) \\ &= 25.4 \times 0.45 \times \frac{0.1}{360} = 0.003\textit{mm} \end{aligned}$$

In practice the axes cannot achieve movements of 3 µm as the minimum incremental movement is affected by many factors. The most practical way to assess the incremental movement is by direct measurement. A dial indicator was used to record the minimum incremental movement using the experimental set up shown in Figure 4.3.

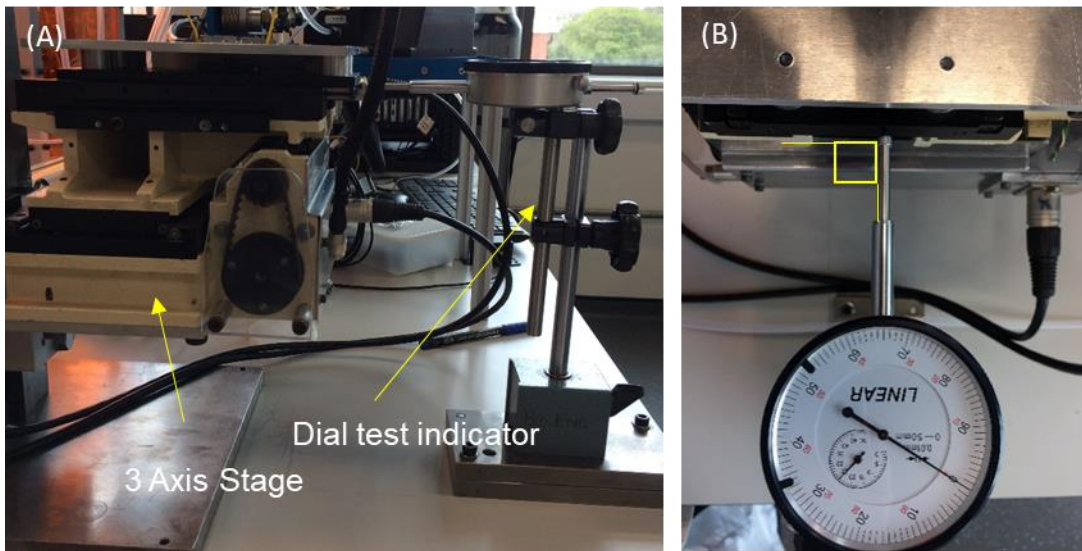


Figure 4.3: Dial indicator set up for measuring axes movements (A) side view showing the experimental set up (B) plan view of the experiment showing dial

In the literature the minimum reported feature width is $10\mu\text{m}$ when measured by optical microscopy [64]. In order to counter the end effects associated with the AJP mechanical shutter, print lengths of 10 times the line width are recommended [22]. Therefore, a stage movement of less than $100\mu\text{m}$ will not be used as it would not be discernible (The 'width' would be larger than the 'length' of the line). The minimum incremental movement measured for each axis was less than $5\mu\text{m}$. Therefore it can be concluded that the stage is suitable as it is capable of producing lines of $100\mu\text{m}$.

Using the same dial test indicator set up, the deviation of the stage was measured at several positions along the X and Y axes, in both the forward driving (positive) and the backward driving (negative) directions. For these measurements the point (0,0) was assumed to be the point at which both axes were at the half way point of both the X and Y axis lead screw. Figure 4.4 and Figure 4.5 show these measured values. The deviations in the X axis are larger than the Y axis and standard lead screw tolerances ($1/1000$ of an inch or around $25\mu\text{m}$). The high deviations on the left side of the axis suggest damage to the lead screw in that area.

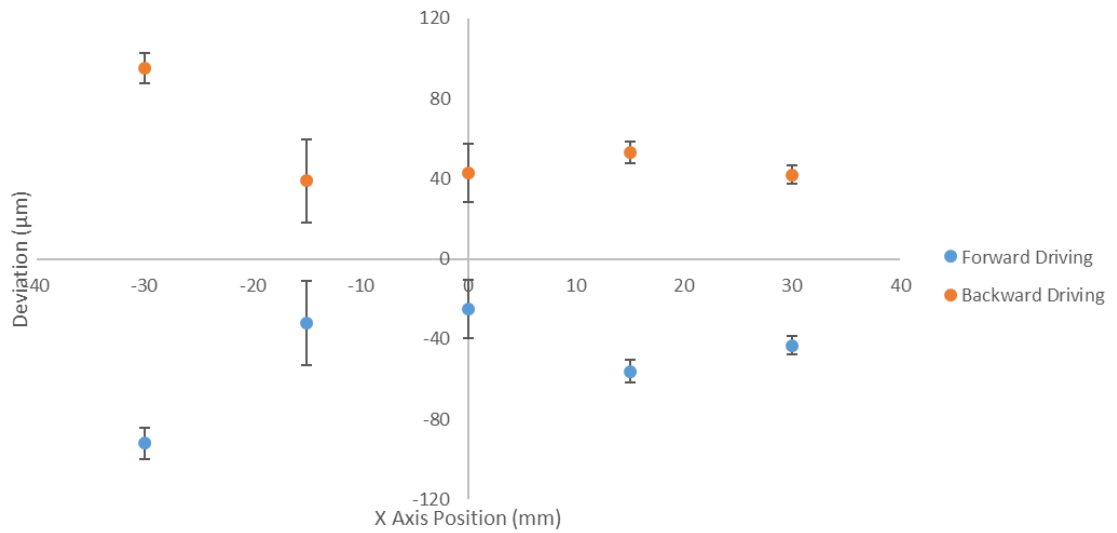


Figure 4.4: Graph to show the measured deviation on approach to specific X axis positions from both directions

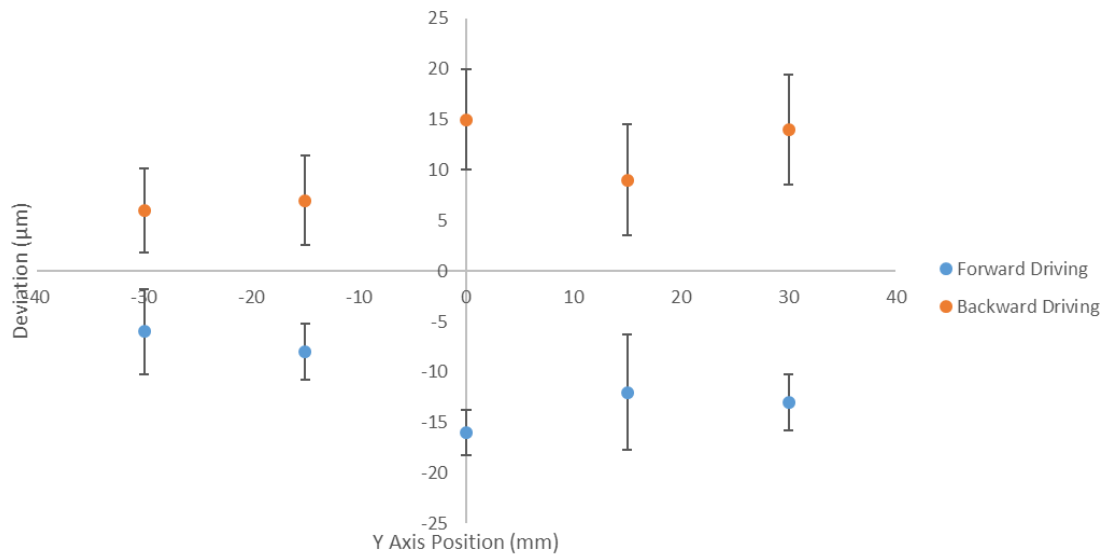


Figure 4.5: Graph to show the measured deviation on approach to specific Y axis positions from both directions

The backlash was calculated from the difference between the forward and backward driving deviations in both axes and is shown in Figure 4.6. The large backlash in the system had some implications for design of printed structures later in the project. The geometrical sizes may not be as designed, circles are challenging to close, and any alignment, either between prints or of geometry must take backlash into consideration. From these results it was inferred that the alignment capability was better in the Y axis than in the X. The top right position

of the stage (positive X and Y axes) had the least backlash, so this area was selected as the preferred print region going forward.

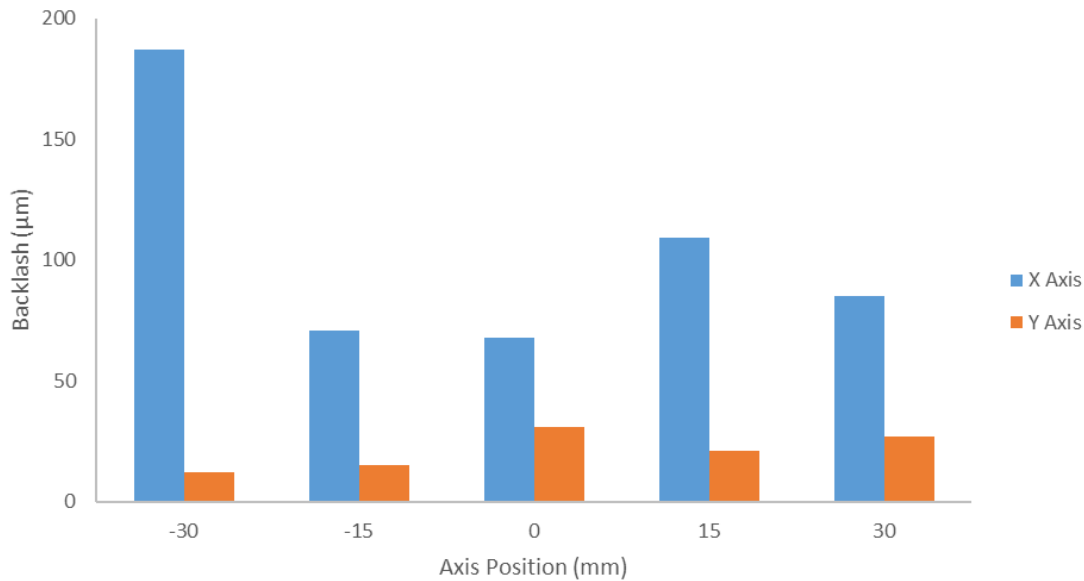


Figure 4.6: Calculated backlash at specific positions on the X and Y axis

4.1.1.2 Z Axis Movement

The Z axis was also specified using British units. As in the X and Y axes, the motor for the Z axis was also 200 steps per rotation. Microstepping was set at 1/8 with the pulses per rotation, higher than required to improve smoothness of the movement. For the Z axis the belt length and pulley sizes were re-calculated. The XL timing belt was driven by a small pulley which had 30 teeth. The small pulley was fixed to the stepper motor shaft. The Z Axis shaft was driven by the large pulley which had 60 teeth, equating to a timing ratio of 0.5 which means a 0.225° rotation in the stepper motor equates to a 0.1125° rotation in the Z axis shaft. The required belt length was 17.6 inches.

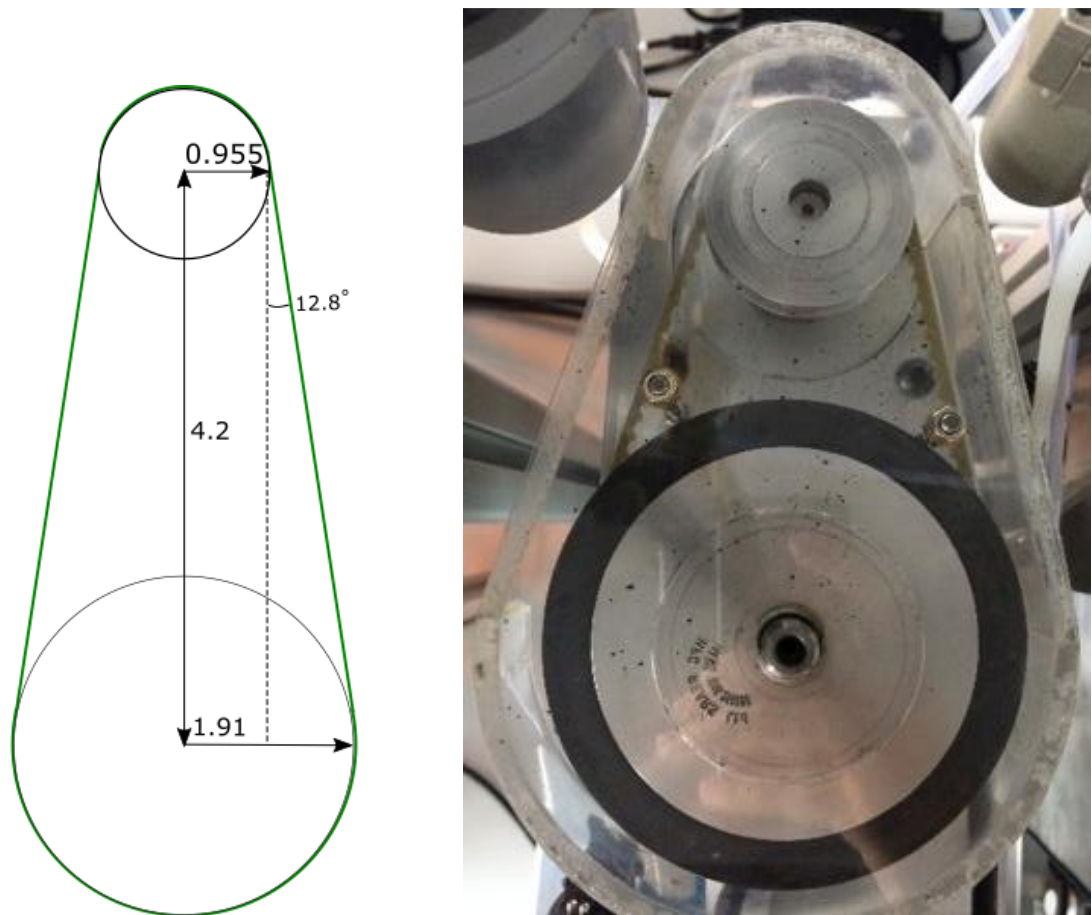


Figure 4.7: Z axis timing belt

The large gear was used to drive a ½ inch British Standard Whitworth threaded bar which was used as a lead screw for the Z axis. The threads per inch of the ½ inch bar is used to calculate the accuracy as in Equation 3.3:

$$\text{Theoretical Accuracy (mm)} = 25.4 \times 0.1125 \times \frac{0.833}{360} = 0.001\text{mm} \quad (3.3)$$

The accuracy of the Z axis was not critical to the same micrometer scale precision as the X and Y axes, due to the range of stand off distances afforded by AJP, discussed previously in Section 2.1.3. Therefore, accuracy of 100µm was deemed acceptable. Calibrated spacer blocks were used to verify the Z axis motion. The set up is shown in Figure 4.8. The stage was moved until the first spacer just fit under a flat reference surface, without fouling. It was then lowered 20mm. This movement was verified by the addition of another calibrated spacer.

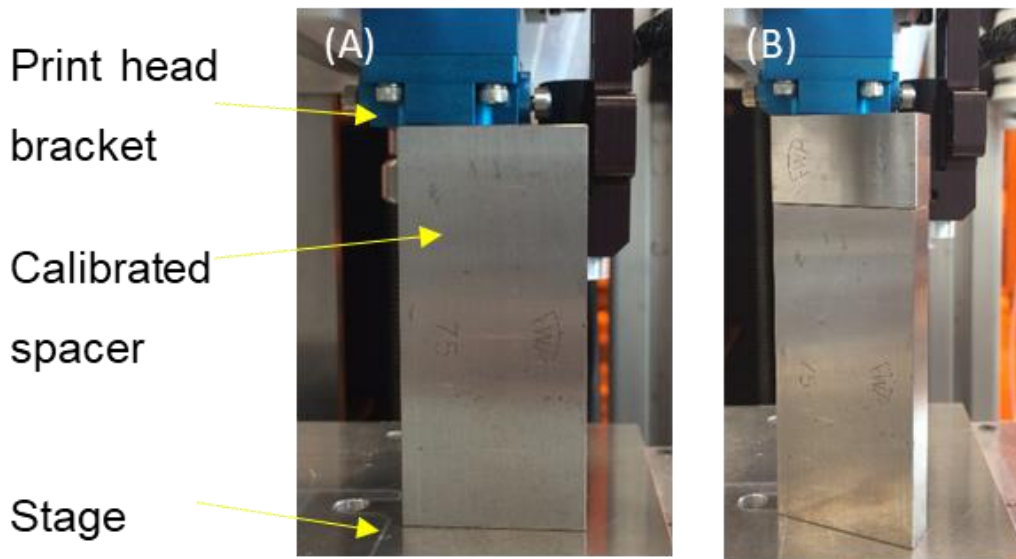


Figure 4.8: Z axis verification. (A) Stage is moved until the spacer just fits between the nozzle bracket and the stage plate. (B) The stage is moved down 20 mm and the movement is verified by the addition of a second calibrated spacer.

The print surface was a thick (10mm) piece of aluminium. This was ground to ensure flatness across the entire area. The flatness of the plate under the print head was verified. The dial indicator was mounted to the print head. The deviations from the centre point of each axis are shown in Figure 4.9. The deviation of the build plate was less than 30µm, even at the extreme ends. The Z deviation across a print sample will be less than 10µm, as the print surfaces will not be as large as the whole build plate. This small deviation in Z height will not affect the focussing of the aerosol stream onto the substrate.

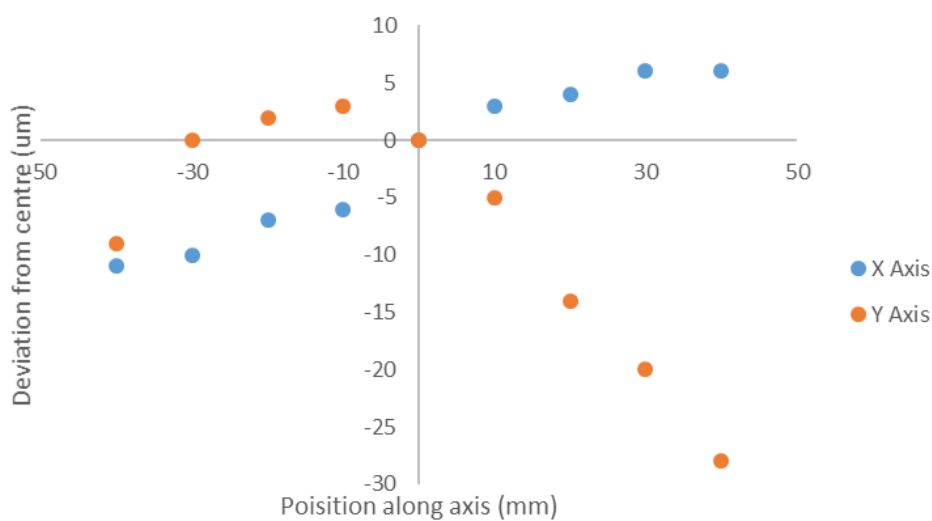


Figure 4.9: Z height deviation from the centre point

4.1.2 Printing Engine Configuration

The print engine consisted of two choices of atomising apparatus, two focussing heads, and the associated controller and sensors. The atomisation technique and head choices were cross compatible. To run the machine, one atomising apparatus and one focussing head was selected. The ultrasonic atomiser and 0.5X print head were chosen for this project, due to the suitability of this configuration to print fine features (discussed previously in Section 2.1.3).

4.1.3 Microscope Specification

A microscope was required to align substrates to the printhead and that was capable of monitoring line width in process if necessary. The desired spatial resolution was down to 5 μ m, to be able to view the edge effects and overspray of the line. This was challenging as this is approaching the wavelength of light, meaning diffraction plays a large role in the calculations.

The following equations can be used to specify spatial resolution of a microscope.

$$\text{Image space resolution (lp/mm)} = \frac{1000(\text{lp/mm})}{2 \times \text{pixel size}} \quad (3.4)$$

$$\text{Primary magnification (PMAG)} = \frac{\text{Sensor size (mm)}}{\text{Field of view (mm)}} \quad (3.5)$$

$$\text{Object resolution (lp/mm)} = \text{image resolution (lp/mm)} \times \text{PMAG} \quad (3.6)$$

$$\text{Object space resolution (\mu m)} = \frac{1000 (\mu\text{m/mm})}{2 \times \text{Object space resolution (lp/mm)}} \quad (3.7)$$

A camera was selected based on its cost and suitability to the application. An EO-5012M camera was purchased from Edmund Optics. The following relevant specifications were taken from the data sheet.

Table 4.1: Relevant EO-5012M specifications

Component	Specification
Camera Sensor Size	1/2"
Sensing Area mm by mm	5.6x4.2
Pixels	2560X1920 (5MP)
Pixel Size μ m	2.2x2.2

Using equation 3.4 the image spatial resolution can be calculated as:

$$\text{Image space resolution (lp/mm)} = \frac{1000(\text{lp/mm})}{2 \times 2.2} = 227 \text{ lp/mm} \quad (3.8)$$

Using a 5X objective lens (PMAG =5) the field of view was calculated:

$$\text{Field of view (mm)} = \frac{5.6\text{mm by } 4.2\text{mm}}{5} = 1.28\text{mm by } 0.96\text{mm} \quad (3.9)$$

$$\begin{aligned} \text{Object space resolution } (\mu\text{m}) &= \frac{1000 (\mu\text{m/mm})}{2 \times \text{image space resolution (lp/mm)} \times \text{PMAG}} \\ &= \frac{1000 (\mu\text{m/mm})}{2 \times 227 (\text{lp/mm}) \times 5} = 0.440\mu\text{m} \end{aligned} \quad (3.10)$$

A limiting factor to the resolution is therefore unlikely to be the hardware. Another limiting factor is the diffraction of the light by the lens. This is observed by rings around small features known as 'Airy Disks'. To examine the limitation due to diffraction the Airy Disk spot size should be minimised. The Airy Disk size depends on wavelength. A single colour was used to illuminate the sample to reduce the wavelength band. Illumination with the lowest visible wavelength (blue light) would result in minimum diffraction. However, the transition of blue light is poor in most glass optics. Quartz based optics are prohibitively expensive, so green light was used as the shortest wavelength with sufficient intensity.

$$f/\# = \frac{1}{2 \times NA} \quad (3.11)$$

The Airy Disk Diameter in μm is

$$\begin{aligned} \text{Airy Disk Diameter } (\mu\text{m}) &= 2.44 \times \gamma(\mu\text{m}) \times \frac{1}{2 \times NA} = 2.44 \times 0.520 \times \frac{1}{0.3} = \\ &4.2\mu\text{m} \end{aligned} \quad (3.12)$$

Therefore, diffraction of the light is the limiting factor and the minimum feature size that can be calculated is $4\mu\text{m}$ using this system. To reduce the minimum resolvable features further quartz lenses and blue or UV illumination must be used, which is prohibitively expensive at this stage. As can be seen in Figure 3.10. The system was proven to distinguish both features such as $50\mu\text{m}$ lines on glass

and 5 μ m etched features. Although the 5 μ m features were small, the feature was clear enough to be used as a fiducial for alignment.

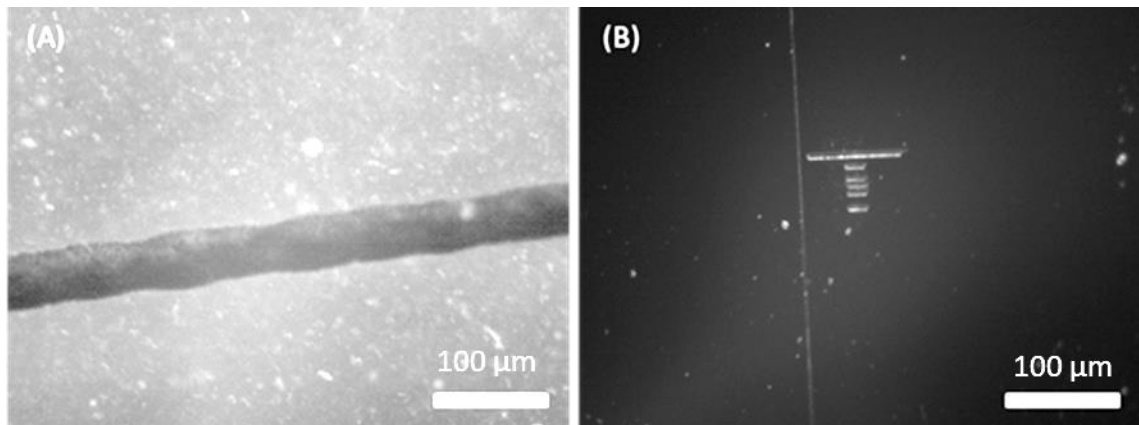


Figure 4.10: Images taken on the in-process camera (A) 50 μ m width line (B) 5 μ m width etched features.

4.1.4 Head Mount and Platform

The short travel distance of the X and Y axis presented a challenge when it came to mounting the print heads and alignment camera. The physical size of the components meant that they could not be mounted in a line. To fit the nozzles and the microscope close enough together they were clustered around the centre of the bed in a triangular shape.

Below this mount, a manual rotating platform was produced, which could be attached onto to the XYZ axis. This rotating platform was used to align substrates made in another process, in a similar method to a mask aligner. A picture detailing these components is shown in Figure 4.11. A digitally controlled cartridge heater and thermocouple were attached to the print platen, to maintain the print surface at a constant temperature.

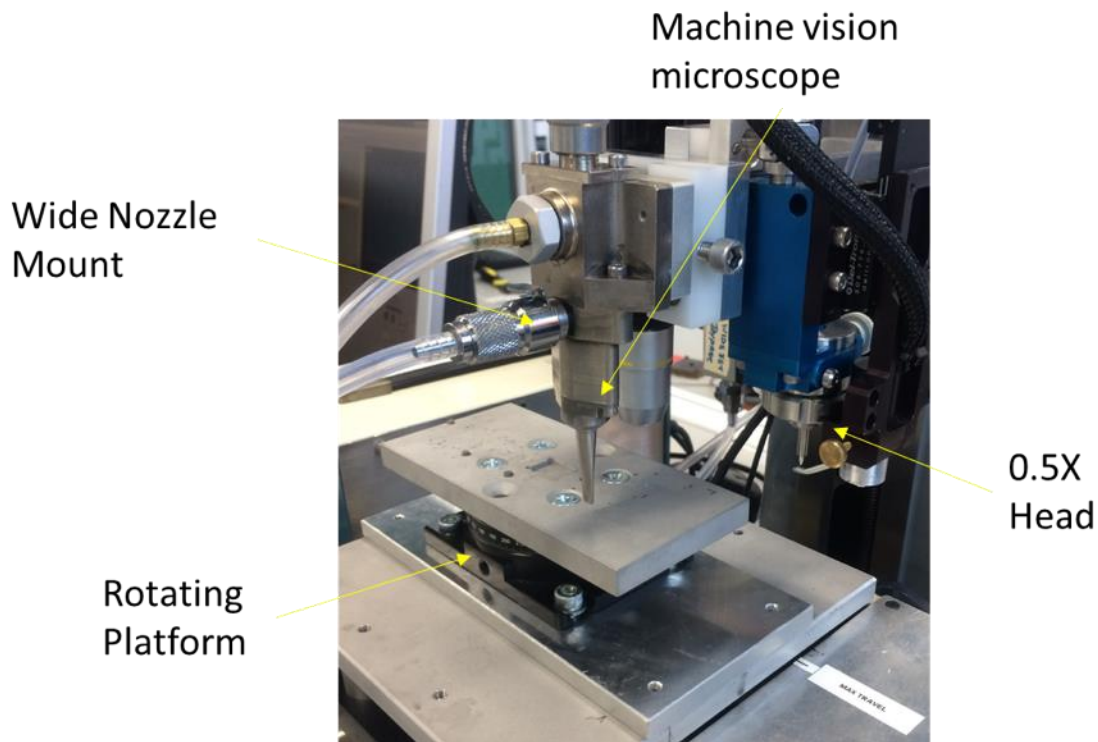


Figure 4.11: Print head mounts and rotating stage

4.1.5 Environment

For comparative purposes the print environment was kept constant where possible. Factors such as ambient temperature and humidity can affect the drying of prints (discussed in Section 2.1.4). All printing was therefore performed at 20°C. In the laboratory there were no open windows and the apparatus was placed away from the doors to reduce turbulent airflow which may have disrupted the printing. In addition, all samples were stored in sealed containers and, where appropriate, these were also filled with clean deionised (DI) water to avoid particles settling.

4.2 Software and Control

The commercial AJP system takes digital design data and converts this to machine control code. However, as only the commercially available part of the print engine was purchased the control code also had to be generated in using a different method. This also provided an opportunity to develop the generator to optimise machine movements for biological applications (by, for example,

minimising shuttering operations), and to ensure its responsiveness to design changes. An open source CNC controller called 'Mach 3' was used to drive the automation process. Mach 3 takes G-code, a well documented machine control code as an input [212]. The instructions contained in G-code define the manipulation of the substrate under the print head. Initially the shapes required were simple enough that the code could be written by hand. A template was developed which was formatted in three sections.

A header script was sent to initialise the printer. In this script the default movement was set to absolute units (G90), canned cycles were deleted (G80), XY plane selected for printing (G17), the machine set to metric (mm, G21), and any tool compensation and offsets were turned off (G40, G49). Although many of these instances are unlikely, the header code was a failsafe and meant the machine was set up the same for each run. The shutter was then closed (M08) and the stage was moved to the datum (G00). The movement speed was also set in the header (F). The full header script is shown below. Everything after the # is a note used only in this thesis.

```
(Begin Start Up)
G90 G80 G17 G21 G40 G49           #Initiation Instruction
M08                               #Open shutter
G00 X0 Y0 Z0                     #Move to origin
F100                             #Set speed
(End Start Up)
```

The body of the code contained the movement script. In G Code G01 is used for linear movements, and G02 and G03 clockwise and anticlockwise arcs. To repeat the pattern and increase the production throughput, handwritten programming used the 'step and repeat' strategy. Local origins were programmed in absolute coordinates, within the global framework of the machine. The individual patterns were programmed in incremental coordinates, where each movement was based off the previous machine location, not the global co-ordinates. The code that

controls the pattern is not stored in body of the code, but is a sub-function called using the M98 command. The controller was switched between absolute and incremental coordinates by calling G90 and G91 respectively. An example code used to print four lines is shown below.

```
G91                # Set to incremental co-ordinates
M98 P1000 L2       # Call function index 1000 and loop twice
G90                # Set to absolute co-ordinates
G00 X-10 Y0        # Move to machine co-ordinates (-10,0)
G91                # Set to incremental co-ordinates
M98 P1000 L2       # Call function index 1000 and loop twice

### END PROGRAM HERE #### #The end program is not described here

O1000              # Defines function index 1000
M09                # Opens shutter
G01 X5             # Move X 5mm from current position
M08                # Close shutter
G00 X-5 Y1         # Move X -5mm Y 1mm from current position
M99                #Return to main body
```

The code end section closed the shutter (M08) returned the machine to its home position, lowered the platform to aid loading and unloading the samples (G00). It then re-wound the code so that it can be run again (M30).

```
(End Section)
M08                #Close Shutter
G00 X-2 Y-2 Z-4    #Move to home position
M30                #End program and re-wind
%
```

4.2.1 Equation Driven G-code Generator

G-code scripts are short for lines and simple circular arcs so in the validation work presented in Chapter 4 the G-code was hand written. However, more complicated shapes such as elliptical and non-circular arcs, or complex splines require definition by approximation using a series of small straight movements called a polyline. The code to produce such features was over 600 lines. Therefore, as the requirements of the printed designs became more complex through the project, Python was used to program procedural algorithms to generate the G-code for complex shapes based on any equation that was desired by the user.

The first method to generate complex curves was by using mathematical equations to describe the shape. A code was developed to take any mathematical equation and boundary conditions and generate a G-code which moved the substrate in that geometry. The method of the code is shown in Figure 4.12.

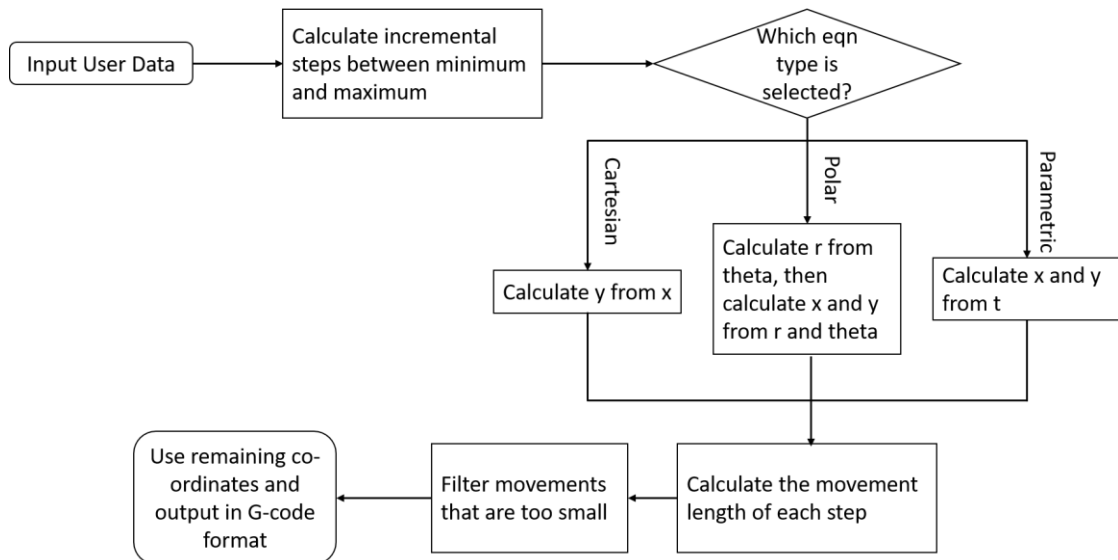


Figure 4.12: Overview of the equation driven G-code generator process

The program could take any equation (cartesian, polar, or parametric) and output X and Y movements in either absolute or incremental steps coordinates, enabling complex curves to be generated. The Python script then automatically appended the header and footer codes as described in Section 4.2.

The user input data starting with a case selector, where cartesian, polar or parametric case was selected. Here was where the minimum step size of the machine, a scaling factor, and an equation, maximum value, minimum value, and equation step size were input. If the parametric case selection was used, two equations (both X and Y) were required or the script did not run and returned an error case to the user.

An array was created of all the values between the equation maximum and minimum, increasing by the equation step size. Depending on the case this represented:

- X Values in the cartesian case
- Theta values in the polar case
- T values in the parametric case

As only one case can be selected per run, no errors were caused by assigning the values in this way. The subsequent X and Y values were then calculated based on the user equation:

- In the cartesian case the y values were directly calculated based on the user equation.
- In the polar case the theta values were calculated from the user equation, and then converted into x and y values.
- In the parametric case the x and y values were calculated from the user equations.

If the equations generate a sharp curve or small circle one phenomenon was that these movements were too small for the machine to actuate. Running the program using a larger step size resulted in a loss of feature resolution elsewhere, so an additional step was needed to filter out small movements. Any movements smaller than the minimum value were deleted. This code was run iteratively until there were no movements too small for the machine to actuate.

Once this process had finished, the X and Y values were formatted and written into a script using the G-code syntax. The output is equivalent to a polyline, so no complex movements or shuttering is required other than the start-up and end sequences. Using the equation-based generator, complex curves can be expressed in format required for the machine. Examples of these complex curves are shown in Figure 4.13.

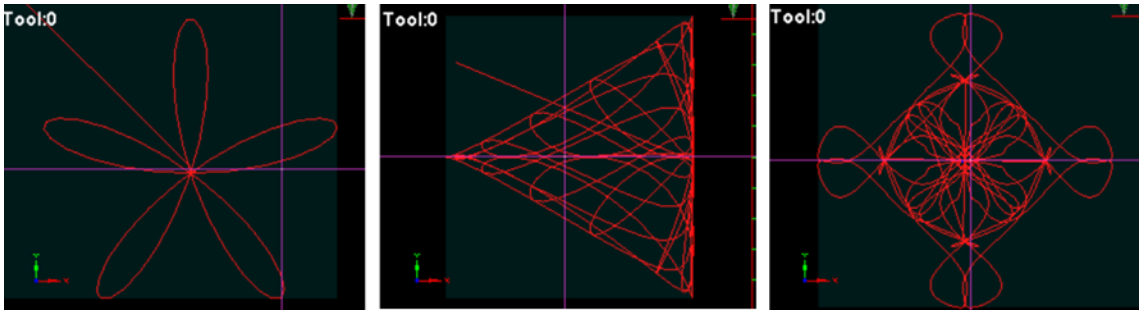


Figure 4.13: Complex curves generated through the equation-based G-code generator

Several curves could be stitched together to generate patterns that cannot be described with a single curve. The program with an example parametric equation can be found in the Appendix B.

4.2.2 DXF Driven G-code Generator

Although complex features were achievable using equations, more controllable, and updatable freeform designs could be produced from a digital design file. By using this method, designs changes can also be instantaneous, and only require a change to the digital design. An industry standard file format is to use a DXF file. This design file type is output by most computer aided design (CAD) programs and is used as an input file in many machines such as laser cutters or, pick and place apparatus.

Most CAD programs can output DXF files. In this project existing SolidWorks licenses or open source software such as libreCAD were used to generate complex designs. One major benefit to using DXF files was the ease with which the designs were scaled up using a linear array function as shown in Figure 4.14.

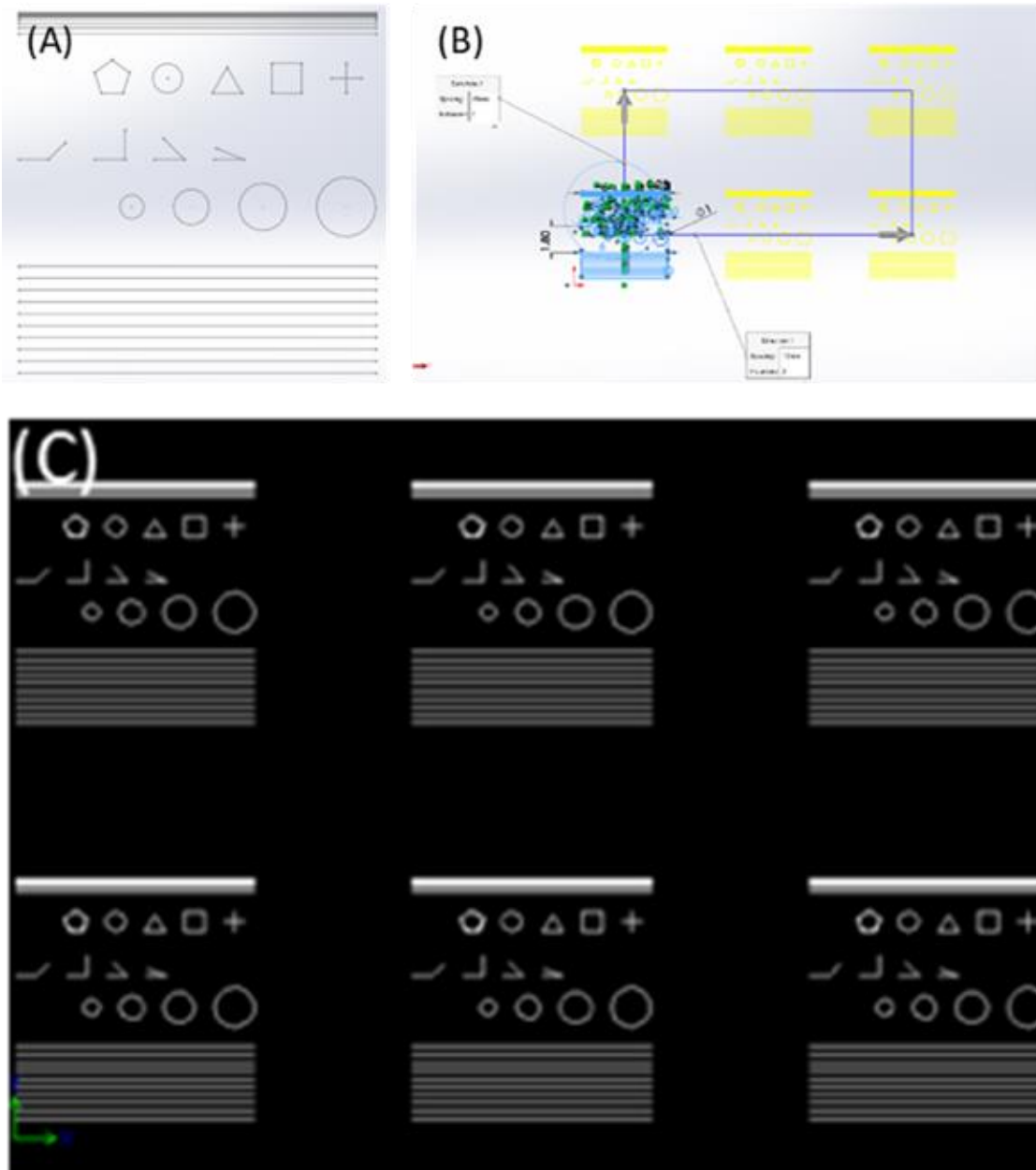


Figure 4.14: (A) Designs are generated in a CAD software. (B) Designs can be instantiated many times to scale up production rates (C) A DXF output file is generated.

Autocad file structure has comprehensive documentation making data extraction possible for this file type. A custom G-Code generator was written which takes a DXF file and outputs a G-code written specifically for the University of Leeds AJP system. The overview of the code is illustrated in Figure 4.15.

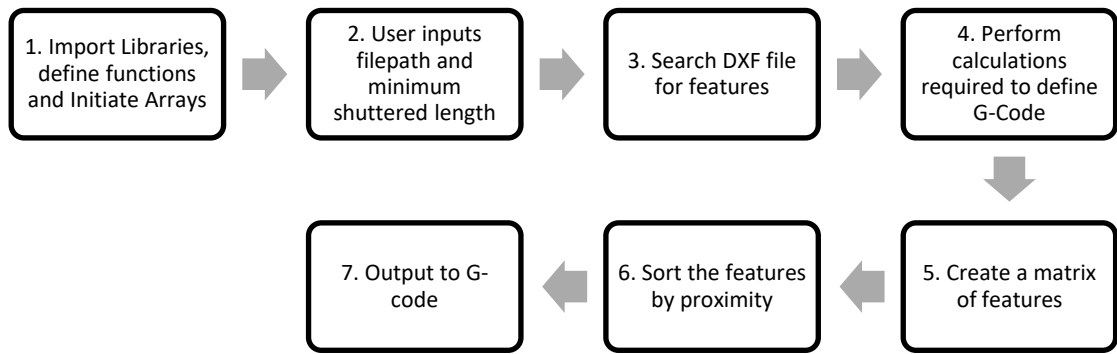


Figure 4.15: Overview of the DXF driven G-code generator

The code relies on the math and NumPy libraries, which are standard, open source data processing tools Python, for trigonometric functions and matrix processes. It also imports the datetime library for file formatting. A series of arrays and constants are defined in the code header, and the user inputs for the DXF file path and the minimum shuttered movement length are required. An empty matrix is defined which will store all the relevant data for features within it.

As an example for the following steps a DXF file with multiple representative geometries was used. The file is shown in Figure 4.16. Although small, the file contains 3 different geometry types which is useful to illustrate the python script.



Figure 4.16: Illustration of a multi-shape test DXF file, and snippets of code with the definition of a line, arc and circle highlighted.

After the initialisation and input steps, step 3 searches the DXF file line by line for recognisable features. This step is also useful as it disregards superfluous

information contained within the DXF file. When a line is encountered the data relevant to drawing it using G-code is extracted following the block diagram in Figure 4.17.

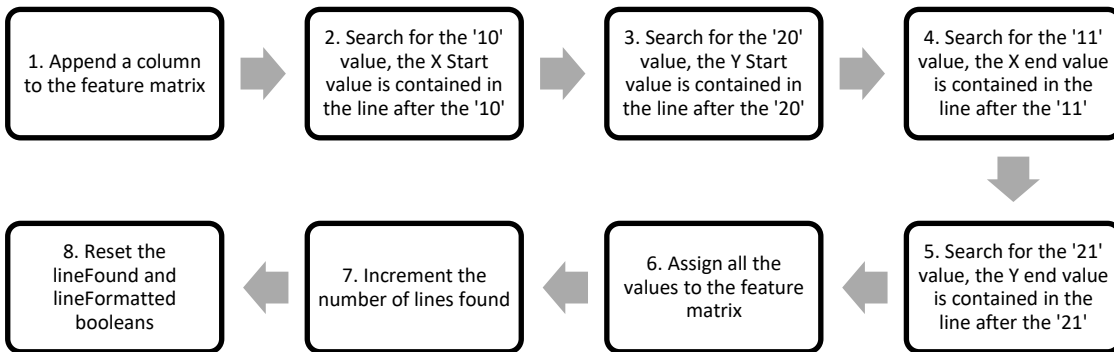


Figure 4.17: Overview of the DXF driven G-code generator

A similar search function is used to find Arcs, Circles and Polylines. The definition of arcs and circles is different in DXF files and in G-code. The definitions are summarised in Table 4.2.

Table 4.2: Circle and arc definitions in DXF files and G-code

DXF files definition	G-code definition
Start angle	X, Y start co-ordinates
End angle	X, Y end co-ordinates
Radius	I value
X, Y centre co-ordinates	J value

So, the DXF values were converted as follows:

```

arcXStart=arcXCentre+arcRadius*cos(arcStartAngle)
arcYStart=arcXCentre+arcRadius*sin(arcStartAngle)
arcXEnd=arcXCentre+arcRadius*cos(arcEndAngle)
arcYEnd=arcXCentre+arcRadius*sin(arcEndAngle)
arcI=arcXCentre-arcXStart
arcJ=arcYCentre-arcYStart
  
```

The program was set up to draw circles from the negative x axis so only the circle X Start, circle Y start, and I value is required.

After the search and calculation functions are carried out the data is stored in an array format in Table 4.3. The array is extended to contain as many features as are identified in the DXF file. At this stage the code does not attempt to sort the

features, and just stores them in the order they appear in the DXF. This is usually the order they are drawn by the user.

Table 4.3: Example of an unsorted feature matrix

0 (X Start)	1 (Y Start)	2 (X End)	3 (Y End)	4 (I Value)	5 (J Value)	6 (Object ID)
14.00	19.00	9.00	21.50	NaN	NaN	0 (Line)
...
13.00	11.20	11.00	13.20	-2.00	0	1 (Arc)
...
6.00	14.00	6.00	14.00	1.00	NaN	3 (Circle)
...

A functioning G-Code could have been generated from this array. However, as the machine movements were mapped to the order the DXF was drawn in, it required many shuttering operations and would take a long time to execute. Therefore, a proximity sorting algorithm is implemented, with the aim of printing the design in the most efficient manner, and with the fewest number of shuttering operations. For example, two toolpaths to print the multi shape design in Figure 4.16 are shown in Figure 4.18. Figure 4.18A shows the toolpath without the sorting algorithm whereas Figure 4.18B shows with the toolpath with the algorithm. The print without sorting would take significantly longer, and each feature would have had end effects associated with shuttering. By implementing the sort function the design is printed in a logical order of discreet shapes, reducing the time taken to print and the number of undesirable artefacts on the finished substrate.

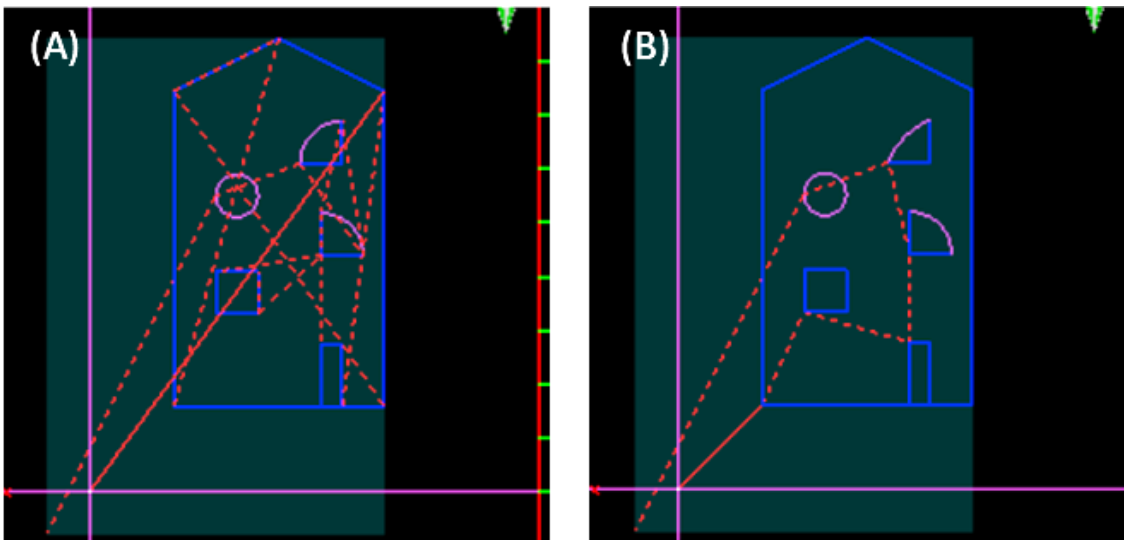


Figure 4.18: (A) G-Code Generated with the unsorted matrix (B) G-code generated using the sorted algorithm. Red dashed lines are shuttered movements, blue and purple lines are print movements.

A short example using a selection of features from the multi-shape design is shown in Figure 4.19 to Figure 4.21. The algorithm starts with an X and Y value set to the origin. The code scans column pairs 0 and 1 (start co-ordinates) and 2 and 3 (end coordinates) for the next closest coordinate. Either of these columns can contain the next closest vertex, meaning they will be selected and used to define the next closest feature to print. Once a feature has been selected it is discarded from the unsorted array and written into a sorted array. If columns 2 and 3 (end co-ordinates) are taken as the closest position then columns 1 and 2 (start coordinates) and 3 and 4 (end co-ordinates) are swapped when transferring to the sorted array. The exception to this is in the case of an arc, where the object identifier is overwritten to 2 (clockwise arc). The end position of this feature is taken as the working tool position. The code loops and selects the next closest feature until all the features are sorted.

In the first iteration (Figure 4.19), the closest co-ordinates to the origin are found in columns (0,1). This entire row is then cut from the unsorted array and is written into the first row of the sorted array. The working co-ordinates are then updated to the end coordinates in the sorted array.

Working (X,Y)=(0,0)

Unsorted Array

14.00	19.00	9.00	21.50	NaN	NaN	0
13.00	11.20	11.00	13.20	-2.00	0	1
6.00	14.00	NaN	NaN	1.00	NaN	3

Sorted Array

6.00	14.00	6.00	14.00	1.00	NaN	3

Figure 4.19: First step in the sorting algorithm, with the next closest co-ordinates highlighted in yellow. As it contains the next closest co-ordinate, row two of the unsorted array is copied to row zero of the sorted array.

In the second iteration (Figure 4.20), the closest co-ordinates are found in columns (2,3). This entire row is then cut from the unsorted array and is written into the second row of the sorted array. However, as the feature is an Arc it must be drawn in the opposite direction, therefore columns (0,1) and (2,3) are swapped. Column 6 is updated to reflect this. The working co-ordinates are then updated to the end coordinates in the sorted array

Working (X,Y)=(6.00,14.00)

Unsorted Array

14.00	19.00	9.00	21.50	NaN	NaN	0
13.00	11.20	11.00	13.20	-2.00	0	1



Sorted Array

6.00	14.00	6.00	14.00	1.00	NaN	3
11.00	13.20	13.00	11.20	-2.00	0	2

Figure 4.20: Second step in the sorting algorithm with the next closest co-ordinate highlighted in yellow. As the next closest co-ordinate in the unsorted array is in columns 2 and 3 of row 1; the start and end co-ordinates are swapped, the direction marker (column 6) is changed, and the row is copied to the sorted array.

In the third iteration (Figure 4.21), the closest co-ordinates are found in columns (0,1). This entire row is then cut from the unsorted array and is written into the third row of the sorted array. The working co-ordinates are then updated to the end coordinates in the sorted array

Working (X,Y)=(13.00,11.20)

Unsorted Array

14.00	19.00	9.00	21.50	NaN	NaN	0
-------	-------	------	-------	-----	-----	---

Sorted Array

6.00	14.00	6.00	14.00	1.00	NaN	3
11.00	13.20	13.00	11.20	-2.00	0	2
14.00	19.00	9.00	21.50	NaN	NaN	0

Figure 4.21: Third step in the sorting algorithm, with the next closest co-ordinates highlighted.

The process is repeated until all the features are sorted. The algorithm then scans the sorted array for adjacent features where the distance between them is less than the minimum shuttered distance. For these features, a shuttering call is not made in the G-code. The result of the sorting algorithm is to reduce the total path length and results in a logical printing order of complete shapes where they exist. This sorted array is then used to write a text file in the G-code syntax. The function is compatible with many different shapes and scenarios, based on the object identifier, and the movement length.

4.3 Chapter Summary

This chapter describes the body of work to produce a system capable of directed chemical treatment onto the surface. This work consisted of the design of the essential automation apparatus and described the complementary processes that enabled successful printing. In addition, a new Python program was produced which generated the necessary control code from DXF design data or mathematical equations.

The commercial AJP system was integrated into a custom three axis stage and combined with an alignment camera and manual rotating platform. The machine is capable of minimum incremental movements of $<10\mu\text{m}$, and the primary printing region was decided as the region of the least backlash ($\sim 25\mu\text{m}$). The movements were controlled using open source Mach3 CNC control software. Mach3 takes G-Code as the control code, and it is this control code which describes the translation of the substrate under the print head, in terms of design and speed. An overview of the manufacturing system is shown in Figure 4.22.

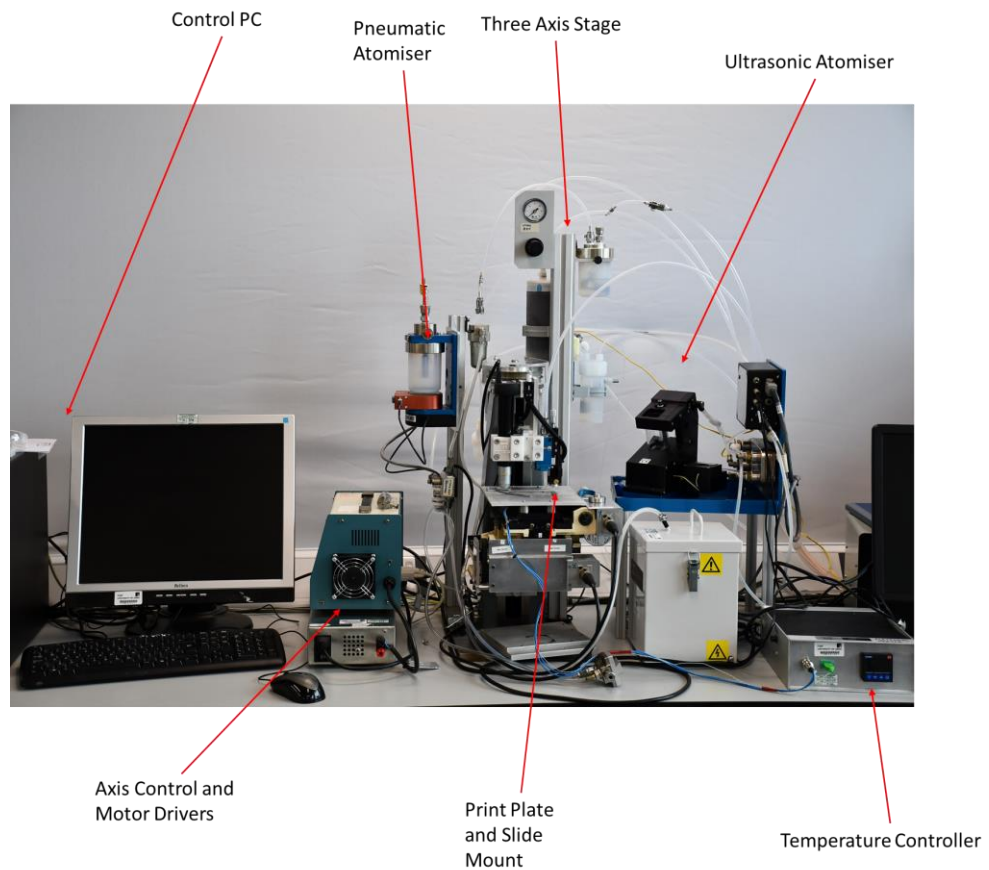


Figure 4.22: Overview of the AJP print engine integrated into a bespoke automated apparatus.

Finally, Python scripts were produced which can generate G-code from equations, or from a DXF design file that could be updated without the cost or time associated with updating a physical mask. The program is capable of reading lines, arcs, circles, and polylines, whilst disregarding the superfluous information contained within the DXF file. The identified features were run through a sorting algorithm which sorted the print order into a logical sequence, thereby reducing the print time and the number of shuttering operations required.

The integration of these methods resulted in a functional apparatus which is used throughout the subsequent chapters.

Chapter 5 Validation of the Manufacturing Process

Reliable printing of micro-scale lines with controlled geometry (e.g. width of line, maximum height, and cross sectional area) depends on the interaction of several processing parameters. This chapter describes the process parameter tests, which were required to produce an accurate, repeatable deposit. The length of time before all the material is used or degrades or had to also be sufficient for multiple prints. All the factors identified in Section 2.1.4 were considered for their impact on the final print quality. No attempt was made to enclose the apparatus or alter its local environment, the printing was conducted at 20°C. In the validation tests a glass substrate was used due to the compatibility of glass slides with many analytical methods, especially optical microscopy, and its known biocompatibility. The aim of the initial screening tests were to define and fix other parameters such as print material, apparatus set up and print designs. Then, processing parameters were assessed. An overview of the validation testing is shown in Figure 5.1, and then expanded below.

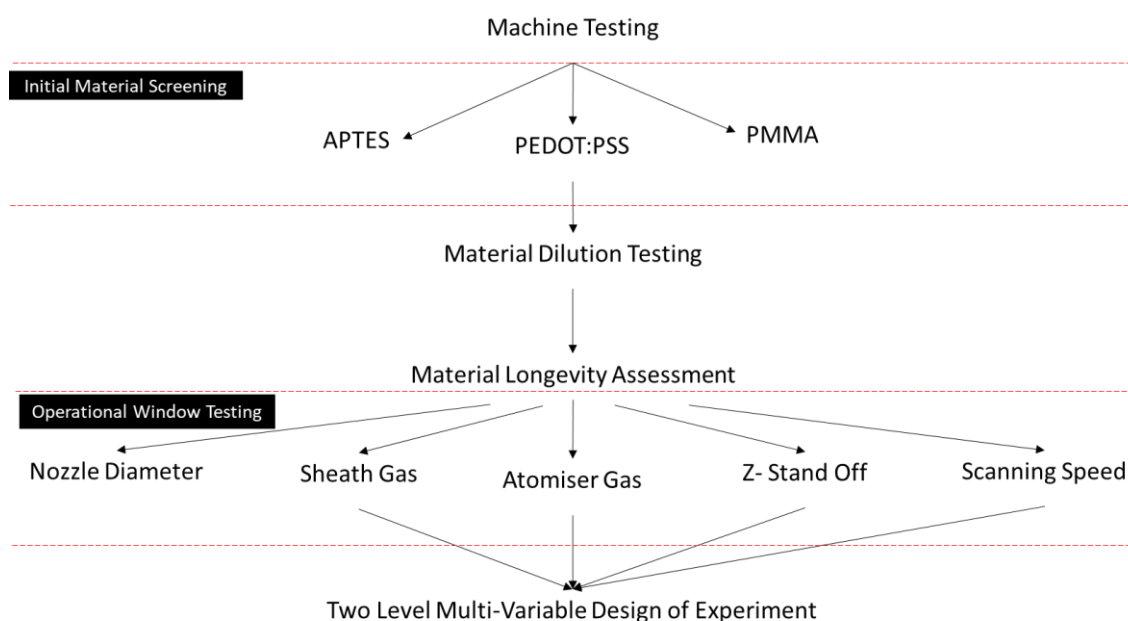


Figure 5.1: Summary of the validation testing in Chapter 4

After building the apparatus, the initial material screening served several purposes:

1. To trial potential functional materials for cell culturing.
2. To validate the automated apparatus.
3. To trial printing of basic designs using hand written G-code

The functional material selection was based on potential biological applications, informed by collaborative partners. In some cases, the ink development could be informed by the literature, and when precedent was available it was used. The decision on functional material choice was driven by the collaborators. Three printing feedstocks based on different functional materials were trialled:

1. A silane (3-Aminopropyl)triethoxysilane (APTES) which is biocompatible and can be used as a substrate for further reactions. No literature precedent was available for making AJP inks from this material.
2. The polymer Poly(methyl methacrylate) (PMMA), an inert polymer that can be used for topographical cues and walls. There was literature precedent for printing this material with AJP, discussed in Section 5.1.2.
3. The polymer PEDOT:PSS, a biocompatible and electrically conductive polymer, which has also been reported to be suitable for AJP in the literature discussed in Section 5.2.

At this stage, to reduce the experimental burden, the assessment of quality was based on an engineering assessment of geometrical features such as width, and visual inspection of the printed line integrity. Biological testing was not conducted during this validation stage. The APTES and PMMA materials each caused processing issues (discussed in 5.1.1 and 5.1.2 respectively), so further testing was conducted with the PEDOT:PSS.

Using the PEDOT:PSS functional material, a formal methodology was established for testing the dilution ratios of two co-solvents for AJP. This experiment was undertaken to highlight the importance of the initial solvent mixture and define a suitable PEDOT:PSS ink to use during subsequent processing. The stability of the ink was demonstrated in a longevity assessment by printing over a two hour window, a substantially longer processing compared with printing the APTES and PMMA inks.

Once a suitable material had been defined, five significant process parameters that had been identified in the literature were investigated to determine the process operational window. Specifically, the nozzle exit diameter, sheath gas, atomiser gas, z stand-off and scanning speed were assessed. The parameters were assessed to determine the upper and lower limits of the operational window and identify key trends in the geometry of the printed features. The geometry of the printed lines was analysed using a combination of optical microscopy and white light interferometry, and some initial proposals on the effect of the four parameters was given. These results informed the high and low values for a two level, multivariable experiment. The operational conditions do not exist in isolation and their interactions can have a substantial effect on the characteristics of the printed structures. The sensitivity of the process to the individual parameters and their interactions was assessed and used to inform specific processing conditions for targeted line geometries.

5.1 Initial Material Screening

Initial materials screening tests were performed to trial the automated apparatus capabilities, potential materials to be used throughout the experimentation, and explore some suitable machine parameters.

5.1.1 Silane Based Functional Material

APTES was used as the basis of the first printing ink. Silane based functional materials were identified as potential attractant materials for cell culture [126]. To produce the ink the APTES was mixed with acetone by agitation at room temperature. APTES has not been printed before using AJP. In the first printing experiment, the concentration of the material was varied, at fixed processing parameters. Figure 5.2 shows that when using a 1% vol/vol concentration of APTES, diluted with 99% vol/vol acetone as a printing ink did not lead to a printed line. However, when the concentration of Acetone was decreased to 90% vol/vol a more suitable deposition was observed.

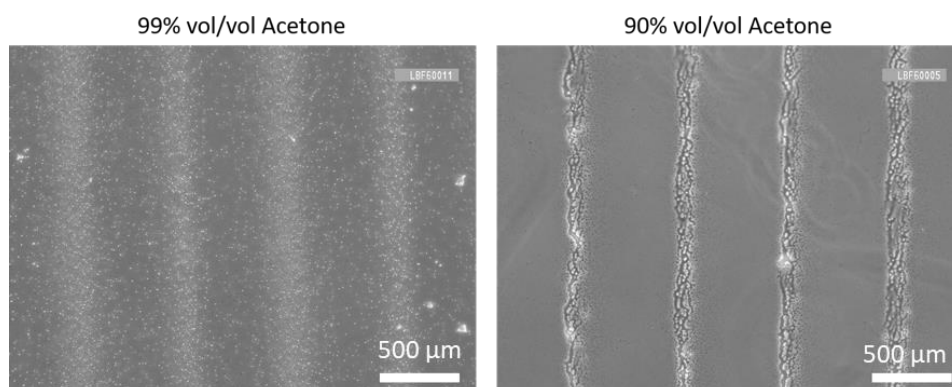


Figure 5.2: Printed lines with two concentrations of APTES ink.

These first experiments were performed to test the extreme ends of the material formulation and processing parameters with large increments. This was the first step in defining the experimental space of to a matrix style design of experiment (DOE) method. The aim at this stage was simply to stably print features with line widths below 50 μ m (to interact on the microscale with cells), with a desirable objective to minimise line width.

For the exploratory testing the geometry was printed using the largest nozzle diameter available (300 μ m). The sheath and atomiser gas parameters were increased until a deposition was seen on a stationary substrate under the nozzle. Suitable deposition occurred when the sheath and atomiser gasses were set to

180sccm and 10sccm respectively. By translating the substrate under the print head a line was printed onto the surface, which was held at room temperature. The deposited line was then dried and sintered in an oven as described in Section **Error! Reference source not found.** to drive off solvents. However, the high gas flow rate caused the printed line to deform during the printing process. The printed line is shown in Figure 5.3, imaged on a microscope.

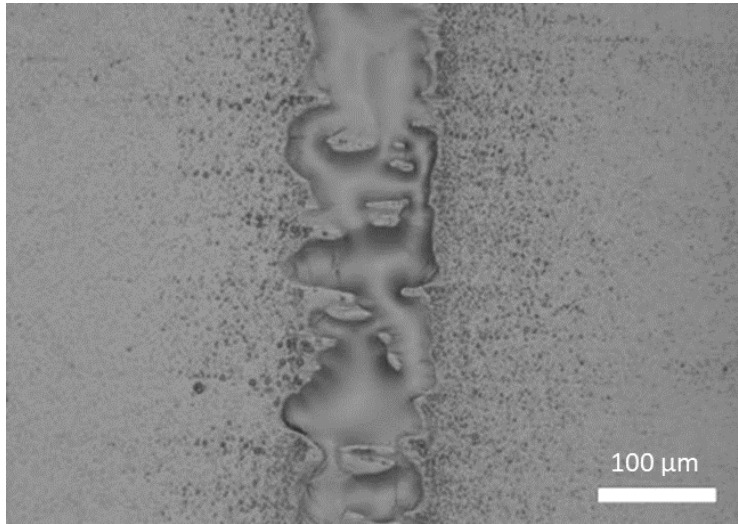


Figure 5.3: Printed APTES line.

By reducing the sheath gas flow rate to 120sccm a conformal line was printed (Figure 5.4). In addition, at these gas flow rates the nitrogen sheath did not interfere with the printing process. However, it was challenging to reduce the line width below 100μm using the 300μm nozzle.

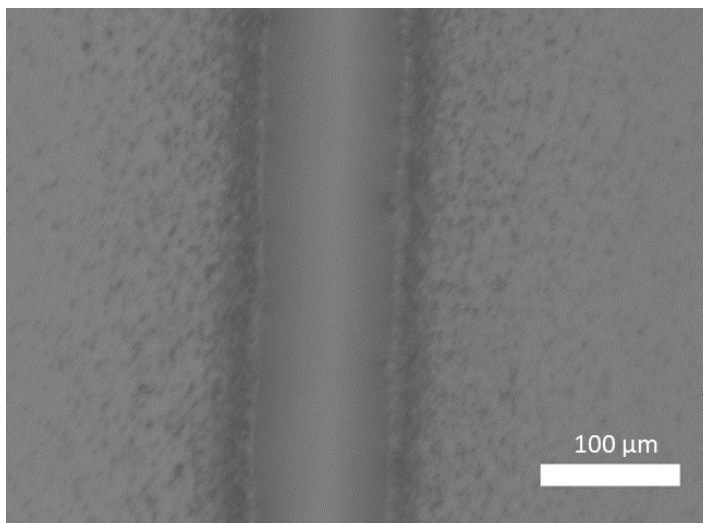


Figure 5.4: Stable printed features using new processing parameters.

Subsequently, printing was repeated using a smaller, 100 μ m nozzle. This enabled smaller line widths to be printed, although necessitated new gas flow rate definitions. To reduce the time taken for identification of suitable print parameters in the future, an automated program was developed that enabled a process overview to be produced. This automated test could be performed at different sheath and atomiser gas flow rates, scanning speeds, z heights, and number of times the head is repeatedly moved over the substrate (termed the number of passes). This program used the step and repeat strategy to populate the features. Each feature was varied by automatically changing the operational conditions. The full program is shown in the Appendix C. A typical output of this test is shown in Figure 5.5. The cross shape was chosen to assess sharp corners and line intersections.

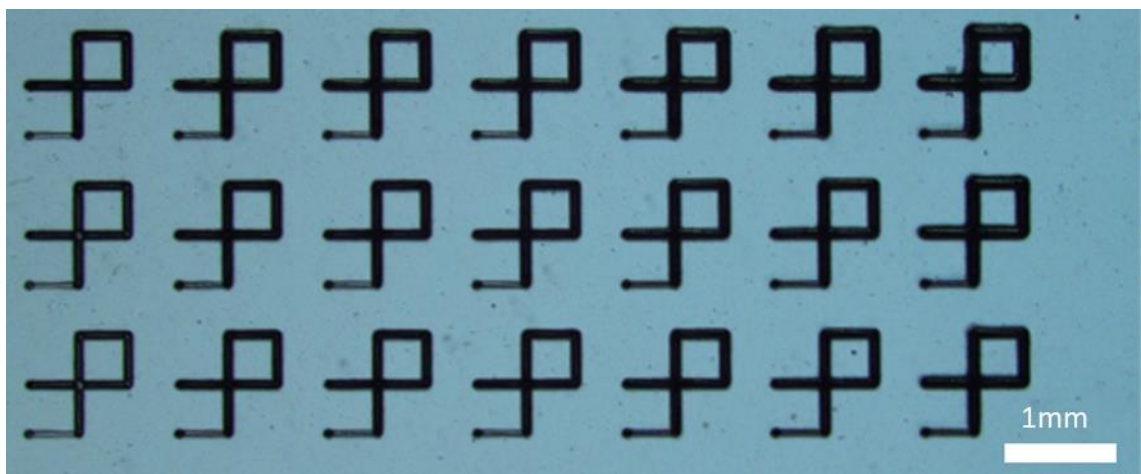


Figure 5.5: An overview example of the results of a typical test, showing the changing geometries at different processing parameters.

Higher magnifications of specific data points enabled key trends to be qualitatively identified. Figure 5.6 highlights the effect of increasing the scanning speed from left to right and increasing the number of passes going down each column.

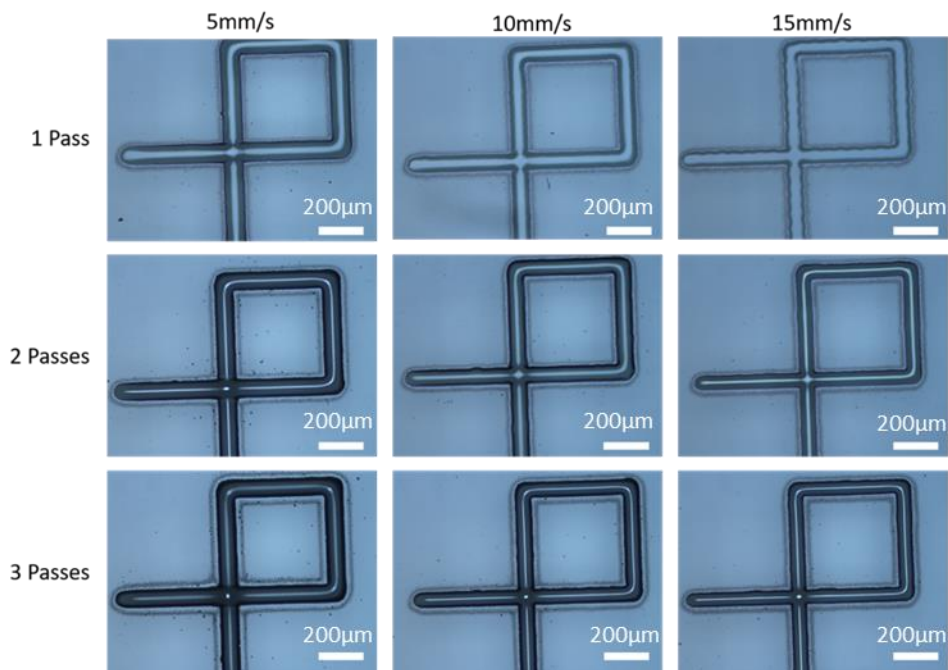


Figure 5.6: The effect of increasing number of passes and increasing scanning speed.

In all the samples increasing the number of passes appeared to increase the line width, and the darker features indicated an increased line thickness. As small features were desirable it was determined that a single pass of the material was suitable at this stage. By increasing the print speed, it appeared a smaller deposit was printed. Changes to the line geometry due to changing Z height were not qualitatively notable as highlighted in Figure 5.7, so the middle point of the range (3mm) was chosen for printing.

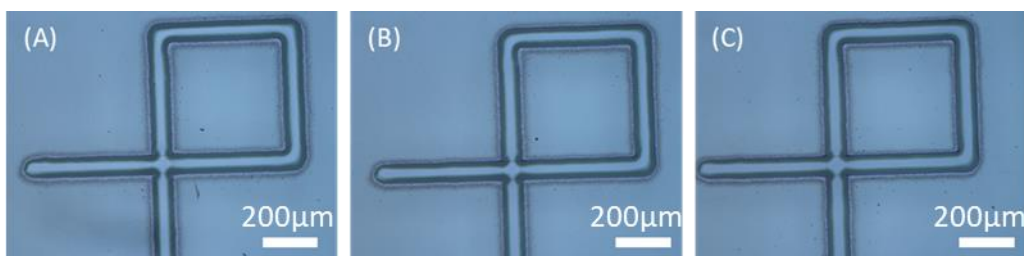


Figure 5.7: Printed features when z stand-off is (A) 2mm (B) 3mm (C) 4mm.

Figure 5.8 illustrates the substantial effect of changing the atomiser gas. In general, the gas flow rates had the biggest effect on the deposit properties. Reducing the atomiser gas appeared to reduce the amount of deposited material. Printing with 5sccm atomiser gas resulted in a non-confluent, patchy deposit.

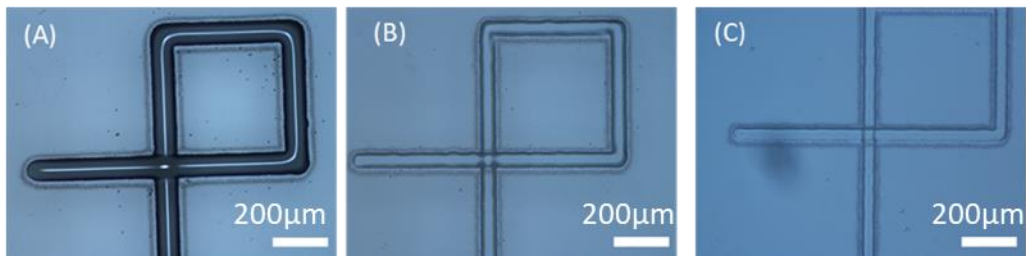


Figure 5.8: Effect of atomiser gas on print geometry (A) 20 sccm (B) 10 sccm (C) 5 sccm.

At the intersection of the lines, the printed feature can be compared to a print with two passes in that local area. The thickness was assessed under white light interferometry, to verify that only the local region of the crossover was affected. Figure 5.9 shows an example of the effect of track cross overs. In Figure 5.9A an optical microscope image of the cross over is shown. Figure 5.9B shows a white light interferometry reading of a typical cross over showing how the thickness increases at the local point only and the surrounding print is not affected.

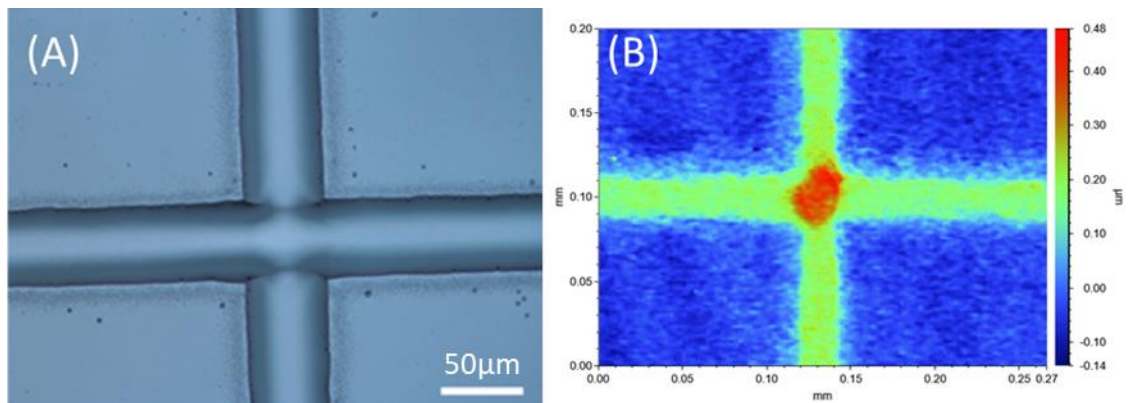


Figure 5.9: (A) The effect of track crossovers. (B) White light interferometry image showing the height change due to the cross over.

Using the APTES ink small features were produced and this printing experiment resulted in several important observations for printed features, such as the effect of changing the scanning speed, number of passes and atomiser gas. However, the print material tended to block the nozzles and due to the small size of the orifice once a nozzle blockage occurred it was challenging to clear. This was exacerbated by the chemical resistance of APTES. Figure 5.10 illustrates the different responses of blocked nozzles and unblocked nozzles during the printing

process. Nozzle blockages could be identified as the pressure did not stabilise and kept increasing to the maximum of 5psi. These nozzle blockages were not easy to clear, especially when a 100 μ m nozzle was used, and the cost of nozzles was high. Dissolving the blockage in solvents, physical clearing with a thin wire, subjecting the blockage to 300psi of water, and burning the silane in a furnace were attempted but did not remove the blockage.

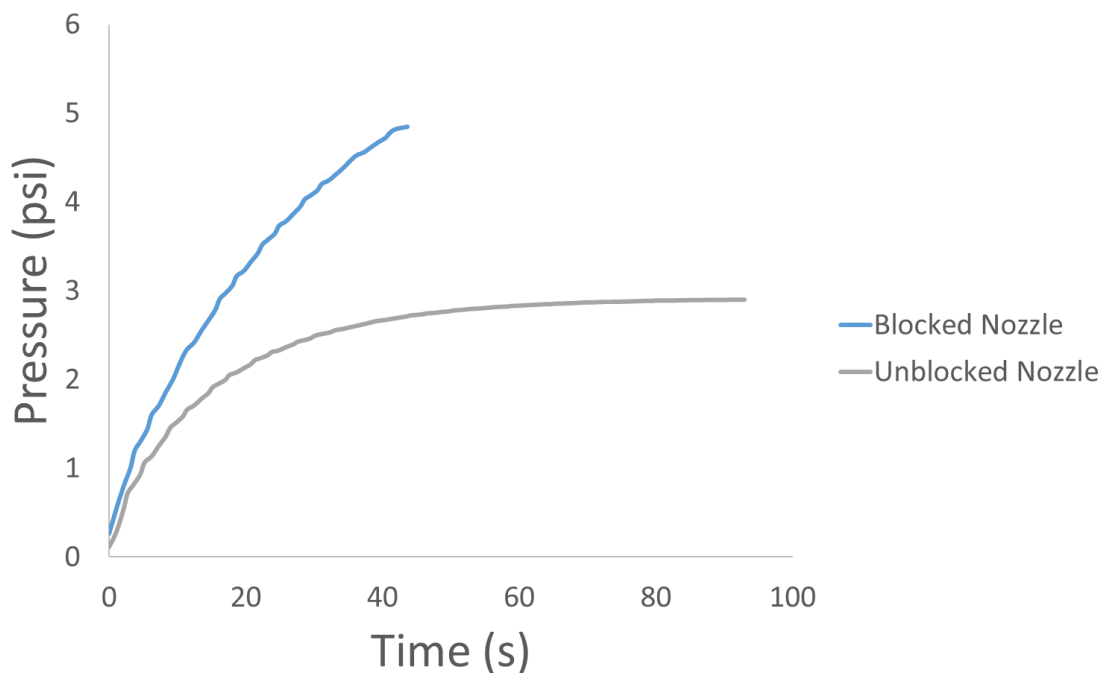


Figure 5.10: Comparison of Blocked and Unblocked nozzle when tested on the Aerosol Jet. The pressure response of blocked nozzles was clear as the pressure would increase at a faster rate and would not stabilise.

5.1.2 Poly(methyl methacrylate) Based Functional Material

Due to the challenges with nozzle blockages when printing with APTES, a new printing material based around a Poly(methyl methacrylate) (PMMA) functional material was developed. PMMA is soluble in acetone which is available in laboratory environments, so any blocked nozzles could be cleared by submerging them in acetone overnight.

From the literature, PMMA has been printed with AJP using an acetone and cyclohexanone co-solvent mixture [141]. Co-solvent mixtures consist of a high volatility solvent, and a miscible low volatility solvent. The benefits of the co-

solvent mixture are print stability over time, and the printing of high aspect ratio features [42], [213].

The high volatility solvent is the principle liquid component of the printing ink. It dissolves or suspends the functional material and lowers the viscosity into the range that can be atomised. However, high volatility solvents have low boiling points, so evaporate in flight resulting in dry deposition and can also evaporate out of the ink reservoir leading to a phenomenon known as ink drying.

The low volatility solvent is the minority component which does not evaporate in flight so is deposited along with the material on the substrate surface, aiding the levelling and packing of the material onto that surface.

PMMA inks have been printed with Aerosol Jet using sheath and atomiser gas values of 20 and 15 sccm respectively [214]. However, these were defined for a 200 μ m nozzle and consequently a line was not printed at these settings (Figure 5.11A). As seen with APTES, this initial print setting can be dialled in to produce a confluent line. By changing the processing parameters the deposit characteristics were improved. In this case doubling the gas values resulted in a printed feature (Figure 5.11B).

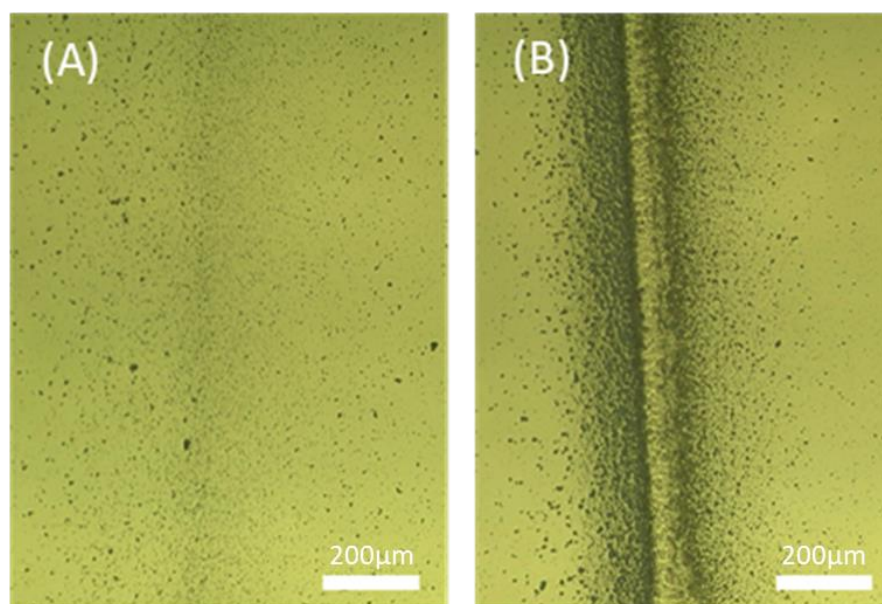


Figure 5.11: PMMA deposit printing at (A) sheath gas 20 sccm, atomiser gas 15 sccm (B) sheath gas 40 sccm, atomiser gas 30 sccm.

Further trials were conducted on increasing the sheath and atomiser parameters and a stable print was achieved when the sheath gas was 30sccm and the atomiser gas was 30sccm (Figure 5.12). These print settings were used for subsequent PMMA printing.

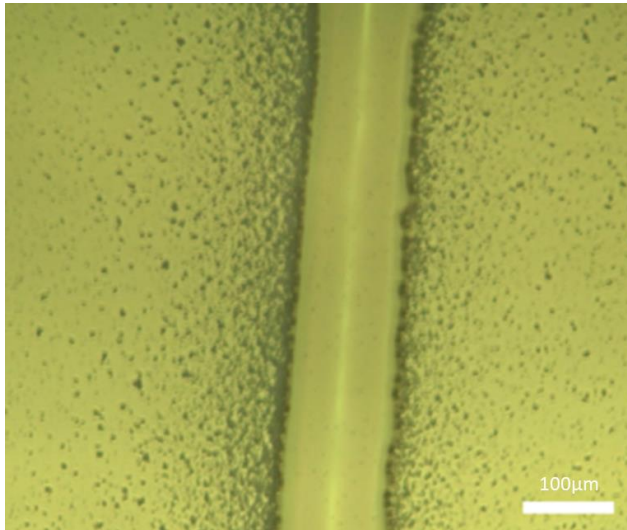


Figure 5.12: A confluent PMMA line

Alongside the materials experimentation, the machine control code was developed to showcase the flexibility of the printing approach (Figure 5.13). The control over the deposit characteristics was shown by reliable printing of lines and pads. In addition, complex patterning was demonstrated using codes output from the mathematical G- code generator described in Section 4.2.1.

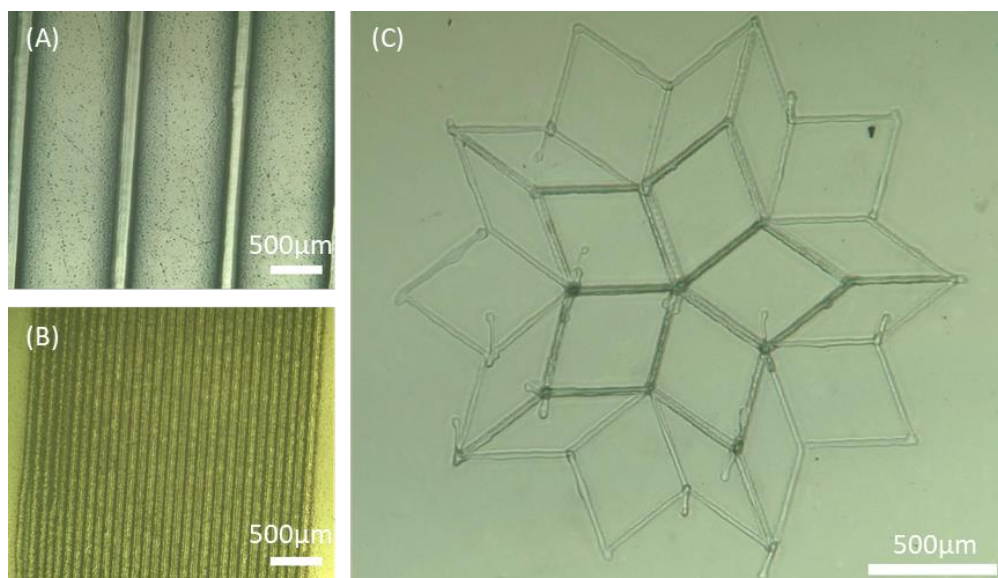


Figure 5.13: Example prints with PMMA (A) reliable printing of lines (B) a printed pad of material (C) Freeform patterning demonstration.

Throughout the trials with the PMMA, the print times achieved were poor. As little as 10 minutes stable printing was achieved before the nozzle was blocked. It was hypothesised that the lower boiling point of the acetone and cyclohexanone solvents exacerbated the ink drying phenomenon described in Section 2.1.1.1 and above. Therefore, the PMMA material was not selected for subsequent experiments.

5.2 PEDOT:PSS Ink Formulation Method

The testing to this point validated the capability of the machine to deposit materials onto substrates in a controlled manner. It also verified that by changing key process parameters the print geometry was changed, and that intricate patterns could be produced by providing specific instructions to the machine. However, the two printing inks that were trialled each presented challenges. The propensity for APTES to block the nozzles and the difficulty in cleaning the nozzles after they had been blocked meant that they could not be re-used. The print times of PMMA were too short. Whilst some patterning could be achieved, it was not practical to change the material after only a few prints.

Therefore, an ink based around PEDOT:PSS was considered as there was literature precedent available and some material formulations were reported. Aga *et al.* adapt an existing ink jetting formulation of PEDOT:PSS (Clevios P Jet N, Heraeus) to make it suitable for printing with Aerosol Jet. By diluting with DI water and alcohols, the viscosity was brought to 3.5mPa-s, within the 1-5mPa-s range of Aerosol Jet. [215]. In subsequent work Aga *et al.* use a different PEDOT:PSS formulation (PEDOT:PSS Conductive Inkjet Ink, Sigma Aldrich) with no alterations [153]. This formulation contains a co-solvent regime of DI water and ethylene glycol but the concentrations are proprietary. The same group have

printed using a proprietary formulation of PEDOT:PSS (C-Nano-NV, Heraeus) [216].

Ha *et al.* also printed using a PEDOT:PSS ink (PH500, H.C. Stark) diluted with 10% vol/vol ethylene glycol to improve printability and increase conductivity of the printed line [217]. The efficacy of this formulation is evident as it is repeatedly used in further work by the research group [137]–[139], [214], [218]. However, the most recent work from the group uses a different supplier (Clevios PH1000, Heraeus) and only a 6% vol/vol ethylene glycol content, suggesting that the ethylene glycol content can be tuned to the application [219].

Inks based on PEDOT:PSS printed stable thin features, and when deposited they form confluent features. In addition, PEDOT:PSS printed stably for long periods of time (>1hr). The applications of PEDOT:PSS in industry include touchscreens [220], solar cells [42], but a relevant application is its use as a non-toxic conductive material for electrical stimulation of cell cultures [221].

From this body of literature it is clear that nanoparticle suspensions of PEDOT:PSS are suitable for processing with Aerosol Jet printing. Commercial nanoparticle inks are supplied as a colloid in high purity DI water. Successful inks using an ethylene glycol co-solvent have been proven, however they are used in different amounts and there is no justification as to the effect of changing the content of ethylene glycol.

A methodology was established to vary the solvent content of the printing ink in a structured manner. The method is adapted from the methodologies of W. Diamond [222]. The process begins by identifying the functional material, which in this case was Clevios PH1000 PEDOT:PSS ink from Heraeus.

Once the functional material is defined, the majority solvent was considered. This was a high volatility solvent with a viscosity between 1 and 5 mPa-s for ultrasonic

atomisation. The solvent didn't need to dissolve the material. It could be used as a suspending medium of a colloid providing the functional material was in a nanoparticle form with an average size of less than 50nm [47]. Clevios PH1000 is a 1-1.3 wt% content of PEDOT:PSS suspended in DI water with an average particle size of 30µm, below the specified value from Optomec.

A minority volume of a miscible co-solvent with a higher boiling point should then be added. Ethylene glycol (198°C boiling point) was selected as it is repeatedly and successfully used as a cosolvent in the literature [137]–[139], [214], [217]–[219].

The next step is to set the upper and lower boundaries of the three-part material concentrations. As a 10% dilution using ethylene glycol is used in the literature, the upper and lower limits in this experiment were set to 0% and 20% by weight to test around an already proven formulation. The nine material formulations are generated at defined locations between the upper and lower concentration bounds.

The PEDOT:PSS suspension was mixed with a DI water and ethylene glycol co-solvent mixture. The Clevios ph1000 is pre-diluted with DI water, fixing its upper concentration limit at 1.3wt%. As the material must always be diluted, it was decided that the upper limit of the functional material was 1.04wt% (corresponding to dilution of 20% vol/vol of the co-solvent mixture) and a lower limit of 0.52%.

Table 5.1: Material concentrations limitations for PEDOT:PSS functional material

Reference	Material	Low (wt%)	High (wt%)
1	PEDOT:PSS	0.52	1.04
2	Ethylene Glycol	0	20
3	DI Water	78.96	99.48

The 9 points selected were used for analysis, allowing potential areas of interest to the formulation to be identified. The method defines the extreme vertices of the

experimental space, in addition to the quartile and middle points, as illustrated in Figure 5.14.

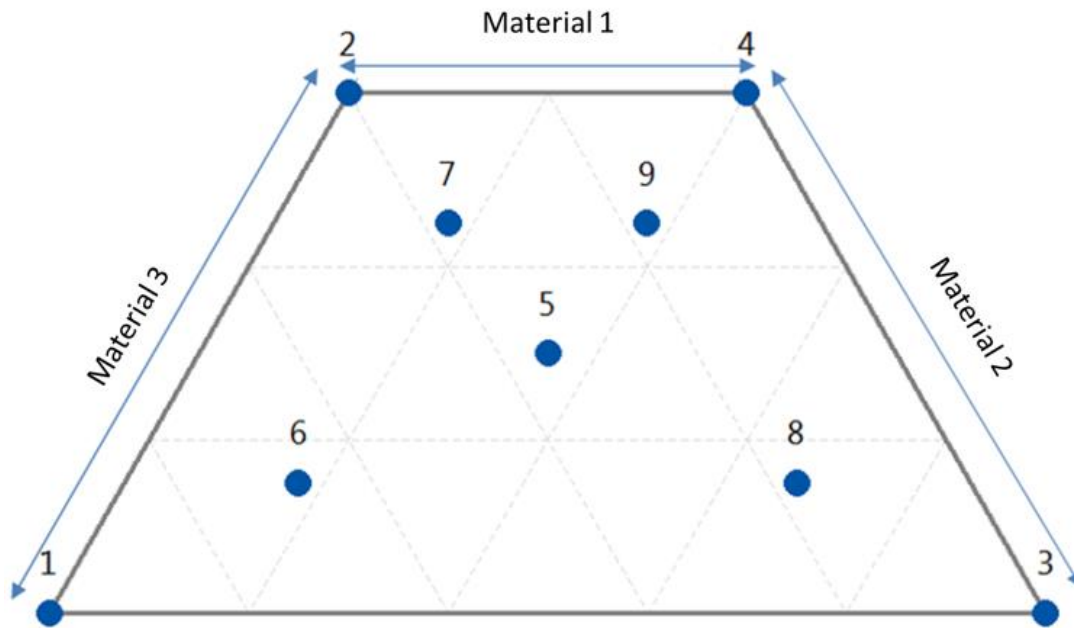


Figure 5.14: Material development method

Those 9 points are defined as the extremes of the material formulation (low and high) and the midpoints of the three materials. For this experiment the formulations are listed in Table 5.2.

Table 5.2: Material formulation boundary conditions

Formulation	PEDOT:PSS (Vol%)	Ethylene Glycol (Vol%)	DI Water (Vol%)
1	0.52%	0	99.48%
2	1.04%	0	98.96%
3	0.52%	20%	79.48%
4	1.04%	20%	78.96%
5	0.52%	10%	89.48%
6	0.78%	0%	99.22%
7	1.04%	10%	88.96%
8	0.78%	20%	79.22%
9	0.78%	10%	89.22%

From the experience gained in initial experiments and advice from Optomec some starting settings were selected. The formulations were printed with the following parameters:

- Nozzle orifice size 200µm

- Sheath and Atomiser Gas set to 50 sccm
- Feed rate 100mm/min and Z height 3mm

After printing, the samples were heated to drive off solvents and sintered in an oven at 150 degrees for 10 minutes. The resulting line was viewed at 10 times magnification under an optical microscope and inspected for line integrity, line width and defects such as satellites, bulges and pinches as previously described.

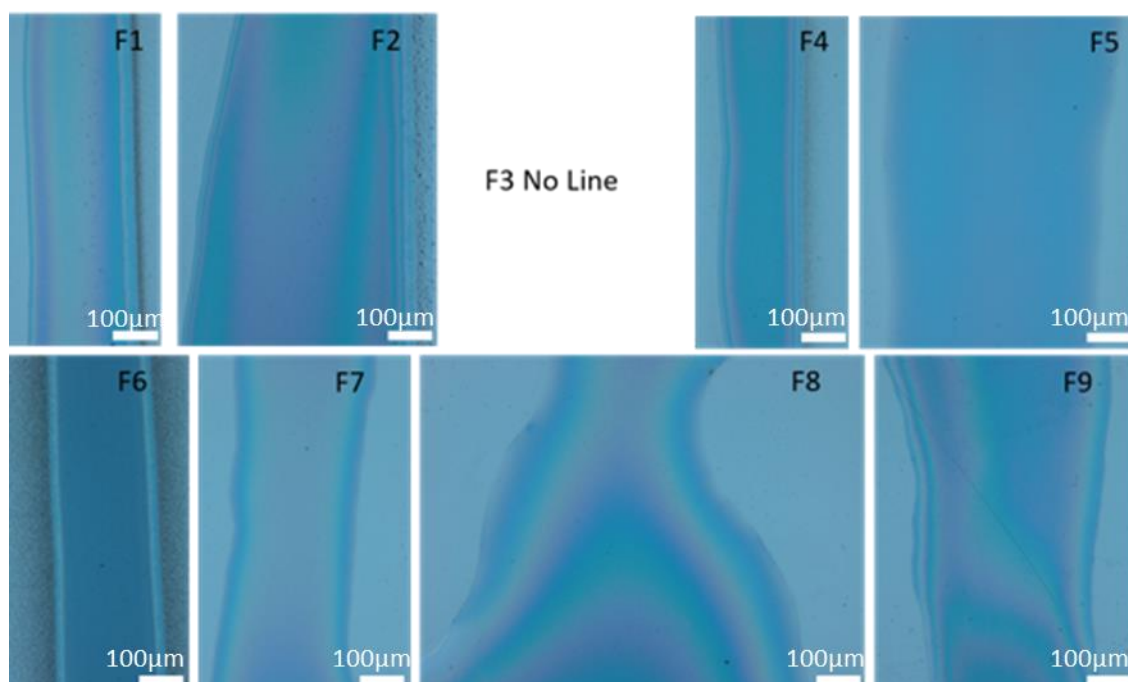


Figure 5.15: Effect of material formulation on PEDOT:PSS prints.

The observations of each result are summarised in Table 5.3. Formulations 1-4 were the extreme limits of the material test, and there was a clear distinction between them. Formulation 1 (F1) and F3 both contained the smallest quantity of PEDOT:PSS (0.52%). F1 printed a stable thin line however, no discernible line was deposited for F3, which was attributed to the small quantity of PEDOT:PSS and addition of ethylene glycol. F2 and F4 had the highest concentration of PEDOT:PSS and had sintered to form a complete line. However, the lines produced by F2 were wide compared to the other samples, and in some areas the bulging phenomenon was observed.

F5-9 investigated the middle of the sample space. As expected, all produced a deposit but the characteristics differed. F5, F7, and F9 produced a wide line which spread on the substrate and appeared to form a thin film (as a refractive pattern is observed on the deposits in Figure 5.15). F6 printed with a reliable line but the overspray was noticeable on the images of this formulation. F8 contained significant bulges which are not suitable for micromanufacturing.

Table 5.3: Deposit width and observations for PEDOT:PSS ink formulations.

Formulation	Line Width (μm)	Observations
1	165	Incomplete line. Overspray significant even after sintering suggesting under deposition of material.
2	219	Complete line. Significant bulges caused by material wetting, or over deposition. No sign of overspray, and line width larger than nozzle suggesting over deposition of material.
3	N/A	No discernible line.
4	150	Complete line. Some overspray. No pinching or bulging.
5	450	Material has spread on substrate causing a wide line. No sign of overspray as this has been covered by material during spreading. Significant bulges due to surface tension effects or over deposition.
6	190	Complete line. Overspray distinguishable on edges of lines. No pinching or bulging.
7	317	Material has spread on substrate causing a wide line. Evidence of bulging.
8	269	Material has spread on substrate causing a wide line. Evidence of bulging.
9	284	Material has spread on substrate causing a wide line. Evidence of bulging.

From this initial analysis F1, F4, and F6 were considered for use further in the project, as they were the thinnest lines to print (165 μm , 150 μm and 190 μm observable width respectively). Any of the three choices fulfilled the criteria of printing a stable feature. When choosing between materials F4 was taken forward for further analysis, due to the known effect of ethylene glycol to improve the print characteristics of PEDOT:PSS lines [221]. F1 and F6 had no ethylene glycol content.

The method can be used to develop a three part ink using different functional materials in the future. The time taken to prepare the ink using this method was

much shorter than the APTES or PMMA inks, as the structured approach to determine the formulations was much faster than trial and improvement methods. A generalised method is shown in Figure 5.16.

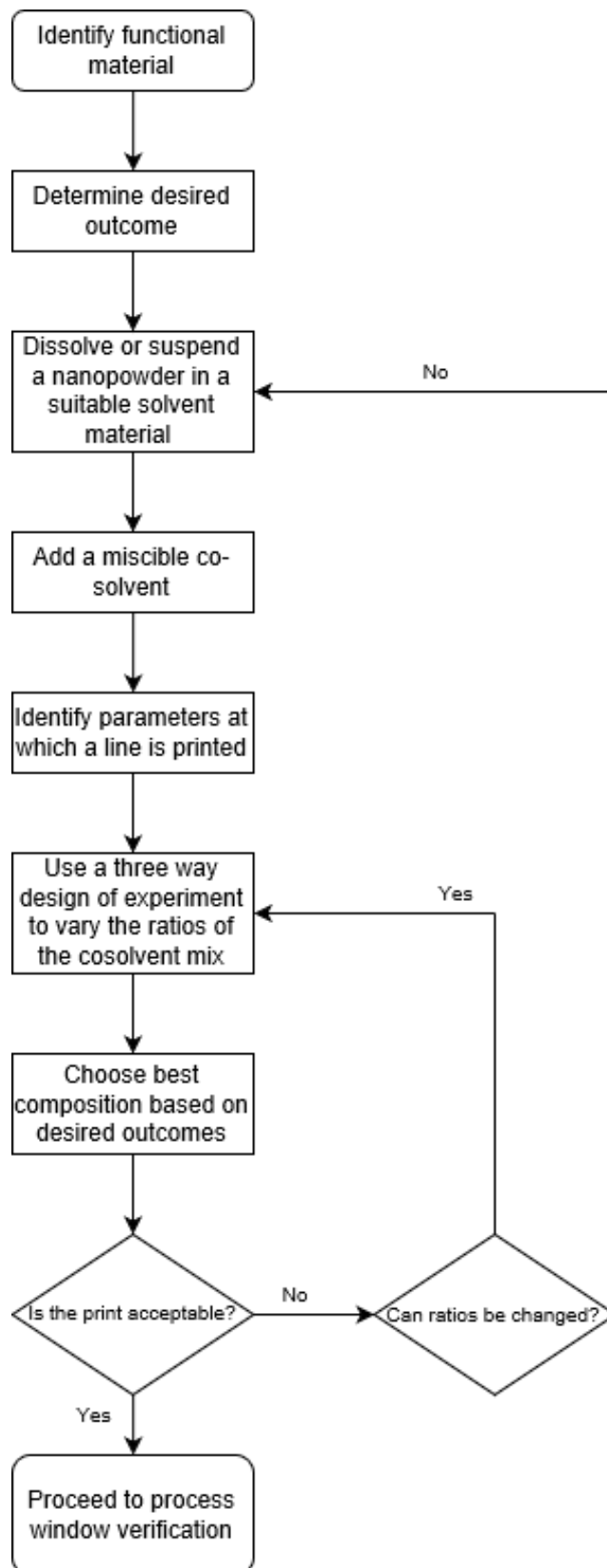


Figure 5.16: Generalised material formulation strategy

5.3 Material Longevity Assessment

Material degradation during the process can reduce the reliability of the printing and can cause damage to the machine if it causes a blockage. When a suspension is atomised there is a bimodal distribution of functional material within the atomised particles. Not every particle will contain a particle of functional material. The droplets containing just solvents will be printed regardless, reducing the solvent content of the remaining ink over time. This leads to ink drying which, after improper materials, is one of the primary failure mechanisms for the process. In the time stability experiment formulation F4 was printed until failure. A line was printed every 5 minutes, a selection of the images are seen in Figure 5.17. The full results are shown in Appendix D. These initial results suggested a stable deposit was formed after only 10 minutes of printing. As the apparatus ran, and the aerosol was printed the properties of the printed features change, even when all other parameters (sheath, atomiser gas, scanning speed etc.) are constant. This change of print characteristic was attributed to changes in the composition of the ink in the chamber, such as the ink drying phenomenon described in Section 2.1.1.1. These small changes influenced the deposit properties, so it was concluded that there was a defined duration of time in which a stable line can be deposited. The effect of ink drying was observed in all the subsequent experiments, however the printing was stable for long enough to run experiments and produce substrates.

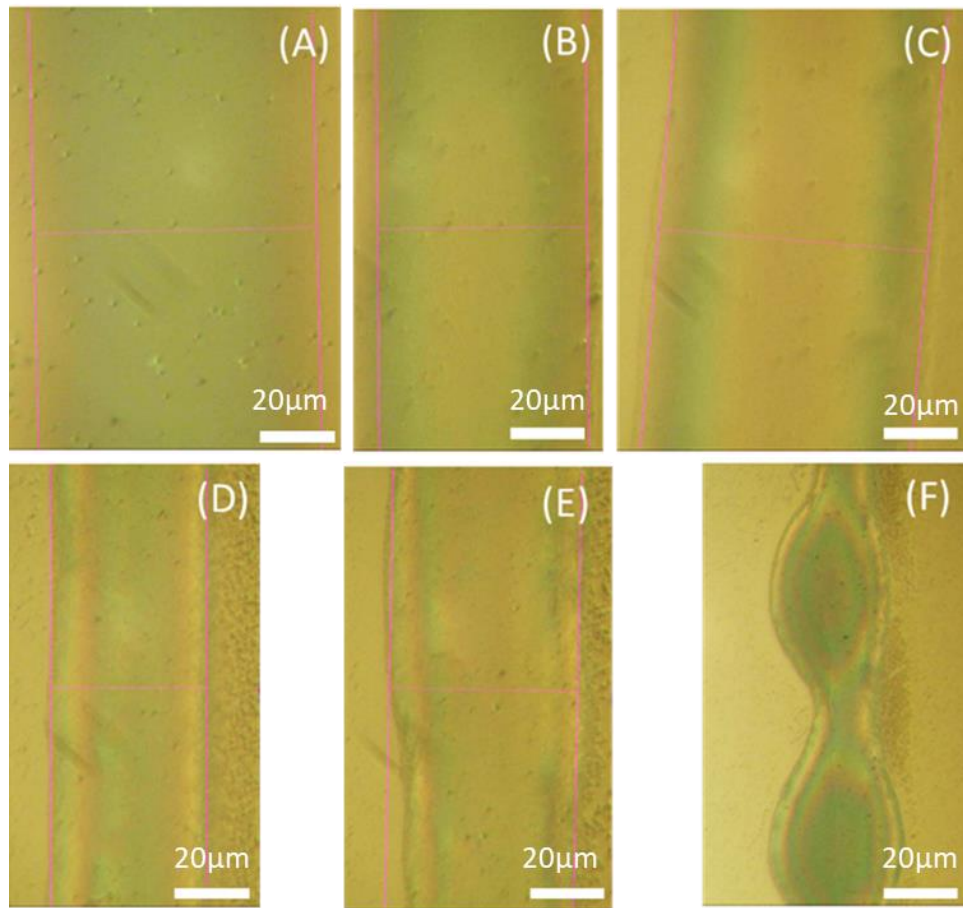


Figure 5.17: Time stability images (A) 10 mins (B) 30 mins (C) 60 mins (D) 90 mins (E) 120 mins (F) 125 mins - atomiser pulsing.

Print failures are challenging to pick up during printing, due to the small scale of the printed patterns. They can be identified on the apparatus by studying the pressure time graph for unexpected changes, such as the increase in both sheath and atomiser gas pressure. Figure 5.18 shows the pressure time graph during the longevity assessment, where the increased pressure at the end of the process is evident.

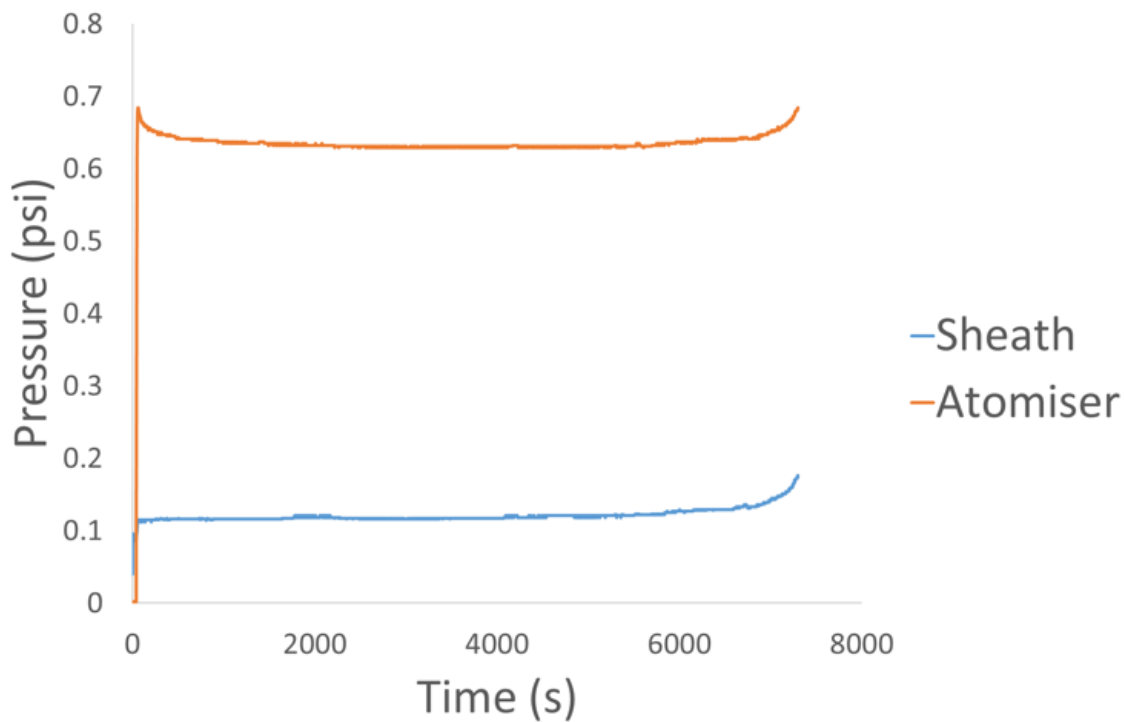


Figure 5.18: Aerosol Jet failures are indicated by changes in pressure time graphs, in this case a rise in pressure due to the nozzle blocking.

5.4 Operational Window Testing for Printing PEDOT:PSS

As each new material is developed a new set of print parameters must be established. In Section 2.1.4 all the possible variations in the process were discussed. The objective of these experiments was to establish whether it was possible to control the interaction of several of these variables, and to set the limits of the operational window. A statistical method (Appendix E) as described by W Diamond [222] was used to ensure the results were reported with a 90% confidence level. These initial experiments were carried out to assess the extreme limits of the printing process and give an overview of the effect of each parameter in isolation. This was in preparation for the design of experiment process. The key parameters were identified from those listed in Section 2.1.4 by assessing the literature and from experience in the initial APTES and PMMA tests.

5.4.1 Test Conditions

All the conditions in this section were the default conditions, used unless specifically stated. The sheath and atomiser gases were then both set to 25 SCCM. This value produced a line at all the nozzle sizes without exceeding the rated pressure of the sensors when using the smaller nozzles. The pressure range at equivalent parameters increased as the nozzle size decreased. 2ml of PEDOT:PSS formulation 4 was atomised in the ultrasonic atomiser, set to 450mA of current. The intermediary liquid was stabilised at 30°C. After switching on, the system was left for 5 minutes whilst the aerosol stabilised. During this time the stage was calibrated so that the top surface of the washed glass substrate was 3mm from the nozzle orifice when printing. The substrate was translated under the nozzle 50mm/min to produce fifteen lines of length 5mm. Printed lines were produced and the result was removed and baked in an oven at 150°C for 10 minutes to drive off the solvents and sinter the PEDOT:PSS particles. Each line was imaged once under a optical microscope at 10X magnification, and measured using the calibrated software.

5.4.2 Changing Nozzle Exit Diameter

For printing features to influence cell cultures, printing with thin lines was desirable, to print features of a scale that correlated to cell culture substrates. The correlation of printing nozzle size and line width was investigated. The five sizes of commercially available nozzles were investigated, and the results are shown in Figure 5.19.

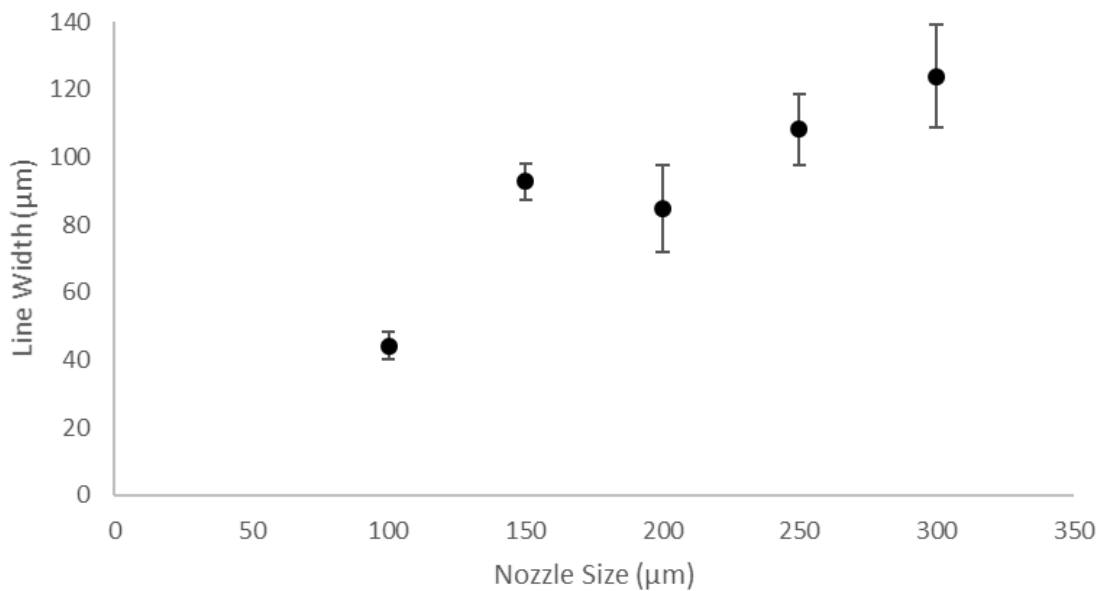


Figure 5.19: Effect of changing nozzle size on line width.

It was observed that decreasing the nozzle size correlated to a reduced line width, except for the 150µm nozzle size. This result agreed with the finding of Mahajan *et al.* and Gupta *et al.* [53], [63]. Not only does increasing the nozzle size at a specific focussing ratio increase line width, but these results highlighted the linear trend between nozzle size and line width. As the 150µm nozzle size was the only result which did not fit the correlation, and this was not reported previously in the literature, the result was taken as anomalous. It may have been caused by the processing steps, substrate, or operator error. The implication of these results combined with the findings of the literature verified that choosing the smallest nozzle size will favour the printing of small size features. So, the 100µm nozzle was preferred in subsequent experimentation.

5.4.3 Changing Scanning Speed

Goth *et al.* have shown that the deposition rate onto the substrate is influenced by the scanning speed of that substrate under the nozzle [57]. This result was verified by Mahajan *et al.* who observed a reduction in line width at a constant focussing ratio [53]. Although the flow rate of material exiting the nozzle is not affected by the speed of the stage, increasing the scanning speed reduces

deposition rate onto the substrate in one location. Therefore, moving the stage faster under the print head caused a reduction in the line width.

The scanning speed was varied between 30mm/s and 90mm/s in large intervals of 20mm/s. 90mm/s was approaching the maximum speed of the automation apparatus. At the processing conditions used for this experimentation, increasing the scanning speed did not result in a significant reduction in line width (Figure 5.20). When the scanning speed was low, an unstable deposit was observed. The ‘bulging’ phenomenon was frequently observed. The deposition rate of material in one place was large resulting in an uncontrolled geometry as the deposit wetted to the substrate surface. As the scanning speed increases the variance of the line decreased, indicating a much more controllable feature was produced. This is expected as there was less time spent depositing over a single area, therefore the material deposition in that specific area was reduced. For this set of processing parameters, increasing the scanning speed above 70mm/min did not reduce the line width. The variance in the results suggest that this was due to experimental variation, however alternative explanations are the wetting properties of the material and substrate, drying patterns, or the interaction of the sheath gas and the material after the deposition [63].

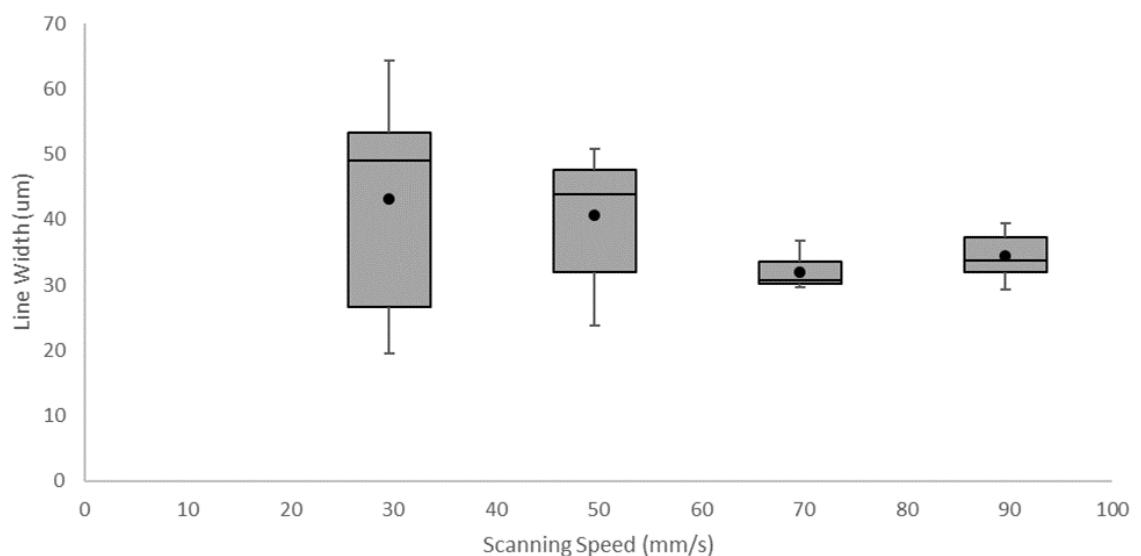


Figure 5.20: Effect of changing scanning speed on line width

The improved control over the line at higher speeds was noted, as was the literature precedent that the line width should reduce, and so this factor was investigated further in the design of experiment stage in Section 5.5.

5.4.4 Changing Z Stand-Off

Optomec, the original equipment manufacturer of the AJP process, specify that a collimated beam is focussed between 1 and 5 mm from the nozzle exit [47]. However, at the lower end of the printing range some variance was reported by Hoey *et al* [78].

The Z-Stand-off between the nozzle exit and the substrate surface was varied between 2 and 4mm to investigate the focal distance. The experimental results are shown in Figure 5.21. In these experiments, changing the Z stand-off height affected the line width, but a linear relationship was not observed. The data suggested a focal point somewhere between 2.5 to 3.5mm stand-off for this set of process parameters. This is in broad agreement with other literature where focal points were found to be dependent on processing conditions [183].

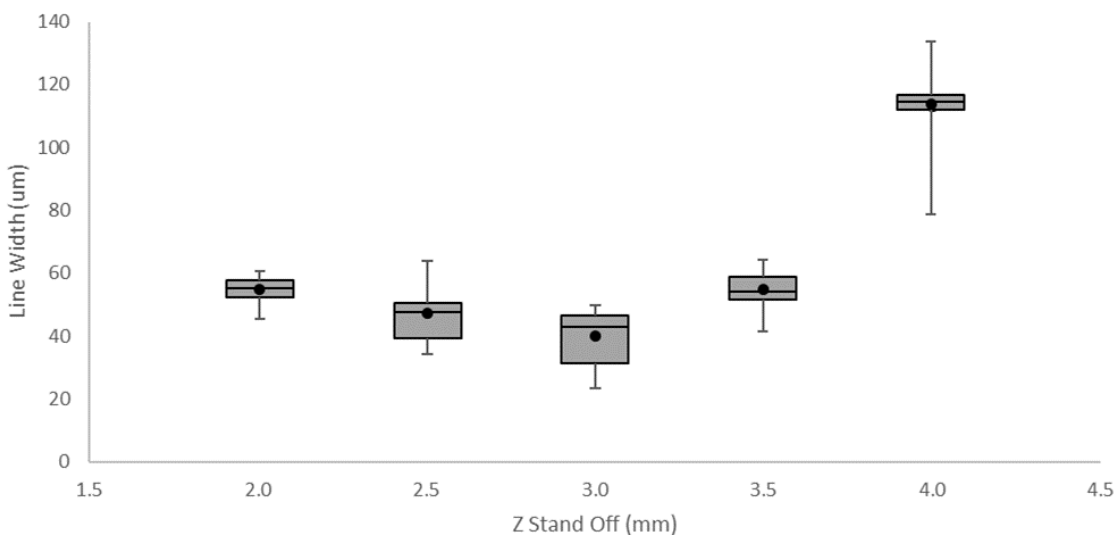


Figure 5.21: Graph to show effect of changing z stand off on line width

The results in this experiment implied that if a minimum line width is to be achieved, it is important to print around the focal area. A Z stand-off smaller than 3.5mm result in small changes, these indicate that the jet is collimated below

3.5mm. However, over 3.5mm the collimation is broken in the 100 μ m nozzle size case.

5.4.5 Changing Focussing Ratio

The critical factors in controlling the transportation and focussing mechanisms of the aerosol jet are two gas flows: the sheath gas and the atomiser gas. The first study to highlight the effect of focussing ratio was Mahajan *et al.*, who identified that the total flow rate through a nozzle does not affect trace width, but that the ratio of sheath gas to the atomiser gas, defined as the focussing ratio, is the critical factor [53]. This result was discussed in many subsequent studies who found that increasing focussing ratio reduced line width [46], [61], [63]. However, these studies measured line width only as the response to the changing focussing ratio. In addition, the papers that focus on changing focussing ratio offer only a partial discussion around independently changing the sheath and atomiser gas, and the effect of changing the total mass flow rate whilst keeping the ratio constant.

The limiting factors on the gas flow rates when printing are the flow capacity of the mass flow rate controllers, and the peak measurement value of the in-built pressure sensors. When printing with the 100 μ m nozzle the maximum recommended sheath gas is 50sccm, as the pressure at this gas flow rate approaches the maximum value. In all cases the maximum atomiser gas flow rate is 200sccm. Therefore, a well-defined field of experimentation can be formed and this can be used to compare the geometry printed with different gas flow rates.

First, the geometry of the printed lines was assessed at different FRs. Each print was conducted on a separate substrate to remove any chance of interference between prints. Before commencing each print, the apparatus was set to the

specific gas flow rates and left to settle for 10 minutes to ensure a continuous stable flow from the nozzle.

Outside the regions specified in Table 5.4 no viable lines were printed. If the FR was below 0.5, it resulted in machine issues such as nozzle clogging. If the FR was above 3.5 the result was little material output, so that a confluent line was not deposited.

Table 5.4: Atomiser Gas flow rate (sccm) with respect to each Sheath Gas and Focusing Ratio combination

Sheath Gas (sccm)	Focussing Ratio						
	0.5	1	1.5	2	2.5	3	3.5
10	5	10	15	20	25	30	35
20	10	20	30	40	50	60	70
30	15	30	45	60	75	90	105
40	20	40	60	80	100	120	140
50	25	50	75	100	125	150	175

The full data set is in Appendix F. The first observation is that at some FRs the printer did not output a line at the lower sheath gas settings. It was hypothesised that this was due to the relatively low atomiser gas stream being blocked by the relatively high sheath gas stream. This effect was seen when the sheath gas value was greater than 3X the atomiser gas, and the atomiser gas was below approximately 10SCCM. This combination resulted in deposition on material onto the substrate that was so small that it was not detected through white light interferometry. Other explanations are that when the aerosol impacted the surface, the change in direction that would usually result in overspray was so high that the material was not deposited underneath the nozzle but spread so thinly over the surface as to be unobservable by the white light interferometer. In either case, this means there is a critical lower limit for each focussing ratio at which no trace is printed.

Table 5.5: White light interferometry data for a focussing ratio of 1

Sheath gas (sccm)	10	20	30	40	50
Atomiser gas (sccm)	10	20	30	40	50
Printed Line	No line	No line			

The trend of increasing line width with increasing gas flow rate was seen at all focussing ratios. A focussing ratio of 0.5 (Table 5.6) had a line output at all 5 sheath gas values that were analysed so gives the clearest indication of the effect of increasing total gas flow rate. In this case, increasing the sheath gas from 10SCCM to 50SCCM, whilst maintaining the FR of 0.5 resulted in a mean increase in height of 19% (from 0.48 μ m to 0.57 μ m), and an increase of width at half maximum increase of 360% (from 68 μ m to 315 μ m).

Table 5.6: White light interferometry data for a focussing ratio of 0.5.

Sheath gas (sccm)	10	20	30	40	50
Atomiser gas (sccm)	5	10	15	20	25
Printed Line					

A similar result was observed in subsequent data sets, and the full results of the geometrical analysis are presented in Figure 5.22. Printing was attempted at all sheath gas values for each focussing ratio, however not all resulted in the

deposition of a line. The maximum height and WHM were assessed as in the previous literature [185]. Figure 5.22A illustrates the effect of total flow rate on the maximum height of the deposit. At low focussing ratios the step height did not substantially increase with an increasing gas flow (for example, the 19% increase associated with the increase of 10-50 sccm sheath gas at 0.5 focussing ratio). When the focussing ratio was higher than 2 the maximum height increases as the total flow rate increases. Other than at focussing ratio of 3.5, as the gas flow rate increased the maximum heights approached the same height, indicating a critical limit to the height of the printed features. Figure 5.22B shows that at all focussing ratios the width increased with an increasing gas flow. The most pronounced increase was seen at the lower focussing ratios, particularly those lower than 2. This behaviour may be interpreted in terms of the material deposition rate and wetting onto the surface of the substrate. At all focussing ratios, as the gas flow rate increased, at least one geometrical feature (height or width) increased, indicating an increased material deposition rate onto the surface substrate. If the material deposition rate was low, increasing it resulted in an increase in deposit height, as more material was deposited in the same area on the substrate. There was also a small increase in width associated with this region. Once a critical height was reached, the deposits did not increase in height, but instead spread to become wider whilst maintaining their maximum height. Figure 5.22A indicates that the maximum deposit height for printed PEDOT:PSS features is in the region of 0.5-0.8 μm , as all the focussing ratios approach this region at high gas flow rates. This limit was a result of the wetting properties of PEDOT:PSS to the PDMS surface.

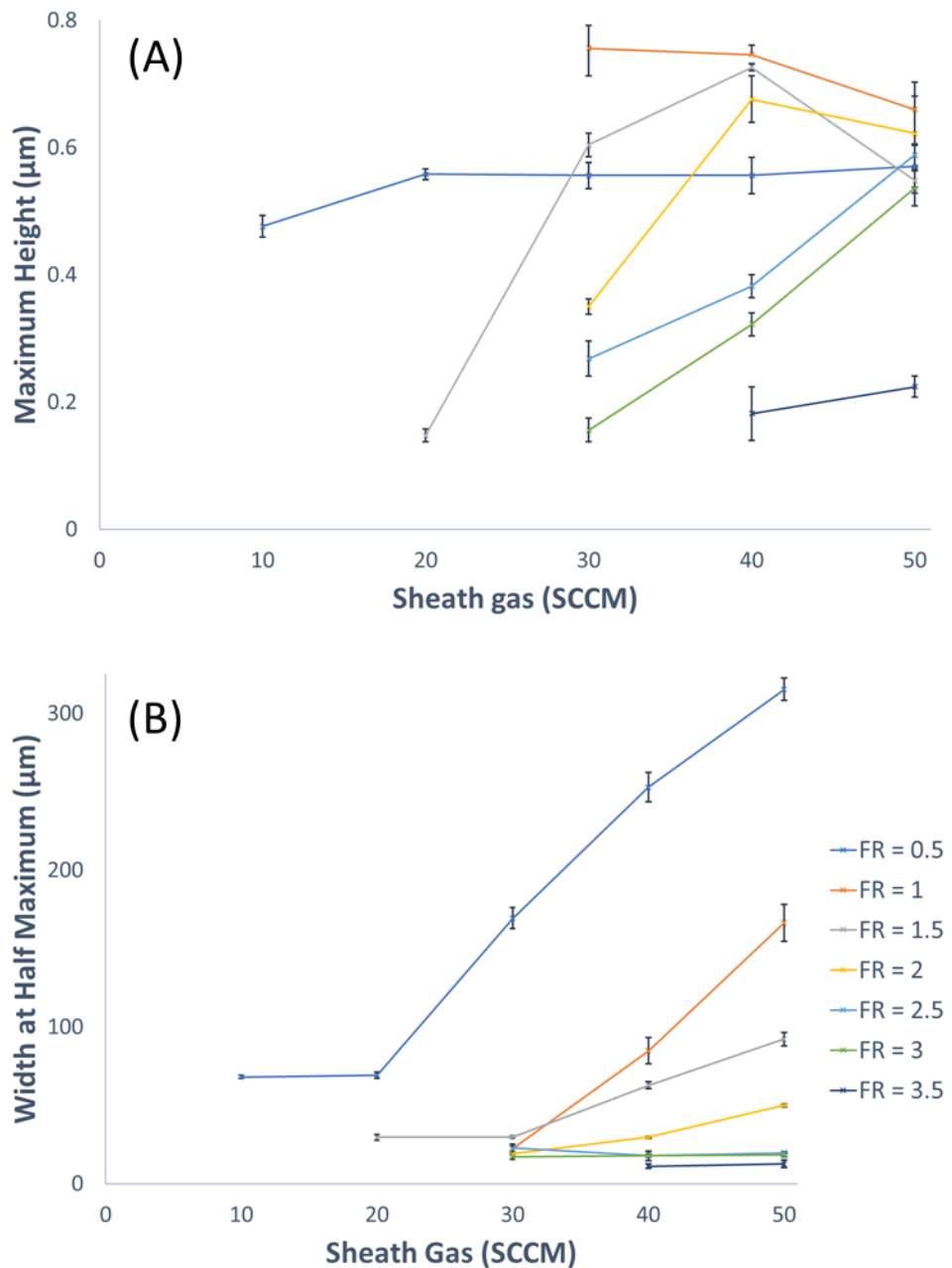
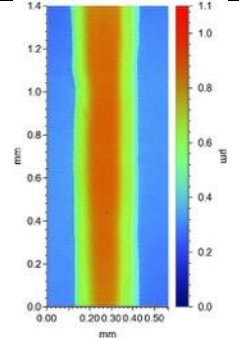
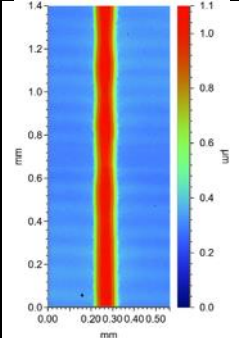
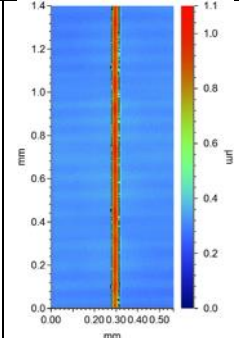
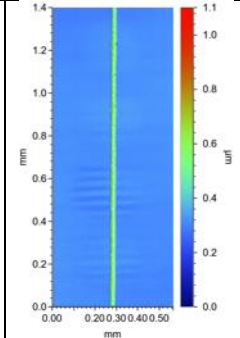


Figure 5.22: Effect of gas flow rate on (A) maximum height and (B) width at half maximum height.

By reading all the results at a one setting for sheath gas (that is, straight down the Y axis at any sheath gas in Figure 5.22), the effect of reducing atomiser gas whilst keeping the sheath gas constant can also be elucidated. The reduction of atomiser gas at a constant sheath resulted in a reduced material flow rate from the atomising chamber. The results in Table 5.7 illustrate this.

Table 5.7 White light interferometry data showing diminishing line geometry as atomiser gas was reduced

Sheath gas (sccm)	40	40	40	40
Focussing ratio	0.5	1	2	3
Atomiser gas (sccm)	80	40	20	13.3
Printed Line				

5.4.6 Summary of Operational Window Testing

The key indications from these experiments is that there is not a proportional change of geometry associated with the z stand-off distance and line geometry. This result suggested that there is a ‘focal point’ of the apparatus when printing small geometries. The controllable variables that influence the print geometry were focussing ratio, atomiser gas flow rate and scanning speed. The sheath and atomiser gas ($FR=S/A$) alter the material mass flow rate from the end of the nozzle. The movement speed of the substrate under the nozzle influenced the material deposition rate onto the surface. Therefore, by increasing the scanning speed, the line is diminished.

Changing the sheath and atomiser gasses, the focussing ratio, and the interactions of the total mass flow rate through the nozzle influence the final print geometries. In general:

- Increasing the focussing ratio diminished the line.
- Increasing the total mass flow rate enlarged the line.
- Increasing the atomiser gas enlarged the line.

The influence of surface free energy on deposit characteristics was identified by Vunnam *et al.* [65]. Drawing on their conclusions, and the observations of the experiments, it is concluded here that the specifics of the line geometry such as the overall shape, maximum height, width at base, WHM, side wall angle and surface roughness are subjected to influences from the material formulation, drying characteristics and interaction of the material and substrate surface. These interactions are summarised in Figure 5.23.

As these phenomena are complex and challenging to control it was suggested that the material deposition rate was the critical factor that could be controlled by changing process parameters alone. The way to incorporate material deposition rates into the testing was to measure the cross-sectional area of the line, which incorporates all aspects of the line geometry. The line height and WHM were still measured during subsequent experiments with the caveat that they are affected by environmental conditions.

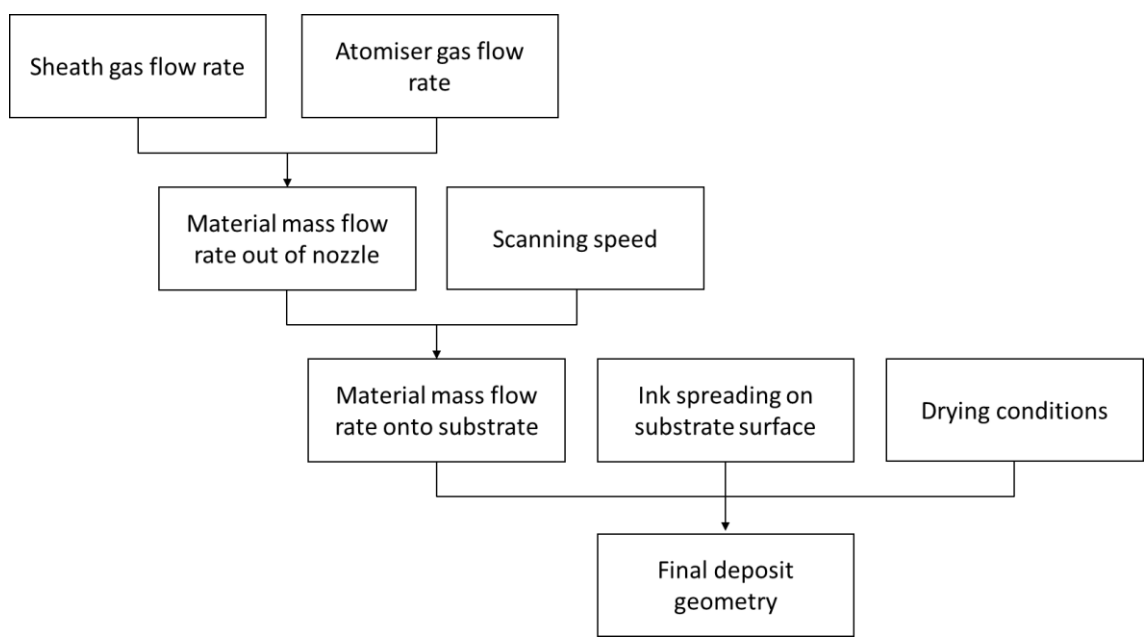


Figure 5.23: Proposed Interactions for Material Deposition Rate

5.5 Two Level Multivariable Experimentation

Using the results of the previous section, a multivariable experiment can be set up which facilitates the comparison of the four controllable variables (sheath gas,

atomiser gas, scanning speed and z stand-off). This method can analyse the interaction of the variables, an observation that cannot be ascertained from changing only one variable in isolation. The experiments were performed with the 100 μ m size nozzle. The process windows used are shown in Table 5.8.

Table 5.8: Processing window for multivariable experimentation

Parameter	Lower Limit	Upper Limit
Sheath gas (sccm)	30	40
Atomiser gas (sccm)	20	25
Scanning speed (mm/min)	70	90
Z stand-off (mm)	2.5	3.5

A Hadamard matrix approach provided an efficient method to reduce the number of tests required to make these comparisons. A full description of the methodology can be found in Appendix G.

Measurements of line maximum height, WHM, and cross-sectional area were taken from a white light interferometry scan. A Zygo NewView 5000 white light interferometer was used to assess features. This apparatus differed from the previous interferometer, as it could be programmed to automatically assess the cross-sectional area, width at base and WHM of the 16 PEDOT:PSS tracks that were deposited onto a glass substrate.

The hypotheses were that line cross sectional area was reduced by:

- Increasing Sheath Gas
- Decreasing Atomiser Gas
- Increasing Stage Scanning Speed
- Moving closer to the system focal point

The interactions of these factors were also analysed. For 95% confidence 7 comparisons were required. A 16X16 Hadamard matrix allowed 8 comparisons so was used for this DOE.

The initial experimental parameters were run three times, on three separate days with a disassembly and clean of the functional end of the machine after each run. The machine was reassembled before each experiment. This improved the reliability of the results as they were not specific to an experimental run (a mean value when n=9 was used to fill the matrix). The maximum and minimum values were applied to the Hadamard matrix and a trial set was generated.

Table 5.9: Hadamard matrix trials

Trial	Sheath gas (sccm)	Atomiser gas (sccm)	Scanning speed (mm/min)	Z stand-off (mm)
1	40	20	70	2.5
2	40	25	70	2.5
3	40	25	90	2.5
4	40	25	90	3.5
5	30	25	90	3.5
6	40	20	90	3.5
7	30	25	70	3.5
8	40	20	90	2.5
9	40	25	70	3.5
10	30	25	90	2.5
11	30	20	90	3.5
12	40	20	70	3.5
13	30	25	70	2.5
14	30	20	90	2.5
15	30	20	70	3.5
16	30	20	70	2.5

Table 5.9 table details the sixteen trials that must be carried out to analyse the data. By pairing the trials in a set order, and comparing the difference between them, several variables and interactions can be analysed in a small number of trials. For example, to examine the effect of turning the sheath gas from low to high eight trial pairs were assessed:

- 1 and 16
- 2 and 13
- 3 and 10
- 4 and 5
- 6 and 11
- 8 and 14
- 9 and 7
- 12 and 15

In each of these comparisons, only the sheath gas value is different, the other three values are constant. Using these comparisons, 8 repeats are made which

is enough to make the results statistically significant. In the same method but using different trial pairs, all variables can be analysed. In addition, trial pairs exist to compare the interactions of different variables. Overall, using this method enables one set of results to be analysed for response to all the variables and both two and three factor interactions. In each trial, each of the three lines were assessed three times for each geometrical feature (n=9). The mean for each trial is shown in Table 5.10.

Table 5.10: Mean data from the white light analysis for each trial

Trial	Cross Sectional Area (μm^2)	Step Height (nm)	WHM (μm)
1	5.95	263	25
2	9.75	308	32
3	8.65	297	28
4	8.06	297	28
5	9.1	247	34
6	6.37	256	25
7	12.1	313	39
8	5.46	232	21
9	8.44	293	27
10	9.71	269	35
11	6.3	230	27
12	6.71	252	24
13	11.93	305	40
14	6.76	234	26
15	8.51	272	30
16	8.29	298	27

The difference of each trial pair was then taken, and the mean values reported.

The values were compared to the objective criteria in Table 5.11 to assess significance.

Table 5.11: Objective Criterion of Each Parameter

Parameter	Objective Criterion for a Significant Result
Cross Sectional Area (μm^2)	1.0
WHM (μm)	1.5
Height (nm)	3.9

For each variable the results are displayed in Table 5.12. The analysis of the two factor interactions is available in Table 5.13 and the interactions of more than two interactions in the Table 5.14.

Table 5.12: Analysis of individual variables (rounded to 1dp).

Effect of	Cross Sectional Area (μm^2)	Maximum Height (nm)	WHM (μm)
Increasing sheath gas	-1.7	4	-6.3
Increasing atomiser gas	2.9	36	7.1
Increasing scanning speed	-1.4	-30	-2.4
Increasing z stand-off	-0.1	-6	-0.2

These results confirm the theory that cross-sectional area is reduced by increasing sheath gas from 30 to 40 sccm, reducing atomiser gas from 25 to 20 sccm, and increasing scanning speed from 70 to 90 sccm. The changes of cross sectional area manifest in changes of width in all cases, and in changes to maximum height in the cases of the atomiser gas and the scanning speed. The analysis of the results did not identify any significant effect of changing the z stand-off between 2.5 to 3.5mm but identified a significant change in step height across this range.

Table 5.13: Analysis of two factor interactions (rounded to 1dp).

Interaction	Cross Sectional Area (μm^2)	Maximum Height (nm)	WHM (μm)
Sheath gas/atomiser gas	-0.3	-2.2	11.6
Atomiser gas/scanning speed	-0.3	-0.7	3.1
Scanning speed/z stand-off	-0.1	0.7	5.1
Sheath gas/scanning speed	0.8	1.1	21.9
Atomiser gas/z stand-off	-0.5	-1.8	-1.4
Sheath gas/z stand-off	0.1	-0.6	5.2

The analyses of the two factor interactions identified no significant effects of cross sectional area or step height. The sheath/atomiser interaction and the sheath/scanning speed interaction significantly increased the width by 11.6 μm and 21.9 μm respectively. The sheath atomiser interaction is the equivalent of increasing the total gas flow rate, so confirms the trend identified in Section 5.4.5.

The effect of increasing sheath and scanning speed together disagrees with the trends identified previously. It was expected that the line was diminished by this interaction. This result may be due to the complex wetting/drying effects of the process, or an anomalous result.

Table 5.14: Analysis of three and four factor interactions (rounded to 1dp).

Interaction	Cross Sectional Area (μm^2)	Maximum Height (nm)	WHM (μm)
Sheath gas/atomiser gas/z stand-off	-0.4	-5.5	-0.3
Sheath gas/atomiser gas/scanning speed	0.1	2	0.7
Atomiser gas/scanning speed/z stand-off	0.1	-8.9	0.3
Sheath gas/scanning speed/z stand-off	0.3	7.2	1.6
Sheath gas/atomiser gas/scanning speed/z stand-off	0.1	4.1	0

None of the multi factor interactions had a significant effect on cross sectional area. Sheath gas/atomiser gas/z stand-off interaction reduced maximum height, as did atomiser gas/scanning speed/z stand-off and sheath/scanning speed/z stand-off. Sheath gas/scanning speed/z stand-off also increased the WHM. Whilst many of the interactions show a small significant effect, overall the effect of the individual factors far outweighs the effect of two and multifactor interactions. Changes to the atomiser gas result in the largest difference in line cross sectional area ($+2.9\mu\text{m}^2$). The line cross sectional area has an inverse relationship to the sheath gas flow rate and the scanning speed ($-1.7\mu\text{m}^2$ and $-1.4\mu\text{m}^2$ respectively). In addition to the statistical data, the cross-sectional area and the geometries can also be compared directly using this data, and a strong logarithmic relationship ($R^2 = 0.906$) was observed between track cross sectional area and WHM, indicating an increase in track in proportion to the square root of the track area. This non-linear relationship is typical of jetting processes, with track widths proportional to the square root of the track area. This trend gave rise to an asymptotic relationship between track width and area.

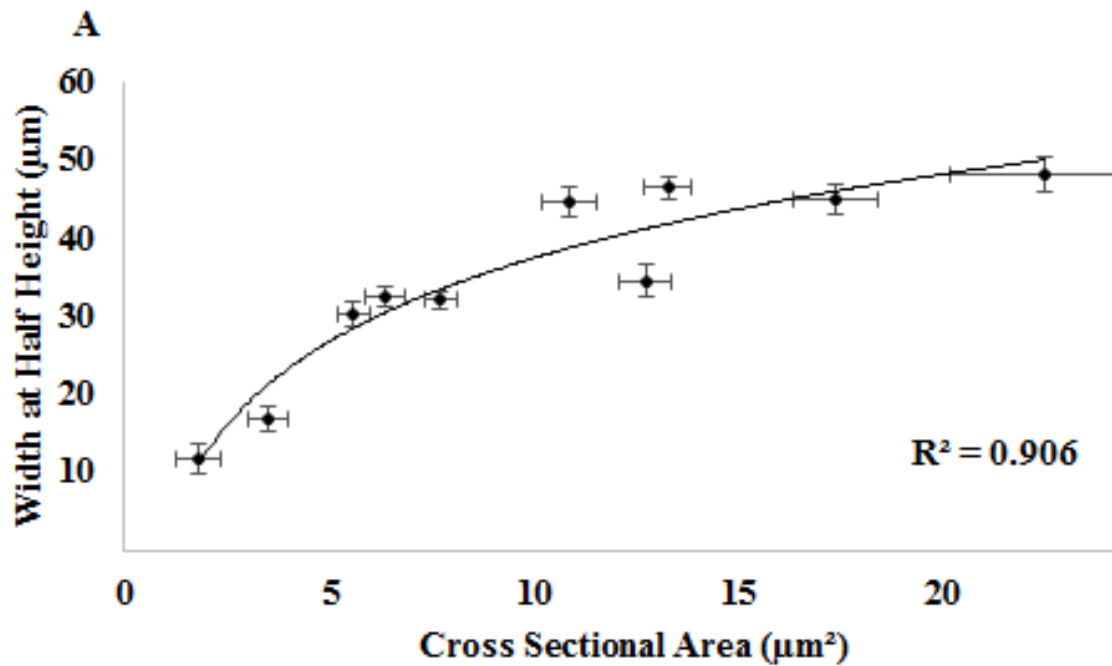


Figure 5.24: The WHM increases with a logarithmic fitting to the cross-sectional area

These informed the settings of processing parameters for future experimentation. To make large changes to the line geometry, the atomiser gas should be changed first. Once a geometry in a suitable region has been achieved, it should be tuned by changes to the sheath gas flow rate. The scanning speed was set to 100mm/min for all subsequent experiments, to improve the throughput of printed samples.

Using the techniques and with a knowledge of the significant parameters identified in this body of work, a new set of definitions for line width were developed using the PEDOT:PSS ink. The predominant settings used to achieve several target line widths are shown in

Table 5.15.

Table 5.15: Print parameters for PEDOT:PSS formulation 4

Target Line Width (µm)	Nozzle Size (µm)	Sheath Gas (sccm)	Atomiser Gas (sccm)	Scanning Speed (mm/min)
15	100	50	20	100
20	100	40	20	100
30	150	50	25	100
40	150	60	27.5	100
50	150	70	30	100

5.6 Chapter Summary

In this chapter a range of objectives are addressed around the validation of the printing apparatus and the deposition of functional inks. Specifically:

- Three new functional materials were trialled in an initial materials screening
- A methodology for evaluating a suitable solvent content of AJP inks was developed
- A suitable material based around PEDOT:PSS was developed and trialled for longevity
- An operational window for printing was established
- Key processing parameters and interactions were assessed

Printing with APTES and PMMA inks highlighted the compatibility with several functional materials, and the ability to improve the line quality by changing process variables. However, each had its own challenges. Inks based on APTES tended to block the nozzle, and inks based on PMMA had short processing windows.

The methodology for evaluating suitable solvent ratios for AJP inks was shown by developing a stable print material that could be reliably printed for longer than two hours.

Next, the effect of printing parameters on the deposit geometry was studied in detail. The formulation of the material is expressed in general terms so that it can be used with other functional materials.

The preliminary experiments with PEDOT:PSS were used to observe trends in the printed line geometry. The effect of individual process variables, the changing focussing ratio, and the interactions of the variables were assessed. The results show that the process is most affected by the atomiser gas, sheath gas, and the scanning speed.

The design of the experiment confirmed that changing process parameters resulted in different material flow rates onto the substrate surface. It is contended that the final line geometry is then dependent on the interaction of the material to the substrate surface and the drying characteristics.

Chapter 6 Application of Selectively Functionalised Substrates to Cell Culture

Established cell culture substrates are poor models of *in vivo* biology. Commonly, flat, untreated glass or polystyrene are used as the culture substrates. These result in two-dimensional cultures, with limited control of spatiotemporal growth [27].

In this chapter the spatial control of the cell cultures by applying printed features is explored. First different shaped deposits are produced via AJP. Then, the application of printed substrates as cell culture substrates is shown, in an attempt to control the growth by topographical and chemical cues. Controlling the spatiotemporal growth of cells is an essential step in the creation of representative tissue engineered models that mimic physiological functions.

The initial proof and most in-depth studies were performed using the HCT-116 colorectal carcinoma cell line. This cell line was chosen as a suitable demonstrator as recently it has been suggested that traditional 2D monolayer cell culture models of colorectal cancer cells are limited in application and more complex models of the disease are required for more effective and efficient pre-clinical evaluations [15]. There are also high rates of incidence and mortality associated with colorectal cancer in the UK [223] and worldwide [224]. Therefore, there is a specific requirement for more advanced *in vitro* models of this disease for laboratory-based testing. An overview of the testing is shown in Figure 6.1.

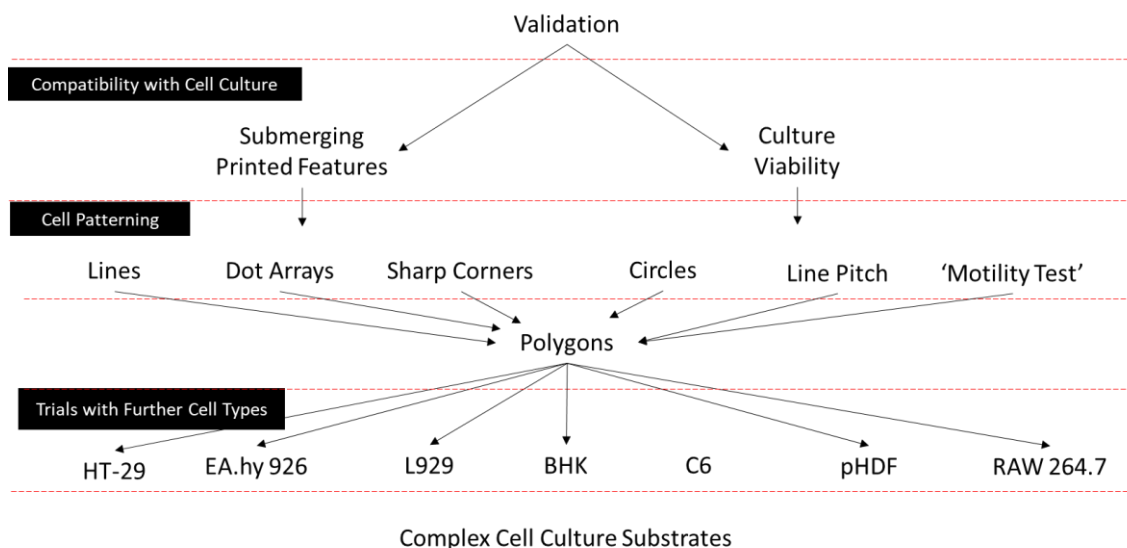


Figure 6.1: Summary of the application testing in Chapter 5

First, the compatibility of the printed substrates with cell culture was shown by submerging the printed features in cell culture media and investigating the culture viability on the printed substrates with routine Live/Dead analysis.

Then, the ability to pattern cells was proven over a series of trials starting with fundamental shapes. As in the literature, these included lines but expanded the range of shapes to showcase corners, circles, investigate the effect on line pitch, and show a functional 'motility test' which was devised with collaborators. The complexity of the shapes was then increased to include polygons.

Subsequently, this process was applied to range of cell types, representing significant tissues from the whole body. Endothelial, fibroblast, neuronal and macrophage cells were patterned from seven cell lines. Namely, HT-29, EA.hy 926, L929, Baby Hamster Kidney (BHK), C6, primary Human Dermal Fibroblast (pHDF) and RAW 264.7 cells were all trialed. Each of these cells have different growth requirements and variety of morphologies, were proved to be compatible with the culture substrates. These tests demonstrated the range of applicability to the wider biological field.

Finally, patterning onto non-planar substrates and large area patterning were shown using the HCT-116 cell line.

6.1 Compatibility with Cell Culture

These first experiments verified the compatibility of the printed substrates with the cell culture environment. They aimed to prove that combination of printed material and substrate are not toxic to the cell cultures. Next, fundamental shapes such as lines, dots, sharp corners, and circles were printed to showcase the capabilities of the apparatus in terms of cornering ability, printing radius' and printing acute, right and obtuse angles. The cell response to these features was also observed, developing a library of shapes that could be replicated by the cells in culture.

First, HCT-116 cells were cultured onto an unpatterned polystyrene substrate to show the chaotic nature of routine cell culturing. This is shown in Figure 6.2.

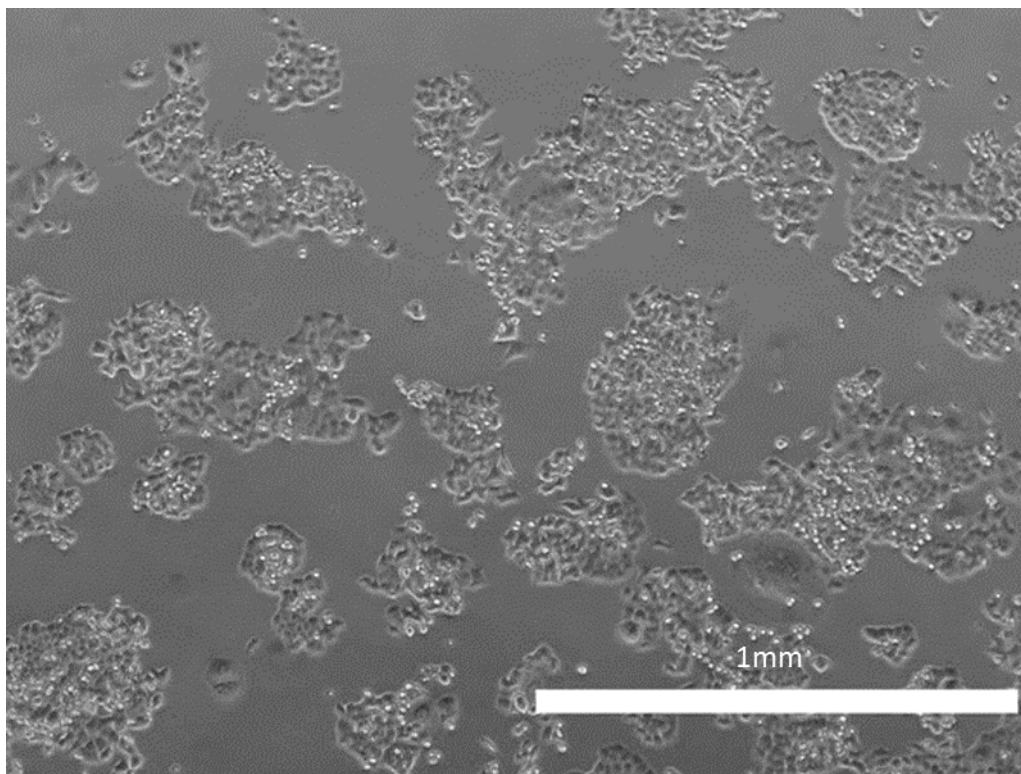


Figure 6.2: Chaotic nature of HCT-116 cell growth on an untreated polystyrene substrate after 48 hrs.

6.1.1 Effect of Submerging PEDOT:PSS Features in Culture Medium

In these cell culturing experiments the substrates were fully submerged in cell culture medium at a raised temperature (37°C) up to one week. When PEDOT:PSS features were submerged for 72 hours in growth matrix, the lines were degraded, and in some cases detached from the substrate surface (Figure 6.3). PEDOT:PSS nanoparticles are hygroscopic, meaning that when submerged in water or aqueous solutions (such as cell culture media) they swell. Therefore, the features did not affect the cell culture in a reliable way for the entire cell culture.

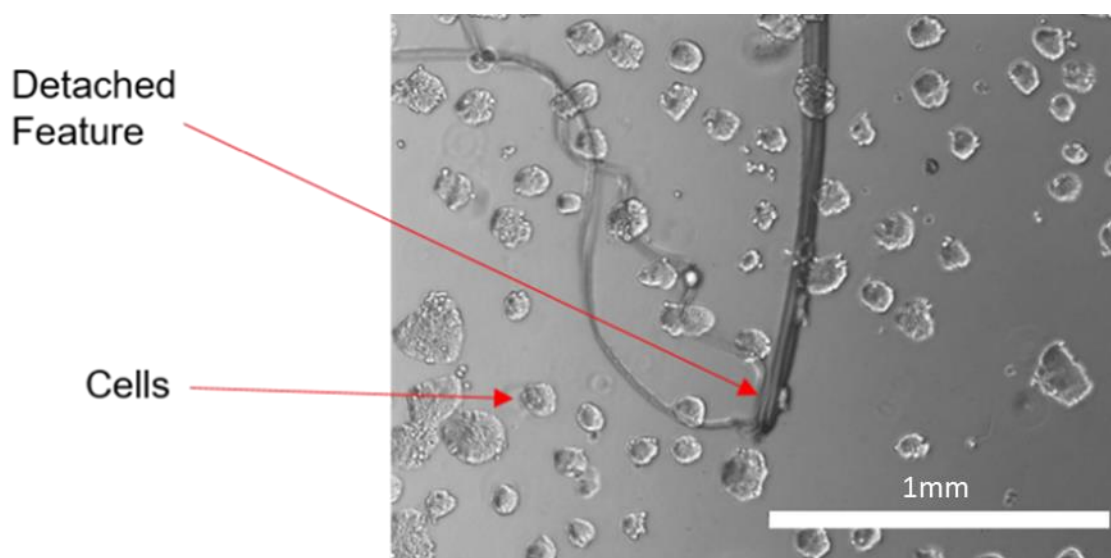


Figure 6.3: Degraded features detach from the surface during cell culturing.

To assess the adhesion to the substrate, a tape test (Section 3.2.4) was performed by printing a pad of PEDOT:PSS onto glass. The formulation scored 0B on the qualitative scale. This is interpreted as more than 65% of the coating detached from the substrate during the test (Figure 6.4). This test was performed in an engineering environment and the pad had not been submerged in cell culture media.

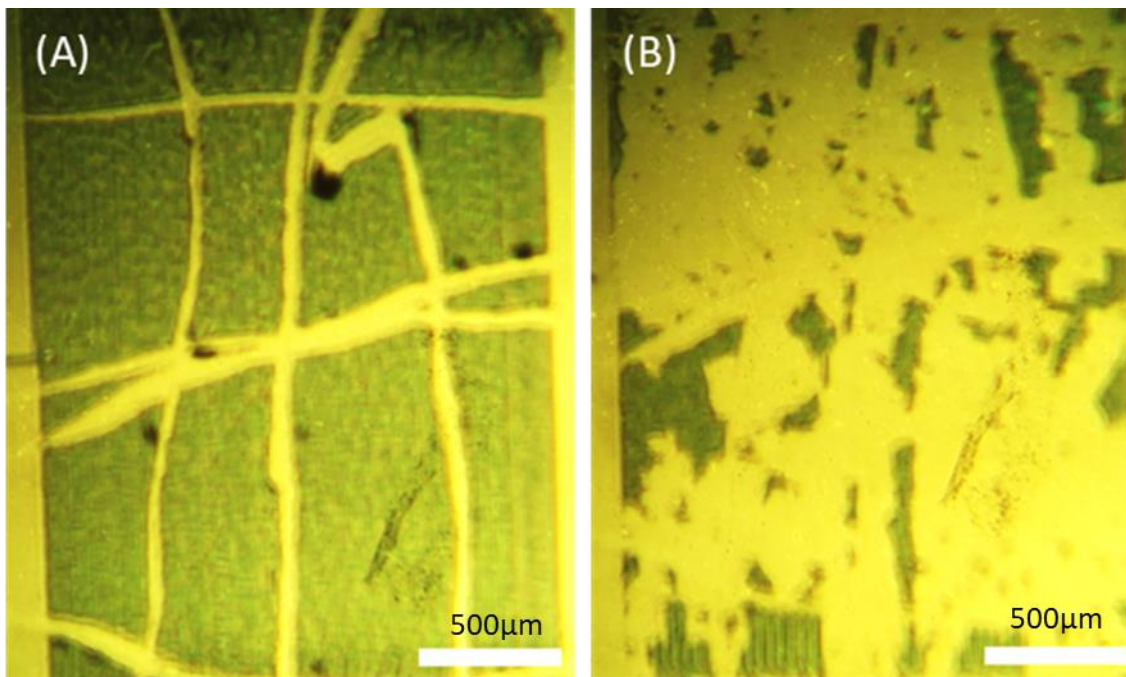


Figure 6.4 PEDOT:PSS F4 (A) Before ASTM Tape Adhesion Test (B) After ASTM Tape Adhesion Test.

As the printed features did not adhere to the substrate, an additive designed to increase adhesion to the surface was incorporated into the formulations. The adhesion promoting additive (3-Glycidyloxypropyl)trimethoxysilane (GOPS) was used. GOPS was chosen as it has been used as an adhesion promotor for PEDOT:PSS electronics. GOPS acts as a crosslinking agent and reduces the ability of PEDOT:PSS molecules to swell in water [225]. Similar to the APTES material described in 5.1.1, GOPS is a silane and has been proved to be biocompatible in other research [221]. The volume percentage of GOPS was minimised to avoid nozzle blockages, and the effect on the ink rheology and was far lower than the amount of APTES that was used in the first printing ink (0.2%Vol GOPS vs 10%Vol APTES).

0.2% vol/vol GOPS was the lowest concentration of GOPS shown to result in suitable adhesion, so it was added to the printing ink. The qualitative score on the ASTM tape test when testing this new formulation on glass is 4B (Figure 6.5). Small flakes of the coating are detached at intersections, and less than 5% of the area is affected.

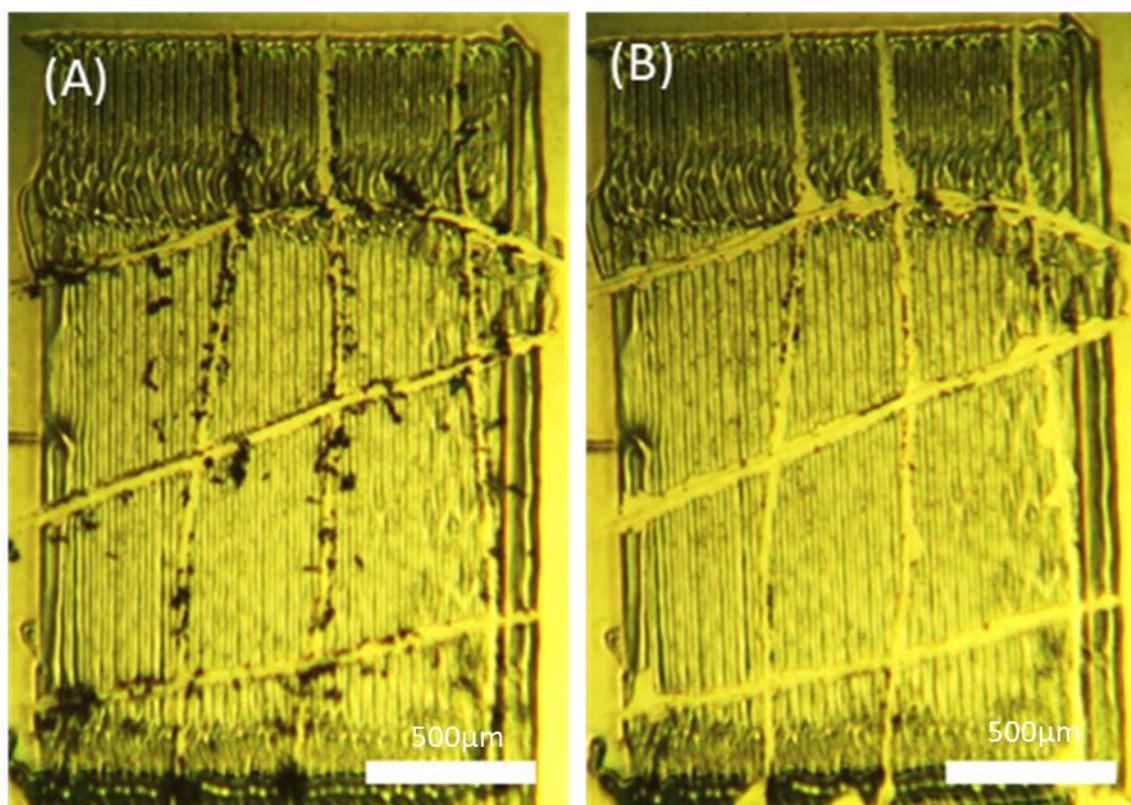


Figure 6.5 PEDOT:PSS Formulation P4 +0.2%Vol GOPS (A) Before ASTM Tape Adhesion Test (B) After ASTM Tape Adhesion Test.

Using this new formulation, there was a noticeable decrease (average 24.2%) in the printed line width at the same process conditions after the addition of the adhesion promotor. The difference in print characteristics is due to the surface interaction of the new ink with the glass substrate. This decrease was accounted for by slight adjustments to the print parameters. There is no visible degradation or peeling after immersion of these printed features in cell culture media for 72 hours. Overall the effects of adding GOPS are desirable and therefore this formulation was used for the printing of cell test environments.

6.1.2 Cell Viability When Exposed to Printed Substrates

A non-directional cell viability test was performed to ensure that the PEDOT:PSS/GOPS coating was not toxic to cells. Colorectal cancer cells were cultured onto a slide which had been covered in the PEDOT:PSS/GOPS material. They were allowed to grow for seven days after which they were stained using

two chemicals in a Live/Dead cell viability assay, the result of which is shown in Figure 6.6. This confirmed that the material is a viable culture material for cells cultured onto the material.

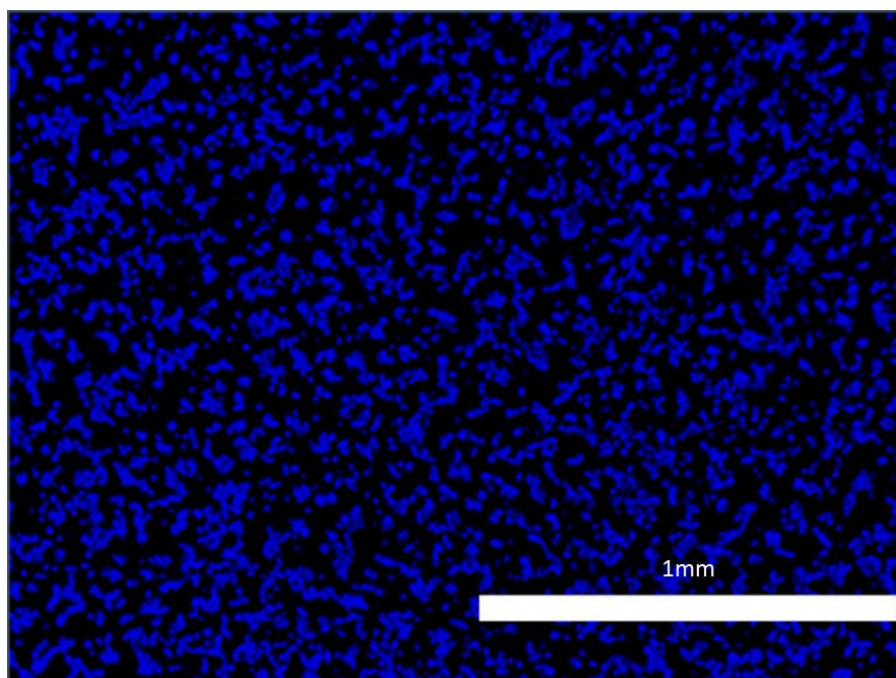


Figure 6.6: Live/dead Staining of colorectal cancer cells cultured onto a PEDOT:PSS coated substrate. blue = Live (Hoechst 33342) red/purple=le= Dead (Propidium Iodide). Note that there were no dead cells hence there is no red/purple colour.

6.2 Basic Cell Patterning

6.2.1 Printed Lines

The initial patterns were a series of lines, with a pitch large enough that the cells respond to the single lines ($20\mu\text{m}$), so that a single cell was only be influenced by one printed line (pitch was twice the line width). The definition of line width and pitch is seen in Figure 6.7.

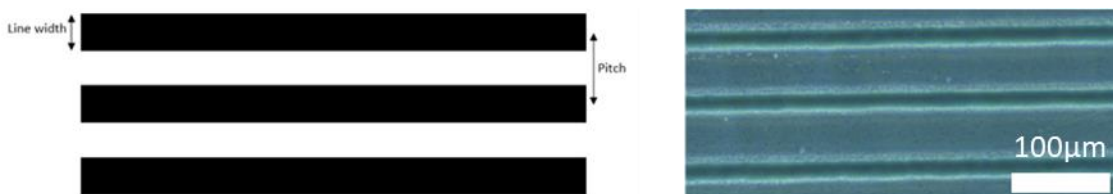


Figure 6.7: (A) Definition of line widths and pitches (B) an example of a print.

The three-dimensional structure of the lines was assessed by white light interferometry (Figure 6.8), to verify the inverted parabolic shape of the deposit was still consistent after the addition of GOPS.

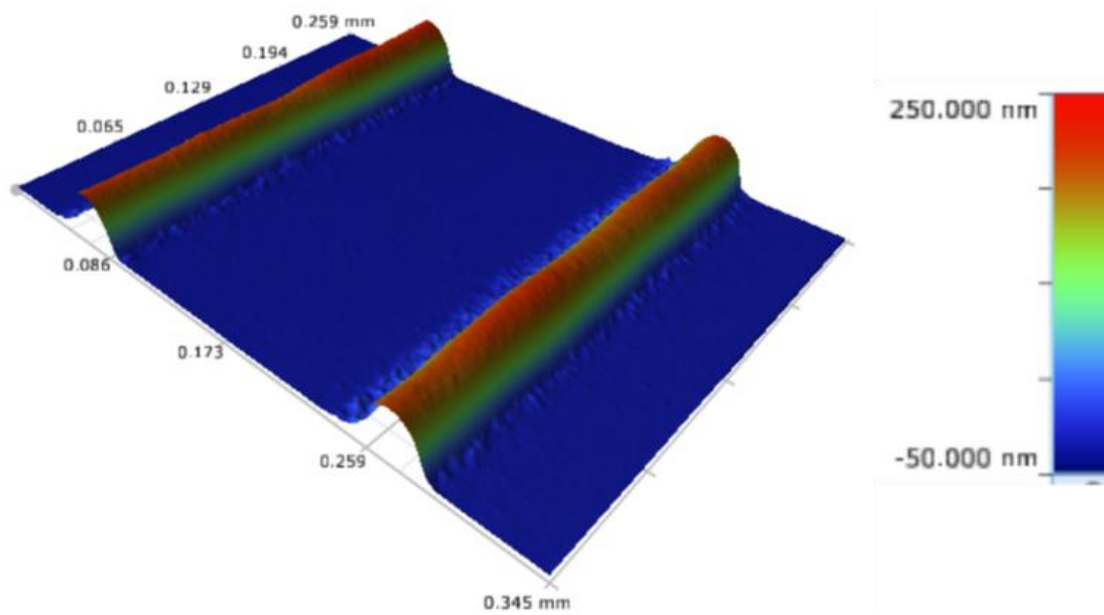


Figure 6.8: White light interferometry measurement of a printed line after the addition of GOPS.

First, to prove the importance of the substrate choice, a treated glass substrate was trialled in the cell culturing. HCT-116 cells easily overgrow the features and only some local regions of the culture are ordered (Figure 6.9). This was due to the propensity for the cells to attach to both the glass substrate and the PEDOT:PSS printed lines.

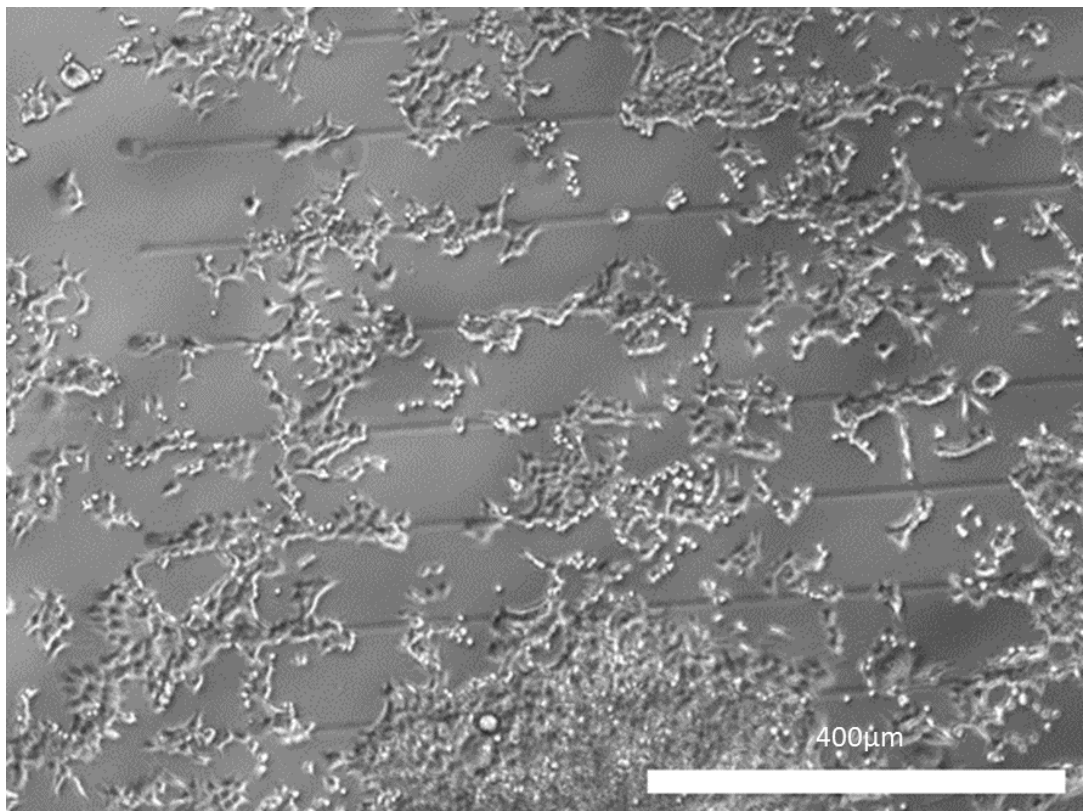


Figure 6.9: HCT-116 cell response to PEDOT:PSS features on glass after 48 hours.

If the substrate used is non-fouling PDMS there was more pronounced attachment and growth to the features. As the cells divide and multiply there is a preferential movement along the printed features, however the cells can outgrow from the features to the underlying substrate. There is a literature precedent that cells exhibit a preferential tethering to hydrophilic surfaces (such as PEDOT:PSS) over hydrophobic ones (such as PDMS) [226].

Due to the inherent random nature of the cell distribution on the surface, and the chaotic nature of cell growth generally, predicting the exact growth patterns of the cells is difficult. However, some initial parameters that were identified as important were the initial cell seeding density, and the length of time the culture was performed for. An illustration of the importance of cell culture density is shown in Figure 6.10. Figure 6.10A is a culture with a low initial seeding density, whereas Figure 6.10B shows a higher cell density per sample seeding density.

In general the cultures with higher cell density had a more chaotic environment than those with lower cell densities. When a part of a high-density culture, the cells could rely on growth factors and interactions with other cells to support their growth. In general the order and control of the substrates improves as the cell seeding density reduced. However, cells do rely on some outside signals to trigger division, so if there are too few cells they either split at a low rate or did not divide at all, meaning the experiment had to be repeated.

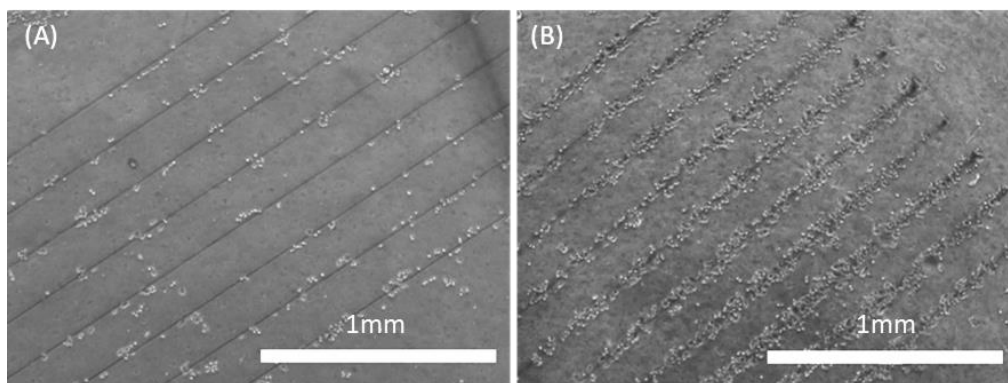


Figure 6.10: Images of cell response after 24 hrs at different seeding densities (A) 6000 cells/sample (B) 10000 cells/sample.

The cellular response was observed on 30µm WHM lines for the first few trials to identify a suitable initial seeding density. Using 3ml of 2.5×10^4 cells per ml, so 7500 cells per sample resulted in a distribution of cells over the surface which was suitable for the application. Cells were observed to grow to the lines in multiple repeated experiments, and additional images are available in Appendix J. Agitating the samples after seeding ensured the cells were evenly distributed over the surface. Fixing the seeding density and distributing the cells led to an improved reliability of the patterning.

After seeding, the samples had to be handled with care until the cells have settled onto the substrate surface. If the cells were disturbed a homogeneous distribution would not be achieved, resulting in regions of higher cell concentrations at the centre of the well, ruining the patterning response.

Once the cells were seeded onto the sample, there was no way to influence their growth in a desirable way. The cellular response to the printed features could therefore only be observed. Due to the gentle shaking to spread the cells, it was expected that the cells would be distributed over the entire surface. However, after 24 hours it was observed that the cells were tethered to the lines and not the substrate. This could be explained if the cells actively migrate across the surface toward them. The experiment was repeated and this behaviour was observed even as soon as 8 hours after seeding. This was the earliest time it was viable to image the cells without disturbing the settling process and is shown in Figure 6.11.

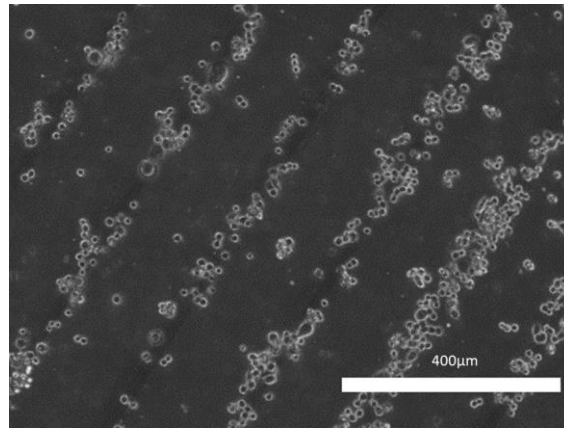


Figure 6.11: A response to printed features was observed after 8 hours of culture.

As the cells divide and their number grows, a preference to grow in line with the features was observed. The growth characteristics of HCT-116 cells over time are illustrated in Figure 6.12. After 24 hours, the cells were distributed over the length of the printed features but did not attach to the underlying PDMS substrate. Cells also attach to the regions containing overspray, indicating that cells can use small particles as small attachment points. After 48 hours the cells have divided so their numbers have increased. It was observed that these new cells grow preferentially along the line, and do not grow outward onto the underlying substrate. After 48 hours the cell division has continued, and the cells have become confluent on the printed features only. The lack of growth onto the PDMS at this stage is remarkable, as the cells have only grown ‘outward’ from the line by relying on those cells that are already tethered to the PEDOT:PSS features. Therefore, even after the initial feature is completely covered by cells, the culture still grows into a shape that is defined by it.

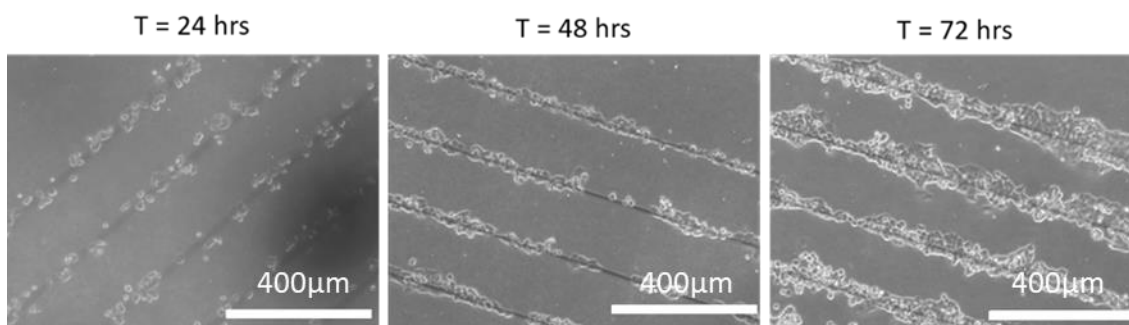


Figure 6.12: HCT-116 growth over 72 hours.

Figure 6.13 shows how close examination of the features under 20X distinguished the difference between the initial growth, contained to the printed feature (Figure 6.13A), and the final stage of growth where the cells grew outward from the printed geometry (Figure 6.13B).

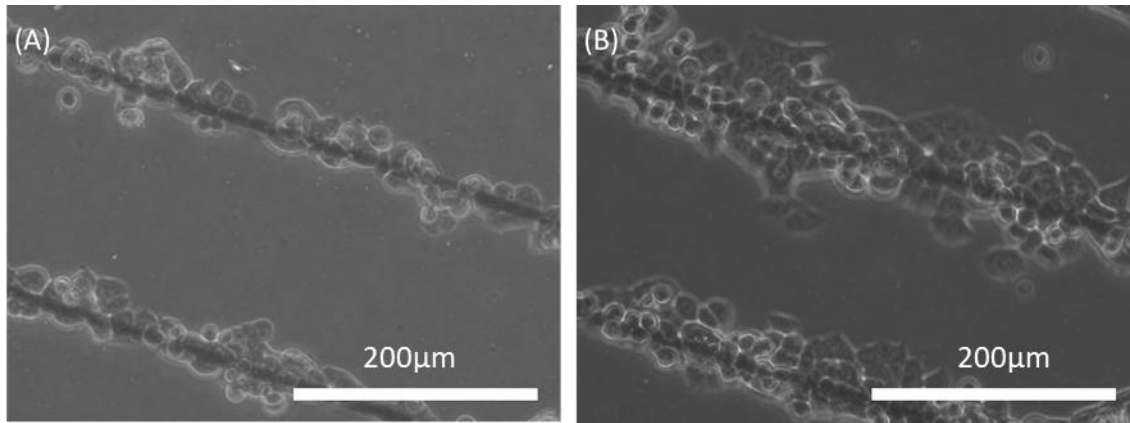


Figure 6.13: 20X optical microscope image of HCT-116 growth after (A) 48 hours (B) 72 hours.

Figure 6.14 shows an experiment run to 96 hours where the cells had engulfed the printed features, and had grown out of the desired areas.

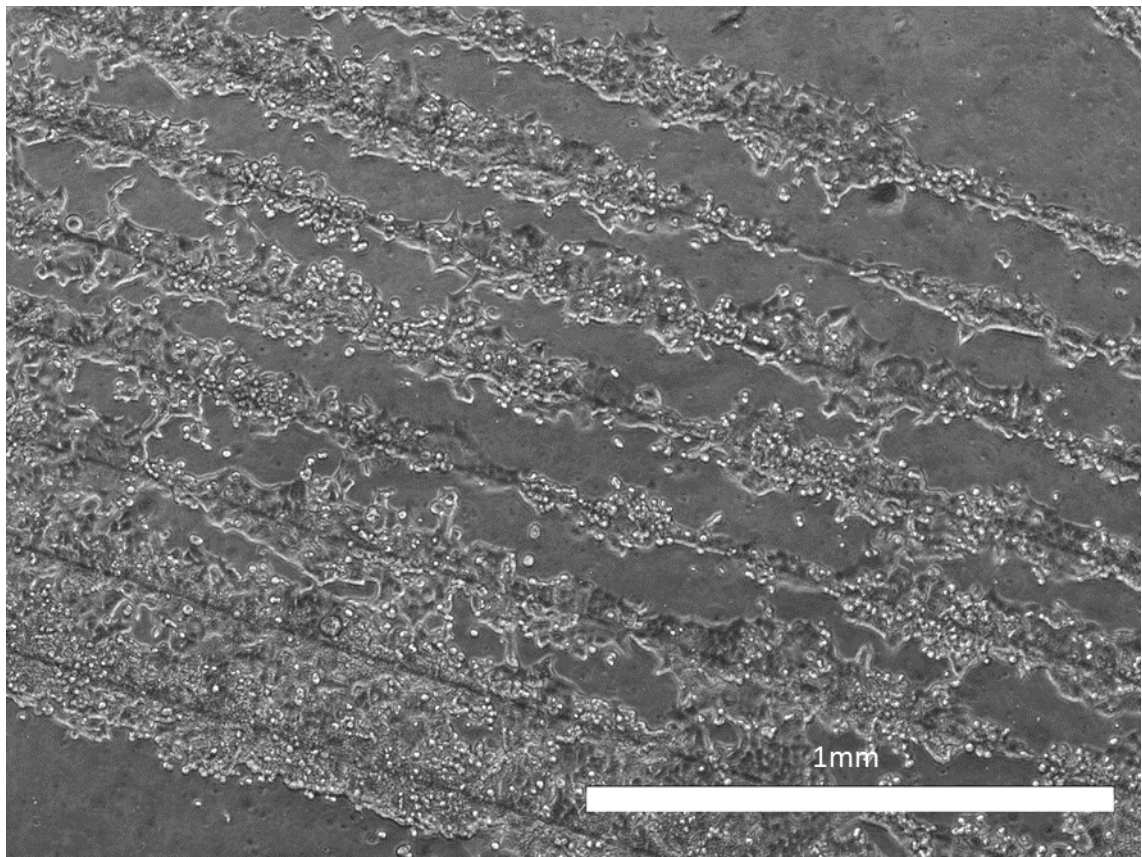


Figure 6.14: HCT-116 cells grow outside the printed features after 96 hours.

This result was expected, as using surface patterns to influence cell growth has been shown previously [27], [207], however the scale of the presented features is an order of magnitude smaller than the scale of the comparable literature. These studies do not analyse the mechanism of the interaction between the cells and the printed features.

SEM analysis of the cells at an early stage of growth (fixed after 8 hours), carried out in this work, verify the attachment of cells to the printed features and not to the underlying substrate (Figure 6.15).

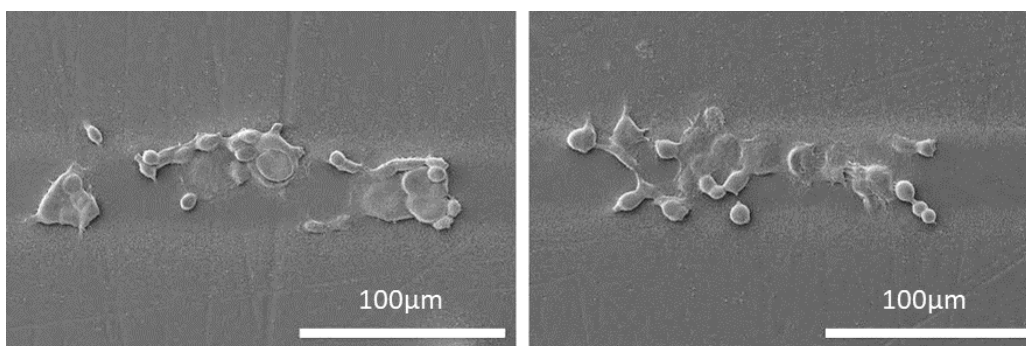


Figure 6.15: SEM image of cells tethering along a PEDOT:PSS printed line.

However, it is also clear under SEM analysis that the cells are also tethered outside the printed regions by attaching to the overspray particles, shown in Figure 6.16.



Figure 6.16: SEM image, taken at a 20 degree angle, showing a cell tethering to the overspray (left).

To verify the mechanism of attachment of the cells, some samples were processed for analysis under high magnification immersion SEM (Figure 6.17). These images verified that on a cellular level the cells (Left of both images) was

preferentially attaching to the round nanoparticles of PEDOT:PSS over the underlying PDMS substrate.

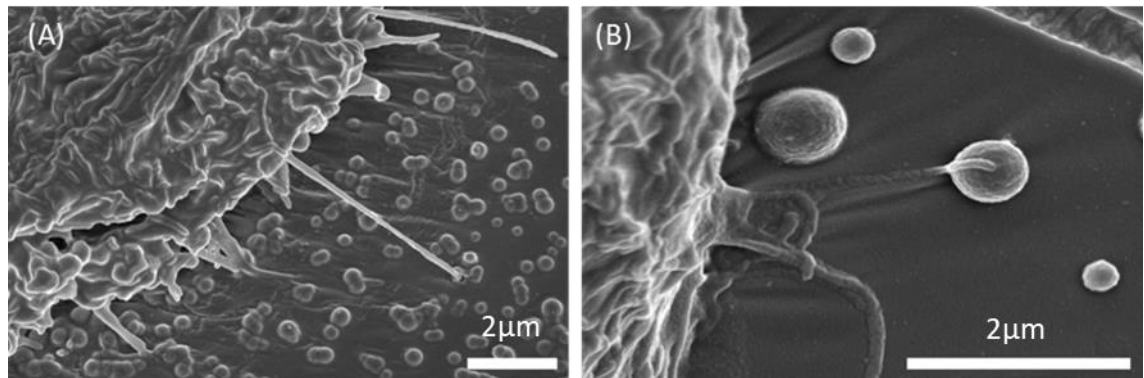


Figure 6.17: Immersion SEM images of cells (Left of both images) extending projections to attach to the deposited nanoparticles of PEDOT:PSS. (A) 10000X (B) 25000X.

In addition, some cells were frozen during the cell division cycle. Both cells have extended projections to the PEDOT:PSS features, showing that there is a response to the printed features during cell division as well as initial tethering.

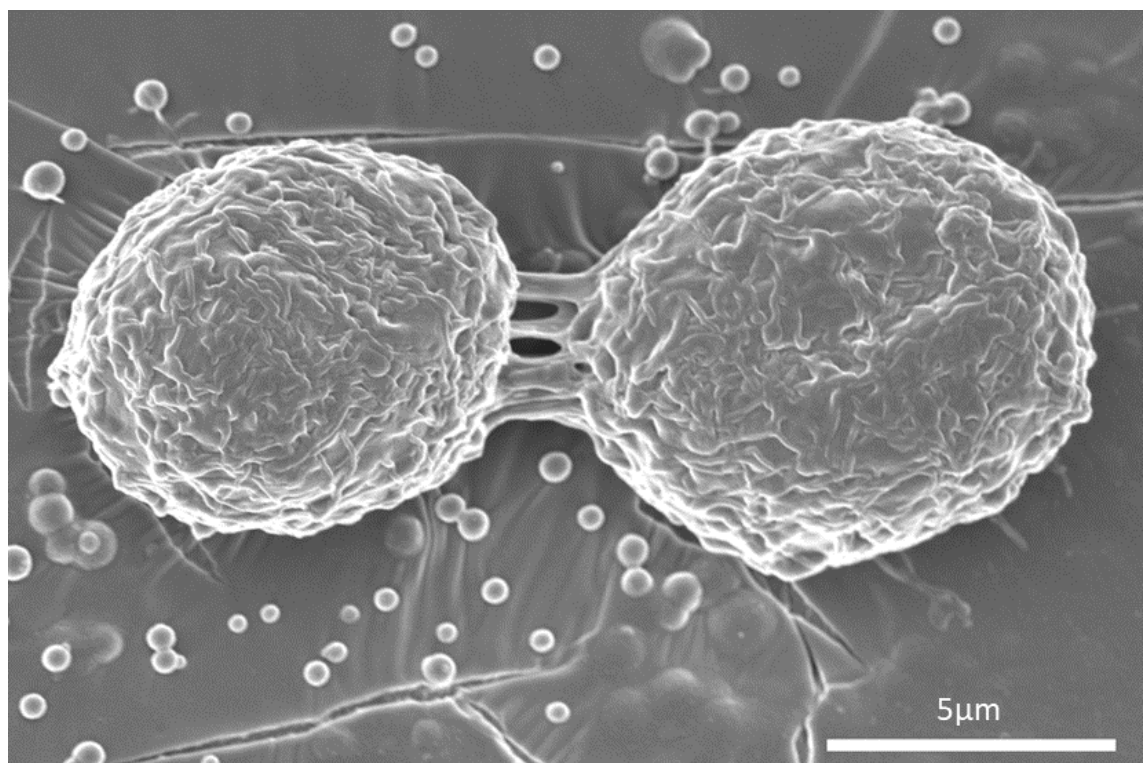


Figure 6.18: Cells during the cell splitting phase extend projections to tether to the PEDOT:PSS particles.

SEM analysis can also indicate how cells that grow outside of the printed regions are able to tether to the substrate. Figure 6.19 shows how even in untreated regions, some PEDOT:PSS nanoparticles have settled onto the surface, and so

the cells extend projections and tether to these nanoparticles. However, these cells were in a minority and did not affect the other patterning that was seen on the printed regions.

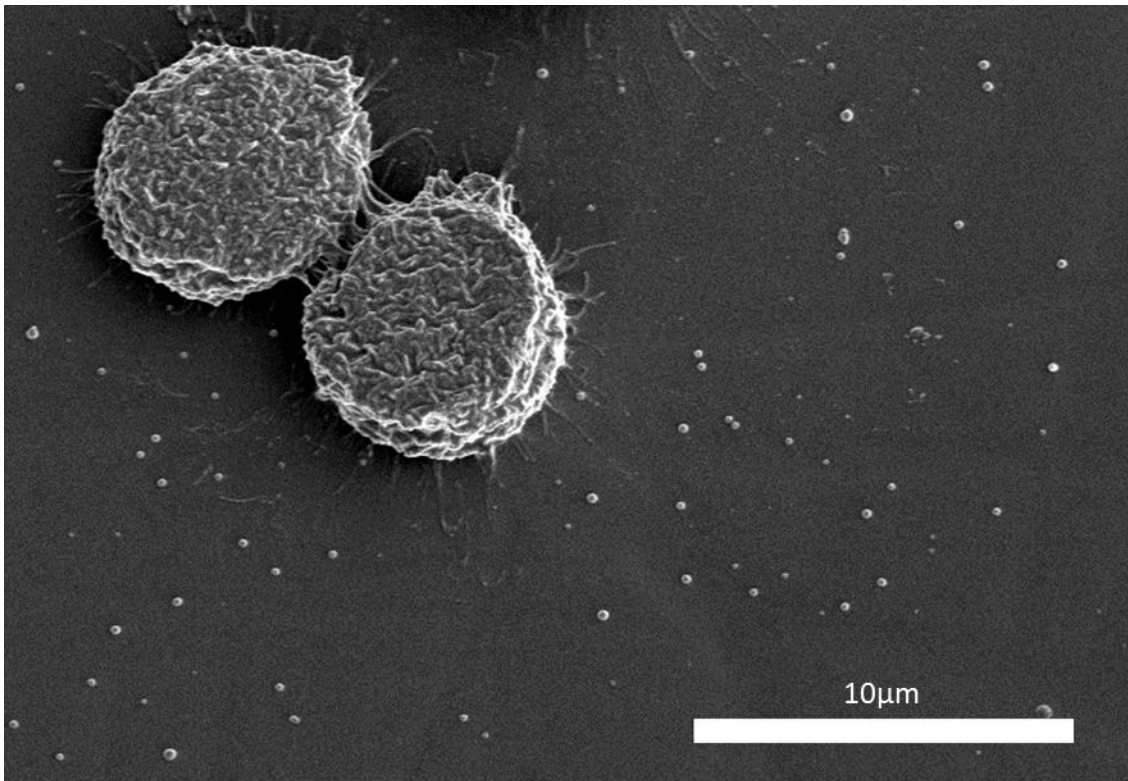


Figure 6.19: Cell tethering to single nanoparticles on an 'unpatterned' PDMS region.

Cell staining and immunofluorescence (Appendix H) are commonly performed to highlight biological regions of interest and to remove unwanted noise from the analysis of the biological system. Stained images are used in other patterning work for this purpose [10].

Staining can be performed with many chemicals and methods, but each highlights a particular organelle and attaches a fluorescent marker to them using either a primary or secondary antibody. This high contrast image can help to visualise the cell response and highlight the areas that contain organic matter, especially over large areas. This is important as over large areas transmitted light images do not have the contrast to highlight individual cells. Immunofluorescence is also useful as it removes artefacts such as substrate perforations, scratches, substrate contamination, and protein build ups in the media, from the analysis. The samples

were tested for their compatibility with this commonly used biological assay, and it was found that they were compatible. However, immunofluorescence works best at high magnifications, so it is not always useful for visualising cell patterning applications. Although the staining technique was not used in every test it was sometimes used when and where it was useful. An example of cell immunofluorescence is shown in Figure 6.20. The cell nucleus is the largest organelle, so highlights the cell location and number. Sometimes it is also useful to highlight the cell cytoskeleton, to show the morphology of the cell at that point. Usually these separate images are overlaid.

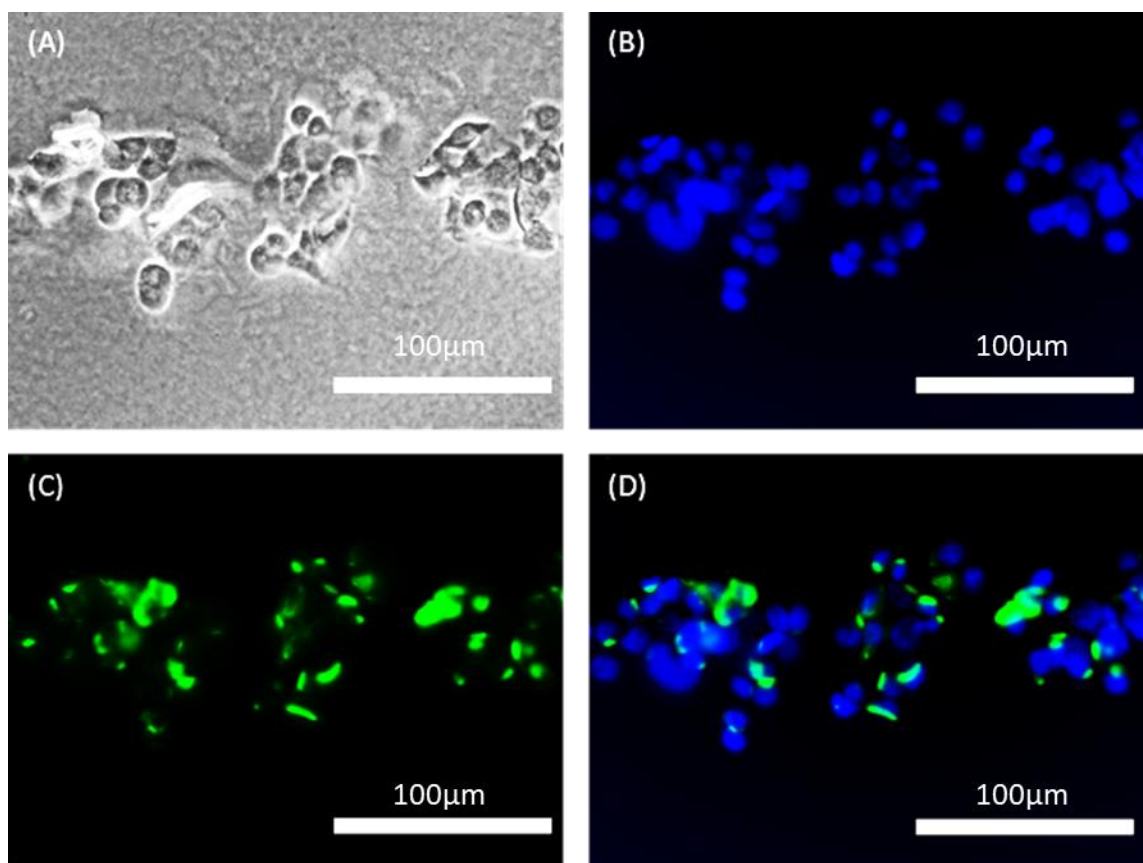


Figure 6.20: (A) 40X image with transmitted light (B) DAPI nucleus staining (C) α -tubulin cytoskeleton staining (D) superimposed image as standard in biological assays.

6.2.2 Dot Arrays

Previous AJP cell patterning literature, considers only straight lines and grids [45], [205]–[207]. A major contribution of this work is producing a library of shapes that can be printed using the AJP process and describing the cellular response to

different printed features. The next trial involved printed arrays of small dots of material which were used to influence cell growth. These tests showcase the discrete and rapid control our apparatus has over the Aerosol Jet, which is not shown in the literature. When using Aerosol Jet, dots can be created by opening and closing the shutter at its maximum speed, without moving the stage. An array of these can be produced by moving the stage once the shutter is closed and repeating the process. The factors that affect the dot size are the same as those that affect normal line deposition except the stage speed is not relevant and the length of time the shutter is open is relevant.

Dots of $50\mu\text{m}$ WHM were produced by using the same settings as when producing a $30\mu\text{m}$ line, with the shutter opening and closing at its maximum speed (sending an open and close command on subsequent lines of G-Code). There is no upper limit to the spacing of these dots. However, the lower limit is defined as the point at which the dots begin to bridge into a larger feature. In this case the minimum dot spacing was $100\mu\text{m}$ as observed in Figure 6.21.

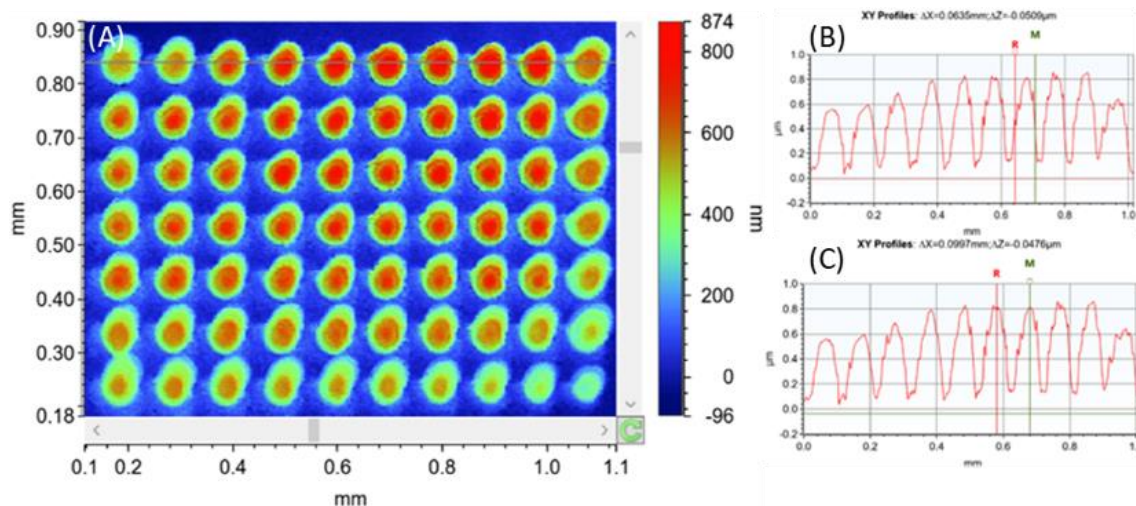


Figure 6.21: Dots with $50\mu\text{m}$ WHM in an array are distinguishable at $100\mu\text{m}$ pitch. (A) White light data. (B) Cross sectional data showing the width at half maximum. (C) Cross sectional data with a pitch measurement.

By reducing the nozzle size and the atomiser gas flow rate to the settings for a $20\mu\text{m}$ WHM line, dots of $20\mu\text{m}$ WHM were produced. These dots also exhibited

a much smaller peak height ($0.6\mu\text{m}$, compared with $0.8\mu\text{m}$). The reduced size of the dots enabled the spacing to be reduced to $30\mu\text{m}$, as shown in Figure 6.22.

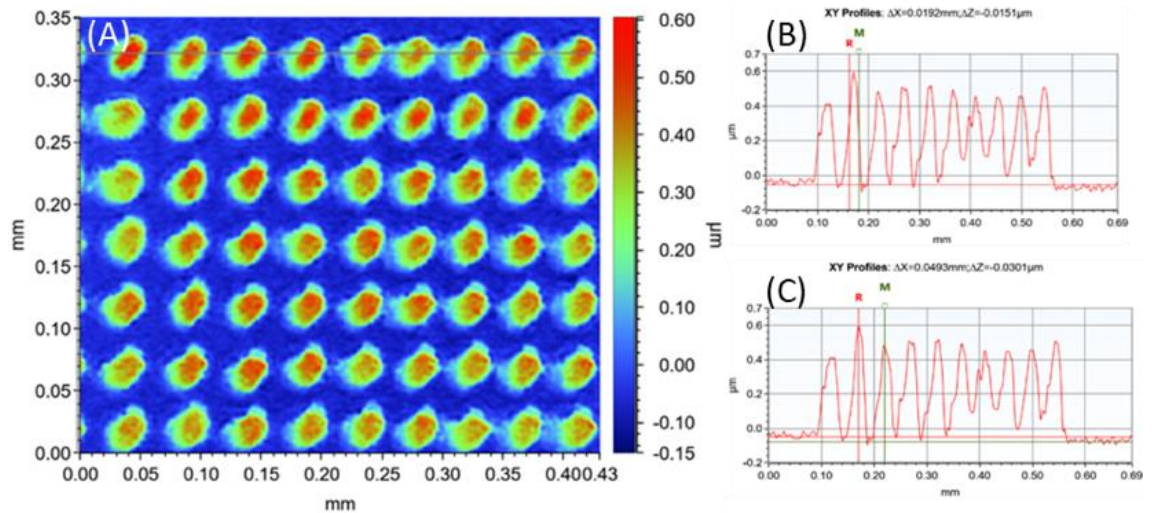


Figure 6.22: Dots with $20\mu\text{m}$ WHM in an array are distinguishable at $40\mu\text{m}$ pitch. (A) White light data. (B) Cross sectional data showing the width at half maximum. (C) Cross sectional data with a pitch measurement.

The first indication of the features being too close to be distinguished is a bridging of overspray between the features. Two sets of overspray can interfere to coat the substrate meaning that the two dots cannot be distinguished. The distance at which this build-up first occurs is challenging to pick up under a white light interferometer but can also be observed under a scanning electron microscope. When $20\mu\text{m}$ WHM dots are printed the interference was observed at a $30\mu\text{m}$ pitch. This was the furthest pitch where the build-up of overspray can cause bridging between the features, seen in Figure 6.23

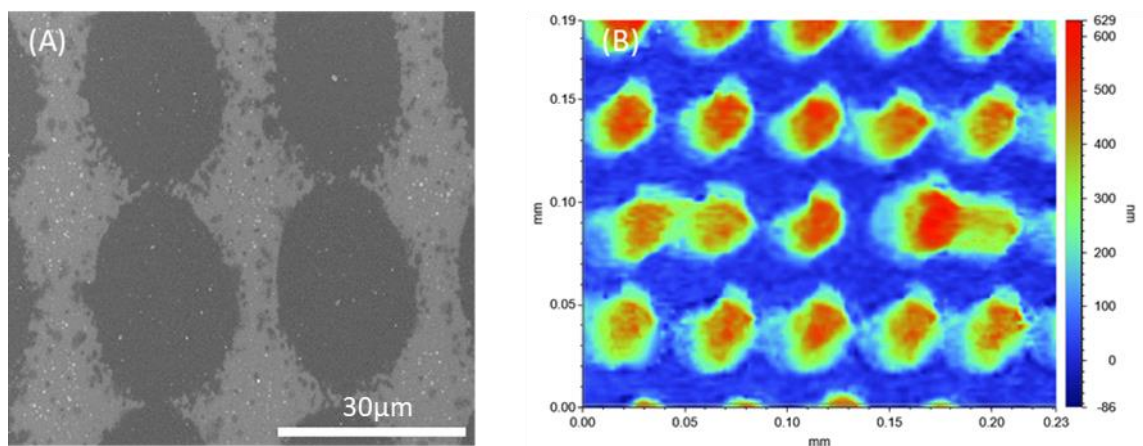


Figure 6.23: (A) Sputtering interference causing features to amalgamate at $30\mu\text{m}$ pitch. (B) White light interferometry image showing bridging between dots of material.

For distinguishable features, with no interference between the dots, it was recommended to have a pitch greater than two times the dot size. The white light interferometry image and under the scanning electron microscope confirm that at this pitch there were no instances of bridging (Figure 6.24).

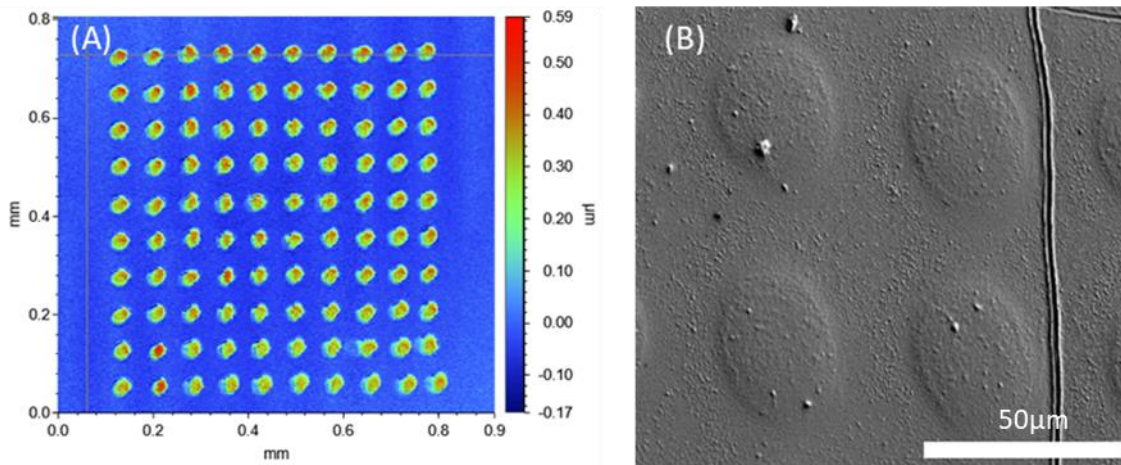


Figure 6.24 (A) Overview of an entire dot array with distinguishable features. (B) SEM image of the dot array.

These patterned substrates were then used as cell culture substrates. The cells created networks of cellular growth between the individual dots over the entire area of printed material. After 24 hours the cells had preferentially tethered to the printed material, and the increased density near the edge of the dot array suggested a migratory response toward the printed region. Cells replicated faster on the printed material, with the increased number of cells resulting in greater cell density on the prints over time. The trends over three pitches of dots is shown in Figure 6.25.

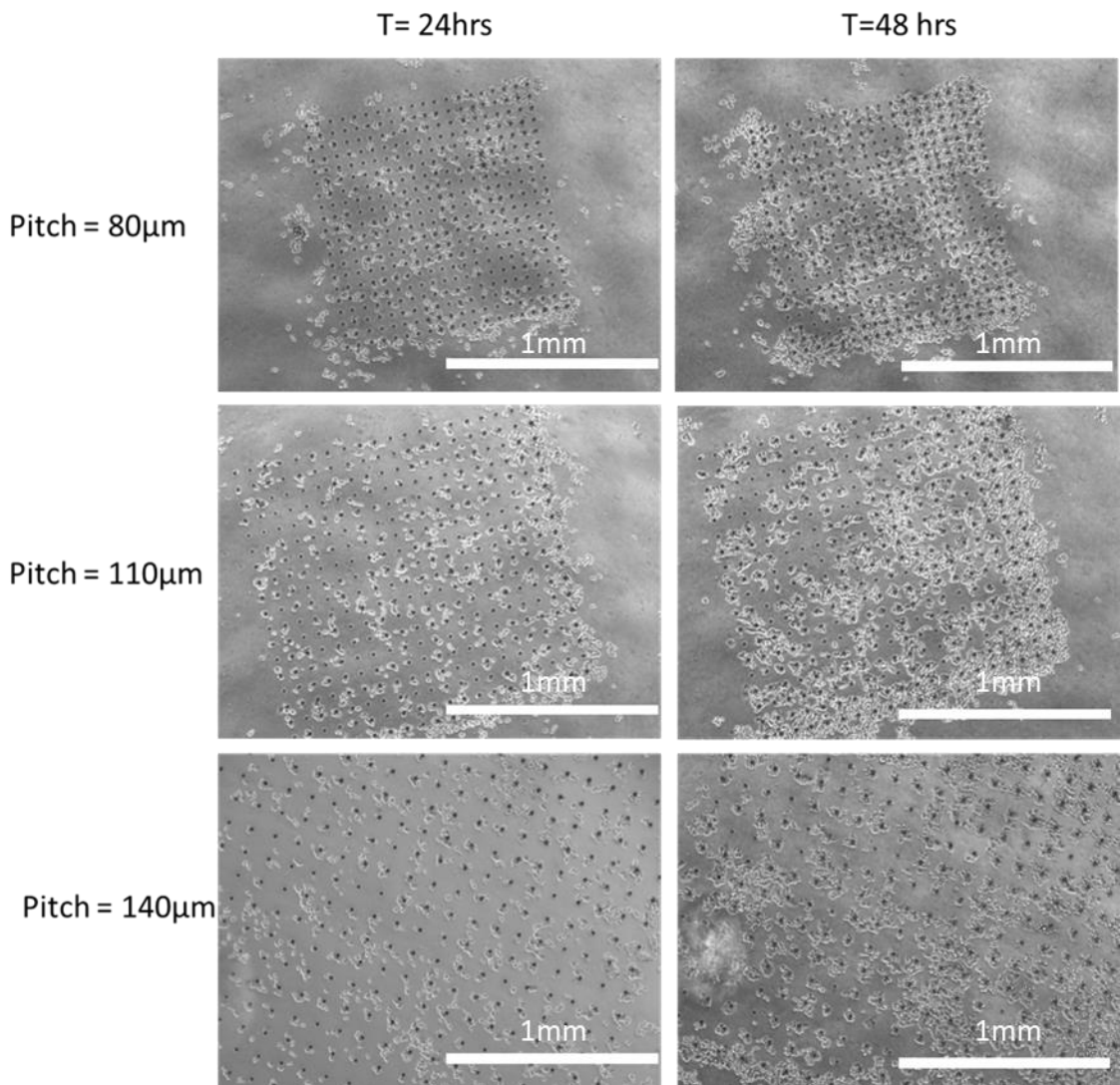


Figure 6.25: HCT-116 growth on three pitches of dot arrays after 24 hrs and 48 hrs.

Figure 6.26 shows how the densification of cells was more pronounced on the smaller pitched dot arrays. When the pitch of the dots was $80\mu\text{m}$, the cells were able to grow within the space between the dots so formed square cultures rather than a network.

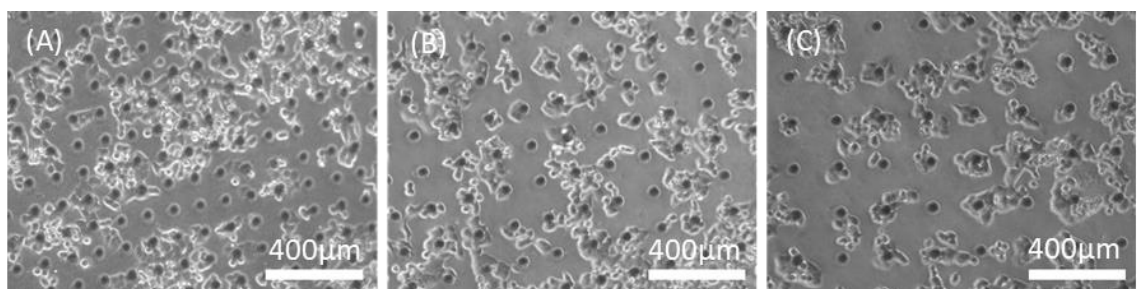


Figure 6.26: HCT-116 growth on three of dot arrays after 48 hrs (A) $80\mu\text{m}$ pitch (B) $110\mu\text{m}$ pitch (C) $140\mu\text{m}$ pitch.

A 20X magnification image of the cell growth on a close pitched dot array is shown in Figure 6.27. The cells were observed to grow between the dots, however as the cells took up the space they also grew into the square gaps.

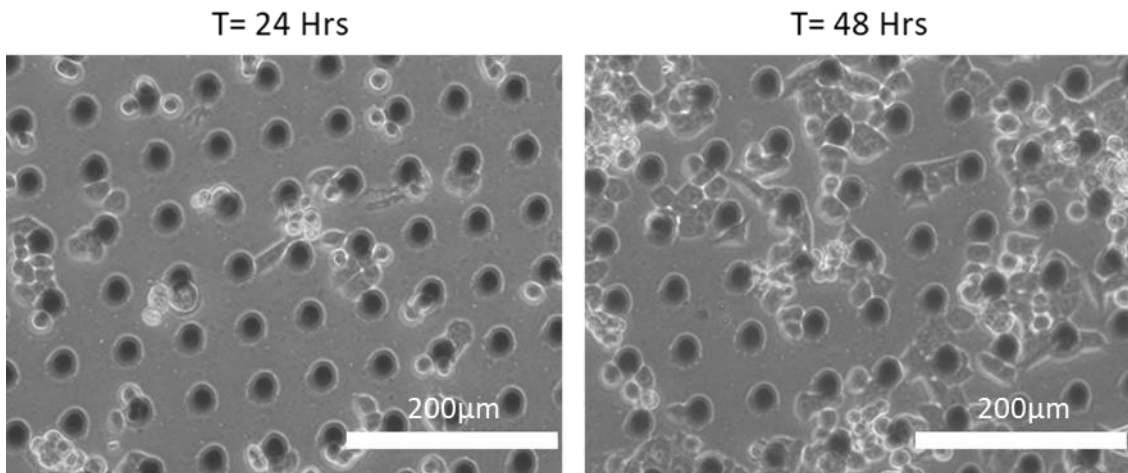


Figure 6.27: 20X magnification image of HCT-116 cell growth of an 80 μm dot array.

In Figure 6.28 the cells were observed growing between dots. As the cells are not directed in the same way as with printed lines, they initially aggregated around the printed dots. As the cells multiplied further the cells groups joined to form lines between the dots.

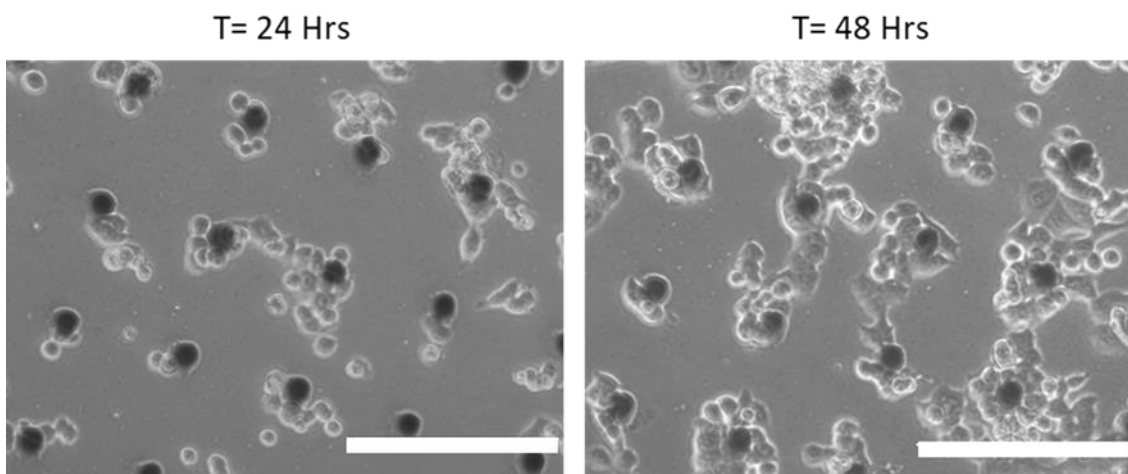


Figure 6.28: 20X magnification image of HCT-116 cell growth on a 140 μm dot array.

Figure 6.28 illustrates the networks growing at a large pitch. The cells were grown over 96 hours, at which point they were confluent on the printed dot array. Figure 6.29 highlights that even after 96 hours of growth, the HCT-116 cells were contained the region that was treated by the printing process. Similar to the

observations when growing on lines, those cells that grow outside the printed dot array were tethered to the rest of the culture. The cells did not grow on the underlying PDMS substrate.

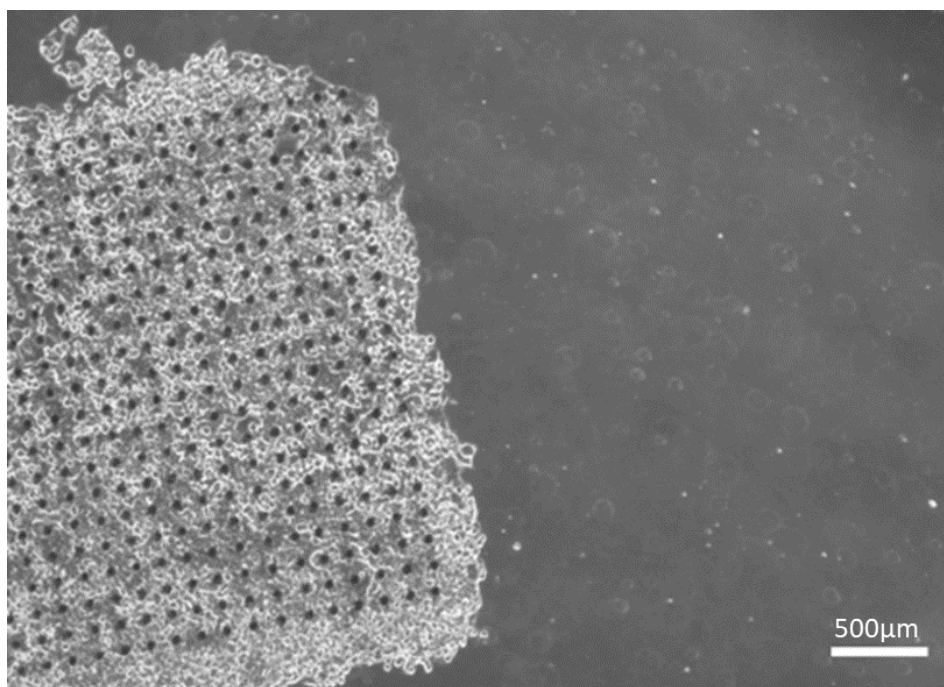


Figure 6.29: Cell growth is contained to the printed region even after 96 hours of growth.

An example of application for arrays of dots is to studying cell morphologies, motility and cell interactions. To observe these interactions it is recommended to have a large pitch in comparison to the dot size ($>2X$), so that the cells can be distinguished from one another. In addition, low pitch dot arrays may be a useful tool if a 'filled' area of a designable cell culture is desirable, using less material than filling with rastered lines, and encouraging confluent areas of cell culture.

6.2.3 Sharp Corners

To print a sharp corner requires a large deceleration/acceleration profile of the substrate under the print head to change the direction. A series of sharp corners were printed to analyse the effect of the changing direction on the deposit geometry. Figure 6.30 shows the angles printed with a $40\mu\text{m}$ WHM and a $20\mu\text{m}$ WHM line. There is a change in height and width in all cases where the shutter is opened before the stage is moving. This is due to the line by line execution

method of G-code, meaning that the shutter must first be opened, then the stage accelerated to the correct speed. The effect is larger when compared to the size in the smaller 20 μm WHM case (360nm height bulge on a 150nm height line) than the 40 μm WHM case (500nm height bulge on a 300nm height line).

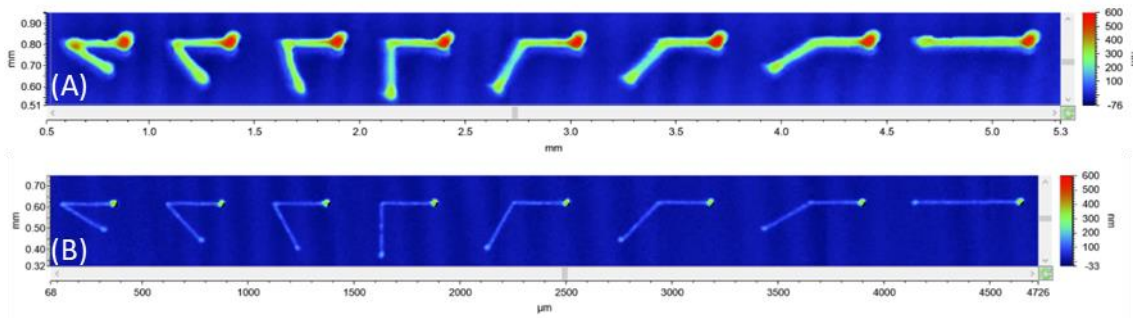


Figure 6.30: White light interferometry of changing angles. (A) Printing with 40 μm WHM. (B) Printing with 20 μm WHM.

When the corner is obtuse, the deposit characteristics are constant over the deposit. For acute and right-angle corners a build-up of material was observed at the vertex. In the acute and right-angle case, one of the driving axes must come to a complete stop, so there is an increased material deposition rate as the stage decelerates toward the vertex and accelerates away. This results in a build-up of material on the sharp edge. As shown in Figure 6.31, material build up was particularly observed in the 40 μm WHM features. This was due to the higher material deposition rate. With the smaller lines this build up is not as noticeable, meaning that more acute angles can be obtained at lower material deposition rates.

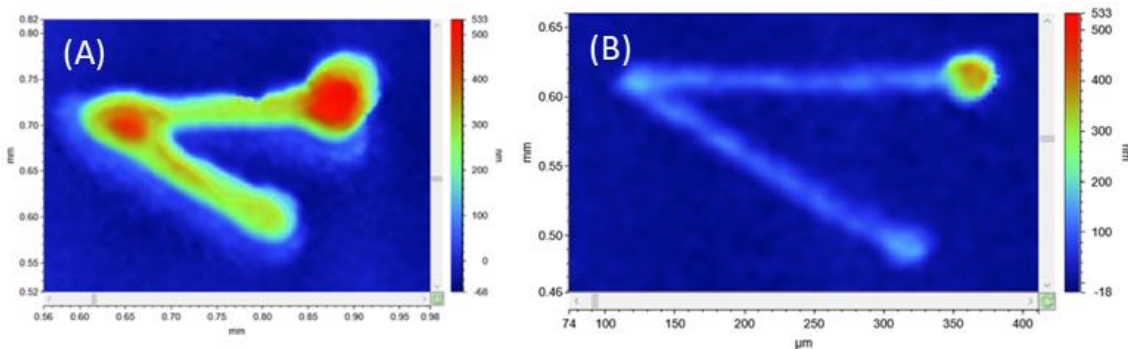


Figure 6.31: Acute angles exhibit a build-up of material at the vertex (A) 40 μm WHM (B) 20 μm WHM

The minimum angle achievable without a sharp corner bulge is 30 degrees when printing with a 20 μ m, but this angle increased as the material deposition rate increased.

When the features, printed on PDMS, are cultured with HCT-116, the cells selectively attached and grew to the shape. This is shown in Figure 6.32.

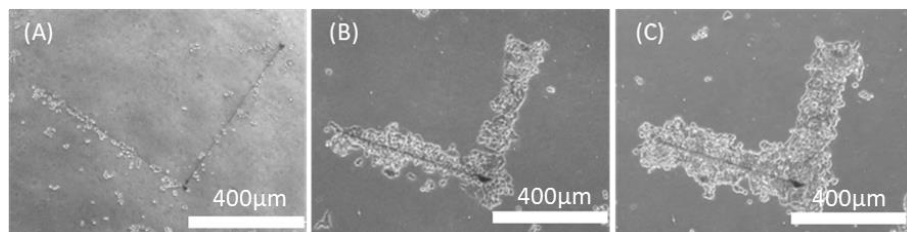


Figure 6.32: Sharp angle printed on PDMS. (A) A 24 hrs HCT-116 cells tether only to the printed regions. (B) After 42 hrs the cells begin to divide and grow preferentially along the feature. (C) After 72 hrs the cells are confluent on the feature.

The response to acute angles was characterised by a bulge of cells around the vertex. This was due to the proximity of the two lines as they approach the vertex. Cell secretions and communications mean that the cells could support each other, and grow outwards from the vertex.

It was observed that on obtuse angles the bridging effect was less common (Figure 6.33). The cells were more likely to exactly represent the printed cell culture, so it was recommended to print an obtuse sharp corner for the best patterning results.

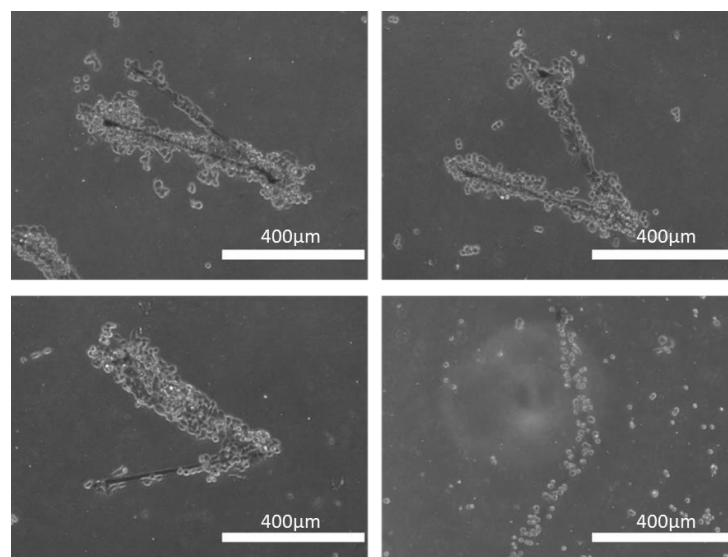


Figure 6.33: HCT-116 cells grow along around some sharp corners of different angles after 24 hours.

6.2.4 Circles

Circles of decreasing size were printed to determine the minimum radius to use in designs. Circles are useful basic shapes, and in addition curving arcs can be used in place of sharp corners in designable cell cultures.

In all these features it was observed under the white light interferometry that the AJP printed circle was not completely round, and that there was a gap between the beginning and end points of the circle. This was attributed to the backlash in the stage. This backlash was measured in Section 4.1.1.1 at $\sim 25\mu\text{m}$, and this was confirmed by measuring the feature. Although backlash can be designed out in many features, for circles it is unavoidable as both axes must always change direction to complete the circle.

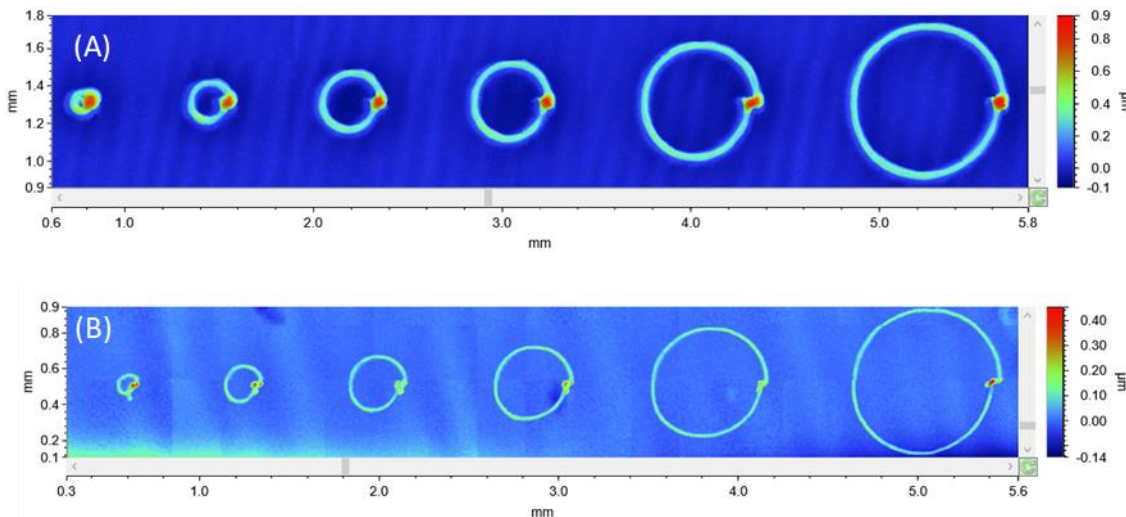


Figure 6.34: White light interferometry of printed circles of decreasing diameter. (A) Printing with 40 μm WHM. (B) Printing with 20 μm WHM.

The smallest diameter circle achievable with the 40 μm lines is 200 μm pitch circle diameter. At diameters smaller than 200 μm the circularity of the print was affected as seen in the smallest circles of Figure 6.34. When the line width is reduced to the order of 20 μm , the minimum achievable diameter is 100 μm . This limit is imposed as the material build up caused by shuttering dominates the small features. To determine if a circle had been printed, a cross section of the circle was assessed. Examples are shown in Figure 6.35. Two distinct peaks were

observed on every circle, confirming that no features had amalgamated. However, on small features, the backlash is relatively worse, and affected the circularity of the printed features. (see the smallest circle in Figure 6.34B). The smaller the diameter of the circle the larger the effect of the backlash on the circularity. Therefore, a minimum recommended circle diameter of 200 μm is recommended for all line widths between 20 and 40 μm .

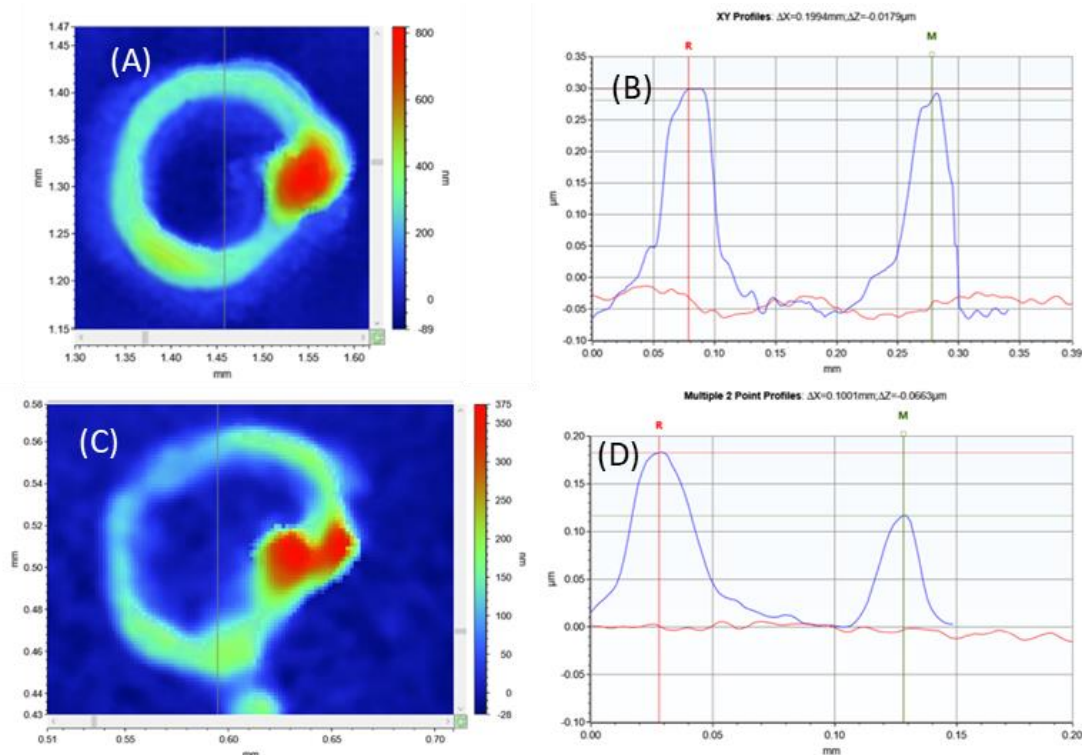


Figure 6.35: (A) 200 μm diameter circle with a 40 μm WHM line (B) A cross sectional data can be used to measure the feature. (C) 100 μm diameter circle printed using a 20 μm WHM line (D) cross sectional assessment shows the distorted nature of the small feature due to different sized peaks.

When PEDOT: PSS is used as a culture substrate HCT-116 cells selectively attach and grow to shapes defined by the printed circles. The growth characteristics observed on lines and sharp angles hold for printed circular features, meaning that the cells initially tether to the circle, before being cultured into the shape of the circle. Due to the relatively larger size of the features, the length of time required to grow to shape is longer. The larger number of cells on these features meant an increased likelihood that some regions did not grow as expected due to the secretions and interactions of the cells (Figure 6.36).

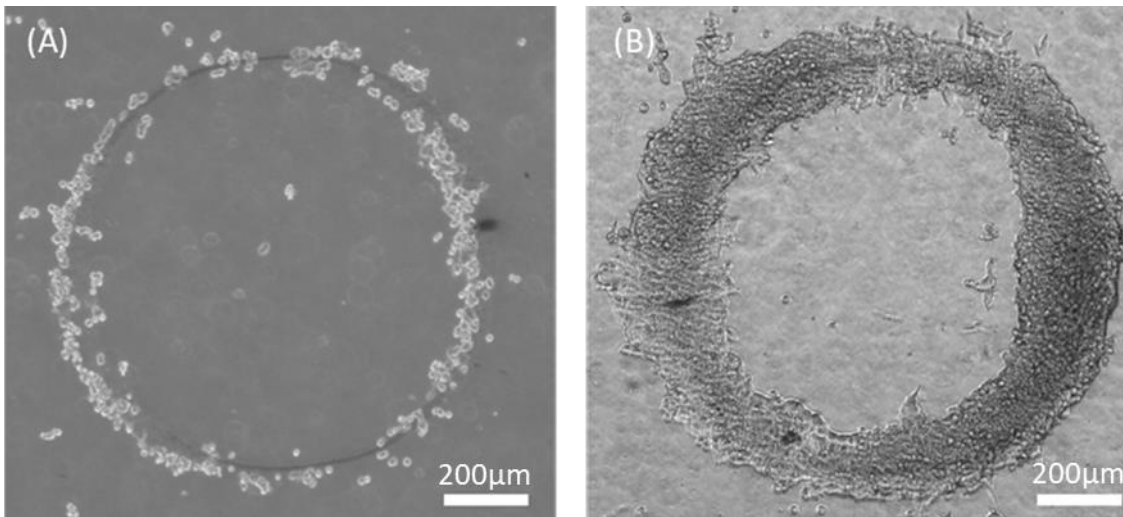


Figure 6.36: (A) Right HCT-116 cells respond to print at 24 hours. (B) Growth after 96 hours.

Unlike previous features the cells were not limited by the size of the circle. Figure 6.37 shows that the cells grew into the circular shape at the full range of sizes down to 100µm radius.

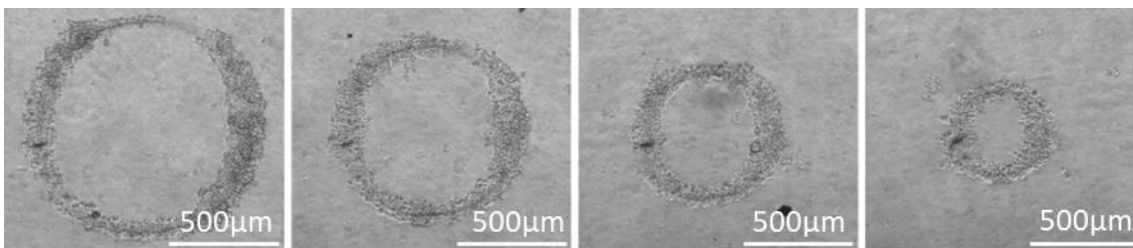


Figure 6.37: HCT-116 cell response to PEDOT:PSS circles on PDMS substrates.

Viewing circular patterns under the SEM highlighted how the cells respond to the incomplete circle caused by the backlash within the stage. This build up of cells results in bulges at the join point of the circles (Figure 6.38).

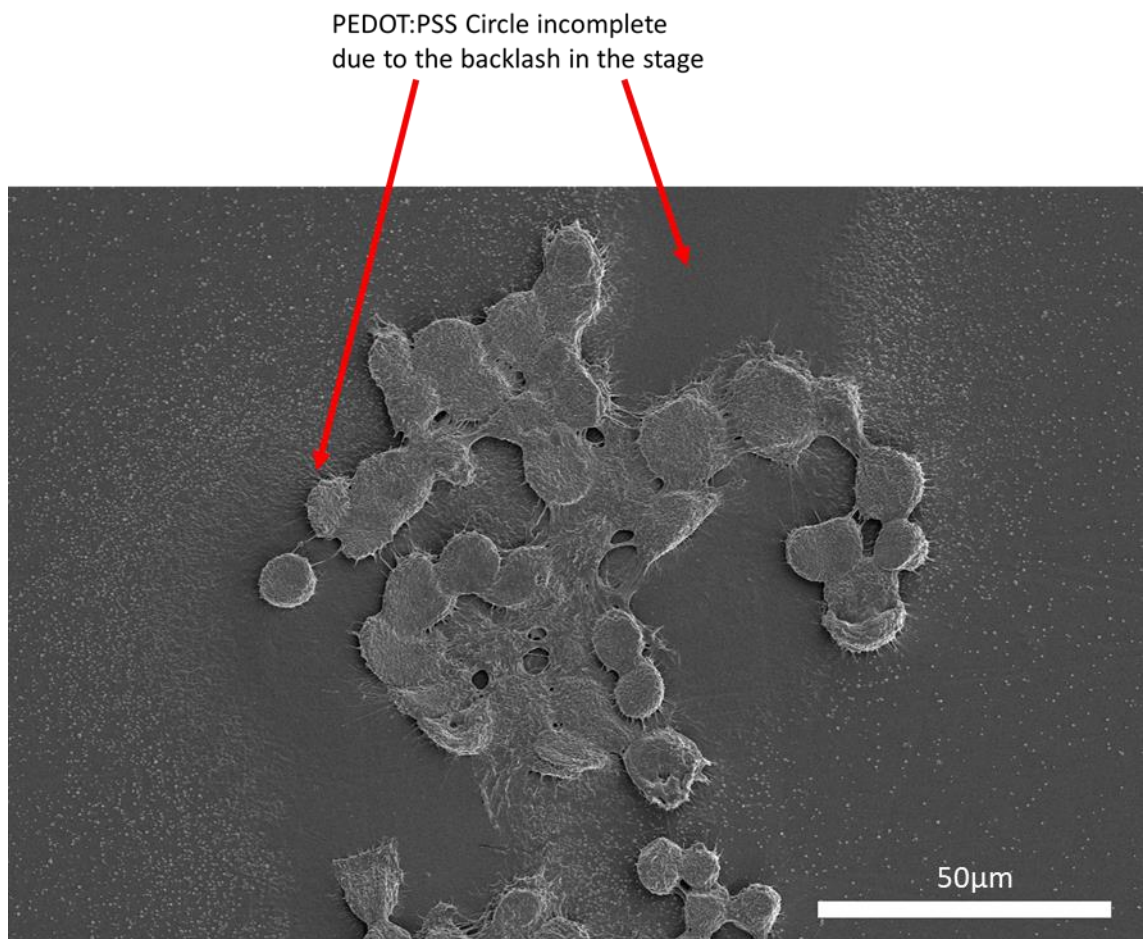


Figure 6.38: Cellular response to incomplete circle.

6.2.5 Pitch

An experiment was undertaken to find the pitch breakdown of a thick AJP printed line and a thin line. The pitch is defined as the distance between the centre of two printed traces. Figure 6.39 shows the experiments used to determine the minimum pitch at different line widths. It is clear from this figure that in general the smaller line width could achieve a smaller pitch, but in both cases there was a limit at which the lines could no longer be resolved.

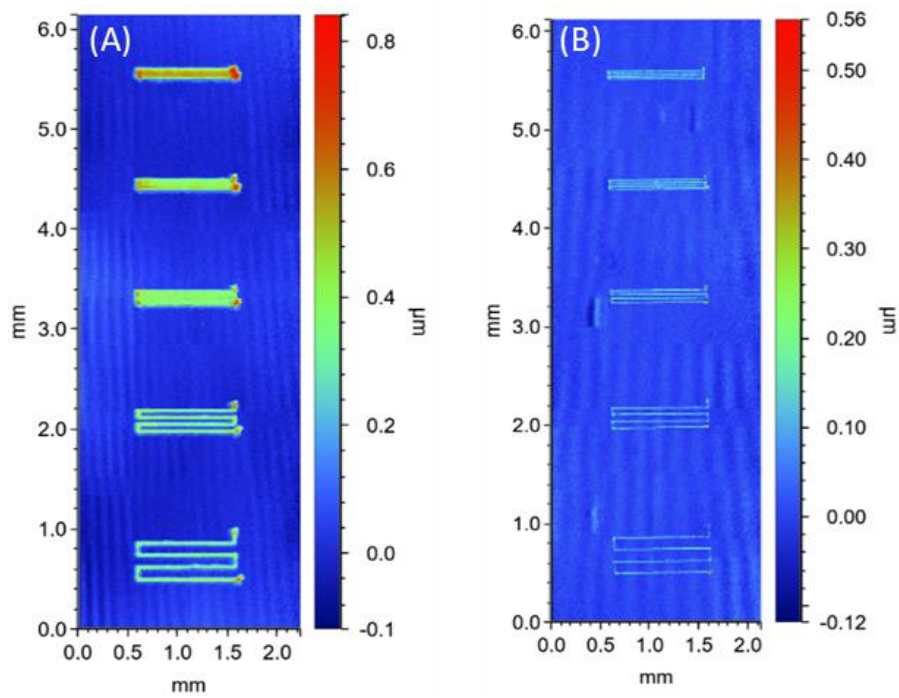


Figure 6.39: (A) 40µm line pitch experiment (B) 20µm line pitch experiment

Closer analysis (Figure 6.40) showed that 40µm lines are resolved when the pitch is over 120µm (three times the line width). When the pitch is reduced to 70µm the lines are still resolvable. When the pitch is reduced to under 60µm the features breakdown and mould into one large feature.

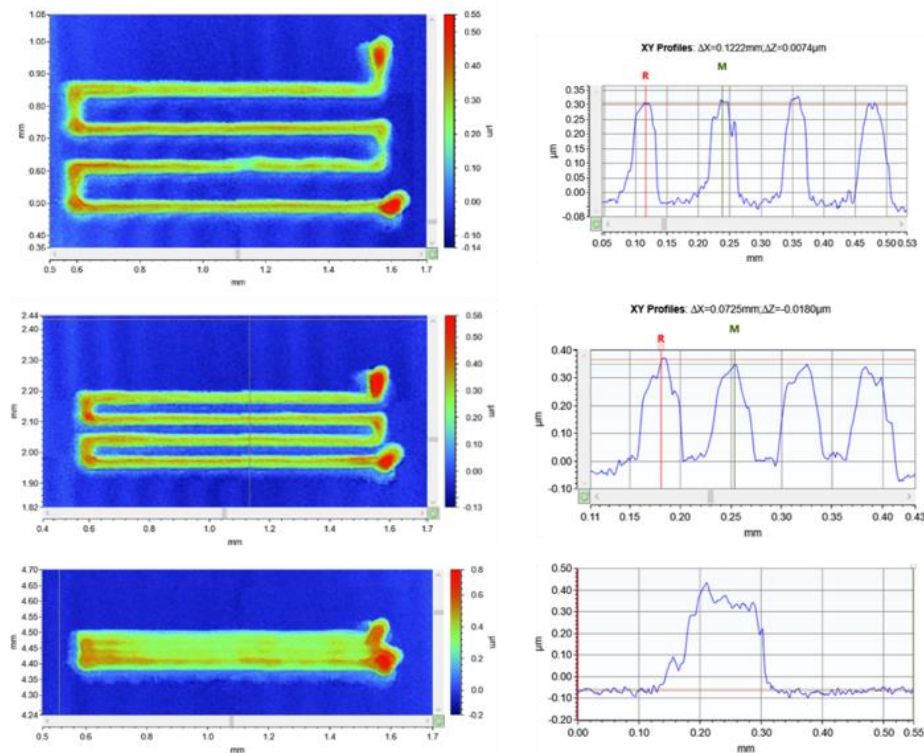


Figure 6.40: Selected points of the pitch experiment showing effect of decreasing pitch, printed with a 40 µm WHM line.

Figure 6.41 shows that 20 μm lines are resolvable above a 30 μm pitch, however when the pitch is reduced to below 30 μm the features begin to breakdown. The lines do not mould together quite as much as the 40 μm instance, but this is due to the overall reduced volume of material on the slide, making blending effect of pitch breakdown less extreme.

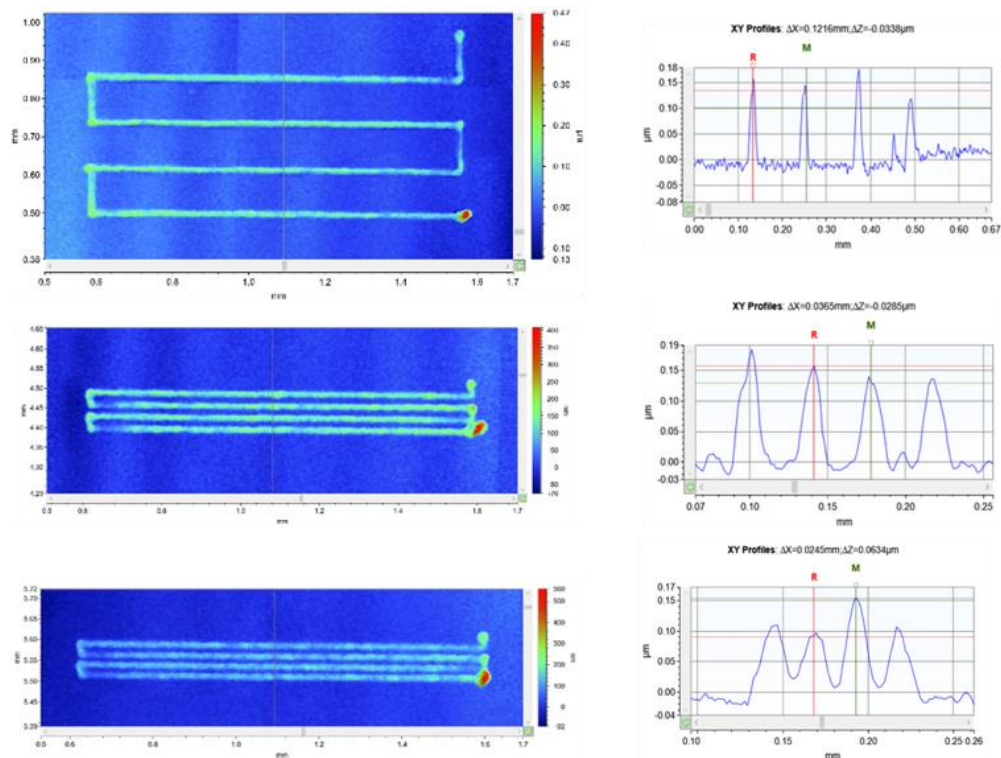


Figure 6.41: Selected points of the pitch experiment showing effect of decreasing pitch, printed with a 20 μm WHM line.

It was expected that HCT-116 cells would preferentially tether to regions of close pitch lines, due to the increased amount of biocompatible material in that specific region. Throughout repeated experiments there was no preference of the high line density regions over the single lines, and in most cases a reduced preference for the high-density region topography which it was thought would encourage cell adhesion, as seen earlier. However, as the cells grew to confluency they did grow to engulf the low pitch features, as shown in Figure 6.42.

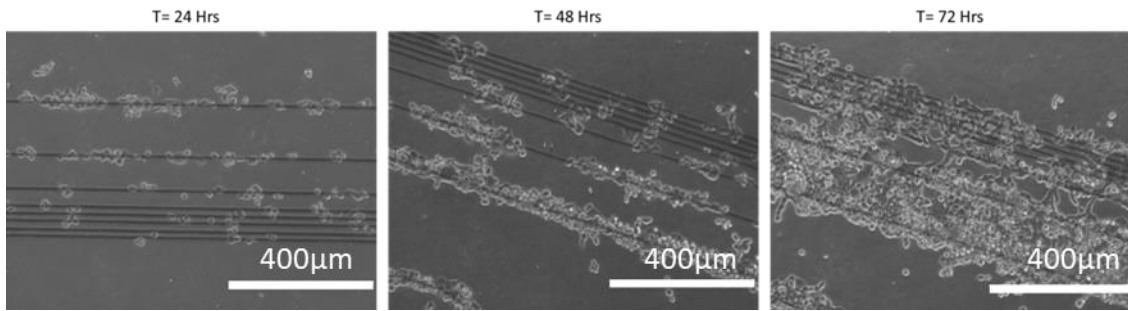


Figure 6.42 Typical response of HCT-116 cells to a pitch test over time.

6.2.6 Motility Testing

Based on the results present in Section 6.2.2 the effect of dot pitch on the ability for two groups of HCT-116 would merge into a single entity.

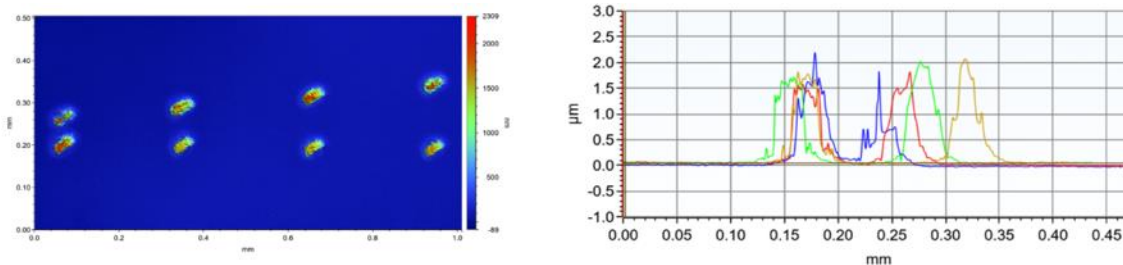


Figure 6.43: White light interferometry scan of cell motility test, and a profile showing the increasing pitch.

Figure 6.44 shows representative results obtained, which illustrate that after 48 hours there is a noticeable difference between the cultures on different dot pitches. Smaller pitch dots have merged into one large aggregate whereas those on larger pitches have not. In general, the aggregates on smaller pitched samples contain more cells. These results suggested that initially the cells multiply outward in a circular shape, however once they can communicate with the other cluster, the groups combine. This combination of the distinct aggregates results in an increased rate of growth, due to the accelerating nature of cell growth as the number of cells in proximity increases.

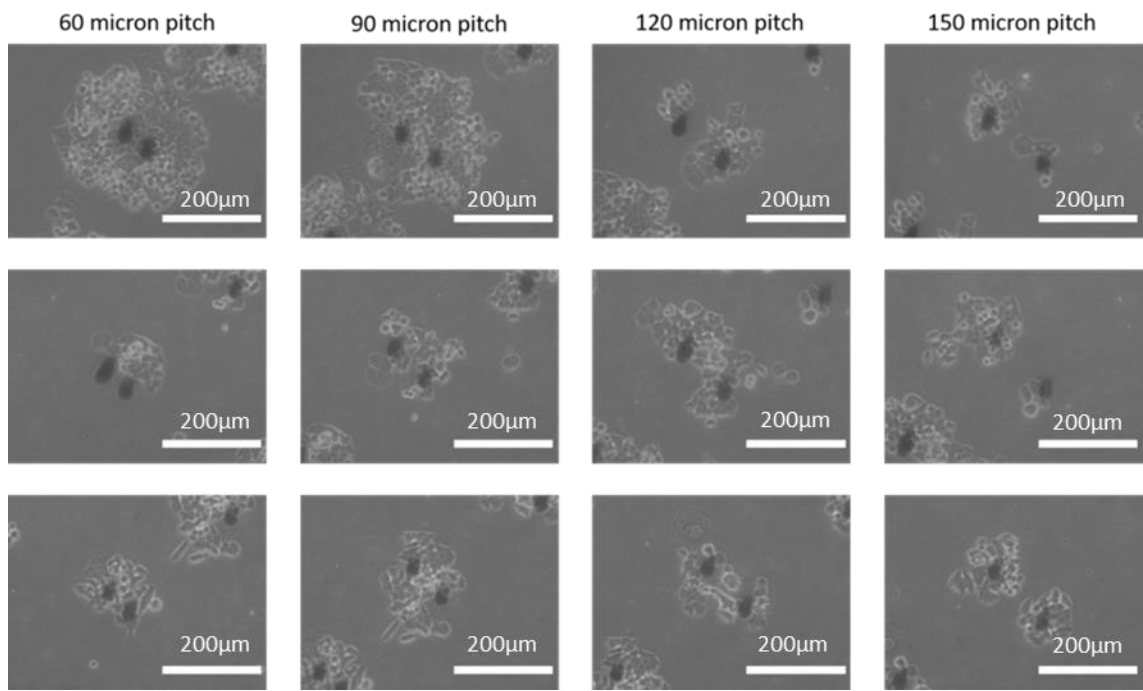


Figure 6.44: Representative results of motility testing with HCT-116 cells, all images after 48 hrs of growth.

IF imaging (Figure 6.45) can be used to distinguish the cultures. High magnification IF imaging confirms that there is no biological matter between the separated cultures.

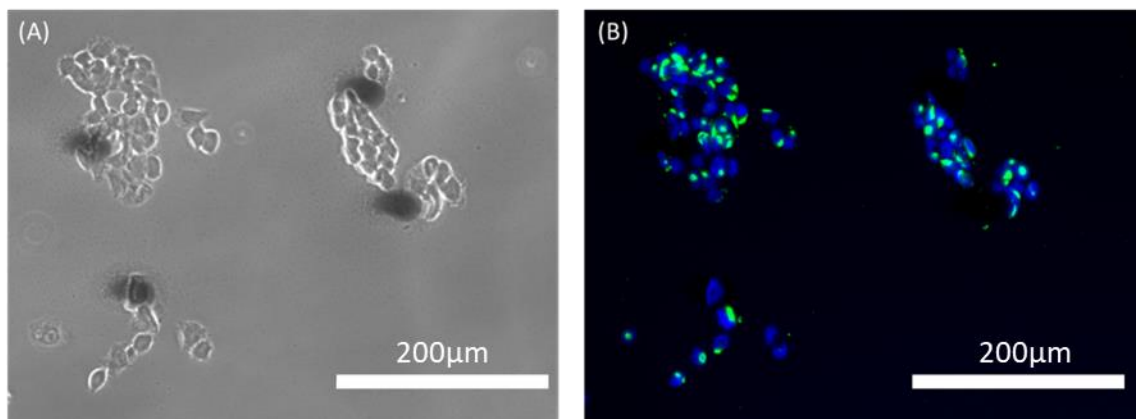


Figure 6.45: IF imaging of the motility test culture.

6.2.7 Summary of Capabilities for Engineered Cell Cultures

These experiments prove the ability to create an ordered cell culture from an initial chaotic environment. Specifically, they expanded the library of cell patterning shapes compared to the literature. These more complex shapes increase the range of scenarios that can be manufactured. Some boundary

conditions for the smallest features achievable by both the manufacturing process cell patterning step were reported. Importantly for this project, the manufacturing capability was not the limiting factor in terms of the cell patterning behaviour. The printer was able to produce smaller and more intricate patterns than those the cells would respond to. The recommendations for successful printing and cell patterning are found in Table 6.1: the pitch of lines should be no less than twice the line width; the diameter of a circle should be no less than 200 μm ; and any sharp corners should be an obtuse angle. The HCT-116 cells responded exactly to printed lines, sharp corners with angles greater than 90 degrees and circles with a diameter greater than 200 μm . Cells did not respond to a decreasing pitch of printed lines or angles smaller than 90 degrees.

Table 6.1: Engineering Capabilities and Biological Observations for Designable cell cultures

Feature	Minimum Engineering Capability	Biological Observations
Lines	None	Cells tether to lines and grow along them.
Dot Arrays	Pitch at least twice the width at half maximum	Cells tether to dots initially and grow into networks defined by them.
Sharp Corners	30° at 20 μm WHM lines	Cells respond exactly to angles larger than 90°. Angles below this cause bridging.
Circles and Arcs	100 μm radius, backlash affects circularity.	Cells will grow exactly to 100 μm diameter circles and arcs.
Line Pitch	Pitch at least twice the width at half maximum	Cells did not respond to series of lines with low pitch.

6.3 Polygons

Other direct write cell patterning techniques, such as ink jet, have been used to pattern the cell into some basic shapes such as squares and triangles [10]. These are more complicated than the single line shapes shown in the previous section. Using new programs with the same methodologies, the next series of experiments highlighted the cell response to simple shapes, which were an order of magnitude smaller than the literature precedent. The geometry was printed

highlights a range of crosses, circles, acute angles, right angles, and obtuse angles, by printing different polygons.

Figure 6.46 shows white light interferometry of these shapes, and pictures of HCT-116 cellular response after 48 hours. The responses after 24 hours are shown in Appendix J Each of the shapes has a material build up at the vertex where the shutter opens and closes. As seen previously, circular deposits have an even deposition of material throughout, sharp angled shapes and right angles have a build-up of material at the corners where the machine has to decelerate to produce the geometry.

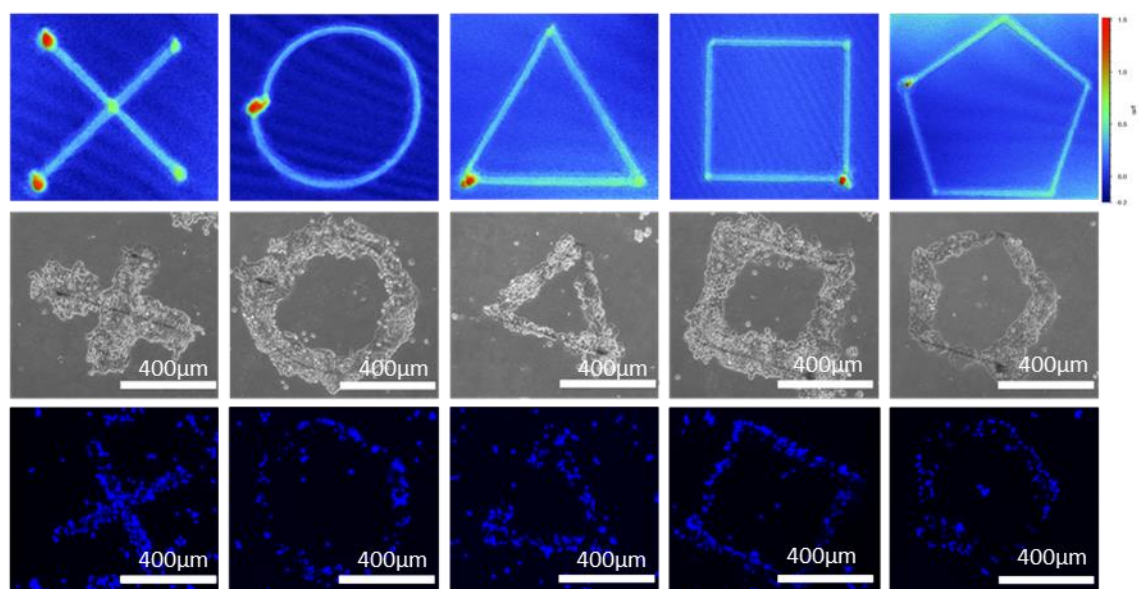


Figure 6.46: HCT-116 cells respond exactly to simple printed shapes under suitable cell seeding densities. 1st row, white light interferometry measurements. 2nd row, transmitted light of cells responding to shapes. 3rd row, DAPI staining of cell nuclei.

6.4 Trials with Further Cell Types

To expand the range of scenarios that can be modelled in the future, it is essential to prove the method is compatible with more than a single cell line. The complexity arises because each cell line has its own requirements and growth characteristics, cell morphology, and space requirements.

The nature of the work and the lack of precedent meant that there were many unknowns. The biological testing of the samples was a significant step requiring many hours of analysis and tuning. Each specific cell type has its own adhesion

characteristics, rate of mitosis and growth pattern, and each requires specific lab and growth conditions. In addition, the initial cell seeding density is of the utmost importance. Too many cells seeded on the substrate obscures the print, meaning that patterning is not seen, whereas too few may result in no growth at all. This is because individual cells rely on the secretion and communication of the other cells in culture.

A single test ran for 7 days, so many cell wells and several weeks were required to screen the results for suitable cell types and cell seeding densities. Due to the large body of work required for this, the printed patterns were refined to incorporate a range of tests onto a single substrate. This meant that a single cell well could be used to study a range of simple geometries, if the cell distribution over its surface was suitable. This test was scaled to fit into either a 12 well culture plate or a 48 well culture plate, depending on the requirement. These combined substrates enabled efficiencies in the number of experiments, cell seeding protocol, and observation of the cell cultures.

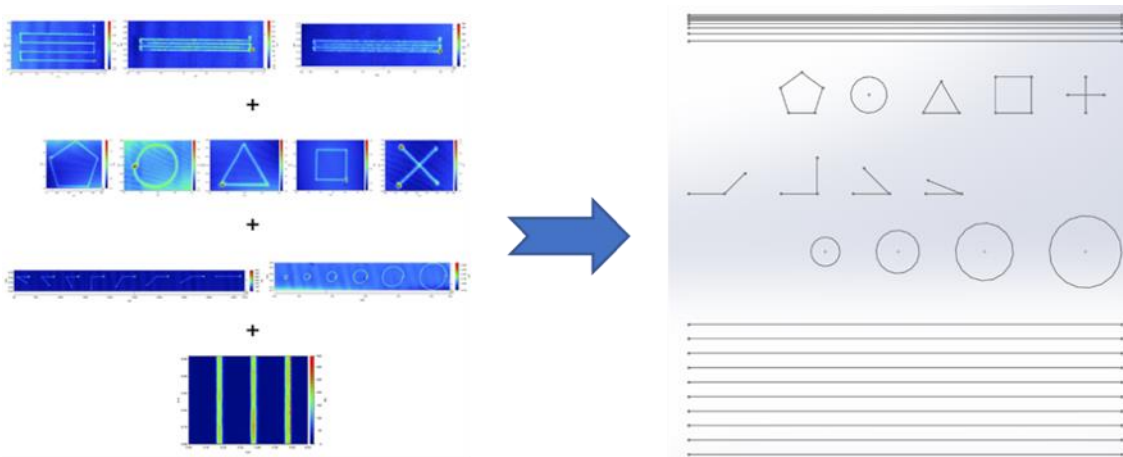


Figure 6.47: Combining tests made it viable to test new cell types in a much faster approach than previously possible

Two additional cell lines were available initially. HT-29 is a lower grade colorectal carcinoma cell line, and EA.hy 926 is a human endothelial cell line. To show the difference in normal growth characteristics the cells were cultured separately onto standard, nontreated cell culture plastic (polystyrene).

Where possible the biological testing conditions were maintained. For the initial tests the cell seeding density and volume of media were fixed, under the same culture conditions. The comparison between the cultures was made from images taken after the same culture time, though some cells took longer to multiply, requiring longer culture times overall. In addition, the EA.hy 926 cells require a different culture medium than HT-29 and HCT-116. These did not influence the engineering challenge. Figure 6.48 shows typical control samples of HCT-116, HT-29, and EA.hy 926 cells.

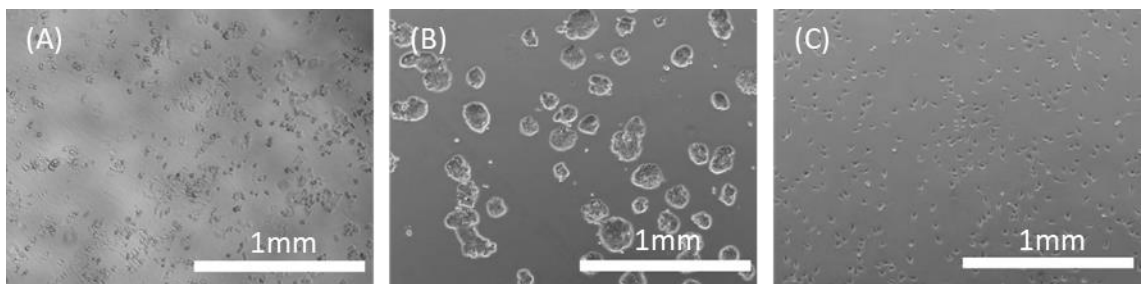


Figure 6.48: Different growth characteristics of (A) HCT-116 (B) HT-29 (C) EA.hy 926. All samples cultures on PS and imaged at 48 hrs.

During growth on non-treated culture plastic it was seen that the growth of all three cell lines was disorganised. The cells can be differentiated in their morphology and growth characteristics. HCT-116 cells grow to fill a given substrate within the two days. As growth continues they densify until they confluent on the substrate. HT-29 cells grow much more slowly and are not motile. They grow outwards from specific regions resulting in the clusters of cells observed in Figure 6.48B. EA.hy 926 cells also grow slowly but spread out to give each cell some space to grow. They tend not to densify over time. The growth of HT-29 cells over time is shown in Appendix J.

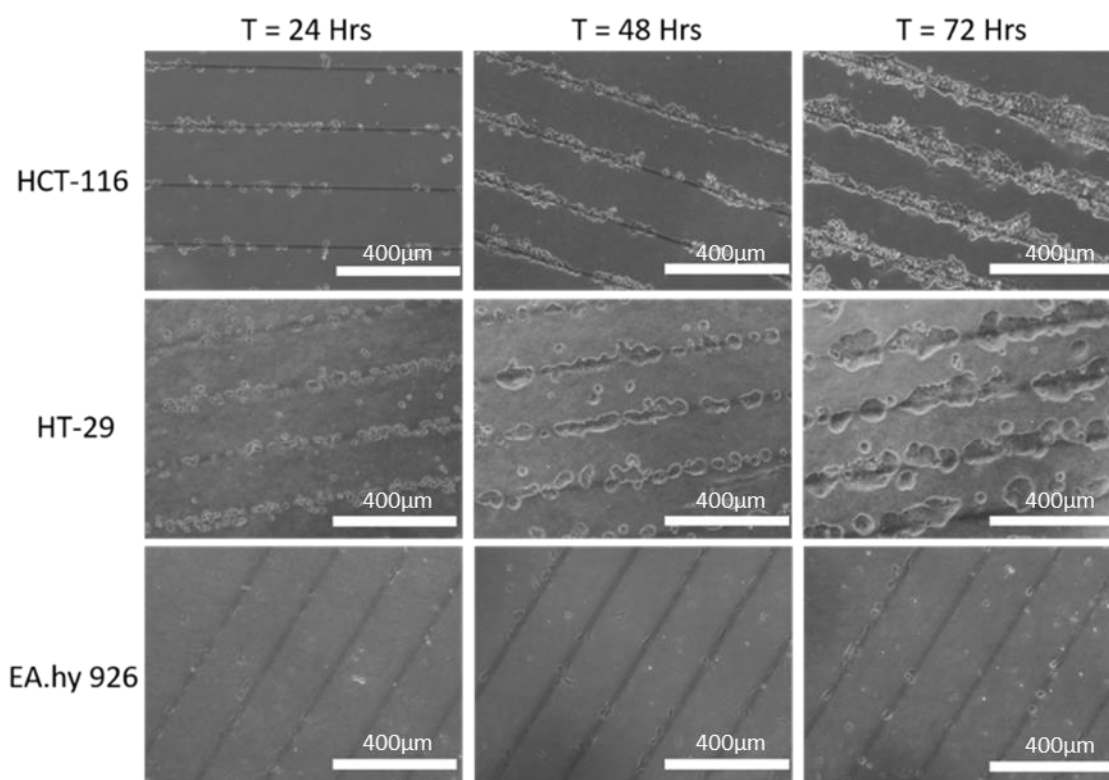


Figure 6.49: Comparison of the growth of HT-29 and HCT features on PEDOT:PSS printed lines at different time points.

The three cell lines all respond directly to the printed lines, resulting in directed growth along the line in all cases. However, the response of each cell line was different and can be attributed to their different growth characteristics. The most aggressive growing cell line of the three was HCT-116, which grew along the features. The cells in the EA.hy 926 cell line were the slowest to multiply, and so few were observed in Figure 6.49. Once cells have attached to the printed features the cells secrete growth factors and interact with other cells in the culture. There is a possibility that the slower growing cells have more time for these interactions to occur, so they are more able to grow outwards based on support from the rest of the culture. This means the patterning is less obvious.

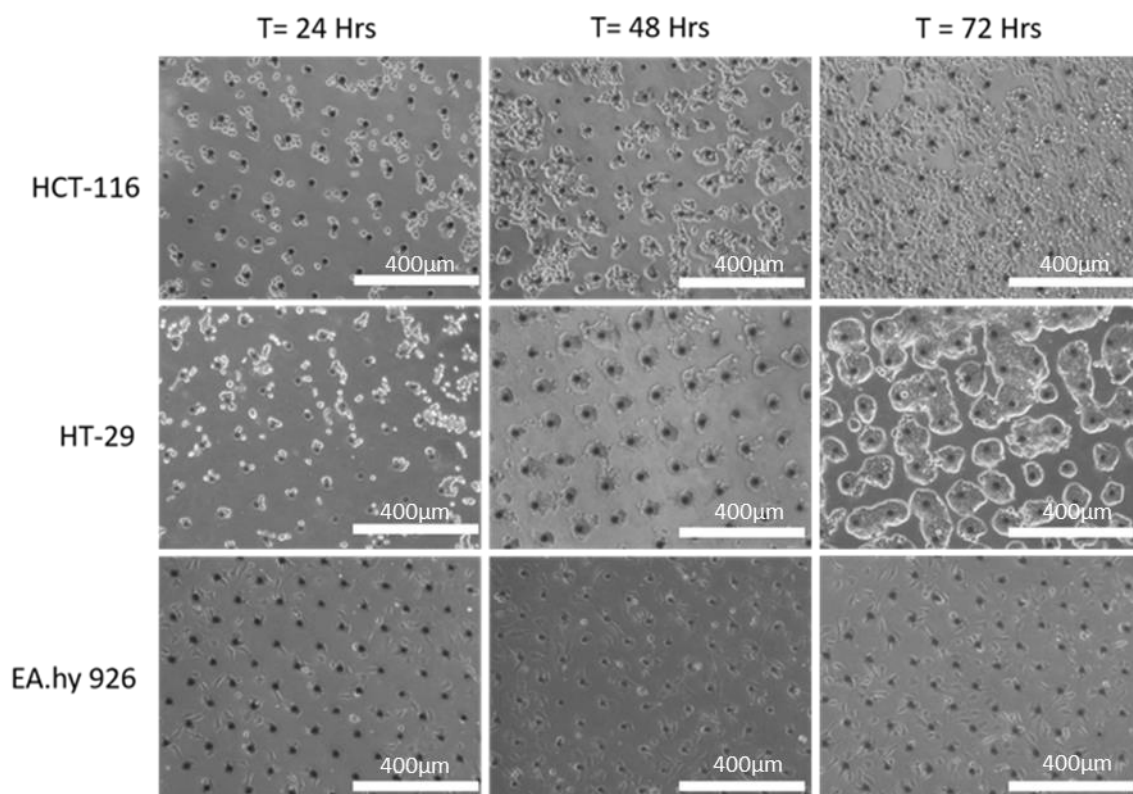


Figure 6.50: HCT-116, HT-29 and EA.hy 926 cell growth on 110µm pitch dot array over time.

Similarly, all three cell lines respond to the printed dot array. Over time the HCT-116 and EA.hy 926 cells stretch themselves outward to connect between two dots of material, creating networks of growth between the dots. The HCT-116 cells then densify to almost full confluency after 72 hours, whereas the EA.hy 926 cells maintain the network like growth pattern. HT-29 cells grow in clusters centred around each dot and grow outwards in a circular pattern, additional images, and the response of the HT-29 cells to a motility test are shown in Appendix J. Once two dots meet they merge into thick interconnecting regions of cells.

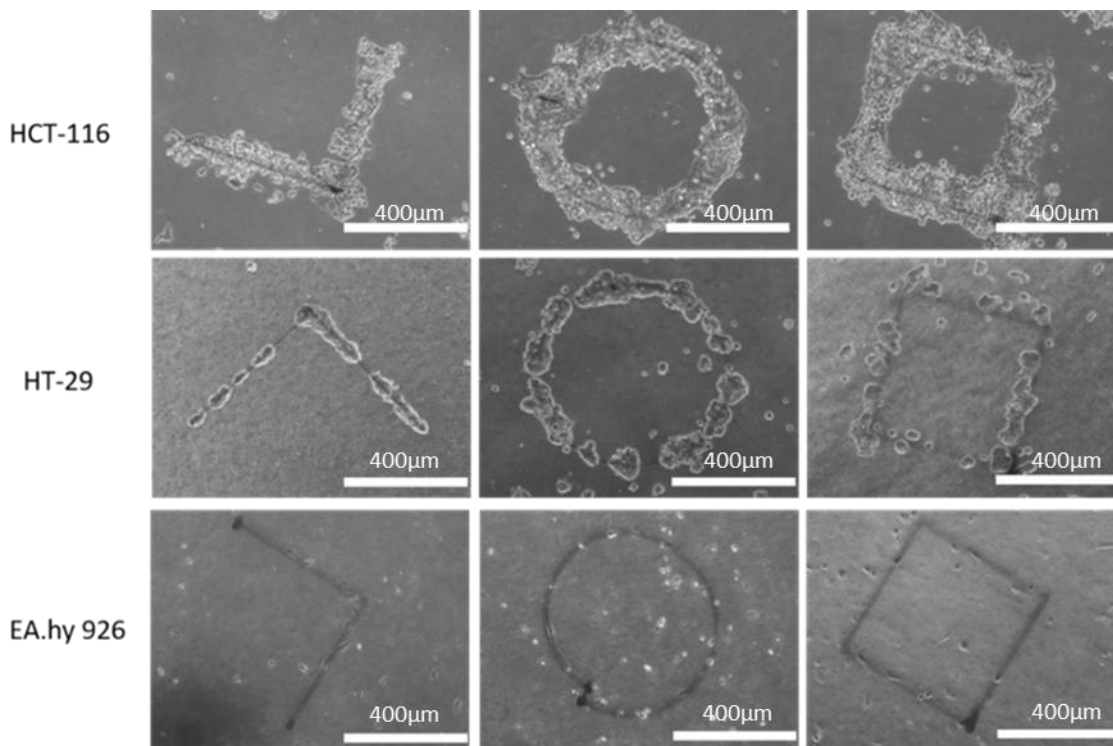


Figure 6.51: Comparison of HCT-116, HT-29 and EA.hy 926 response to printed shapes after 48 hours.

All three cell lines also responded to the printed shapes. The response of HCT-116 was the most pronounced, as visible patterning was seen after 48 hours. They also responded well to the printed features, and as seen in Appendix J and Figure 6.52, after 72 hours, confluency was achieved on some shapes.

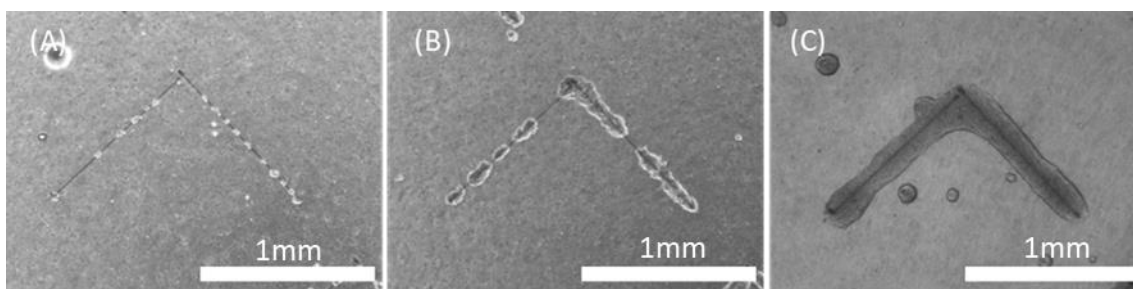


Figure 6.52: Sharp angle printed on PDMS. (A) After 24 hrs HT-29 Colonic rectal cancer cells tether only to the printed regions. (B) After 48 hrs the cells begin to divide and grow preferentially along the feature. (C) After 72 hrs the cells are confluent on the feature and grow outward forming a tumour.

EA.hy 926 cells proved the hardest to pattern, due to their slow division rate, and requirement of space for successful growth. Higher magnification images, such as in Figure 6.53 show some cells responding to curved regions of growth. It was theorised that the slower growing cell types had longer to excrete proteins which enabled cells to attach to the surface, making the patterning less successful.

However, these results are promising and show that the technique could be applied to multiply cell lines.

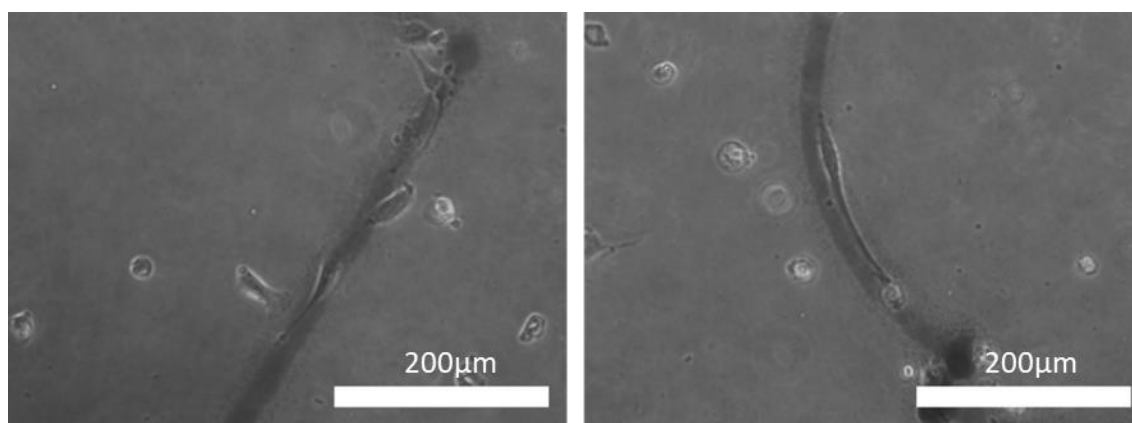


Figure 6.53: Some EA.hy 926 cells respond by elongating along lines and curves.

6.4.1 Collaborative Work

Substrates were sent out to collaborators at the University of Leeds Department of Biology for use as cell culture substrates. The cell lines were selected to showcase the reaction of a range of distinct cell morphologies. Six cell lines were tested, and in each case the growth conditions were varied to suit the specific requirements of the cell line, these conditions are shown in Appendix H. Early cell response is shown in Appendix H.

6.4.1.1 L929

L929 cells are mouse fibroblast cells. Fibroblasts are found in connective tissue and responsible for secreting extracellular matrix and collagen. After 2 days the L929 cells had moved to the printed features as seen in the previous work. Some cells were able to tether to the PDMS surface. After 4 days the cells had grown to the printed features, though there was also growth on some non-treated regions (Figure 6.54). After 7 days the cells were confluent on the surface, so the patterning effect had been lost on the standard microscopy images. The Live/Dead analysis highlighted some elements of patterning, especially when the circular shapes are analysed. The lower degree of patterning observed may be

due to the secretion of extracellular matrix by the fibroblasts. Once a single cell had tethered outside the printed regions, it could support the growth of other cells. The live dead analysis was performed after 7 days and confirmed low cell death (red) when compared to viable cells (green).

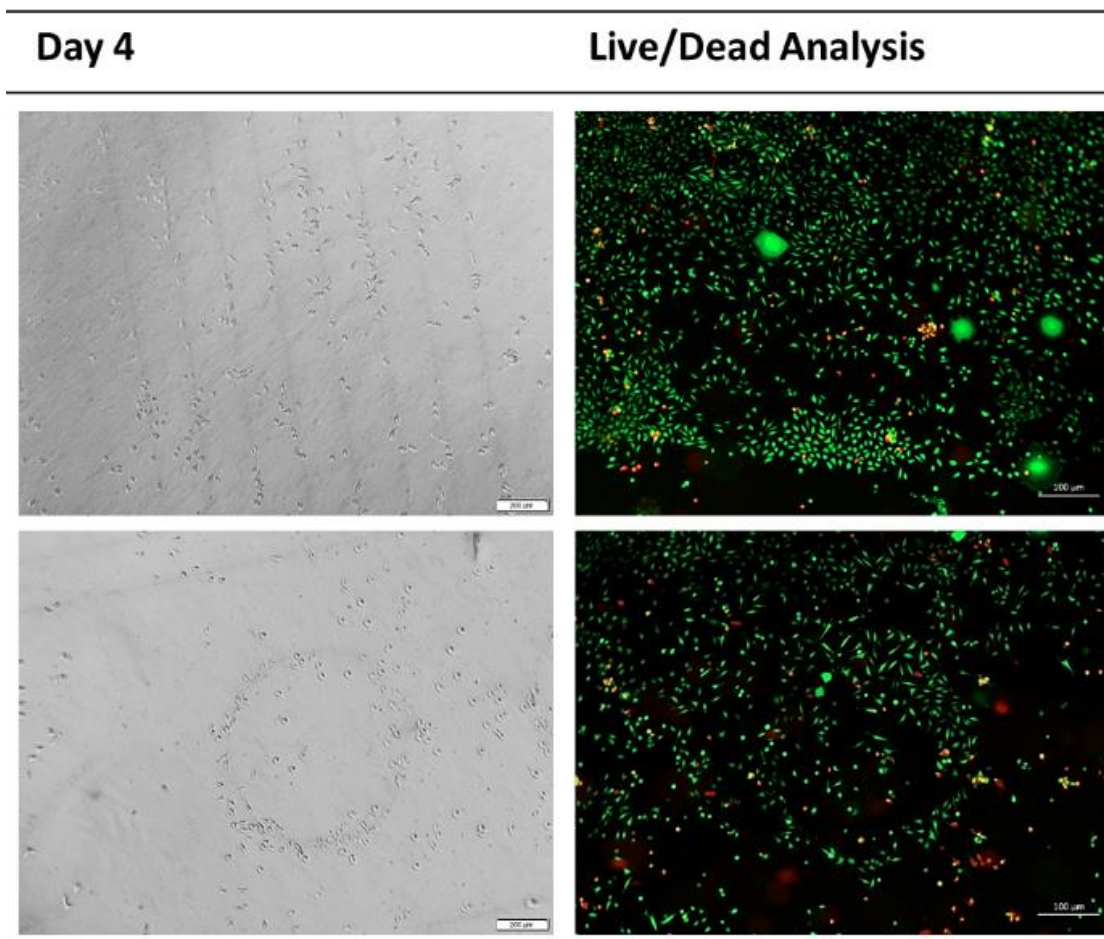


Figure 6.54: L929 cellular response to PEDOT:PSS printed features on PDMS. Day 4 and Live/Dead (Day 7).

6.4.1.2 BHK

BHK cells are a second fibroblast cell line, used in virology applications. BHK cells had tethered to the cell culture after 2 days. After 4 days the cells had multiplied and were patterned by the printed features (Figure 6.55). After 7 days, the cells were bridging between the lines, and the substrate was overgrown (results not shown). Regardless the Live/Dead analysis after 7 days illustrated high cell viability and a cellular response to the lines and circular features.

Day 4

Live/Dead Analysis

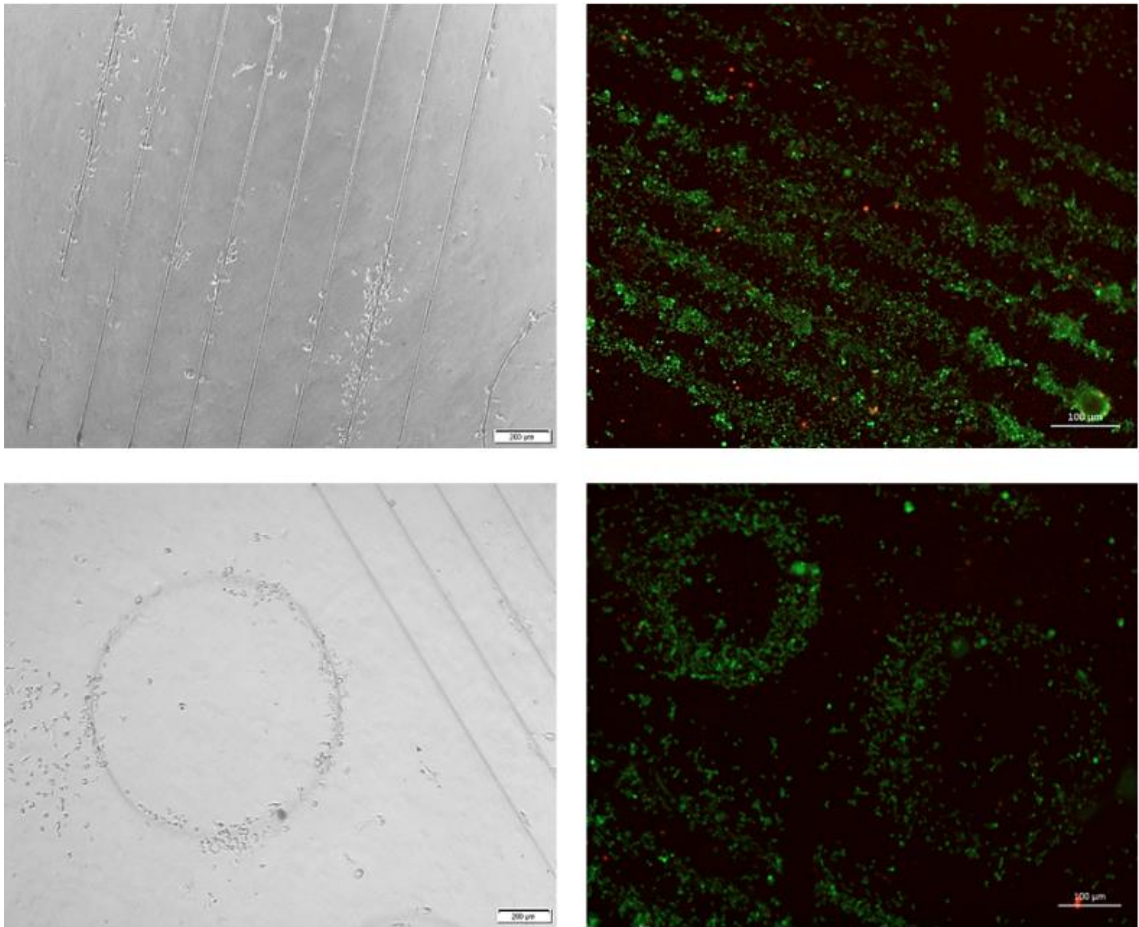


Figure 6.55: BHK cell line response to PEDOT:PSS printed features on PDMS. Days 4 and Live/Dead (Day 7).

6.4.1.3 C6

The C6 rat nerve cell is a neuronal morphology cell which has been used in cytotoxicity applications. On day 2, the cells had preferentially tethered to the PEDOT:PSS features. By day 4, the cells had growth down the features. The observations on day 7 are shown in Figure 6.56. The cells had grown along lines and had recreated some of the more complex shaping. There was also alignment observed on the cell projections that give neuronal cells their characteristic shape. The Live/Dead analysis highlighted these projections interacting between cells: the precursor to neuronal communication.

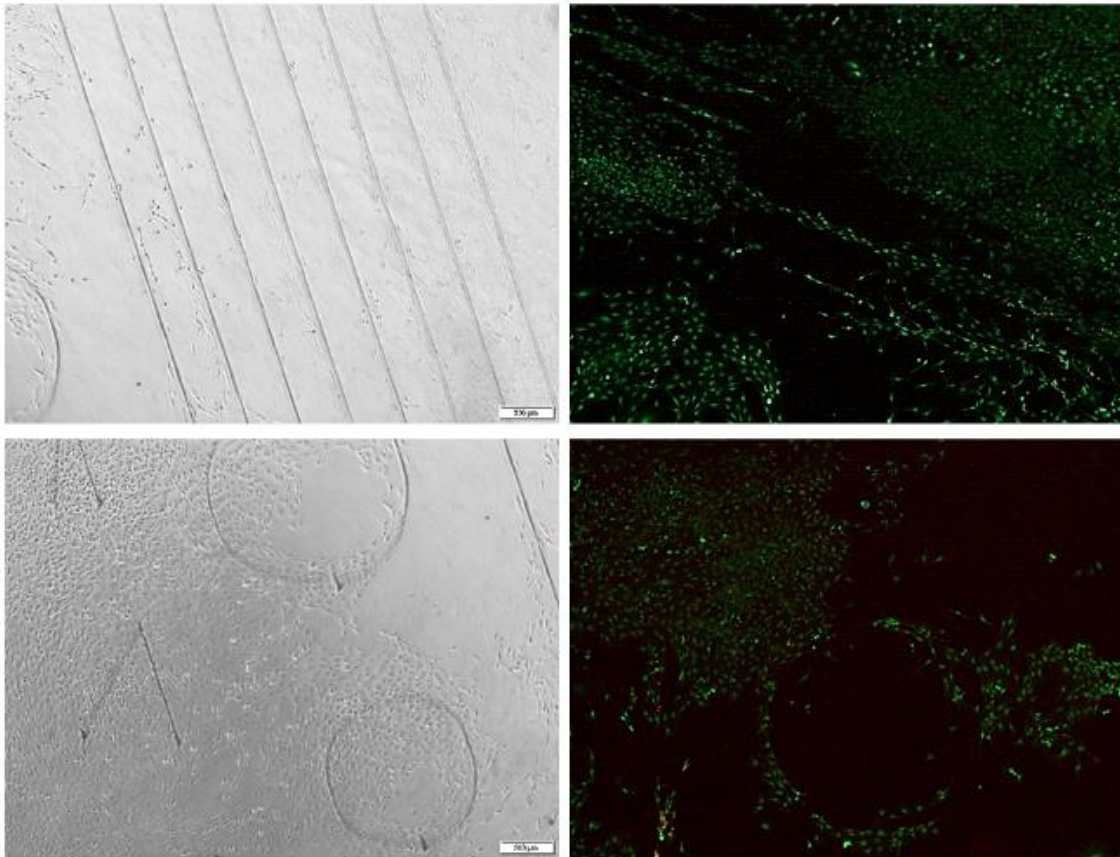


Figure 6.56: C6 cell line response to PEDOT:PSS printed features on PDMS. Day 7 and Live/Dead (Day 7).

6.4.1.4 pHDF

HDF cells are regularly used in injury recovery, connective tissue research, and wound healing experiments. Primary cells are taken directly from a donor and mimic the cells *in vivo* more closely than immortal cell lines. The pHDF cells initially tether to the PEDOT:PSS features, as observed on day 2. After 4 days there was limited multiplication of cells. Those cells that did split tethered to the PEDOT:PSS. After 7 days, the cells had multiplied and had conformed to the patterns. The cells had taken particularly well to the circle and triangle.

Day 7

Live/Dead Analysis

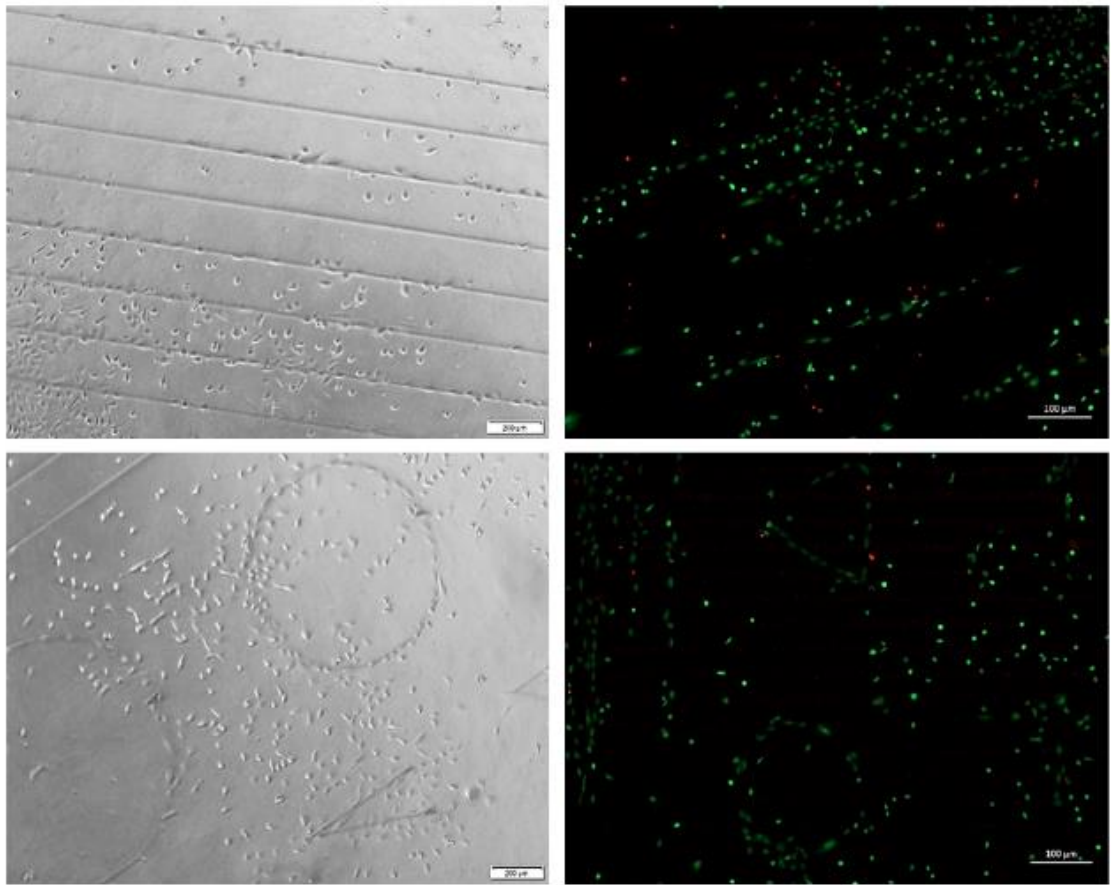


Figure 6.57: pHDF cell line response to PEDOT:PSS printed features on PDMS. Day 7 & Live/Dead.

6.4.1.5 RAW 264.7

RAW cells are murine macrophage-like cells used in metabolic studies and drugs testing. RAW cells initially tethered to the PEDOT:PSS features, but also to the underlying cell substrate. When the cells multiply they grow both along the features and outwards. The day 7 and Live/Dead analysis are shown in Figure 6.58.

Day 7

Live/Dead Analysis

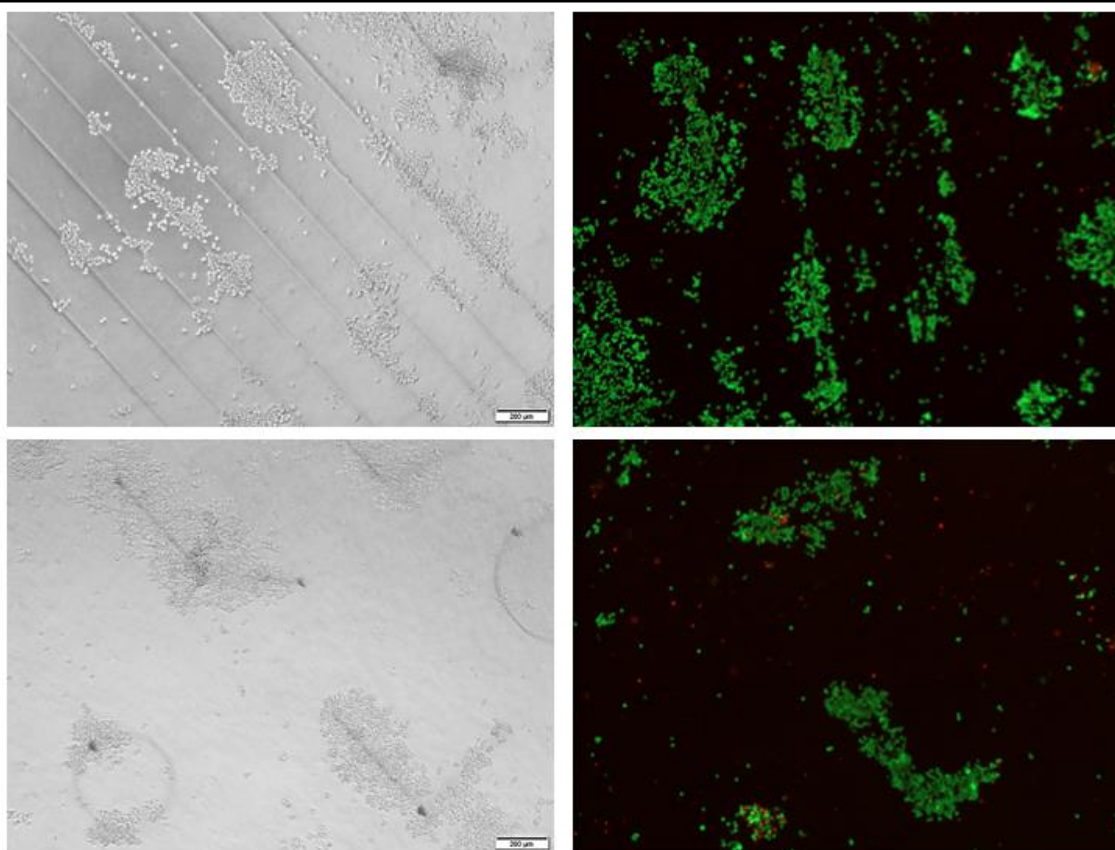


Figure 6.58: RAW cell line response to PEDOT:PSS printed features on PDMS. Day 7& Live/Dead.

6.4.1.6 PC12 cells

PC-12 cells are rat adrenal gland cells, which did not react to the PEDOT:PSS printed features. The cell line is known for being lightly adherent and preferring to grow in the cell media as a suspension, rather than onto the cell culture substrates.

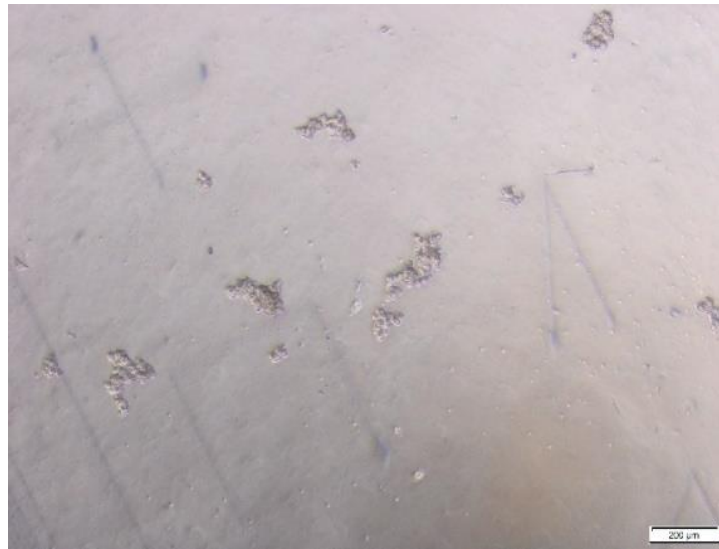


Figure 6.59: PC-12 non-adherent cell line is not patterned.

6.4.2 Summary of Experiments with Further Cell Types

A degree of cell patterning was observed on all adherent cell types that were tried in this experiment. Cells that grow in suspension are not patterned as they do not interact with the substrate surface in the same way. The manner of the interaction was dependent on the cell type, in the same way that all cultures differ between different cell types. It is clear from these results that each cell line requires analysis and background knowledge of its specific growth mannerisms to ensure that suitable cell culture environments can be produced. This highlights how the digital nature of the process increases the rapidity with which designs can be updated, and the ability to produce suitable environments for the cells to grow is a huge advantage for the biological community.

6.5 Complex Cell Culture Substrates

Further testing was performed using HCT-116 cells, to incorporate non-planar substrates, develop patterns with greater complexity, and treat larger areas than previous tests.

6.5.1 Non-planar Substrates

An initial feasibility trial into printing and cell patterning on non-planar substrates was carried out. The patterning of non-planar substrates is a significant advantage over other patterning techniques, particularly those reliant on templates or stamping. The process was carried out with the same methodology as printing on flat substrates, but with a curved substrate with a radius of 25mm. This gently curving surface was produced by casting into a cylindrical glass mould, and then printing only onto a small area at the top of the substrate, shown in red in Figure 6.60.

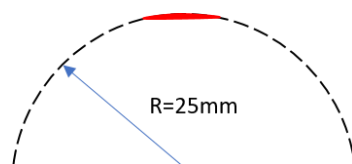


Figure 6.60: Representation of the curved substrate with the printing region highlighted in red.

The cellular response was similar to that of a flat substrate, and perhaps even more pronounced in some sections. It was theorised that this was due to the cells ‘falling’ from the curved substrate due to gravity, and therefore not having enough time to secrete the growth factors to tether to the PDMS surface. The only cells that could grow on the substrate were those that came into contact with the printed regions as they settled, and therefore tethered to that region.

The biggest challenge of this test was in the imaging of the samples. Moving to a non-flat substrate precluded the use of standard lab microscopes, so SEM images were used. These were able to image the cell growth. However, it was challenging to capture the perspective of the curved surface, due to the small scale of the cells. In addition, getting perspective with an SEM was challenging due to the micro-scale patterning on a macro scale curve. A sharp edge was cut into the PDMS on one sample, and the curve is shown in Figure 6.61.

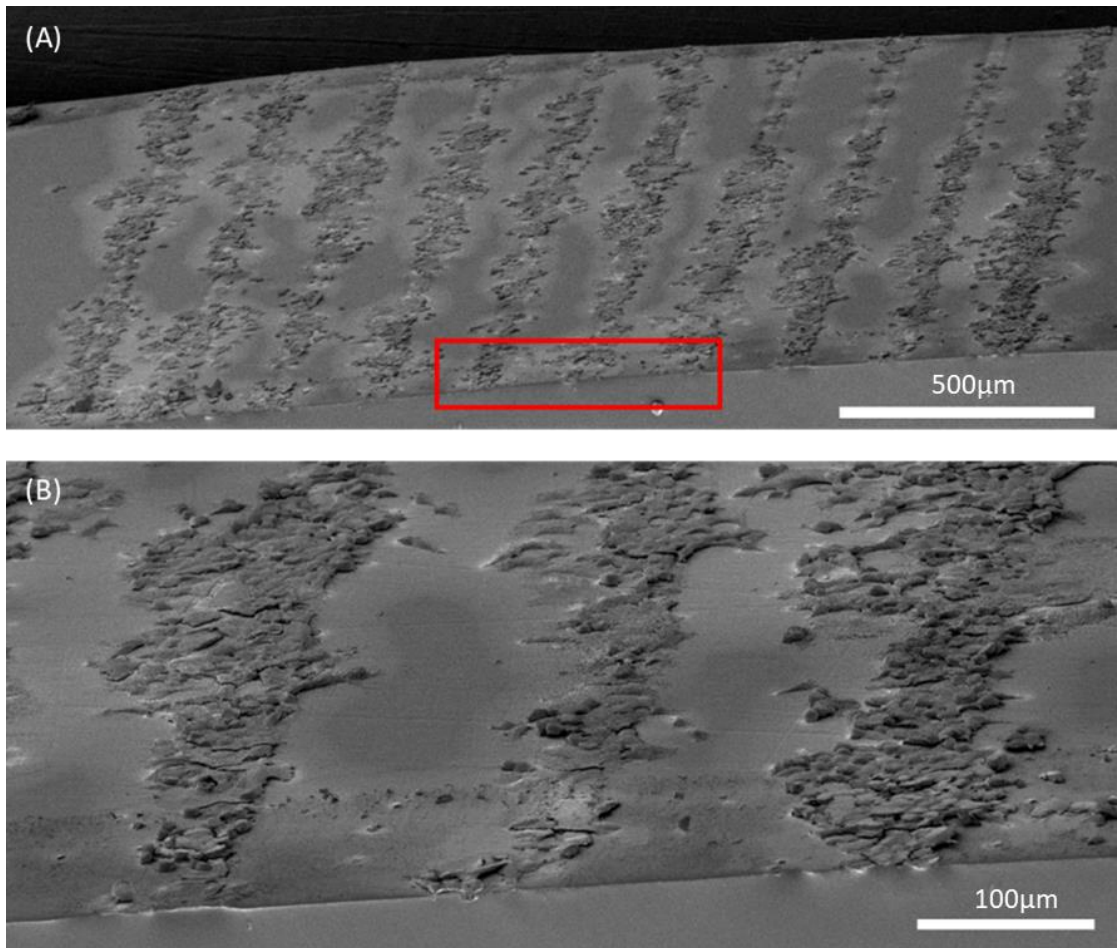


Figure 6.61: Cells patterned and printed onto a curved surface with perspective. (A) a low magnification image imparts perspective on the curved surface. (B) higher magnification shows the cells adhering only to the PEDOT:PSS features.

Cutting a sharp edge to highlight lines is possible, but it is hard to cut a sharp edge to highlight every feature shown previously. Without the ability to include a sharp edge, the curved substrate is hard to distinguish (Figure 6.62).

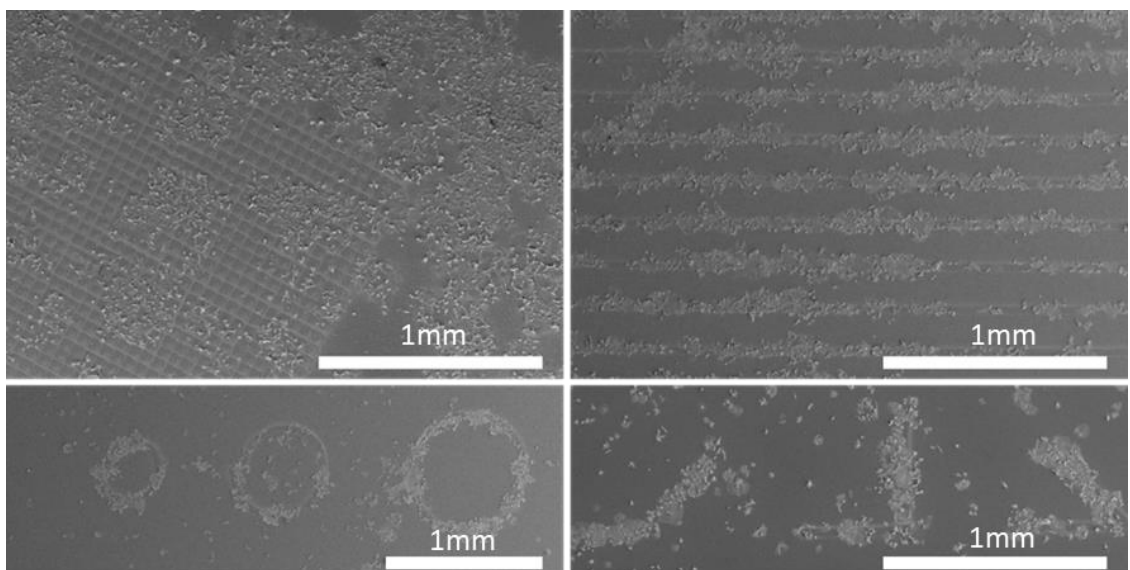


Figure 6.62: Cellular response to features printed onto a 25mm radius curved surface.

The challenge was increased further by incorporating a double curved surface. An 8mm radius hemisphere was also produced and patterned with lines. Figure 6.63 shows the contrast between regions that have been printed (top right) and non-printed regions. Cells grow well on the printed regions, whereas elsewhere the cells do not grow. Figure 6.63 also shows a high magnification image of the cell growth. The circular marks on the substrate are the machining marks in the mould, present even after polishing. This is due to the manufacturing method, an ideal mould would be glass based as in the first 3D mould used. Further SEM images of cells growing on a double curved surface are included in Appendix H.

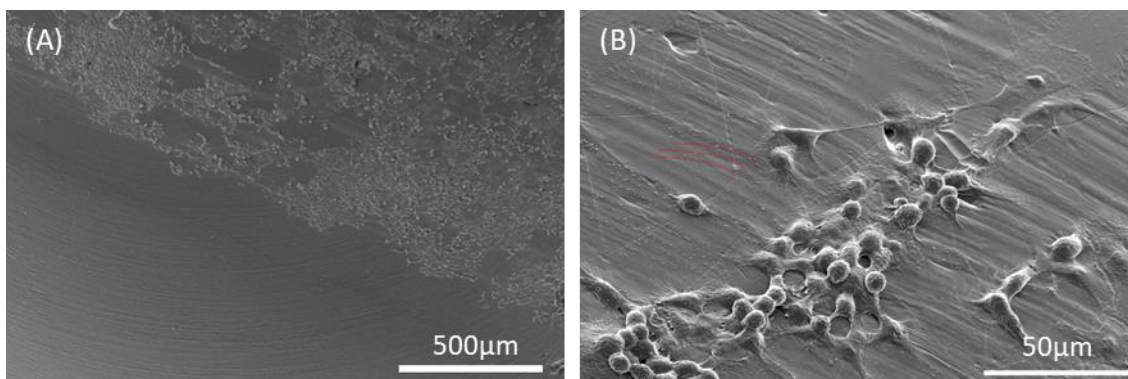


Figure 6.63: (a) Cell response to printed lines on a double curved surface. (b) magnified image of the cells on a line, curved surface highlighted in red.

6.5.2 Freeform Patterning

By increasing the length of the control code, more complex designs can be accurately produced, over a larger printed area. For large area or particularly complex shapes, these codes can be thousands of code lines. To reduce the time between conception to printing, a program to convert DXF design data to machine control code was used (detailed in Section 4.2.2). This enabled complex designs to be incorporated into processing within a few hours. In the past, small iterative changes in the design were prevented by the cost and lead time of template production. In this process, the machine control code can be altered to update the pattern and simple changes can be achieved in seconds. Even more complex changes or new designs can be output within a few hours. This flexibility also

promotes creativity in the biological designs, as the consequence of unsuccessful changes is easily undone or updated. These new capabilities were exploited in several new tests that would not have normally been attempted.

The freeform capability of the manufacturing process enabled meant that many complex and intricate shapes could be printed on a small scale. The freeform capability was showcased by printing the University of Leeds logo shown in Figure 6.64.

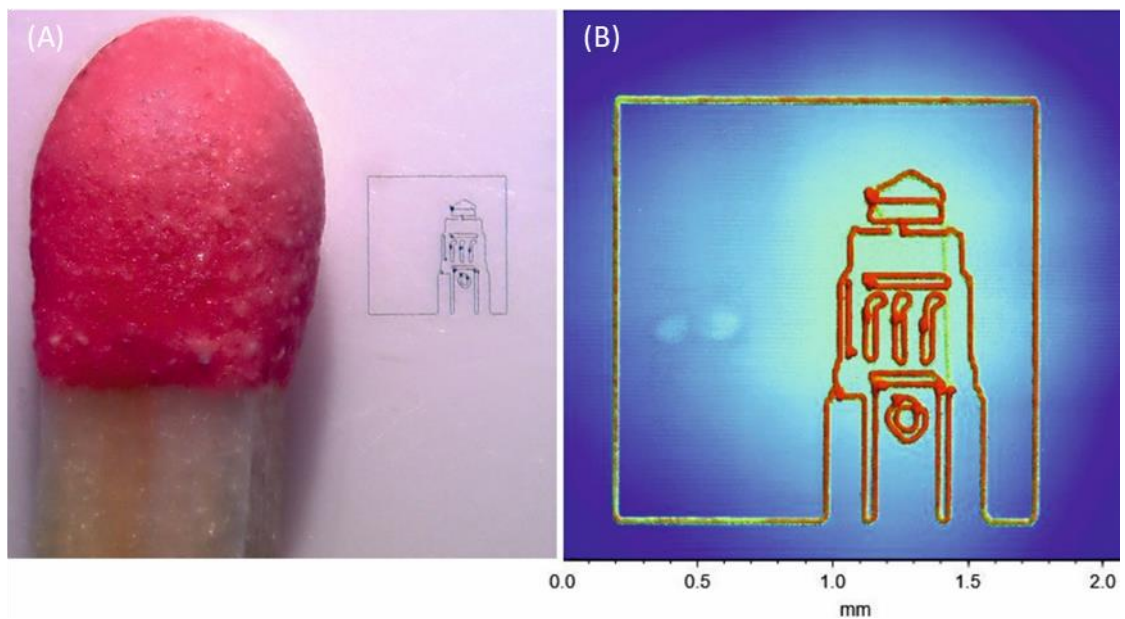


Figure 6.64: Printed University of Leeds logo demonstrating freeform capability. (A) Image next to a matchstick for scale. (B) White light interferometry data.

A branching structure was printed as a demonstration of a functional shape. EA.hy 926 cells grew to these complex features. These functional shape types may have applications in realistic *in vivo* models in the future.

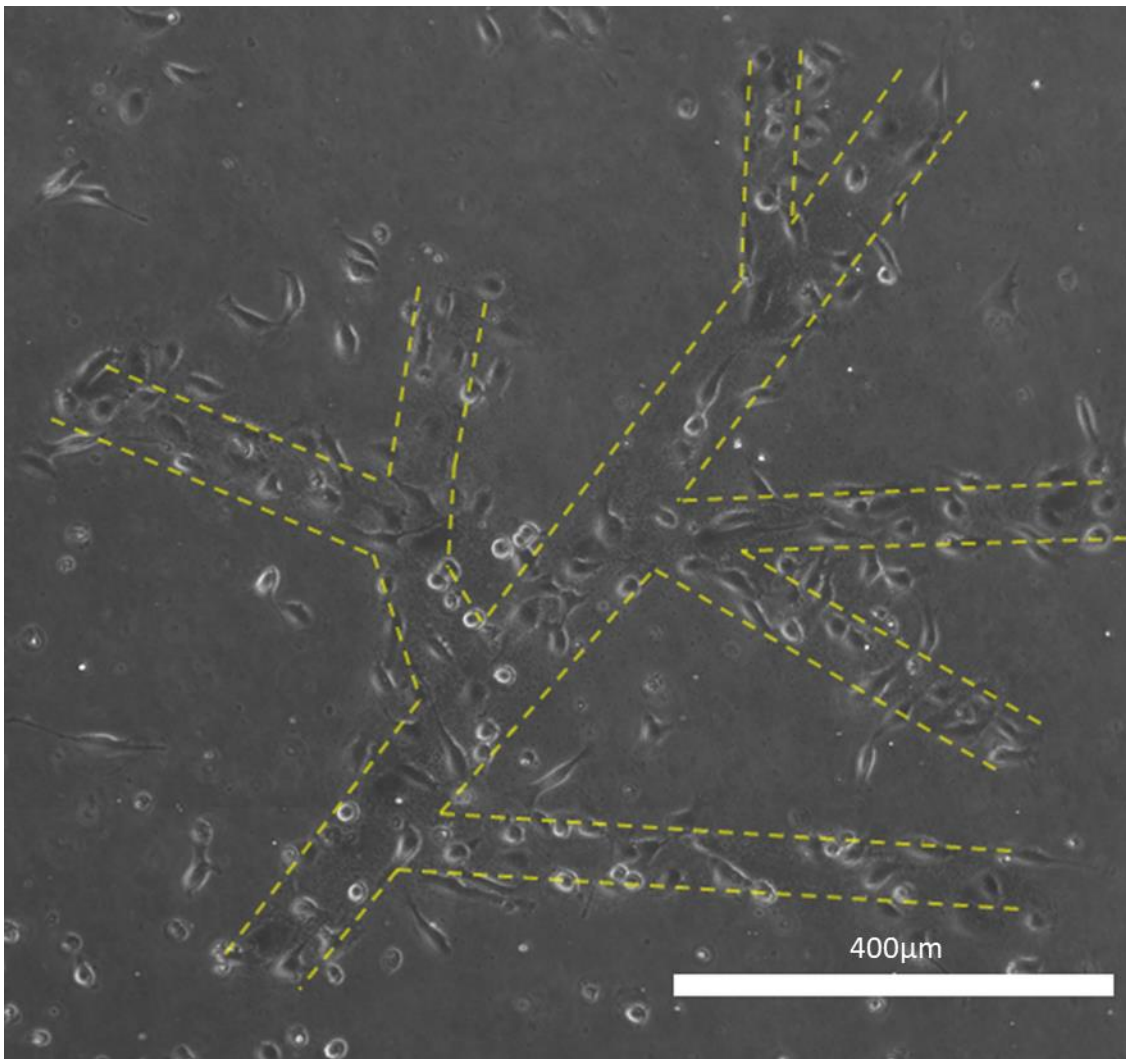


Figure 6.65: EA.hy 926 cells growing into a branching structure. Yellow lines outline the AJ printed feature.

In addition, this code can produce complex curves, due to its compatibility with polylines (These approximate complex curves with smaller lines). The patterns were printed over large areas greater than 1mm^2 . Due to the random nature of the initial cell distribution, complete control over this large area is not commonly observed. Due to the sheer number of interactions over this area some deviation is to be expected from these large area treatments.

The progression of growth is similar to the progression on smaller shapes. Initially a few cells are randomly distributed over the pattern. It was observed that in the regions around the printed features the density of cells was greatly reduced, suggesting that there was a preferential response to the treated features. Due to the size of these complex patterns, there were some cases where cells did attach

to the surrounding PDMS. The cause of these imperfections could have been either contamination from dust or other chemicals, or the secretion of extracellular matrix from the cells onto the surface of the PDMS. The large area and the high number of cells in that area means that it is likely that some imperfections exist. Those cells that do attach to the patterns multiply and grow into a culture whose shape is defined by those printed regions. Figure 6.66 shows the progression of growth on two large area complex patterns.

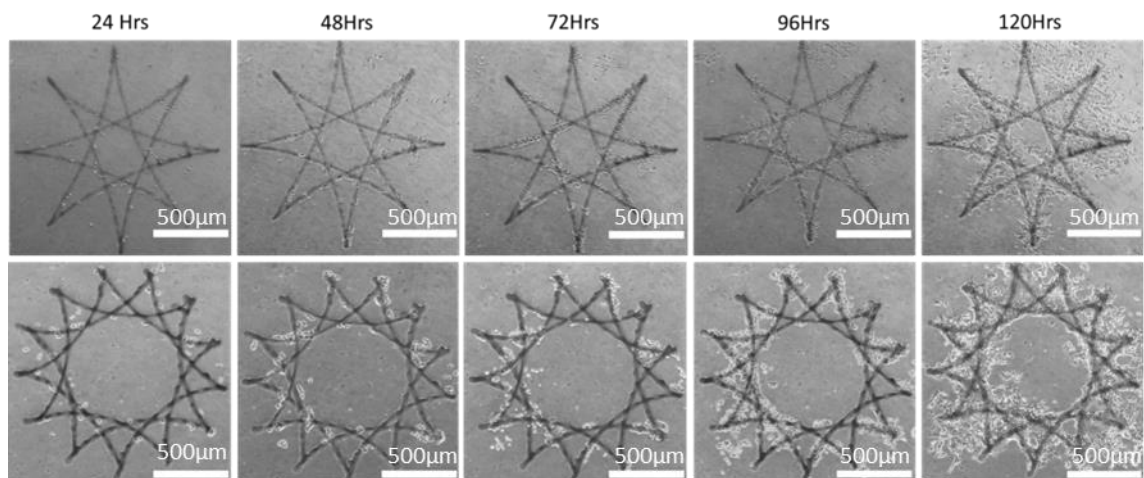


Figure 6.66: Complex 'star' designs and cellular response over time.

Controlling growth over this long time is harder than the 48 hour experiments typical of the simpler shapes. The rate of cell growth is not linear and once the cells attach they immediately begin to secrete growth factors and interact with other cells. In practical terms, this means that the more cells are in proximity to each other, the shorter the time between divisions, so the faster they grow. The growth factors and proteins secreted provide an environment for growth outside the printed regions. Therefore, as time progressed the cells were not always contained to the line. After 120 hours of growth this phenomenon is clearly seen in both the examples shown in Figure 6.66. In some cases, the space enclosed completely by printed regions were entirely covered in cells, meaning that the patterning was lost in some small internal features.

There is no need for these large-scale complex features to be made from confluent lines, as a patterning response can be achieved from a series of dots, as shown in Figure 6.67.

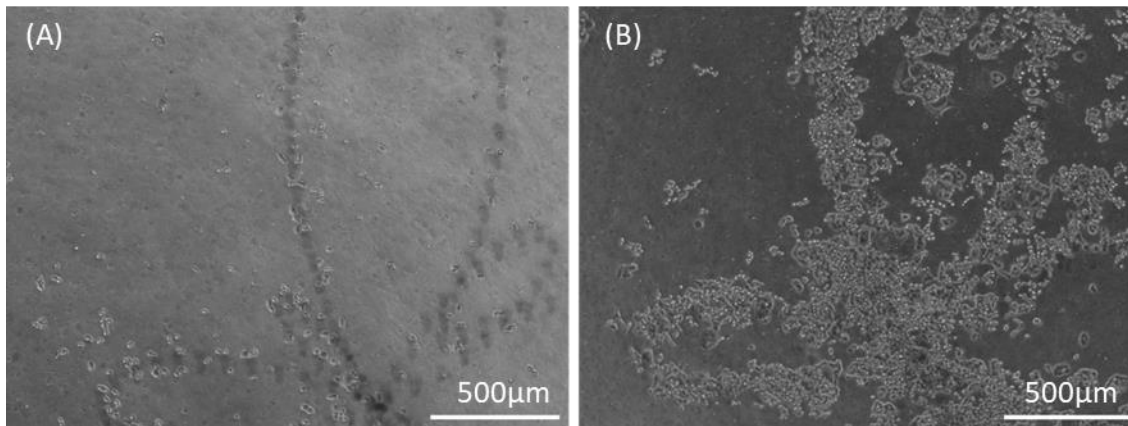


Figure 6.67: (A) Cells adhere to a complex pattern made of dots after 24 hours. (B) After 72 hours the cells have grown to mirror the printed line of dots.

Over such large tests the contrast perceived between the cells and the background is low, especially as the large area images are taken on low magnification or by stitching high magnification images. Immunofluorescence imaging enables certain organelles to be stained and highlighted. So, the nucleus was stained to increase contrast and verify the cells had grown to the patterned shape. This staining procedure also verifies that the pattern is made from biological entities with a nucleus, in this case confirming that it is indeed the HCT-116 cells that have grown into this pattern. The protocols used for staining the organelles involve ‘fixing’ the cells in paraformaldehyde, a process which kills the cells, meaning that these kinds of image are only available at the end of testing. Figure 6.68 shows the result of a transmitted microscope image, nucleus staining, and cell body staining.

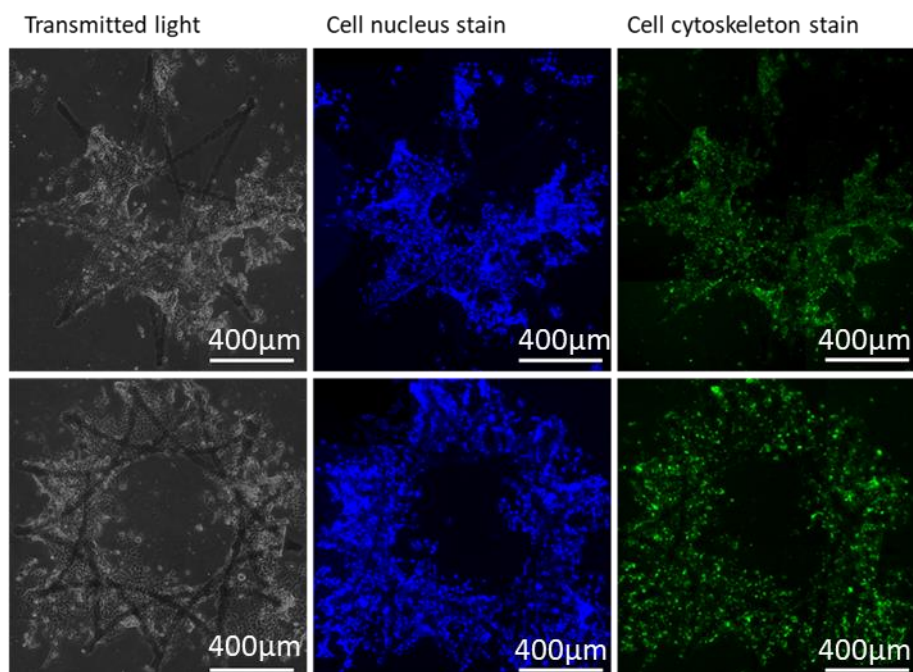


Figure 6.68: Large area images of stained cell cultures.

The visualisation of cells over a large area was made possible by manually stitching together several frames, taken at 10 times magnification, into one image. Whilst labour intensive, these large area images enable the observation over that entire large area. From observing these images, it was observed that the cells have grown into well defined patterns in some areas. The regions without cell growth are due to the distribution of cells at the beginning of the experiment, or in rare cases weakly tethered cells were washed off during the staining procedure. The PEDOT:PSS deposit itself blocked some of the fluorescent light, explaining the apparent lack of cells on top of the prints themselves (as in the black star drawn in the IF images). By analysing the transmitted light photos it is clear however that there are cell bodies on the line.

At 10 times magnifications the fluorescence of the cell cytoskeleton is much lower than the nucleus. Therefore, the images are dominated by the nucleus image as seen in Figure 6.69.

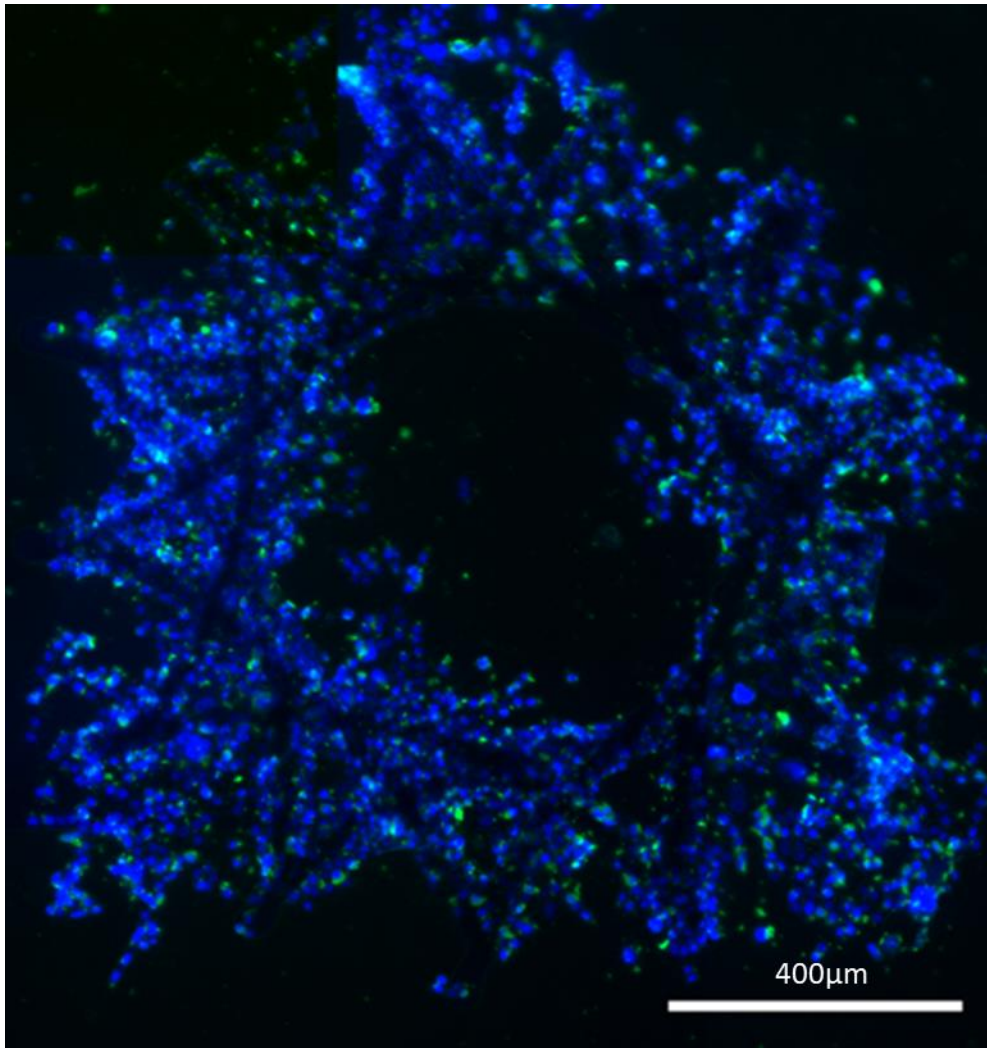


Figure 6.69: Large area merged image of cell nucleus and cell body staining.

It was possible to take images at 20 times magnification, and at these magnifications a high level of detail was discerned (Figure 6.70). However, the process to stitch images together was manual, so to take the images using 20 times magnification was an impractically long process. For this reason, when using IF imaging to highlight large area images, the cell nucleus staining image was predominantly used as it verifies the biological response, giving a high contrast image for analysis in the least time-intensive manner. Instead, the higher magnification images can be used to elucidate much more detail of specific regions of large area tests identified at lower magnifications, or, by reducing the size of the features, entire tests can be designed to fit in one frame.

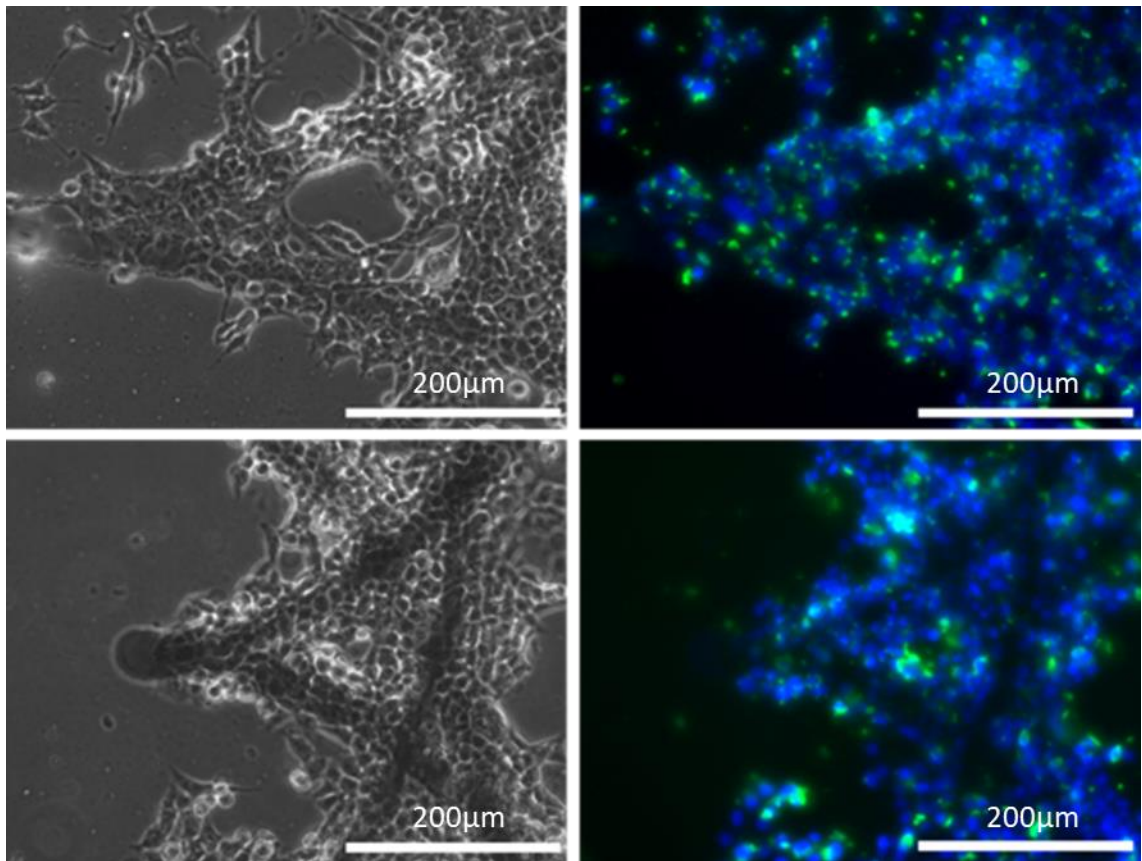


Figure 6.70: Higher magnification image showing the cell density of two vertices of the star.

A '2018' design was chosen to highlight the ability to pattern lines, curves, intersections, corners, and circles.

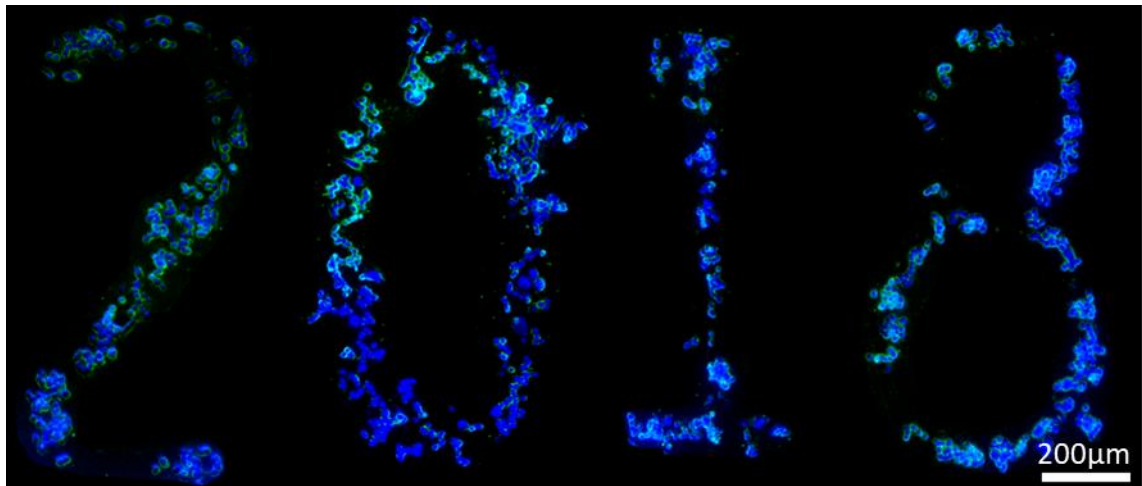


Figure 6.71: Immunofluorescence image of HCT-116 cells. Blue = cell nucleus, green = cell cytoskeleton.

Figure 6.72 illustrates the largest area patterning that was achieved throughout the project. This highlights both the size and complexity of the high fidelity patterning enabled by this method.

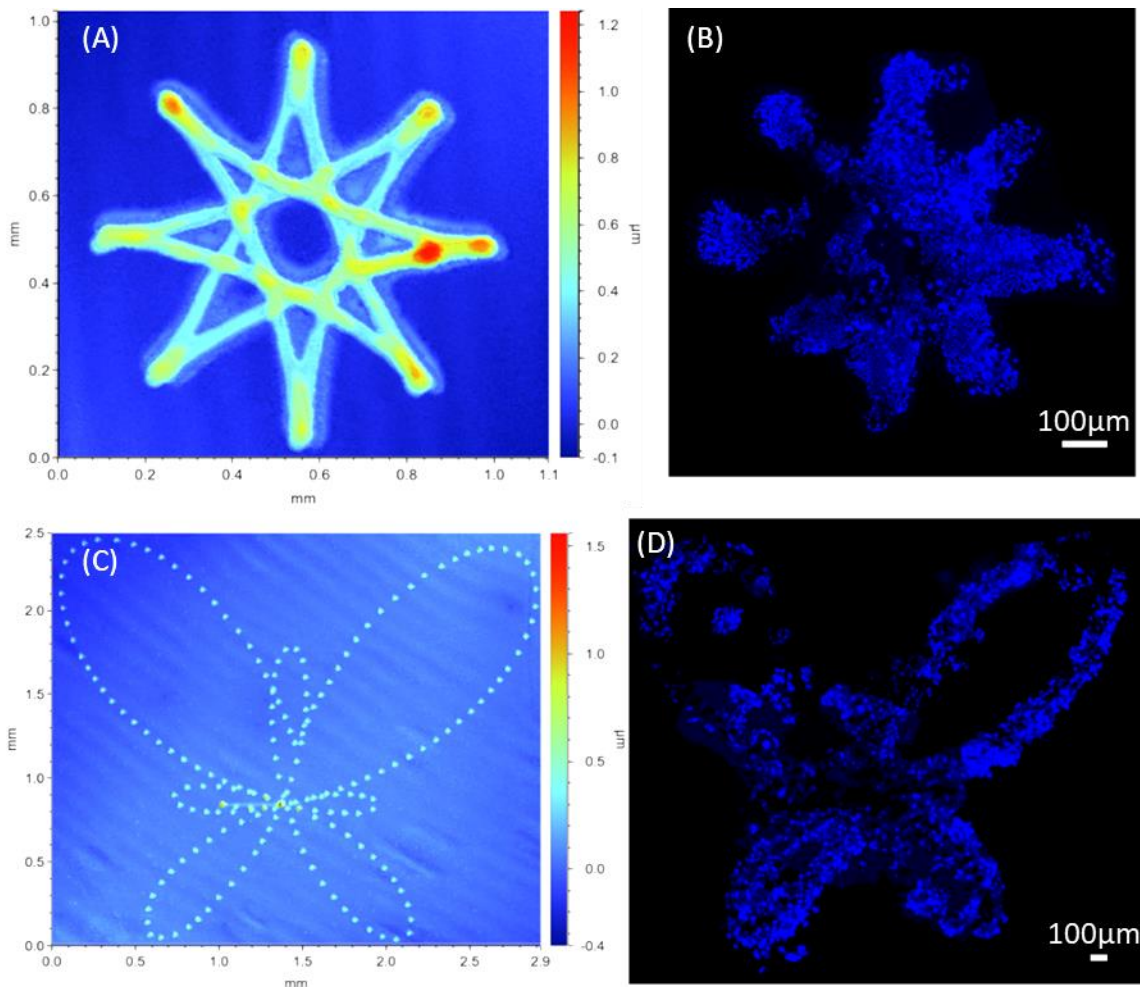


Figure 6.72: Large area control of cell growth. (A&C) White light interferometry image of complex patterns. (B&D) Image of cell nuclei to show cell response after 72 hours. Blue colour is DAPI stain of nucleus, Scale = 100 μ m.

6.6 Chapter Summary

In this chapter the reliable production of PEDOT:PSS treated substrate was exploited to produce novel and complex cell culture substrates. These surface-treated cell culture substrates were proved to be biocompatible and non-toxic to cell cultures. Importantly, when HCT-116 colorectal carcinoma cells were seeded onto the substrates, those that tethered to the PEDOT:PSS features multiplied and grew into shapes defined by those treated regions. Those that landed onto the PDMS substrate did not tether or had their growth retarded by the inability to attach to the surface. The cells were subject to the cell interactions and secretion of proteins, which make it possible to grow over the PDMS surface if given enough time.

The testing of production capabilities in terms of printing limitations and cellular response to challenging geometries was explored in detail, and engineering recommendations for designable cell culture can be provided. It is recommended that lines be printed at a pitch of no smaller than twice the line width, for the radius of printed circles and arcs to be above 100µm, and sharp corners to be obtuse if possible. However, angles as sharp as 30° can be used in this application. These recommendations were used to showcase a range of shapes and an exact cellular response from the HCT-116 cells.

The degree of complexity was taken further using the capabilities of the equation driven G-code generator to produce star shaped prints and the 'butterfly curve'. Cells were shown to respond almost exactly, even to these highly complex printed features, and nearly exact cell patterning was demonstrated over an area greater than 25mm², large in terms of cell culture environments.

The manufacturing process was altered to enable printing on non-planar surfaces. These were produced with the same fidelity as on planar surfaces, and a similar cell response was seen as in planar substrates. A functional test of motility was produced for collaborators in St. James' University Hospital, which led to the understanding of growth characteristics when two clusters of cells grow at different distances from each other.

Using the DXF to G-code converter the testing was refined for use with multiple cell lines, both in house and by sending substrates to collaborators. In total, a positive cell response was seen from 8 separate adherent cell lines.

Chapter 7 Conclusions

An automated AJP apparatus was created and successfully used to pattern substrates at the microscale. These substrates were subsequently shown to influence the spatiotemporal growth of cells in culture.

The technology has been shown to surpass the capabilities of other surface patterning processes in terms of the small scale, complexity, and flexibility of the printed patterns. This manufacturing process can therefore increase the complexity and functionality of cell culture substrates, improving their use as a model of *in vitro* conditions.

This thesis has presented a review of the technology and applications of AJP. The flexibility of AJP in terms of material and processing conditions enable flexibility of design at high resolution. The range of applications of were assessed and key information on material selection and processing conditions was extracted from the literature. In comparison to other DW methods used for biological patterning, such as ink jetting and material extrusion, AJP has several advantages such as:

- Large range of compatible viscosities
- Fine feature patterning that would be challenging for the other technologies
- Wider range of standoff distances

By establishing a digitally-driven and computer-controlled automation apparatus around AJP, a process was developed to manufacture cell culture substrates. A major contribution of the automation apparatus is that it enables higher orders of pattern complexity and flexibility than template based methods. The digital nature removes the bottleneck of tooling changes associated with template based methods. The practical implications of this are that the time taken to implement

new designs is a matter of minutes, compared to typically 1+ weeks for template based methods, and at a fraction of the costs.

The design, build and testing of the automation apparatus is outlined in detail. The stage was capable of minimum incremental movements of $<10\mu\text{m}$ and had a backlash of $25\mu\text{m}$ in the printing region. This high accuracy movement was necessary to produce the fine features associated with cell patterning.

In addition, the cleaning and sterilisation methodology to prepare the printed substrates for cell culture was developed during the testing phase. The stringent requirements of testing in a hospital research centre were met by developing a clean room standard regime (to remove greases, oils, and blemishes), supplemented with a 70:30 ethanol:DI water wash to swell and burst any organic contaminants. The specific biological protocols were developed during the testing phases, by adapting existing biological protocols to meet the new engineering requirements. Factors such as initial cell culture density, culture medium, and culture time were developed specifically for this project. Adapting the manufacturing of the substrates to fit new biological assays was routinely implemented to enable a range of relevant testing to be conducted.

The print material experiments and studies on print refinement and reliability were presented. Key interactions between the sheath and atomiser gas flowrates and the scanning speed of the substrate beneath the print head were statistically evaluated. At all focussing ratios, the material deposition rate was proportional to the total gas flow rate. The surface interactions of material and substrate affect the printed line geometry. The plasma treatment step to turn the PDMS surface hydrophilic is essential to the process. With regard to the process parameters, increasing the gas flow rate resulted in larger geometry. These manifested as either maximum height increase, or once a critical point is reached, an increase

in line width. The approach to specifying a line width should be to first set an appropriate atomiser gas to achieve a stable deposit, followed by tuning the focussing ratio. It was recommended that for successful printing, the pitch of lines be no less than twice the line width, the diameter of a circle should be no less than 200 μm , and any sharp corners should be an obtuse angle. Process parameters to reliably deposit several print geometries were defined. The smallest printed feature had a WHM of 20 μm , approaching the physical limit for the AJP focussing apparatus.

The production of the G-code was not trivial, especially for large complex shapes. Custom Python programs were developed so that even complex geometries, any shapes that can be represented in a DXF design file, or generated mathematically, could quickly be transferred onto the apparatus. Indeed, this process was so fast that it was possible to incorporate small changes to the control code, with none of the time or cost implications associated with template based processes.

The applicability of this manufacturing process to cell culture was demonstrated as treated surfaces were used as cell culture substrates. It was shown that when PDMS surfaces were treated with microscale PEDOT:PSS features, that HCT-116 cells exhibited a preferential tethering to the PEDOT:PSS over the underlying PDMS substrate. As the cells grow in culture, there is also a preferential growth along the printed features, compared to growth outward onto the underlying substrates. Essentially this process enables high fidelity control of the spatiotemporal cell response to a digital design. The key differential between this digitally driven process and previous template based processes is the flexibility enabled by the digitally driven nature. This flexibility was showcased by a range of designs such as the University of Leeds Logo, the star fractal shapes, the butterfly curve, and the 2018 design, which all exhibited intricate features as well

as line cross overs and sharp angles. This response was observed over culture areas as large as 2.5mm² in the case of the butterfly curve.

Subsequently, this technique was applied to eight distinct cell lines to show the applicability to a range of biological fields. The reliable and rapid turnaround of custom cell culture substrates, and variety of cell types influenced prove that this new manufacturing process is suited to the production of custom cell culture substrates.

As Figure 7.1 represents the overall manufacturing process. By building this machine and developing this process, new capabilities and avenues for biological research have been enabled. The method can be applied to create and refine cell culture substrates in the widest possible range of material and substrate combinations and shapes. The designs can be produced from digital data, which can be complex and is rapidly updatable.

It was concluded that the new capabilities enabled by this manufacturing technique had been showcased. This new manufacturing method has been proven across multiple cell lines and so will be relevant to many applications in the future.

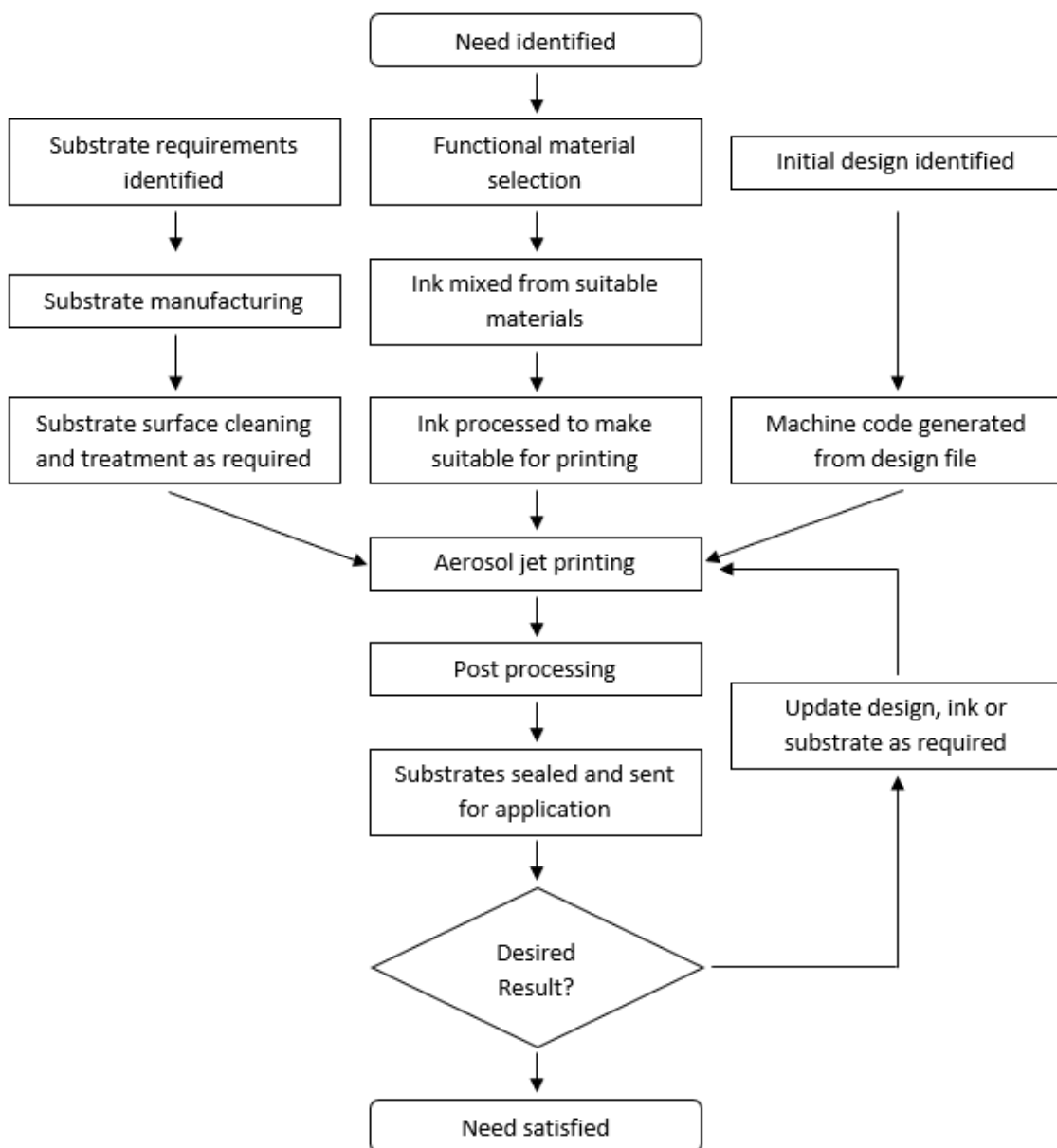


Figure 7.1: Final process overview

7.1 Future Work

This new manufacturing process chain has been demonstrated and proved to produce cell culture substrates that can influence cell growth. As with any new manufacturing process, the true potential lies in expanding the capabilities and applying the technique to new challenges.

7.1.1 Material development

The most straightforward approach to developing the process is to increase the range of functional materials and substrate choices. The methods supplied in this

thesis show a practical route to defining these new materials and substrates. By applying new combinations of treatments and substrates new avenues of research may be opened. For example, if a non-adherent functional material such as PTFE, patterned on a cell adherent glass will enable negative patterning of cells. Depositing drugs or other bio-active materials may also enable new routes of study but present their own challenges such as specifying dissolution rates in the cell media.

7.1.2 Machine development

In terms of machine development, increasing the number of automated axes from three to five (by adding two automated rotational axes), will enable the incorporation of truly three-dimensional substrates. The capabilities of the apparatus combined with this stage set ups will enable cell culture substrates, which could not be replicated by any other current manufacturing process. Even other direct write technologies are limited by their tight processing requirements. The use of specific componentry and tight environmental control (particularly temperature) will enable much smaller minimum incremental movements and smaller backlashes, with the associated improvements in patterning accuracy and fidelity to the original design. In preliminary work two-dimensionally patterned substrates, produced by casting from photolithography masks, have been aligned and printed into on the AJP apparatus.

7.1.3 Increasing throughput

The incorporation of several print heads onto the system will enable multi-material surface treatments and structures to be printed. In addition, there is no requirement that these have the same geometries or print characteristics which can enable new combinations to be printed. An example of this would be the concurrent printing of a structural functional inks. Further, by adopting new

focussing techniques, such as the CAB-DW technology or focussing through an Aerodynamic lens, the geometrical deposit size can be reduced.

7.1.4 Co-culturing onto substrate

The final recommendation is to apply the manufactured substrates to a biological co-culture incorporating multiple cell types into a single culture to make a more representative *in vivo* model. From the cell morphologies currently proved, some interesting combinations would be:

- Introducing fibroblasts to any of the other cell cultures
- Introducing endothelial cells to a carcinoma culture
- Introducing macrophage cells into a carcinoma culture

Although this study proves the concept of cell growth on the defined prints, proper biological analysis of these systems is required to identify the combinations to make valid models and may even consist of more than two cell lines.

Many of these avenues for research are directly attributable to the capabilities of the manufacturing process created during the course of this project. The vast range of modelling capabilities are enabled specifically by this apparatus and the associated processes. In the future, it is hoped that new applications and uses will emerge.

7.2 Pilot Studies

Pilot studies out of the scope of this thesis were undertaken.

7.2.1 Printing into channels

A PDMS substrate was cast onto a mould to produce a non-planar substrate containing channels, shown in **Error! Reference source not found.**

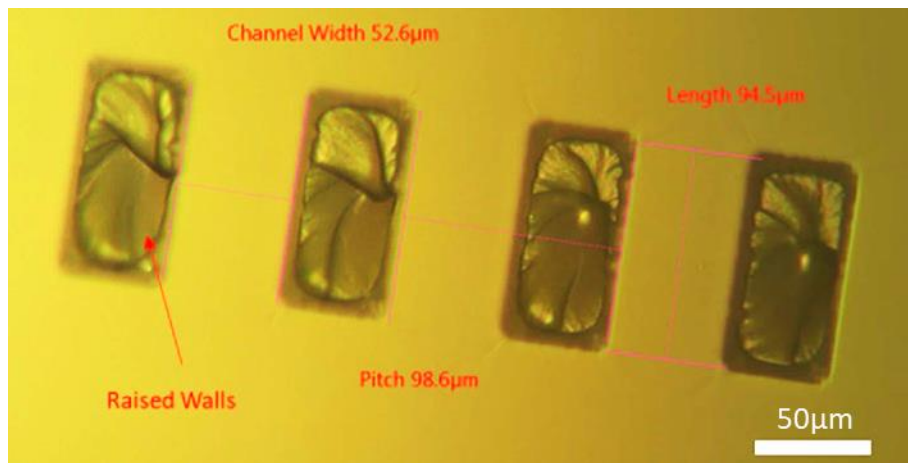


Figure 7.2: A high fidelity PDMS substrate is cast from the photolithography mould.

The substrates were coarsely aligned by placement markings on the print plate surface. Using the in-built process alignment camera, the substrates were manipulated so that a fiducial mark was under the camera. The angular alignment of the substrates was changed by rotating the stage, and verified by movement along a linear feature, such as the edge of one of the channels. Using this method the process was able to repeatedly deposit into the 50µm channels

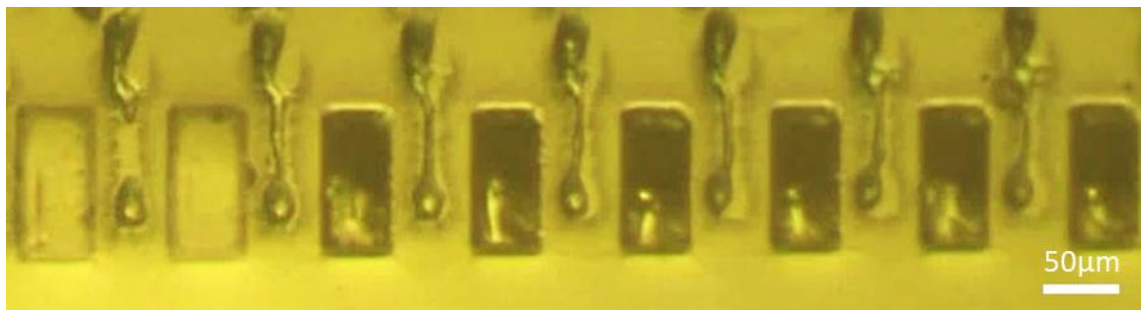


Figure 7.3: The process printed repeatably into 50µm wide channels.

Higher magnification images show that the deposits were printed directly into the channel, because the line widths were smaller than the channel size (**Error! Reference source not found. A**). **Error! Reference source not found. B** shows how by refining the process further printing into 20µm channels was demonstrated.

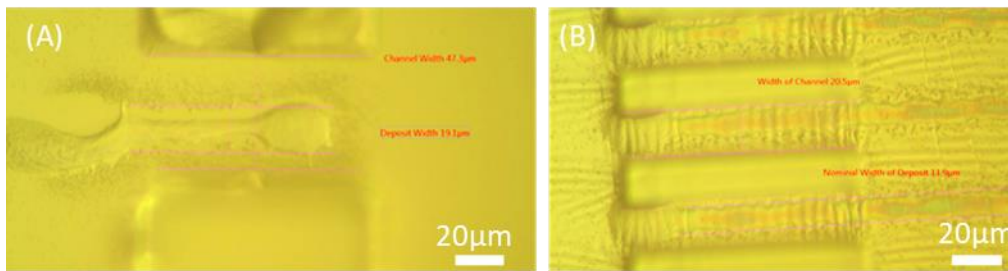


Figure 7.4: (A) 20X magnification image of printed line in a 50µm wide channel. (B) PEDOT:PSS was printed into channels with 20 µm width.

7.2.2 Electrical integration of cell culture substrates

The currently produced PEDOT:PSS devices can be electrically stimulated, and this effect should be exploited in the medium term, as specific applications are identified, in specific cell culturing fields. This conductive trace could be used to directly stimulate the cells, or a circuit can be incorporated into an integrated electrical systems such as electroactive polymers, for phenomenon such as mechanotransduction, and stimulating with light or heat energy.

Preliminary work has shown how printed PEDOT:PSS features can be incorporated into an electrical circuit. The electrical conductivity of PEDOT:PSS was investigated previously on cell cultures and has been shown to have positive effects on the culture in general, as cells *in vivo* are subject to tiny electrical stimulation [221]. Therefore, a design and device, shown in **Error! Reference source not found.**, were created to incorporate the printed structures into a circuit. The functionalisation of the surface in this way also has applications outside *in vitro* models.

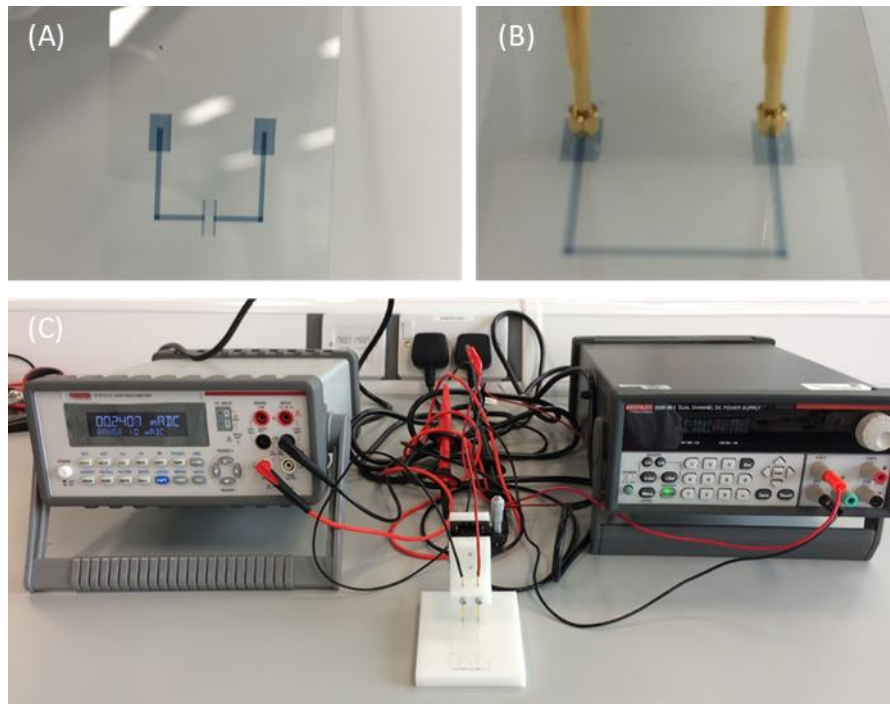


Figure 7.5: PEDOT:PSS printing incorporated into an electrical circuit. (A) A printed interconnect. (B) A microcontact apparatus was manufactured to incorporate the printed designs. (C) The apparatus could be attached to power supplies and measurement apparatus.

The prints are high resistance, so the several layers were printed to reduce the resistance. The same structures built with two passes of material reduced the resistance by a factor of 10.

Electrical stimulation of cell culture relies on short pulses of current to avoid localised heating that kills the cells. In this set up a square wave driven through a signal generator was used to stimulate the device.

The intermittent stimulation was visualised by incorporating an LED into the circuit. By plasma bonding a PDMS well onto the glass, an isolated culture environment is manufactured, which can be electrically stimulated.

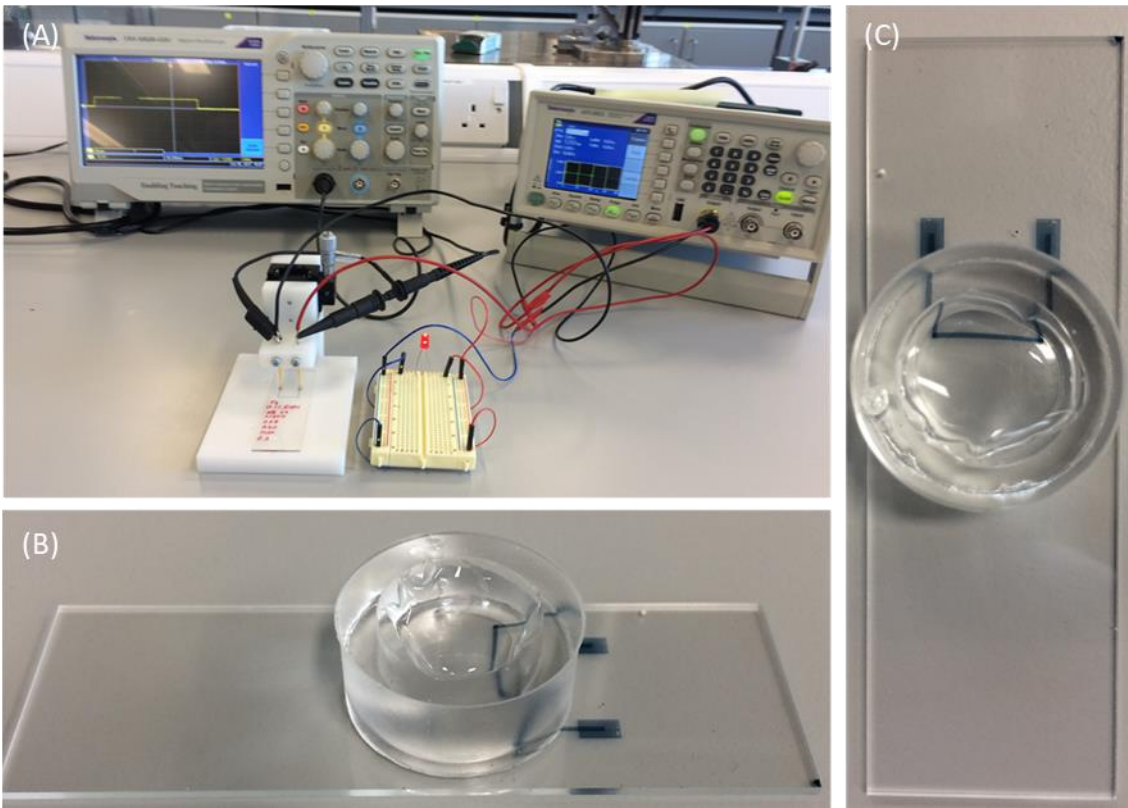


Figure 7.6: (A) PEDOT:PSS structures are stimulated by small electrical pulses, an LED light confirms when the pulsed current is on. (B) Plasma bonding a PDMS cylinder onto the glass results in a usable cell well. (C) Top view of the device, filled with DI water.

References

- [1] J. L. Charest, M. T. Eliason, A. J. García, and W. P. King, "Combined microscale mechanical topography and chemical patterns on polymer cell culture substrates," *Biomaterials*, vol. 27, no. 11, pp. 2487–2494, Apr. 2006.
- [2] E. . Roth, T. Xu, M. Das, C. Gregory, J. . Hickman, and T. Boland, "Inkjet printing for high-throughput cell patterning," *Biomaterials*, vol. 25, no. 17, pp. 3707–3715, Aug. 2004.
- [3] E. Cersosimo, X. Xu, S. Upala, C. Triplitt, and N. Musi, "Acute insulin resistance stimulates and insulin sensitization attenuates vascular smooth muscle cell migration and proliferation," *Physiological Reports*, vol. 2, no. 8, p. e12123, Aug. 2014.
- [4] N. Nikolić, S. W. Görgens, G. H. Thoresen, V. Aas, J. Eckel, and K. Eckardt, "Electrical pulse stimulation of cultured skeletal muscle cells as a model for in vitro exercise - possibilities and limitations," *Acta Physiologica*, vol. 220, no. 3, pp. 310–331, Jul. 2017.
- [5] BSI, "BS EN ISO/ASTM 52900:2017 Additive manufacturing General principles Terminology," 2017.
- [6] I. Gibson, D. W. Rosen, and B. Stucker, *Additive Manufacturing Technologies*. Boston, MA: Springer US, 2010.
- [7] Microchem, "SU-8 2000 Permanent Epoxy Negative Photoresist," *Processing Guidelines*, 2015.
- [8] C. D. James *et al.*, "Aligned microcontact printing of micrometer-scale poly-L-Lysine structures for controlled growth of cultured neurons on planar microelectrode arrays," *IEEE Transactions on Biomedical Engineering*, vol. 47, no. 1, pp. 17–21, 2000.
- [9] M. J. Renn, B. H. King, M. Essien, G. J. Marquez, M. G. Giridharan, and J.-C. Sheu, "Apparatuses and Methods for Maskless Mesoscale Material

Deposition,” US 7,485,345 B2, 2013.

- [10] C. Jia *et al.*, “Precise and Arbitrary Deposition of Biomolecules onto Biomimetic Fibrous Matrices for Spatially Controlled Cell Distribution and Functions,” *Advanced Materials*, vol. 29, no. 35, p. 1701154, Sep. 2017.
- [11] B.-J. de Gans, P. C. Duineveld, and U. S. Schubert, “Inkjet Printing of Polymers: State of the Art and Future Developments,” *Advanced Materials*, vol. 16, no. 3, pp. 203–213, Feb. 2004.
- [12] P. Calvert, “Inkjet Printing for Materials and Devices,” *Chemistry of Materials*, vol. 13, no. 10, pp. 3299–3305, Oct. 2001.
- [13] A. Kamyshny and S. Magdassi, “Conductive Nanomaterials for Printed Electronics,” *Small*, vol. 10, no. 17, pp. 3515–3535, Sep. 2014.
- [14] J. M. Hoey, A. Lutfurakhmanov, D. L. Schulz, and I. S. Akhatov, “A Review on Aerosol-Based Direct-Write and Its Applications for Microelectronics,” *Journal of Nanotechnology*, vol. 2012, pp. 1–22, 2012.
- [15] K. Stock *et al.*, “Capturing tumor complexity in vitro: Comparative analysis of 2D and 3D tumor models for drug discovery,” *Scientific Reports*, vol. 6, no. 1, p. 28951, Jul. 2016.
- [16] D. Espinosa-Hoyos *et al.*, “Engineered 3D-printed artificial axons,” *Scientific Reports*, vol. 8, no. 1, p. 478, Dec. 2018.
- [17] M. Maher, A. Smith, and J. Margiotta, “A synopsis of the Defense Advanced Research Projects Agency (DARPA) investment in additive manufacture and what challenges remain,” 2014, vol. 8970, p. 897002.
- [18] J. M. Fitz-Gerald *et al.*, “Maple direct write: A new approach to fabricate ferroelectric thin film devices in air at room temperature,” *Integrated Ferroelectrics*, vol. 28, no. 1–4, pp. 13–28, Mar. 2000.
- [19] “nScript.” [Online]. Available: <https://www.nscript.com/>. [Accessed: 18-

Aug-2018].

- [20] J. Longtin, S. Sampath, S. Tankiewicz, R. Gambino, and R. Greenlaw, "Sensors for Harsh Environments by Direct-Write Thermal Spray," *IEEE Sensors Journal*, vol. 4, no. 1, pp. 118–121, Feb. 2004.
- [21] M. Hedges, M. Renn, and M. Kardos, "MESOSCALE DEPOSITION TECHNOLOGY," 2005.
- [22] T. Seifert, E. Sowade, F. Roscher, M. Wiemer, T. Gessner, and R. R. Baumann, "Additive Manufacturing Technologies Compared: Morphology of Deposits of Silver Ink Using Inkjet and Aerosol Jet Printing," *Industrial & Engineering Chemistry Research*, vol. 54, no. 2, pp. 769–779, Jan. 2015.
- [23] J. M. Meruga, A. Baride, W. Cross, J. J. Kellar, and P. S. May, "Red-green-blue printing using luminescence-upconversion inks," *Journal of Materials Chemistry C*, vol. 2, no. 12, p. 2221, 2014.
- [24] E. B. Secor and M. C. Hersam, "Emerging carbon and post-carbon nanomaterial inks for printed electronics," *Journal of Physical Chemistry Letters*, vol. 6, no. 4, pp. 620–626, 2015.
- [25] K. Obata, "Hybrid Micro-stereo-lithography by Means of Aerosol Jet Printing Technology," *Journal of Laser Micro/Nanoengineering*, vol. 9, no. 3, pp. 242–247, Nov. 2014.
- [26] K. Obata *et al.*, "Hybrid 2D patterning using UV laser direct writing and aerosol jet printing of UV curable polydimethylsiloxane," *Applied Physics Letters*, vol. 111, no. 12, p. 121903, Sep. 2017.
- [27] E. . Roth, T. Xu, M. Das, C. Gregory, J. . Hickman, and T. Boland, "Inkjet printing for high-throughput cell patterning," *Biomaterials*, vol. 25, no. 17, pp. 3707–3715, Aug. 2004.
- [28] D. Kleinfeld, K. H. Kahler, and P. E. Hockberger, "Controlled outgrowth of

dissociated neurons on patterned substrates.,” *The Journal of neuroscience : the official journal of the Society for Neuroscience*, vol. 8, no. 11, pp. 4098–120, Nov. 1988.

- [29] M. A. Hughes, P. M. Brennan, A. S. Bunting, M. J. Shipston, and A. F. Murray, “Cell Patterning on Photolithographically Defined Parylene-C: SiO₂ Substrates,” *Journal of Visualized Experiments*, no. 85, 2014.
- [30] R. F. Valentini, T. G. Vargo, J. a Gardella, and P. Aebischer, “Patterned neuronal attachment and outgrowth on surface modified, electrically charged fluoropolymer substrates,” *Journal of Biomaterials Science, Polymer Edition*, vol. 5, no. 1–2, pp. 13–36, Jan. 1994.
- [31] A. Welle, S. Horn, J. Schimmelpfeng, and D. Kalka, “Photo-chemically patterned polymer surfaces for controlled PC-12 adhesion and neurite guidance,” *Journal of Neuroscience Methods*, vol. 142, no. 2, pp. 243–250, Mar. 2005.
- [32] A. F. Hirschbiel *et al.*, “Photolithographic Patterning of 3D-Formed Polycarbonate Films for Targeted Cell Guiding,” *Advanced Materials*, vol. 27, no. 16, pp. 2621–2626, Apr. 2015.
- [33] M. Essien, W. Hegge, S. M. Barnes, D. A. Bohling, J. Chou, and P. Schottland, “Direct Aerosol Jet Printing of Fine Conductor and Transparent Dielectric Jumpers for Touch Screen Display Substrates,” *Scientific Conference Proceedings LOPE-C 2011*, pp. 209–212, 2011.
- [34] D. Zhao, T. Liu, J. G. Park, M. Zhang, J.-M. Chen, and B. Wang, “Conductivity enhancement of aerosol-jet printed electronics by using silver nanoparticles ink with carbon nanotubes,” *Microelectronic Engineering*, vol. 96, pp. 71–75, Aug. 2012.

- [35] M. Mashayekhi *et al.*, "Evaluation of Aerosol, Superfine Inkjet, and Photolithography Printing Techniques for Metallization of Application Specific Printed Electronic Circuits," *IEEE Transactions on Electron Devices*, vol. 63, no. 3, pp. 1246–1253, Mar. 2016.
- [36] X. Lan *et al.*, "Direct On-Chip 3-D Aerosol Jet Printing With High Reliability," *IEEE Transactions on Components, Packaging and Manufacturing Technology*, vol. 7, no. 8, pp. 1369–1376, Aug. 2017.
- [37] M. Hedges and A. B. Marin, "3D Aerosol Jet Printing- Adding Electronics Functionality to RP/RM," in *DDMC*, 2012.
- [38] K. Wang, Y.-H. Chang, C. Zhang, and B. Wang, "Conductive-on-demand: Tailorable polyimide/carbon nanotube nanocomposite thin film by dual-material aerosol jet printing," *Carbon*, vol. 98, pp. 397–403, Mar. 2016.
- [39] M. J. Renn, B. H. King, M. Essien, and L. J. Hunter, "Apparatuses and Method for Maskless Mesoscale Material Deposition," US 7,045,015 B2, 2006.
- [40] W. Verheecke, M. Van Dyck, F. Vogeler, A. Voet, and H. Valkenaers, "Optimizing aerosol jet® printing of silver interconnects on polyimide film for embedded electronics applications," *8th International DAAAM Baltic Conference of Industrial Engineering*, pp. 373–379, 2012.
- [41] B. H. King and M. J. Renn, "Aerosol Jet® Direct Write Printing for Mil-Aero Electronic Applications," *WHITEPAPER - Optomec*, 2008.
- [42] C. Yang, E. Zhou, S. Miyanishi, K. Hashimoto, and K. Tajima, "Preparation of Active Layers in Polymer Solar Cells by Aerosol Jet Printing," *ACS Applied Materials & Interfaces*, vol. 3, no. 10, pp. 4053–4058, Oct. 2011.
- [43] J. A. Paulsen and M. J. Renn, "Maskless Printing of Miniature Polymer Thick Film Resistors for Embedded Applications," *IPC 3rd International*

Conference on Embedded Technology, vol. 2, 2006.

- [44] A. Mette, P. L. Richter, M. Hörteis, and S. W. Glunz, "Metal aerosol jet printing for solar cell metallization," *Progress in Photovoltaics: Research and Applications*, vol. 15, no. 7, pp. 621–627, Nov. 2007.
- [45] I. Grunwald *et al.*, "Surface biofunctionalization and production of miniaturized sensor structures using aerosol printing technologies," *Biofabrication*, vol. 2, no. 1, p. 014106, Mar. 2010.
- [46] M. Smith, Y. S. Choi, C. Boughey, and S. Kar-Narayan, "Controlling and assessing the quality of aerosol jet printed features for large area and flexible electronics," *Flexible and Printed Electronics*, vol. 2, no. 1, p. 015004, Mar. 2017.
- [47] Optomec, "Tips, Tricks and Materials," in *Optomec International User Group Meeting 25th/26th Apr*, 2016.
- [48] B. H. King, M. J. O'Reilly, and S. M. Barnes, "Characterizing aerosol Jet® multi-nozzle process parameters for non-contact front side metallization of silicon solar cells," in *2009 34th IEEE Photovoltaic Specialists Conference (PVSC)*, 2009, pp. 001107–001111.
- [49] V. A. Marple and C. M. Chien, "Virtual impactors: a theoretical study.," *Environmental Science & Technology*, vol. 14, no. 8, pp. 976–985, Aug. 1980.
- [50] P. J. Crosland-Taylor, "A Device for Counting Small Particles suspended in a Fluid through a Tube," *Nature*, vol. 171, no. 4340, pp. 37–38, Jan. 1953.
- [51] J. M. Hoey, I. S. Akhatov, O. F. Swenson, and D. L. Schulz, "Convergent-Divergent-Convergent Nozzle Focusing of Aerosol Particles for Micron Scale Direct Writing," US 20100322867A1, 2009.
- [52] B. E. Dahneke and S. K. Friedlander, "Velocity characteristics of beams of

- spherical polystyrene particles,” *Journal of Aerosol Science*, vol. 1, no. 4, pp. 325–339, Jan. 1970.
- [53] A. Mahajan, C. D. Frisbie, and L. F. Francis, “Optimization of Aerosol Jet Printing for High-Resolution, High-Aspect Ratio Silver Lines,” *ACS Applied Materials & Interfaces*, vol. 5, no. 11, pp. 4856–4864, Jun. 2013.
- [54] P. Kopola *et al.*, “Aerosol jet printed grid for ITO-free inverted organic solar cells,” *Solar Energy Materials and Solar Cells*, vol. 107, pp. 252–258, Dec. 2012.
- [55] T. Rahman, L. Renaud, D. Heo, M. Renn, and R. Panat, “Aerosol based direct-write micro-additive fabrication method for sub-mm 3D metal-dielectric structures,” *Journal of Micromechanics and Microengineering*, vol. 25, no. 10, p. 107002, Oct. 2015.
- [56] Optomec, “Aerosol Jet 5X System,” 2014. [Online]. Available: <http://www.optomec.com/printed-electronics/aerosol-jet-printers/aerosol-jet-5x-system/>. [Accessed: 18-Apr-2016].
- [57] C. Goth, S. Putzo, and J. Franke, “Aerosol Jet printing on rapid prototyping materials for fine pitch electronic applications,” in *2011 IEEE 61st Electronic Components and Technology Conference (ECTC)*, 2011, pp. 1211–1216.
- [58] Optomec, “Aerosol jet ® 200 datasheet,” 2015.
- [59] W. Hegge, D. A. Bohling, J. Chou, M. Mcallister, and P. Schottland, “Direct Dielectric Line Printing for Touch Panel Display Jumpers Using Transparent Dielectric Inks and Aerosol Jet ® Deposition Methods,” in *SID Symposium Digest of Technical Papers*, 2011, pp. 837–840.
- [60] J. M. Hoey *et al.*, “Rapid Prototyping RFID Antennas Using Direct-Write,” *IEEE Transactions on Advanced Packaging*, vol. 32, no. 4, pp. 809–815, Nov. 2009.

- [61] E. B. Secor, "Principles of aerosol jet printing," *Flexible and Printed Electronics*, vol. 3, no. 3, p. 035002, Sep. 2018.
- [62] S. Agarwala, G. L. Goh, and W. Y. Yeong, "Optimizing aerosol jet printing process of silver ink for printed electronics," *IOP Conference Series: Materials Science and Engineering*, vol. 191, p. 012027, Apr. 2017.
- [63] A. A. Gupta, A. Bolduc, S. G. Cloutier, and R. Izquierdo, "Aerosol Jet Printing for printed electronics rapid prototyping," in *2016 IEEE International Symposium on Circuits and Systems (ISCAS)*, 2016, vol. 2016-July, pp. 866–869.
- [64] F. Cai, Y. H. Chang, K. Wang, C. Zhang, B. Wang, and J. Papapolymerou, "Low-Loss 3-D Multilayer Transmission Lines and Interconnects Fabricated by Additive Manufacturing Technologies," *IEEE Transactions on Microwave Theory and Techniques*, vol. PP, no. 99, pp. 3208–3216, 2016.
- [65] S. Vunnam, K. Ankireddy, J. Kellar, and W. Cross, "Surface modification of indium tin oxide for direct writing of silver nanoparticulate ink micropatterns," *Thin Solid Films*, vol. 531, pp. 294–301, Mar. 2013.
- [66] M. P. Groover, *Fundamentals of Modern Manufacturing, Materials Process and Systems*. John Wiley and Sons Inc, 2002.
- [67] S. Halldorsson, E. Lucumi, R. Gómez-Sjöberg, and R. M. T. T. Fleming, "Advantages and challenges of microfluidic cell culture in polydimethylsiloxane devices," *Biosensors and Bioelectronics*, vol. 63, pp. 218–231, Jan. 2015.
- [68] D. Qin, Y. Xia, and G. M. Whitesides, "Soft lithography for micro- and nanoscale patterning," *Nature Protocols*, vol. 5, no. 3, pp. 491–502, Mar. 2010.
- [69] G. M. Whitesides, E. Ostuni, S. Takayama, X. Jiang, and D. E. Ingber, "Soft

- Lithography in Biology and Biochemistry,” *Annual Review of Biomedical Engineering*, vol. 3, no. 1, pp. 335–373, Aug. 2001.
- [70] A. Llobera, B. Ibarlucea, C. Fernández-Sánchez, S. Demming, S. Büttgenbach, and A. Llobera, “Biofunctionalization of PDMS-based microfluidic systems,” *Protocol Exchange*, pp. 1–17, Nov. 2011.
- [71] J. P. Rolland, E. C. Hagberg, G. M. Denison, K. R. Carter, and J. M. De Simone, “High-Resolution Soft Lithography: Enabling Materials for Nanotechnologies,” *Angewandte Chemie International Edition*, vol. 43, no. 43, pp. 5796–5799, Nov. 2004.
- [72] Y. Xia and G. M. Whitesides, “Soft Lithography,” *Annual Review of Materials Science*, vol. 28, no. 1, pp. 153–184, Aug. 1998.
- [73] J. Zhou, A. V. Ellis, and N. H. Voelcker, “Recent developments in PDMS surface modification for microfluidic devices,” *Electrophoresis*, vol. 31, no. 1, pp. 2–16, 2010.
- [74] H. Becker, “It’s the economy...,” *Lab on a Chip*, vol. 9, no. 19, p. 2759, 2009.
- [75] A. Oláh, H. Hillborg, and G. J. Vancso, “Hydrophobic recovery of UV/ozone treated poly(dimethylsiloxane): Adhesion studies by contact mechanics and mechanism of surface modification,” *Applied Surface Science*, vol. 239, no. 3–4, pp. 410–423, 2005.
- [76] H. Hillborg, N. Tomczak, A. Oláh, H. Schönherr, and G. J. Vancso, “Nanoscale Hydrophobic Recovery: A Chemical Force Microscopy Study of UV/Ozone-Treated Cross-Linked Poly(dimethylsiloxane),” *Langmuir*, vol. 20, no. 3, pp. 785–794, Feb. 2004.
- [77] J. Tong, C. a Simmons, and Y. Sun, “Precision patterning of PDMS membranes and applications,” *Journal of Micromechanics and*

Microengineering, vol. 18, no. 3, p. 037004, Mar. 2008.

- [78] J. Hoey *et al.*, “CAB-DW for 5 micrometer trace-width deposition of solar cell metallization top-contacts,” in *2009 34th IEEE Photovoltaic Specialists Conference (PVSC)*, 2009, no. 1, pp. 001857–001861.
- [79] V. R. Marinov *et al.*, “Direct-Write Vapor Sensors on FR4 Plastic Substrates,” *IEEE Sensors Journal*, vol. 7, no. 6, pp. 937–944, Jun. 2007.
- [80] G. Chen, Y. Gu, H. Tsang, D. R. Hines, and S. Das, “The Effect of Droplet Sizes on Overspray in Aerosol-Jet Printing,” *Advanced Engineering Materials*, vol. 1701084, p. 1701084, Apr. 2018.
- [81] R. Shankar, L. Groven, A. Amert, K. W. Whites, and J. J. Kellar, “Non-aqueous synthesis of silver nanoparticles using tin acetate as a reducing agent for the conductive ink formulation in printed electronics,” *Journal of Materials Chemistry*, vol. 21, p. 10871, 2011.
- [82] C. Werner, D. Godlinski, V. Zöllmer, and M. Busse, “Morphological influences on the electrical sintering process of Aerosol Jet and Ink Jet printed silver microstructures,” *Journal of Materials Science: Materials in Electronics*, vol. 24, no. 11, pp. 4367–4377, 2013.
- [83] V. Zöllmer *et al.*, “Printing with aerosols,” *European Coatings Journal*, vol. 49, no. 7–8, pp. 46–50, 2006.
- [84] K. Schuetz, J. Hoerber, and J. Franke, “Selective light sintering of Aerosol-Jet printed silver nanoparticle inks on polymer substrates,” in *AIP Conference Proceedings*, 2014, vol. 1593, pp. 732–735.
- [85] E. Jabari and E. Toyserkani, “Aerosol-Jet printing of highly flexible and conductive graphene/silver patterns,” *Materials Letters*, vol. 174, pp. 40–43, Jul. 2016.
- [86] J. Hoerber, C. Goth, J. Franke, and M. Hedges, “Electrical functionalization

- of thermoplastic materials by Aerosol Jet Printing,” in *2011 IEEE 13th Electronics Packaging Technology Conference*, 2011, pp. 813–818.
- [87] T. Seifert, M. Baum, F. Roscher, M. Wiemer, and T. Gessner, “Aerosol Jet Printing of Nano Particle Based Electrical Chip Interconnects,” *Materials Today: Proceedings*, vol. 2, no. 8, pp. 4262–4271, 2015.
- [88] M. T. Rahman, J. McCloy, C. V Ramana, and R. Panat, “Structure, electrical characteristics, and high-temperature stability of aerosol jet printed silver nanoparticle films,” *Journal of Applied Physics*, vol. 120, no. 7, p. 075305, Aug. 2016.
- [89] N. A. Luechinger, E. K. Athanassiou, and W. J. Stark, “Graphene-stabilized copper nanoparticles as an air-stable substitute for silver and gold in low-cost ink-jet printable electronics,” *Nanotechnology*, vol. 19, no. 44, p. 445201, Nov. 2008.
- [90] A. A. Efimov, P. V. Arsenov, N. V. Protas, K. N. Minkov, M. N. Urazov, and V. V. Ivanov, “Dry aerosol jet printing of conductive silver lines on a heated silicon substrate,” *IOP Conference Series: Materials Science and Engineering*, vol. 307, no. 1, p. 012082, Feb. 2018.
- [91] S. Maleki, F. Lot, M. Barzegar-jalali, and O. Ag, “Antimicrobial activity of the metals and metal oxide nanoparticles,” *Materials Science and Engineering C*, vol. 44, pp. 278–284, 2014.
- [92] H. Bahadar, F. Maqbool, K. Niaz, and M. Abdollahi, “Toxicity of Nanoparticles and an Overview of Current Experimental Models,” *Iranian Biomedical Journal*, vol. 20, no. January, pp. 1–11, 2016.
- [93] S. Padovani *et al.*, “New method for head-up display realization by mean of Chip On Board and Aerosol Jet process,” in *3rd Electronics System Integration Technology Conference ESTC*, 2010, pp. 1–3.

- [94] Z. Zhan, L. Yu, J. Wei, C. Zheng, D. Sun, and L. Wang, "Application of Aerosol Jet technology in through-via interconnection for MEMS wafer-level packaging," *Microsystem Technologies*, vol. 21, no. 2, pp. 451–455, 2014.
- [95] S. Stoukatch *et al.*, "Evaluation of aerosol jet printing (AJP) technology for electronic packaging and interconnect technique," *2012 4th Electronic System-Integration Technology Conference, ESTC 2012*, 2012.
- [96] C. Kaestle, J. Hoerber, F. Oechsner, and J. Franke, "Prospects of wire bonding as an approach for contacting additive manufactured Aerosol Jet printed structures," in *2015 European Microelectronics Packaging Conference (EMPC)*, 2015, pp. 1–6.
- [97] B. Khorramdel, A. Torkkeli, and M. Mantysalo, "Electrical Contacts in SOI MEMS Using Aerosol Jet Printing," *IEEE Journal of the Electron Devices Society*, vol. 6, pp. 34–40, 2017.
- [98] Y.-H. Y. Chang, K. Wang, C. Wu, Y. Chen, C. Zhang, and B. Wang, "A facile method for integrating direct-write devices into three-dimensional printed parts," *Smart Materials and Structures*, vol. 24, no. 6, p. 065008, 2015.
- [99] E. Berthier, E. W. K. Young, and D. Beebe, "Engineers are from PDMS-land, Biologists are from Polystyrenia," *Lab on a Chip*, vol. 12, no. 7, p. 1224, 2012.
- [100] A. Mahajan, L. F. Francis, and C. D. Frisbie, "Facile method for fabricating flexible substrates with embedded, printed silver lines," *ACS Applied Materials and Interfaces*, vol. 6, no. 2, pp. 1306–1312, 2014.
- [101] J. Reboun, S. Pretl, J. Navratil, and J. Hlina, "Bending endurance of printed conductive patterns on flexible substrates," in *2016 39th International*

- Spring Seminar on Electronics Technology (ISSE)*, 2016, vol. 2016-Septe, pp. 184–188.
- [102] E. Jabari and E. Toyserkani, “Micro-scale aerosol-jet printing of graphene interconnects,” *Carbon*, vol. 91, no. 27, pp. 321–329, Sep. 2015.
- [103] I. Barbulovic-Nad, S. H. Au, and A. R. Wheeler, “A microfluidic platform for complete mammalian cell culture,” *Lab on a Chip*, vol. 10, no. 12, p. 1536, 2010.
- [104] E. K. Sackmann, A. L. Fulton, and D. J. Beebe, “The present and future role of microfluidics in biomedical research.,” *Nature*, vol. 507, no. 7491, pp. 181–9, 2014.
- [105] K. K. Christenson, J. A. Paulsen, M. J. Renn, K. Mcdonald, J. Bourassa, and S. Paul, “Direct Printing of Circuit Boards Using Aerosol Jet ®,” in *27th International Conference on Digital Printing Technologies, Technical Program and Proceedings*, 2011, pp. 433–436.
- [106] C. E. Folgar, C. Suchicital, and S. Priya, “Solution-based aerosol deposition process for synthesis of multilayer structures,” *Materials Letters*, vol. 65, no. 9, pp. 1302–1307, May 2011.
- [107] M. Carter, T. Amundson, J. Colvin, and J. Sears, “Characterization of soft magnetic nano-material deposited with M3D technology,” *Journal of Materials Science*, vol. 42, no. 5, pp. 1828–1832, Mar. 2007.
- [108] M. T. Rahman, R. Panat, and D. Heo, “3-D Antenna Structures Using Novel Direct-Write Additive Manufacturing Method,” in *Proceedings of the ASME 2015 International Technical Conference and Exhibition on Packaging and Integration of Electronic and Photonic Microsystems*, 2015.
- [109] B. L. Xu *et al.*, “Aerosol Jet Printing on Radio Frequency IDentification Tag Applications,” *Key Engineering Materials*, vol. 562–565, pp. 1417–1421, Jul.

2013.

- [110] L. Harle, C. Oakley, and J. Papapolymerou, "3D-printed dual band planar inverted F antenna," in *2016 IEEE International Symposium on Antennas and Propagation (APSURSI)*, 2016, pp. 817–818.
- [111] Y. He *et al.*, "RF characterization of coplanar waveguide (CPW) transmission lines on single-crystalline diamond platform for integrated high power RF electronic systems," *IEEE MTT-S International Microwave Symposium Digest*, pp. 517–520, 2017.
- [112] J. Hester, E. Nguyen, J. Tice, and V. Radisic, "A novel 3D-printing-enabled 'roller coaster' transmission line," in *2017 IEEE International Symposium on Antennas and Propagation & USNC/URSI National Radio Science Meeting*, 2017, pp. 2639–2640.
- [113] Fan Cai *et al.*, "Aerosol jet printing for 3-D multilayer passive microwave circuitry," in *2014 44th European Microwave Conference*, 2014, pp. 512–515.
- [114] F. Cai, Y. Chang, K. Wang, W. T. Khan, S. Pavlidis, and J. Papapolymerou, "High resolution aerosol jet printing of D- band printed transmission lines on flexible LCP substrate," in *2014 IEEE MTT-S International Microwave Symposium (IMS2014)*, 2014, pp. 1–3.
- [115] X. Lan *et al.*, "Ultra-wideband microwave components fabricated using low-cost aerosol-jet printing technology," in *2015 IEEE Radio and Wireless Symposium (RWS)*, 2015, pp. 156–158.
- [116] C. Oakley, A. Kaur, J. A. Byford, and P. Chahal, "Aerosol-Jet Printed Quasi-Optical Terahertz Filters," in *2017 IEEE 67th Electronic Components and Technology Conference (ECTC)*, 2017, pp. 248–253.
- [117] F. J. Berger *et al.*, "From Broadband to Electrochromic Notch Filters with

- Printed Monochiral Carbon Nanotubes,” *ACS Applied Materials and Interfaces*, vol. 10, no. 13, pp. 11135–11142, 2018.
- [118] X. Li *et al.*, “Desktop aligner for fabrication of multilayer microfluidic devices,” *Review of Scientific Instruments*, vol. 86, no. 7, p. 075008, Jul. 2015.
- [119] K. Drew, S. Hopman, M. Hörteis, S. W. Glunz, and F. Granek, “Combining laser chemical processing and aerosol jet printing: a laboratory scale feasibility study,” *Progress in Photovoltaics: Research and Applications*, vol. 19, no. 3, pp. 253–259, May 2011.
- [120] A. Kalio, M. Leibinger, A. Filipovic, K. Kürger, M. Glatthaar, and J. Wilde, “Development of lead-free silver ink for front contact metallization,” *Solar Energy Materials and Solar Cells*, vol. 106, pp. 51–54, 2012.
- [121] Y. Tamari, A. Gautrein, C. Schmiga, S. Binder, M. Glatthaar, and S. W. Glunz, “Synthesis of a Lead- and Particle-free Metal-organic Ink for Front Side Metallization of Crystalline Silicon Solar Cells,” *Energy Procedia*, vol. 55, pp. 708–714, 2014.
- [122] M. F. A. M. van Hest *et al.*, “Direct write metallization for photovoltaic cells and scaling thereof,” in *2010 35th IEEE Photovoltaic Specialists Conference*, 2010, pp. 003626–003628.
- [123] H. A. S. Platt, Y. Li, J. P. Novak, and M. F. A. M. van Hest, “Non-contact printed aluminum metallization of Si photovoltaic devices,” in *2012 38th IEEE Photovoltaic Specialists Conference*, 2012, no. June, pp. 002244–002246.
- [124] B. A. Williams, A. Mahajan, M. A. Smeaton, C. S. Holgate, E. S. Aydil, and L. F. Francis, “Formation of copper zinc tin sulfide thin films from colloidal nanocrystal dispersions via aerosol-jet printing and compaction,” *ACS Applied Materials and Interfaces*, vol. 7, no. 21, pp. 11526–11535, 2015.

- [125] S. Bag, J. R. Deneault, and M. F. Durstock, "Aerosol-Jet-Assisted Thin-Film Growth of $\text{CH}_3\text{NH}_3\text{PbI}_3$ Perovskites-A Means to Achieve High Quality, Defect-Free Films for Efficient Solar Cells," *Advanced Energy Materials*, vol. 7, no. 20, p. 1701151, Oct. 2017.
- [126] M. Pardo-Figuerez, N. R. W. Martin, D. J. Player, A. J. Capel, S. D. R. Christie, and M. P. Lewis, "Neural and Aneural Regions Generated by the Use of Chemical Surface Coatings," *ACS Biomaterials Science & Engineering*, vol. 4, no. 1, pp. 98–106, Jan. 2018.
- [127] J. Rodriguez *et al.*, "Dielectric Patterning Using Aerosol Jet Printing," *Journal of Imaging Science and Technology*, vol. 56, no. 4, pp. 1–7, Dec. 2012.
- [128] J. H. Cho *et al.*, "Printable ion-gel gate dielectrics for low-voltage polymer thin-film transistors on plastic," *Nature Materials*, vol. 7, no. 11, pp. 900–906, Nov. 2008.
- [129] C. S. Jones, X. Lu, M. Renn, M. Stroder, and W.-S. Shih, "Aerosol-jet-printed, high-speed, flexible thin-film transistor made using single-walled carbon nanotube solution," *Microelectronic Engineering*, vol. 87, no. 3, pp. 434–437, Mar. 2010.
- [130] H. Li, Y. Tang, W. Guo, H. Liu, L. Zhou, and N. Smolinski, "Polyfluorinated Electrolyte for Fully Printed Carbon Nanotube Electronics," *Advanced Functional Materials*, vol. 26, no. 38, pp. 6914–6920, Oct. 2016.
- [131] C. Cao, J. B. Andrews, A. Kumar, and A. D. Franklin, "Improving Contact Interfaces in Fully Printed Carbon Nanotube Thin-Film Transistors," *ACS Nano*, vol. 10, no. 5, pp. 5221–5229, May 2016.
- [132] C. Cao, J. B. Andrews, and A. D. Franklin, "Completely Printed, Flexible, Stable, and Hysteresis-Free Carbon Nanotube Thin-Film Transistors via

- Aerosol Jet Printing,” *Advanced Electronic Materials*, vol. 3, no. 5, p. 1700057, May 2017.
- [133] M. Rother *et al.*, “Aerosol-Jet Printing of Polymer-Sorted (6,5) Carbon Nanotubes for Field-Effect Transistors with High Reproducibility,” *Advanced Electronic Materials*, vol. 3, no. 8, p. 1700080, Aug. 2017.
- [134] X. Wu *et al.*, “Printable poly(methylsilsesquioxane) dielectric ink and its application in solution processed metal oxide thin-film transistors,” *RSC Advances*, vol. 5, no. 27, pp. 20924–20930, 2015.
- [135] L. Qian *et al.*, “Electrical and Photoresponse Properties of Printed Thin-Film Transistors Based on Poly(9,9-dioctylfluorene- co -bithiophene) Sorted Large-Diameter Semiconducting Carbon Nanotubes,” *The Journal of Physical Chemistry C*, vol. 117, no. 35, pp. 18243–18250, Sep. 2013.
- [136] R. Liu *et al.*, “All-carbon-based field effect transistors fabricated by aerosol jet printing on flexible substrates,” *Journal of Micromechanics and Microengineering*, vol. 23, no. 6, p. 065027, Jun. 2013.
- [137] M. Ha *et al.*, “Aerosol Jet Printed, Low Voltage, Electrolyte Gated Carbon Nanotube Ring Oscillators with Sub-5 μ s Stage Delays,” *Nano Letters*, vol. 13, no. 3, pp. 954–960, Mar. 2013.
- [138] K. Hong *et al.*, “Aerosol Jet Printed, Sub-2 V Complementary Circuits Constructed from P - and N -Type Electrolyte Gated Transistors,” *Advanced Materials*, vol. 26, no. 41, pp. 7032–7037, Nov. 2014.
- [139] S. H. Kim, K. Hong, K. H. Lee, and C. D. Frisbie, “Performance and Stability of Aerosol-Jet-Printed Electrolyte-Gated Transistors Based on Poly(3-hexylthiophene),” *ACS Applied Materials & Interfaces*, vol. 5, no. 14, pp. 6580–6585, Jul. 2013.
- [140] J. G. Tait *et al.*, “Uniform Aerosol Jet printed polymer lines with 30 μ m width

for 140ppi resolution RGB organic light emitting diodes,” *Organic Electronics*, vol. 22, pp. 40–43, Jul. 2015.

- [141] L. Zhou, J. Y. Zhuang, M. S. Song, W. M. Su, and Z. Cui, “Enhanced performance for organic light-emitting diodes by embedding an aerosol jet printed conductive grid,” *Journal of Physics D: Applied Physics*, vol. 47, no. 11, p. 115504, Mar. 2014.
- [142] H. Li, M. Yang, H. Liu, Y. Tang, W. Guo, and K. Smolinski, “Printing Pixel Circuits on Light Emitting Diode Array for AMOLED Displays,” *SID Symposium Digest of Technical Papers*, vol. 46, no. 1, pp. 1217–1220, Jun. 2015.
- [143] E. M. Ahmed, “Hydrogel: Preparation, characterization, and applications: A review,” *Journal of Advanced Research*, vol. 6, no. 2, pp. 105–121, Mar. 2015.
- [144] W. Liu *et al.*, “Rapid Continuous Multimaterial Extrusion Bioprinting,” vol. 1604630, pp. 1–8, 2017.
- [145] I. T. Ozbolat, W. Peng, and V. Ozbolat, “Application areas of 3D bioprinting,” *Drug Discovery Today*, vol. 21, no. 8, pp. 1257–1271, Aug. 2016.
- [146] D. B. Kolesky, R. L. Truby, A. S. Gladman, T. A. Busbee, K. A. Homan, and J. A. Lewis, “3D bioprinting of vascularized, heterogeneous cell-laden tissue constructs,” *Advanced Materials*, vol. 26, no. 19, pp. 3124–3130, 2014.
- [147] M. Maiwald, C. Werner, V. Zoellmer, and M. Busse, “INKtelligent printed strain gauges,” *Sensors and Actuators A: Physical*, vol. 162, no. 2, pp. 198–201, Aug. 2010.
- [148] D. Zhao, T. Liu, M. Zhang, R. Liang, and B. Wang, “Fabrication and characterization of aerosol-jet printed strain sensors for multifunctional

- composite structures,” *Smart Materials and Structures*, vol. 21, no. 11, p. 115008, 2012.
- [149] M. T. Rahman, R. Moser, H. M. Zbib, C. V. Ramana, and R. Panat, “3D printed high performance strain sensors for high temperature applications,” *Journal of Applied Physics*, vol. 123, no. 2, p. 024501, Jan. 2018.
- [150] M. T. Rahman, A. Rahimi, S. Gupta, and R. Panat, “Microscale additive manufacturing and modeling of interdigitated capacitive touch sensors,” *Sensors and Actuators A: Physical*, vol. 248, pp. 94–103, Sep. 2016.
- [151] J. B. Andrews, C. Cao, M. A. Brooke, and A. D. Franklin, “Noninvasive Material Thickness Detection by Aerosol Jet Printed Sensors Enhanced Through Metallic Carbon Nanotube Ink,” *IEEE Sensors Journal*, vol. 17, no. 14, pp. 4612–4618, Jul. 2017.
- [152] J. Fessler, F. Mach, and J. Navratil, “Numerical and experimental analysis of electrostatic adhesion force generated by interdigital electrodes,” *2017 18th International Symposium on Electromagnetic Fields in Mechatronics, Electrical and Electronic Engineering, ISEF 2017*, vol. c, no. 1, pp. 1–2, 2017.
- [153] R. S. Aga, J. P. Lombardi, C. M. Bartsch, and E. M. Heckman, “Performance of a printed photodetector on a paper substrate,” *IEEE Photonics Technology Letters*, vol. 26, no. 3, pp. 305–308, 2014.
- [154] J. Lombardi *et al.*, “Nanoparticle Based Printed Sensors on Paper for Detecting Chemical Species,” in *2017 IEEE 67th Electronic Components and Technology Conference (ECTC)*, 2017, pp. 764–771.
- [155] F.-X. Wang, J. Lin, W.-B. Gu, Y.-Q. Liu, H.-D. Wu, and G.-B. Pan, “Aerosol-jet printing of nanowire networks of zinc octaethylporphyrin and its application in flexible photodetectors,” *Chemical Communications*, vol. 49,

no. 24, p. 2433, 2013.

- [156] R. Eckstein *et al.*, “Aerosol-Jet Printed Flexible Organic Photodiodes: Semi-Transparent, Color Neutral, and Highly Efficient,” *Advanced Electronic Materials*, vol. 1, no. 8, p. 1500101, Aug. 2015.
- [157] R. Eckstein, N. Strobel, T. Rödlmeier, K. Glaser, U. Lemmer, and G. Hernandez-Sosa, “Fully Digitally Printed Image Sensor Based on Organic Photodiodes,” *Advanced Optical Materials*, vol. 6, no. 5, p. 1701108, Mar. 2018.
- [158] R. Ichiyama, Z. Ninkov, S. Williams, R. Robinson, and S. Bhaskaran, “Using quantum-dots to enable deep-UV sensitivity with standard silicon-based imaging detectors,” in *Proceedings of SPIE*, 2017, vol. 10110, p. 1011011.
- [159] M. Landgraf, S. Reitelshofer, J. Franke, and M. Hedges, “Aerosol jet printing and lightweight power electronics for dielectric elastomer actuators,” in *2013 3rd International Electric Drives Production Conference (EDPC)*, 2013, pp. 1–7.
- [160] I. S. Yoo, M. Landgraf, C. Ramer, S. Reitelshöfer, C. Ziegler, and J. Franke, “My new colleague has artificial muscles: a DEA based approach for inherently compliant robotic systems,” *Production Engineering*, vol. 8, no. 6, pp. 711–717, Dec. 2014.
- [161] R. Liu, H. Ding, J. Lin, F. Shen, Z. Cui, and T. Zhang, “Fabrication of platinum-decorated single-walled carbon nanotube based hydrogen sensors by aerosol jet printing,” *Nanotechnology*, vol. 23, no. 50, p. 505301, Dec. 2012.
- [162] P. Kuberský, J. Altšmíd, A. Hamáček, S. Nešpůrek, and O. Zmeškal, “An Electrochemical NO₂ Sensor Based on Ionic Liquid: Influence of the

- Morphology of the Polymer Electrolyte on Sensor Sensitivity,” *Sensors*, vol. 15, no. 11, pp. 28421–28434, Nov. 2015.
- [163] H. Yang, M. T. Rahman, D. Du, R. Panat, and Y. Lin, “3-D printed adjustable microelectrode arrays for electrochemical sensing and biosensing,” *Sensors and Actuators B: Chemical*, vol. 230, pp. 600–606, Jul. 2016.
- [164] A. A. Vasiliev *et al.*, “Additive technologies for ceramic MEMS sensors,” *Procedia Engineering*, vol. 120, pp. 1087–1090, 2015.
- [165] A. A. Vasiliev *et al.*, “Automotive MEMS sensors based on additive technologies,” *IOP Conference Series: Materials Science and Engineering*, vol. 151, p. 012024, 2016.
- [166] T. Reitberger, J. Hoerber, R. Schramm, S. Sennefelder, and J. Franke, “Aerosol Jet Printing of Optical Waveguides,” in *2015 38th International Spring Seminar on Electronics Technology (ISSE)*, 2015, pp. 5–10.
- [167] T. Reitberger, G.-A. Hoffmann, T. Wolfer, L. Overmeyer, and J. Franke, “Printing polymer optical waveguides on conditioned transparent flexible foils by using the aerosol jet technology,” in *Proceedings Volume 9945, Printed Memory and Circuits II*, 2016, vol. 9945, p. 99450G.
- [168] G. Hoffmann, T. Reitberger, J. Franke, and L. Overmeyer, “Conditioning of Surface Energy and Spray Application of Optical Waveguides for Integrated Intelligent Systems,” *Procedia Technology*, vol. 26, pp. 169–176, 2016.
- [169] T. Reitberger, J. Franke, G.-A. Hoffmann, L. Overmeyer, L. Lorenz, and K.-J. Wolter, “Integration of polymer optical waveguides by using flexographic and aerosol jet printing,” in *2016 12th International Congress Molded Interconnect Devices (MID)*, 2016, pp. 1–6.

- [170] S. Reitelshöfer, M. Göttler, P. Schmidt, P. Treffer, M. Landgraf, and J. Franke, "Aerosol-Jet-Printing silicone layers and electrodes for stacked dielectric elastomer actuators in one processing device," *Proc. SPIE 9798, Electroactive Polymer Actuators and Devices (EAPAD) 2016*, vol. 9798, no. 0, pp. 8–16, 2016.
- [171] S. Reitelshofer, M. Landgraf, D. Graf, L. Bugert, and J. Franke, "A new production process for soft actuators and sensors based on dielectric elastomers intended for safe human robot interaction," in *2015 IEEE/SICE International Symposium on System Integration (SII)*, 2015, pp. 51–56.
- [172] A. M. Suresh, T. Jenkins, P. Gardner, R. M. Miller, and T. L. Reitz, "Investigation of Aerosol Jet Deposition Parameters for Printing SOFC Layers," in *ASME 2010 8th International Fuel Cell Science, Engineering and Technology Conference: Volume 1*, 2010, pp. 325–332.
- [173] A. M. Suresh *et al.*, "Aerosol Jet Printing and Microstructure of SOFC Electrolyte and Cathode Layers," 2011, vol. 35, no. 1, pp. 2151–2160.
- [174] M. Suresh A., F. Meisenkothen, P. Gardner, and T. L. Reitz, "Aerosol Jet® Printing of functionally graded SOFC anode interlayer and microstructural investigation by low voltage scanning electron microscopy," *Journal of Power Sources*, vol. 224, pp. 295–303, Feb. 2013.
- [175] M. P. Sealy, G. Madireddy, R. E. Williams, P. Rao, and M. Toursangsaraki, "Hybrid Processes in Additive Manufacturing," *Journal of Manufacturing Science and Engineering*, vol. 140, no. 6, p. 060801, Mar. 2018.
- [176] C. E. Folgar, L. N. Folgar, and D. Cormier, "Multifunctional material direct printing for laser sintering systems," in *Solid Freeform Fabrication Symposium*, 2013, pp. 282–296.
- [177] J. A. Paulsen, M. Renn, K. Christenson, and R. Plourde, "Printing conformal

- electronics on 3D structures with aerosol jet technology,” in *FIIW 2012 - 2012 Future of Instrumentation International Workshop Proceedings*, 2012, pp. 47–50.
- [178] M. S. Saleh, C. Hu, and R. Panat, “Three-dimensional microarchitected materials and devices using nanoparticle assembly by pointwise spatial printing,” *Science Advances*, vol. 3, no. 3, p. e1601986, Mar. 2017.
- [179] M. S. Saleh, J. Li, J. Park, and R. Panat, “3D printed hierarchically-porous microlattice electrode materials for exceptionally high specific capacity and areal capacity lithium ion batteries,” *Additive Manufacturing*, vol. 23, pp. 70–78, Oct. 2018.
- [180] M. Sadeq Saleh, M. HamidVishkasougheh, H. Zbib, and R. Panat, “Polycrystalline micropillars by a novel 3-D printing method and their behavior under compressive loads,” *Scripta Materialia*, vol. 149, pp. 144–149, May 2018.
- [181] I. S. Akhatov, J. M. Hoey, O. F. Swenson, and D. L. Schulz, “Aerosol focusing in micro-capillaries: Theory and experiment,” *Journal of Aerosol Science*, vol. 39, no. 8, pp. 691–709, Aug. 2008.
- [182] I. S. Akhatov, J. M. Hoey, O. F. Swenson, and D. L. Schulz, “Aerosol flow through a long micro-capillary: collimated aerosol beam,” *Microfluidics and Nanofluidics*, vol. 5, no. 2, pp. 215–224, Aug. 2008.
- [183] D. L. Schulz *et al.*, “Collimated aerosol beam deposition: sub 5-micrometer resolution of printed actives and passives,” in *2008 Flexible Electronics and Displays Conference and Exhibition*, 2008, vol. 33, no. 2, pp. 1–8.
- [184] X. Wang and P. H. McMurry, “A Design Tool for Aerodynamic Lens Systems,” *Aerosol Science and Technology*, vol. 40, no. 5, pp. 320–334, 2006.

- [185] L. Qi, P. H. McMurry, D. J. Norris, and S. L. Girshick, "Micropattern Deposition of Colloidal Semiconductor Nanocrystals by Aerodynamic Focusing," *Aerosol Science and Technology*, vol. 44, no. 1, pp. 55–60, Jan. 2010.
- [186] S. L. Girshick, "Aerosol processing for nanomanufacturing," *Journal of Nanoparticle Research*, vol. 10, no. 6, pp. 935–945, Aug. 2008.
- [187] J. Park, J. Jeong, C. Kim, and J. Hwang, "Deposition of Charged Aerosol Particles on a Substrate by Collimating Through an Electric Field Assisted Coaxial Flow Nozzle," *Aerosol Science and Technology*, vol. 47, no. 5, pp. 512–519, May 2013.
- [188] Sonaer Ultrasonics, "Ultrasonic Atomizer Spray Nozzle Technology." [Online]. Available: http://www.sonozap.com/Atomizer_Nozzles.html. [Accessed: 11-May-2016].
- [189] Sono-Tek, "MicroMist Ultrasonic Nozzle." [Online]. Available: <http://www.sono-tek.com/micromist/>. [Accessed: 10-May-2016].
- [190] K. Tokarska *et al.*, "Selective cancer-killing ability of new efficient porphyrin-based nanophotosensitizer in Lab-on-a-chip system," *Sensors and Actuators B: Chemical*, vol. 282, pp. 665–674, Mar. 2019.
- [191] A. W. Justin, R. A. Brooks, and A. E. Markaki, "Multi-casting approach for vascular networks in cellularized hydrogels," *Journal of The Royal Society Interface*, vol. 13, no. 125, p. 20160768, Dec. 2016.
- [192] C. Cimmino, L. Rossano, P. A. Netti, and M. Ventre, "Spatio-Temporal Control of Cell Adhesion: Toward Programmable Platforms to Manipulate Cell Functions and Fate," *Frontiers in Bioengineering and Biotechnology*, vol. 6, Dec. 2018.
- [193] Z. Tong *et al.*, "Engineering a functional neuro-muscular junction model in

- a chip," *RSC Adv.*, vol. 4, no. 97, pp. 54788–54797, 2014.
- [194] B. Guillotin and F. Guillemot, "Cell patterning technologies for organotypic tissue fabrication," *Trends in Biotechnology*, vol. 29, no. 4, pp. 183–190, 2011.
- [195] J. P. K. Armstrong *et al.*, "Engineering Anisotropic Muscle Tissue using Acoustic Cell Patterning," *Advanced Materials*, vol. 30, no. 43, pp. 1–7, 2018.
- [196] J. A. Park *et al.*, "Freeform micropatterning of living cells into cell culture medium using direct inkjet printing," *Scientific Reports*, vol. 7, no. 1, pp. 1–11, 2017.
- [197] C. Colosi *et al.*, "Microfluidic Bioprinting of Heterogeneous 3D Tissue Constructs Using Low-Viscosity Bioink," *Advanced Materials*, vol. 28, no. 4, pp. 677–684, Jan. 2016.
- [198] Q. Gao, Y. He, J. Fu, A. Liu, and L. Ma, "Biomaterials Coaxial nozzle-assisted 3D bioprinting with built-in microchannels for nutrients delivery," *Biomaterials*, vol. 61, pp. 203–215, 2015.
- [199] L. Ouyang, R. Yao, X. Chen, J. Na, and W. Sun, "3D printing of HEK 293FT cell-laden hydrogel into macroporous constructs with high cell viability and normal biological functions 3D printing of HEK 293FT cell-laden hydrogel into macroporous constructs with high cell viability and normal biological funct," 2015.
- [200] M. Wang, J. He, Y. Liu, M. Li, D. Li, and Z. Jin, "The trend towards in vivo bioprinting," *International Journal of Bioprinting*, no. September, 2015.
- [201] K. B. Lee, J. H. Lim, and C. A. Mirkin, "Protein nanostructures formed via direct-write dip-pen nanolithography," *Journal of the American Chemical Society*, vol. 125, no. 19, pp. 5588–5589, 2003.

- [202] R. O. Hynes, "The Extracellular Matrix: Not Just Pretty Fibrils," *Science*, vol. 326, no. 5957, pp. 1216–1219, Nov. 2009.
- [203] E. K. F. Yim, S. W. Pang, and K. W. Leong, "Synthetic Nanostructures Inducing Differentiation of Human Mesenchymal Stem Cells into Nueronal Lineage," *NIH Public Access*, vol. 72, no. 2, pp. 181–204, 2011.
- [204] A. Perl, D. N. Reinhoudt, and J. Huskens, "Microcontact Printing: Limitations and Achievements," *Advanced Materials*, vol. 21, no. 22, pp. 2257–2268, Jun. 2009.
- [205] G. J. Marquez, M. J. Renn, and W. D. Miller, "Aerosol-Based Direct-Write of Biological Materials for Biomedical Applications," *MRS Proceedings*, vol. 698, p. Q5.2.1, Jan. 2001.
- [206] M. Große Holthaus and K. Rezwan, "Comparison of Three Microstructure Fabrication Methods for Bone Cell Growth Studies," in *ASME 2008 International Manufacturing Science and Engineering Conference, Volume 2*, 2008, pp. 483–490.
- [207] M. N. De Silva, J. Paulsen, M. J. Renn, and D. J. Odde, "Two-step cell patterning on planar and complex curved surfaces by precision spraying of polymers," *Biotechnology and Bioengineering*, vol. 93, no. 5, pp. 919–927, Apr. 2006.
- [208] P. M. Van Midwoud, A. Janse, M. T. Merema, G. M. M. Groothuis, and E. Verpoorte, "Comparison of biocompatibility and adsorption properties of different plastics for advanced microfluidic cell and tissue culture models," *Analytical Chemistry*, vol. 84, no. 9, pp. 3938–3944, 2012.
- [209] G. Shao, J. Wu, Z. Cai, and W. Wang, "Fabrication of elastomeric high-aspect-ratio microstructures using polydimethylsiloxane (PDMS) double casting technique," *Sensors and Actuators A: Physical*, vol. 178, pp. 230–

236, May 2012.

- [210] ASTM International, "Standard Test Methods for Measuring Adhesion by Tape Test," 2013.
- [211] Little Machine Shop, "Stub Acme Thread Data Sheets." [Online]. Available: https://littlemachineshop.com/images/gallery/instructions/Stub_Acme_Thread_Data_Sheets_Rev_A.pdf. [Accessed: 18-Aug-2018].
- [212] Autodesk, "Getting Started with G-code." [Online]. Available: <https://www.autodesk.com/industry/manufacturing/resources/manufacturing-engineer/g-code>. [Accessed: 03-Oct-2018].
- [213] R. Eckstein, G. Hernandez-Sosa, U. Lemmer, and N. Mechau, "Aerosol jet printed top grids for organic optoelectronic devices," *Organic Electronics*, vol. 15, no. 9, pp. 2135–2140, Sep. 2014.
- [214] M. Ha, W. Zhang, D. Braga, M. J. Renn, C. H. Kim, and C. D. Frisbie, "Aerosol-Jet-Printed, 1 Volt H-Bridge Drive Circuit on Plastic with Integrated Electrochromic Pixel," *ACS Applied Materials & Interfaces*, vol. 5, no. 24, pp. 13198–13206, Dec. 2013.
- [215] R. Aga, C. Jordan, R. S. Aga, C. M. Bartsch, and E. M. Heckman, "Metal electrode work function modification using aerosol jet printing," *IEEE Electron Device Letters*, vol. 35, no. 11, pp. 1124–1126, 2014.
- [216] J. Navratil, A. Hamacek, J. Reboun, and R. Soukup, "Perspective methods of creating conductive paths by Aerosol Jet Printing technology," *Proceedings of the International Spring Seminar on Electronics Technology*, vol. 2015-Septe, pp. 36–39, 2015.
- [217] M. Ha *et al.*, "Printed, Sub-3V Digital Circuits on Plastic from Aqueous Carbon Nanotube Inks," *ACS Nano*, vol. 4, no. 8, pp. 4388–4395, Aug. 2010.

- [218] K. Hong, S. H. Kim, A. Mahajan, and C. D. Frisbie, "Aerosol Jet Printed p- and n-type Electrolyte-Gated Transistors with a Variety of Electrode Materials: Exploring Practical Routes to Printed Electronics," *ACS Applied Materials & Interfaces*, vol. 6, no. 21, pp. 18704–18711, Nov. 2014.
- [219] F. Zare Bidoky and C. D. Frisbie, "Parasitic Capacitance Effect on Dynamic Performance of Aerosol-Jet-Printed Sub 2 V Poly(3-hexylthiophene) Electrolyte-Gated Transistors," *ACS Applied Materials & Interfaces*, vol. 8, no. 40, pp. 27012–27017, Oct. 2016.
- [220] T. Mochizuki, Y. Takigami, T. Kondo, and H. Okuzaki, "Fabrication of flexible transparent electrodes using PEDOT:PSS and application to resistive touch screen panels," *Journal of Applied Polymer Science*, vol. 135, no. 10, p. 45972, Mar. 2018.
- [221] F. Pires, Q. Ferreira, C. A. V. Rodrigues, J. Morgado, and F. C. Ferreira, "Neural stem cell differentiation by electrical stimulation using a cross-linked PEDOT substrate: Expanding the use of biocompatible conjugated conductive polymers for neural tissue engineering," *Biochimica et Biophysica Acta - General Subjects*, vol. 1850, no. 6, pp. 1158–1168, Jun. 2015.
- [222] W. J. Diamond, *Practical Experiment Designs for Engineers and Scientists*, 2nd Editio. New York: Van Nostrand Reinhold, 1989.
- [223] Cancer Research UK, "Bowel cancer statistics," 2018. [Online]. Available: www.cancerresearchuk.org/health-professional/cancer-statistics/statistics-by-cancer-type/bowel-cancer#heading-One. [Accessed: 09-Apr-2018].
- [224] World Health Organization, "Cancer Factsheet," 2018. [Online]. Available: <http://www.who.int/mediacentre/factsheets/fs297/en/>. [Accessed: 12-Apr-2018].

- [225] E. Stavrinidou *et al.*, “Direct Measurement of Ion Mobility in a Conducting Polymer,” *Advanced Materials*, vol. 25, pp. 4488–4493, 2013.
- [226] M. Lampin, C. Legris, and M. Degrange, “Correlation between substratum roughness and wettability, cell adhesion, and cell migration - Lampin - 1998 - Journal of Biomedical Materials Research.pdf,” 1996.
- [227] M. Khodaie, “Statistical Design and Analysis of Experiments.” [Online]. Available: <https://ysjournal.com/archive/issue-6/statistical-design-and-analysis-of-experiments/>. [Accessed: 14-Dec-2016].

Appendix A: White Light Data Processing

1. Unprocessed image data viewed on the Vision64 software

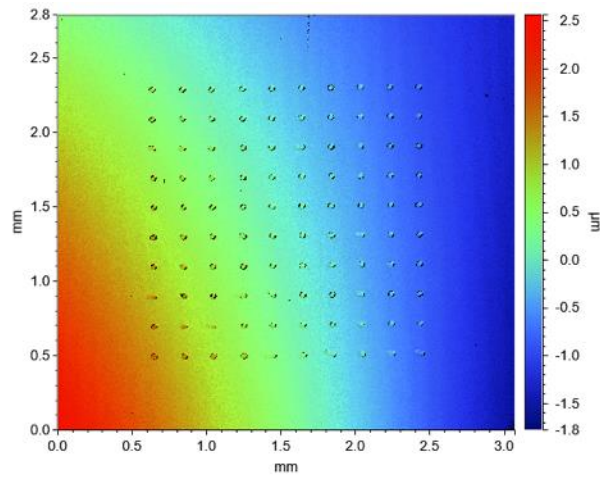


Figure E1: Unprocessed white light data

2. The features are masked

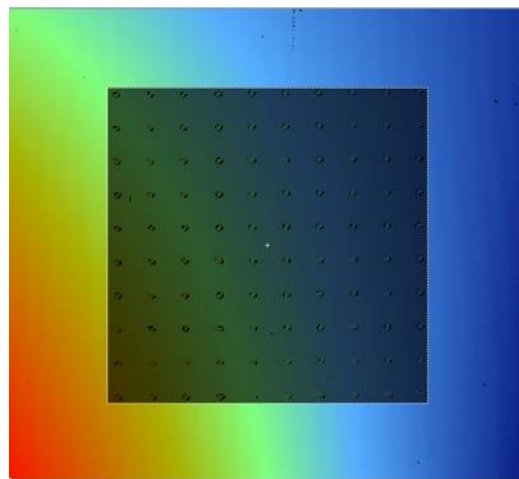


Figure E2: Masking step

3. The background is flattened using a terms removal

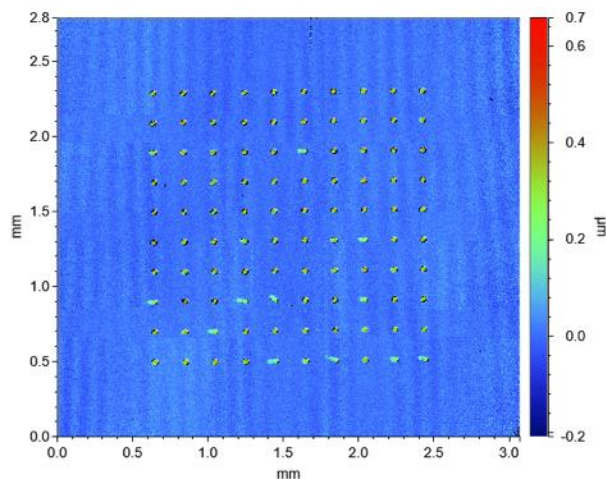


Figure E3: Data after flattening

4. Any artefacts are removed with a data restore, which fills blank pixels using an average of the surrounding features

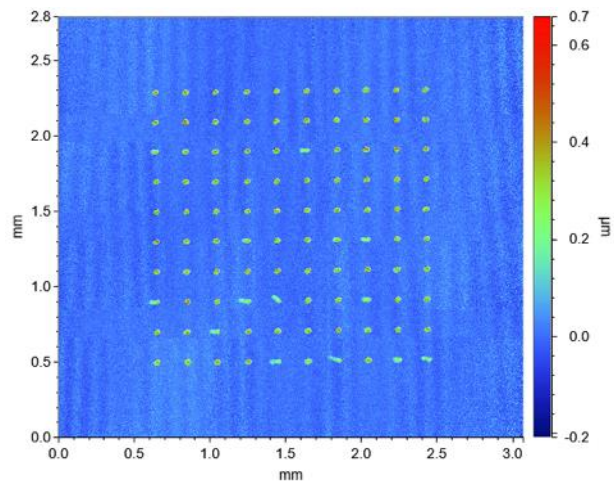


Figure E4: Data after data restore

5. Noise is removed by running a sigma filter

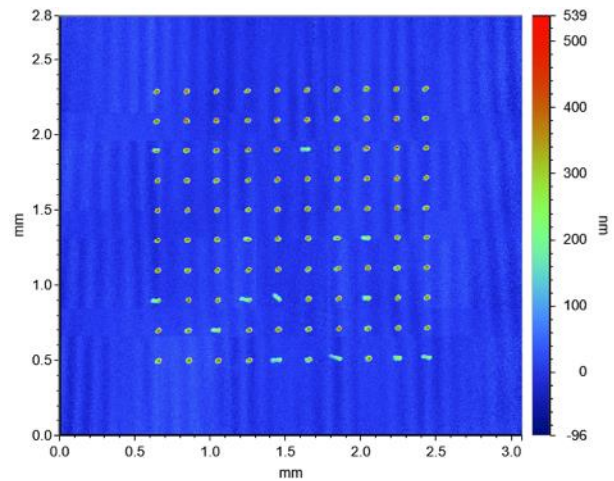


Figure E5: Data after filter

6. Data is rotated and magnified.

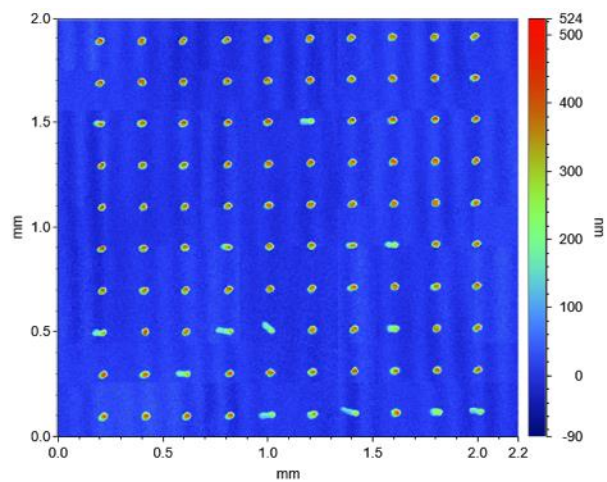


Figure E6: Data after rotation and magnification

Appendix B: Python Code to Generate Shapes from Equations

```
#Import libraries

import math

#Defines a subroutine that is useful for stepping by non-integers
def drange(start,stop,step):

    r = start

    while r<stop:

        yield r

        r+=step

#Define input variables

#Add equation further down, needs to be edited in the for loop currently
caseSelector=2 #0 is cartesian, 1 is polar, 2 is parametric

intermittent=0 #Decides if the code will output intermittent or continuous, 0
continuous, 1 intermitent.

minStepSize=0.08 #Minimum step size of the machine

scale=1 #scale

eqnStep=(minStepSize/(scale*0.1) #equation step size (preferably much smaller
than minimum step size of the machine

eqnMinValue=1 #equation min

eqnMaxValue = 3.14159 #equation up to

#Set up arrays and index initialisers
```

```

floatInput=list(drangle(eqnMinValue,eqnMaxValue,eqnStep)) #generate float
values for x

arrayLength =int(1+(eqnMaxValue-eqnMinValue)/eqnStep) #Calculates required
array length

#Delete any errors due to rounding floats
if len(floatInput)<arrayLength:
    arrayLength=arrayLength-1

tArray=[0]*arrayLength #Set up tArray
rArray=[0]*arrayLength #Set up rArray
thetaArray=[0]*arrayLength #Set up thetaArray
xArray=[0]*arrayLength #Set up xArray for absolute coordinates
yArray=[0]*arrayLength #Set up yArray for absolute coordinate
xModArray=[0]*arrayLength #Set up xDifArray for incremental coordinates
yModArray=[0]*arrayLength #Set up yDifArray for incremental coordinates
modArray=[0]*arrayLength #Set up modArray for the movements

#Populate Absolute and Modulator
if caseSelector==0: #Cartesian case
    for idx in range (1,arrayLength,1):
        xArray[idx]=floatInput[idx] #populates x with floatInput
        yArray[idx]=xArray[idx]**3 #input equation here
elif caseSelector==1: #Polar Case
    for idx in range (1,arrayLength,1):
        thetaArray[idx]=floatInput[idx]
        rArray[idx]=(3**2)/thetaArray[idx]#input equation here
        xArray[idx]=rArray[idx]*math.cos(thetaArray[idx])

```

```
yArray[idx]=rArray[idx]*math.sin(thetaArray[idx])
```

```
elif caseSelector==2:
```

```
for idx in range (1,arrayLength,1):
```

```
    tArray[idx]=floatInput[idx]
```

```
    xArray[idx]=1*(math.sin(tArray[idx])*(exp(math.cos(tArray[idx])-
```

```
2*math.cos(4*tArray[idx])-math.sin(tArray[idx]/12)**5) #input x equation here
```

```
    yArray[idx]=1*(math.cos(tArray[idx])*(exp(math.cos(tArray[idx])-
```

```
2*math.cos(4*tArray[idx])-math.sin(tArray[idx]/12)**5) #input y equation here
```

```
for scaleIdx in range (1,arrayLength,1):
```

```
    xArray[scaleIdx]=scale*xArray[scaleIdx] #Apply scale factor to x and y  
coordinates
```

```
    yArray[scaleIdx]=scale*yArray[scaleIdx]
```

```
for modIdx in range (1,arrayLength,1):
```

```
    xModArray[modIdx]=xArray[modIdx]-xArray[modIdx-1] #x values to calculate  
modulus
```

```
    yModArray[modIdx]=yArray[modIdx]-yArray[modIdx-1] #y values to calculate  
modulus
```

```
modArray[modIdx]=math.sqrt((xModArray[modIdx]**2)+(yModArray[modIdx]**2))
```

```
#calcualte modulus, square root of X squared + Y squared
```

```
#Delete move that are too small
```

```
delIdx=arrayLength-1
```

```

while (delIdx>=1): #while index is larger than 1
    if modArray[delIdx]<minStepSize: #if the modulus of that index is bigger than
a set value
        whileLoopModValue=modArray[delIdx-1] #record the value of the modulus
you will delete
        del modArray[delIdx-1] #delete the modulus value
        del xArray[delIdx-1] #delete the x value
        del yArray[delIdx-1] #delete the y value
        modArray[delIdx-1]=modArray[delIdx-1]+whileLoopModValue #add the
recorded (and deleted) value onto the old modulus, to make the new modulus
value
        whileArrayLength=len(modArray)-1 #a value has been deleted so the length
is reduced by one
        delIdx=whileArrayLength-1 #the index is re-set so the code is checked again
for the beginning
    else: #or else
        delIdx-=1 #just reduce the index and keep checking

#Setting up new indexes and arrays
newArrayLength=len(xArray)
xDifArray=[0]*newArrayLength #Set up xDifArray for incremental coordinates
yDifArray=[0]*newArrayLength #Set up yDifArray for incremental coordinates

#Populate incremental coordinate arrays
for idx in range (1,newArrayLength,1):
    xDifArray[idx]=xArray[idx]-xArray[idx-1]

```

```
yDifArray[idx]=yArray[idx]-yArray[idx-1]
```

```
idx=idx+1
```

```
#delete redundant point
```

```
del xArray[0]
```

```
del yArray[0]
```

```
del xDifArray[0]
```

```
del yDifArray[0]
```

```
newArrayLength=newArrayLength-1
```

```
#Output file absolute
```

```
text_file=open("Absolute.txt","w")
```

```
text_file.write("(Begin Start Up)\nG90 G80 G17 G21 G40
```

```
G49\nM08\nG00X0Y0Z0\nF100\n(End Start Up)\nM09\n")
```

```
if intermittent==0:
```

```
    for writeldx in range (0,newArrayLength):
```

```
        line = "G01 X{0:.6g} Y{1:.6g}\n".format(xArray[writeldx],yArray[writeldx])
```

```
        text_file.write(line)
```

```
else:
```

```
    for writeldx in range (0,newArrayLength):
```

```
        line = "G01 X{0:.6g} Y{1:.6g}\n".format(xArray[writeldx],yArray[writeldx])
```

```
        text_file.write(line)
```

```
        text_file.write(line)
```

```
text_file.write("(End Program)\nM08\nG00 X-2 Y-2 Z-4\nM30\n%\n")
```

```
text_file.close()
```

```

#Output file incremental

text_file=open("Incremental.txt","w")

text_file.write("(Begin   Start   Up)\nG90   G80   G17   G21   G40
G49\nM08\nG00X0Y0Z0\nF100\n(End Start Up)\nM09\nM98 P1000 L1\n(End
Program)\nM08\nG90\nG00 X-2 Y-2 Z-4\nM30\n%\n\nO1000\nG91")

if intermittent==0:

    for writeldx in range (0,newArrayLength):

        line           =           "G01           X{0:.6g}
Y{1:.6g}\n".format(xDifArray[writeldx],yDifArray[writeldx])

        text_file.write(line)

    else:

        for writeldx in range (0,newArrayLength):

            line           =           "G01           X{0:.6g}
Y{1:.6g}\nM09\nM08\n".format(xDifArray[writeldx],yDifArray[writeldx])

            text_file.write(line)

text_file.write("M99\n")

text_file.close()

print "The code has executed"

```

Appendix C: Automated Machine Testing G-Code Script

%
OMTSP (Material Test Standard Pattern)
(TEST PATTERN SET UP FOR LINE WIDTH OF 50 MICROMETERS)

(BEGIN START UP)
G90 G80 G17 G21 G40 G49
M08
F15
G00 X0 Y0 Z0
(END START UP)

(DRAW AXIS)
G00 X-1 Y-1
M09
G01 X14
G91
G01 X-0.3 Y-0.3
M08
G01 X0.3 Y0.3
M09
G01 X-0.3 Y0.3
M08
G90
G00 X-1 Y-1
M09
G01 Y5
G91
G01 X-0.3 Y-0.3
M08
G01 X0.3 Y0.3
M09
G01 X0.3 Y-0.3
M08
G90
G00 X0 Y0
(END DRAW AXIS)

(START Patterning)
O3000
(START 1A)
G52 X0 Y0 Z0
M98 P2000 L1
(END A)
(START 1B)
G52 X1.5 Z1
M98 P2000 L1
G52 X0 Z0
(END B)

```

(START 1C)
G52 X3 Z2
M98 P2000 L1
G52 X0 Y0 Z0
(END 1C)
(START 2A)
G52 X4.5
M98 P2000 L2
(END 2A)
(START 2B)
G52 X6 Z1
M98 P2000 L2
G52 X0 Z0
(END 2B)
(START 2C)
G52 X7.5 Z2
M98 P2000 L2
G52 X0 Y0 Z0
(END 1C)
(START 3A)
G52 X9
M98 P2000 L3
(END 3A)
(START 3B)
G52 X10.5 Z1
M98 P2000 L3
G52 X0 Z0
(END 3B)
(START 3C)
G52 X12 Z2
M98 P2000 L3
G52 X0 Y0 Z0
(END 3C)
G00 X-5 Y-5 Z40
M08
M09
M08
M09
M08
M09
M30
(END Patterning)
M30

(START Feed Rate Subroutine)
O2000
(START I)
F15
M98 P1000 L1
(END 1AI)

(START II)

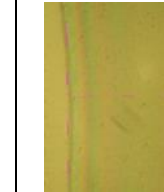
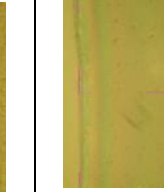
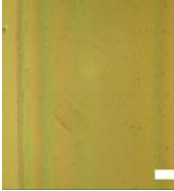
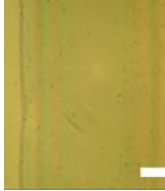
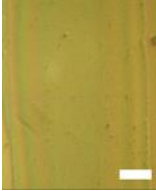
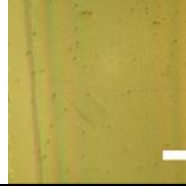
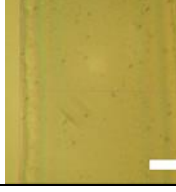
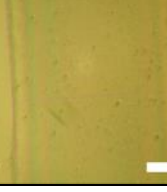
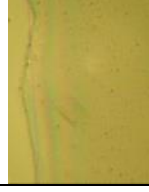
```

G52 Y1.5
F10
M98 P1000 L1
G52 Y0
(END II)

(START III)
G52 Y3
F5
M98 P1000 L1
G52 Y0
(END III)
(END Feed Rate Subroutine)
M99
(END 1)

(START TEST PATTERN SUBROUTINE)
O1000
G00 X0 Y0
M09
G00 X0.5
G01 Y1
G01 X1
G01 Y0.5
G01 X0
M08
G00 Y0
M99
(CLEAR TOOL - OR TO NEXT PRINT)
(END TEST PATTERN SUBROUTINE)

Appendix D: Time Stability Test Results

Min	5	10	15	20	25	30	35
Result							
Min	40	45	50	55	60	65	70
Result							
Min	75	80	85	90	95	100	110
Result							
Min	115	120	125	130	135	140 -- Failure	
Results							All scale bars 20μm

Appendix E: Operational Window Testing

Experimental Design

Effect of nozzle exit diameter on trace width at a constant pressure ratio

For these initial parametric tests material-substrate choices are inconsequential as the objective is to simply to verify the reduced trace width. Therefore the experiment was run using PEDOT:PSS formulation 4 onto a clean glass substrate. This was chosen as acceptable results were seen during the material composition testing. For this first test the value of the population variation was not known. Therefore the sample variation is used and a t-distribution is assumed instead of a normal distribution.

Assumptions

As the variance of the population is not known before the experiment, and it is assumed the variances will not be equal, a t distribution will be required. This distribution has an equivalent shape to the normal distribution, but the curve is wider. The width of the curve is a function of the number of the degrees of freedom of the experiment.

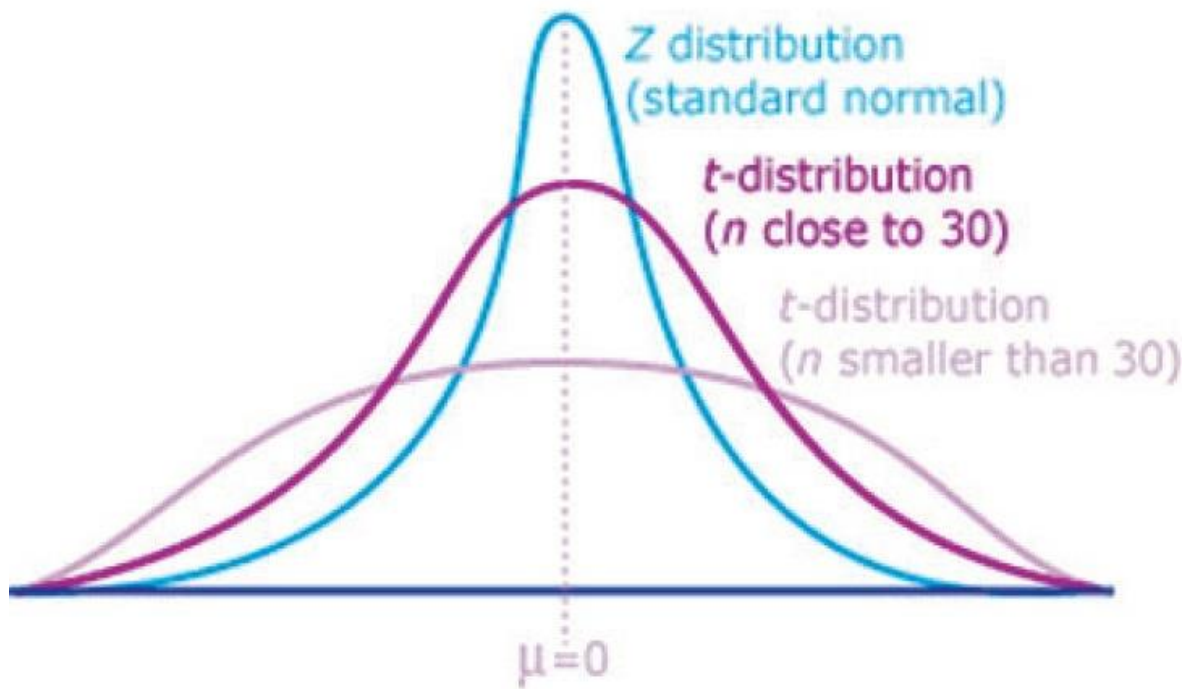


Figure D1: T-Distribution Compared to Normal Distribution [227]

In these conditions, two techniques exist to analyse the data successfully. Either estimating the variance (σ^2_x), or estimating the definition of a significant result (δ). Estimating the variance is seen as bad statistical practice if other methods are available, so an arrangement was used where it is assumed a significant result would be one standard deviation from the mean. i.e. $\delta = 1\sigma$. This method requires that the significant criterion to be established after the experiment is concluded.

Hypothesis

Null Hypothesis: Changing the nozzle size does not have an effect on line width.

$$H_0: \mu_{n200} = \mu_{n150} = \mu_{n100}$$

Alternative hypothesis: Changing the nozzle size reduces line width by a significant amount.

$$H_a: \mu_{n200} > \mu_{n150} > \mu_{n100}$$

Table D1: Observation matrix for nozzle size experiment

Observation

		No change in μ	Reduction in μ of δ
Truth	No change in μ	Understanding that the line width is not reduced by reduced nozzle diameter at the same operating pressure ratio $P=(1-\alpha)=90\%$	Experimenter makes alpha error $P=\alpha=10\%$ This error is not noticed and subsequent experimentation non-ideal.
	Reduction in μ of δ	Experimenter makes beta error $P=\beta=10\%$ This error is not noticed and subsequent experimentation non-ideal.	Understanding that the line width is reduced by reduced nozzle diameter at the same operating pressure ratio $P=(1-\beta)=90\%$

Initial Sample Size

As the population variances are unknown before the experiment. the required sample size can be calculated by

$$N_a=N_b=2(U_\alpha + U_\beta)^2 \left(\frac{\sigma}{\delta}\right)^2 = 2(U_\alpha + U_\beta)^2 \quad , as \delta = \sigma$$

$$= 2(1.282 + 1.282)^2 = 13.14$$

Where U_α and U_β are looked up in a table [222]. The initial number of trials to ensure >90% confidence level. For this situation $N_a=N_b>13.14$. Therefore in an efficient, valid test $N_a=N_b=14$. To confirm the requirement for a t-test the number of degrees of freedom was analysed using

$$\varphi = N_a + N_b - 2 = 14+14-2 = 26$$

As the degrees of freedom is significantly less than 60, the distribution is wider than a normal distribution. The requirement for a t-test to be carried out is confirmed.

Revised sample size for t test

As a t test is required, the number of samples required must be re-calculated to ensure statistical validity using this method. Therefore:

$$N_{at}=N_{bt}=2(t_\alpha + t_\beta)^2 \left(\frac{\sigma}{\delta}\right)^2 = 2(t_\alpha + t_\beta)^2 \quad , as \delta = \sigma$$

$$= 2(1.32 + 1.32)^2 = 13.94$$

Where t_α and t_β are looked up in a table [222]. To ensure >90% confidence level for this situation $N_{at}=N_{bt}>13.94$

Therefore, in an efficient, valid test $N_{at}=N_{bt}=14$

Methodology

The sheath and atomiser gases were then both set to a 1:1 flow rate ratio. The value for both flow rates was 25 SCCM, as this value produces a line at the selected nozzle sizes without exceeding the rated pressure of the sensors when using the smaller nozzles.

Results

Table D2: Results for nozzle size experiment

Nozzle Size (µm)	Measurements (µm)													
	1	2	3	4	5	6	7	8	9	10	11	12	13	14
300	95	103	128	132	104	132	124	108	133	127	133	147	135	134
250	98	122	97	101	103	105	112	120	121	96	98	108	106	128
200	105	93	90	103	96	96	80	78	78	86	67	67	68	81
150	88	101	96	100	92	90	89	90	98	91	91	89	84	100
100	44	41	43	44	55	44	45	44	50	45	42	39	40	43

Analysis

Table D3: Analysis of nozzle size experiment

Nozzle Size (µm)	\bar{X}	S^2	S
300	124	231	15
250	108	114	11
200	85	164	13
150	93	28	5
100	44	16	4

Objective criterion

A significant difference in results is

$$(\bar{X}_a - \bar{X}_b)^* = t_\alpha \sqrt{\frac{S_a}{N_{at}} + \frac{S_b}{N_{bt}}}$$

Nozzles were directly compared with the size above and below.

Significant Difference between 200 and 150 micron nozzles:

$$(\bar{X}_{200} - \bar{X}_{150})^* = 1.32 \sqrt{\frac{13.30}{14} + \frac{6.05}{14}} = 1.55 \mu\text{m}$$

Significant Difference between 150 and 100 micron nozzles:

$$(\bar{X}_{150} - \bar{X}_{100})^* = 1.32 \sqrt{\frac{6.05}{14} + \frac{4.06}{14}} = 1.12 \mu\text{m}$$

Objective Criterion and Assumptions for Subsequent Testing

- The variation of the line widths will not change through the subsequent experimentation
i.e. $\sigma^2_{s1} = \sigma^2_{s2} = \sigma^2_{s3}$
- The variance of the line widths is the population variance of the previous experiment. i.e. $S^2 = 16.49$

As the variance is known and assumed to be equal a t test is not required. The values of the constants are $U_\alpha = U_\beta = 1.282$. The output for the sample size is 13.14 requiring 14 samples to be taken in each case as long as the experiment is expressed as a one sided problem (i.e. an increase or decrease, not just a change).

The objective criterion is calculated using the assumed value of variance.

$$(\bar{X}_a - \bar{X}_b)^* = 1.282 \times 4.06 \sqrt{\frac{1}{14} + \frac{1}{14}} = 1.97 \mu\text{m}$$

Therefore, a change in the average line width of 2 micrometres is seen as a significant result in the following experimentation in this section.

Changing Scanning Speed

Hypothesis

Null Hypothesis: Changing the scanning speed does not have an effect on line width.

$H_0: \mu_{s10} = \mu_{s30} = \mu_{s50} = \mu_{s70} = \mu_{s90}$

Alternative hypothesis: Increasing the scanning speed reduces the line width.

$H_a: \mu_{s10} > \mu_{s30} > \mu_{s50} > \mu_{s70} > \mu_{s90}$

		Observation	
		No reduction in μ	Reduction in μ of 2 μm
Truth	No reduction in μ	Understanding that the line width is not affected by a changing scanning speed $P=(1-\alpha) = 90\%$	Experimenter makes alpha error $P= \alpha = 10\%$
	Reduction in μ of δ of 2 μm	Experimenter makes beta error $P=\beta=10\%$	Understanding that the line width is reduced by increasing scanning speed $P=(1-\beta)=90\%$

Test conditions

The test conditions are as described in section 5.4.1. The value of scanning speed only is varied.

Results

Table D4: Scanning Speed Results

Feed Rate	Measurements (μm)													
	1	2	3	4	5	6	7	8	9	10	11	12	13	14
30	20	23	27	26	28	56	56	49	52	53	48	49	52	63
50	29	24	44	40	36	50	47	47	29	50	31	49	44	47
70	30	37	30	31	34	30	31	35	30	31	34	34	31	34
90	38	30	36	36	30	31	33	32	38	39	34	36	34	38

Analysis

Table D5: Analysis of nozzle size experiment

Feed Rate	\bar{X}	S^2	S
30	42.94	215.60	14.68
50	40.52	83.03	9.11
70	32.14	4.80	2.19
90	34.56	10.16	3.19

Effect of changing Z height on trace width.

Hypothesis

Null Hypothesis: Changing the Z Standoff does not have an effect on line width.

$H_0: \mu_{z2} = \mu_{z2.5} = \mu_{z3} = \mu_{z3.5} = \mu_{z4}$

Alternative hypothesis: Increasing the Z Standoff increases line width.

$$H_a: \mu_{z2} > \mu_{z2.5} > \mu_{z3} > \mu_{z3.5} > \mu_{z4}$$

		Observation	
		No change in μ	Increase in μ of δ
Truth	No change in μ	Understanding that the line width is not affected by a changing Z stand off $P=(1-\alpha)$	Experimenter makes alpha error $P= \alpha$
	Increase in μ of δ	Experimenter makes beta error $P=\beta$	Understanding that the line width is affected by a changing Z stand off $P=(1-\beta)$

Test conditions

The test conditions are as described in section 5.4.1. The value of Z standoff only is varied.

Results

Table D6: Z Standoff Results

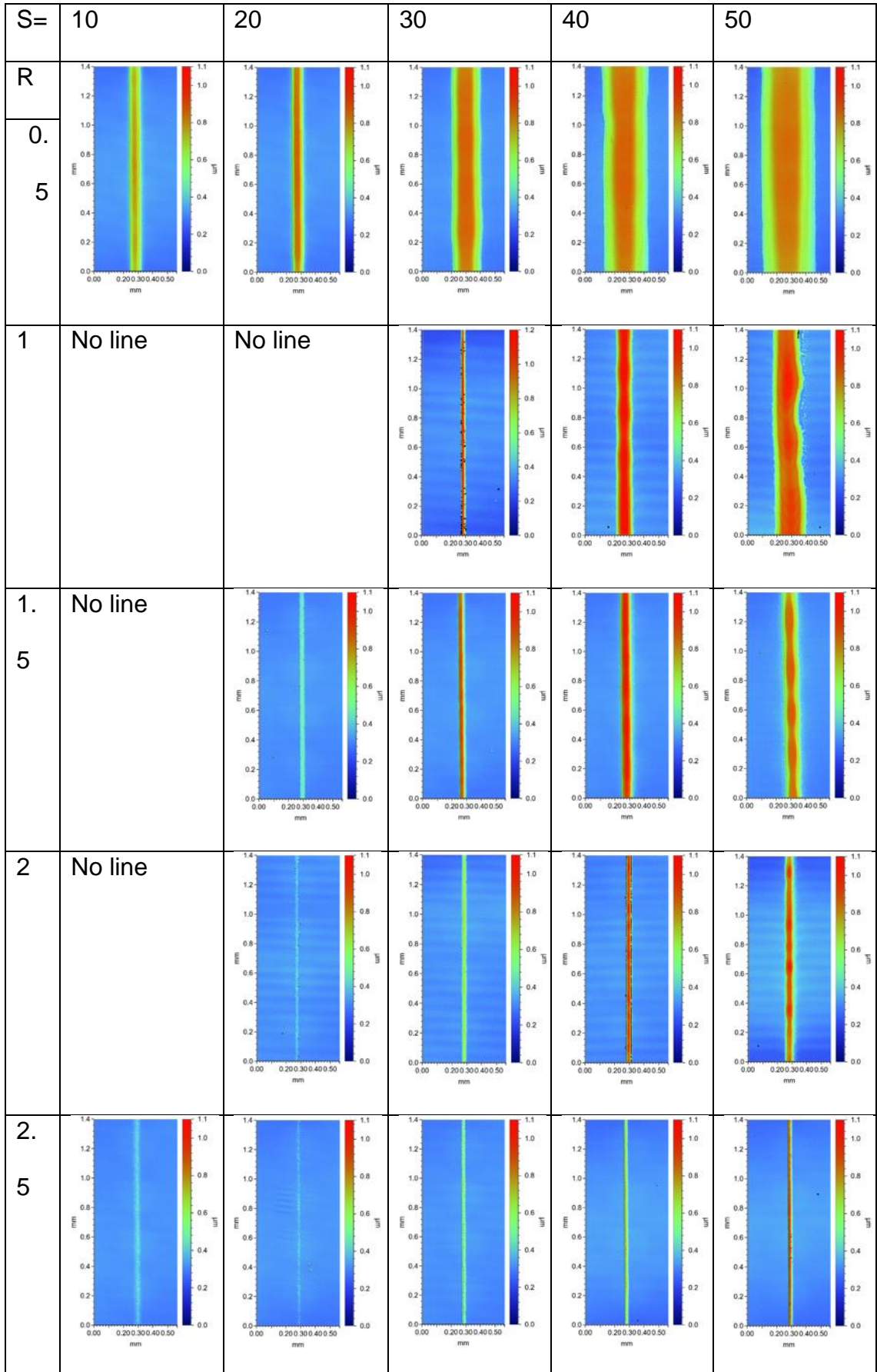
Z Height	Measurements (μm)													
	1	2	3	4	5	6	7	8	9	10	11	12	13	14
2.0	50	48	60	54	57	52	57	58	46	61	56	60	55	58
2.5	49	35	40	60	48	51	39	49	37	45	51	62	40	64
3.0	29	24	44	40	36	50	47	47	29	50	31	49	44	47
3.5	54	60	58	58	51	42	46	52	55	65	52	63	61	55
4.0	114	123	118	115	111	114	115	111	116	133	112	116	79	112

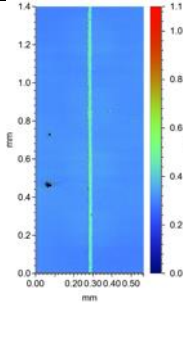
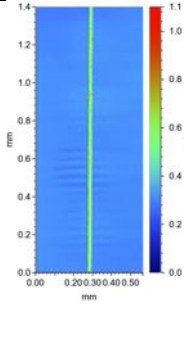
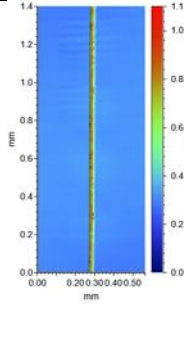
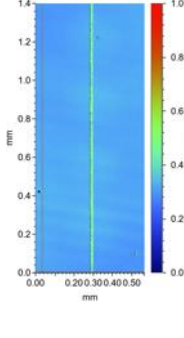
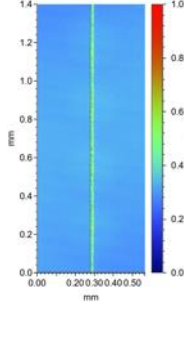
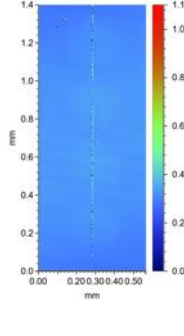
Analysis

Table D7: Analysis of Z Standoff Experiment

Z Height (mm)	\bar{X}	S^2	S
2.0	55.10	20.96	4.58
2.5	47.86	86.66	9.31
3.0	40.52	83.03	9.11
3.5	55.09	39.60	6.29
4.0	113.34	133.70	11.56

Appendix F: Full Focussing Ratio Test Results



3	No line	No line			
3. 5	No line	No line	No line		
4	No line	No line	No line	No line	

Appendix G: Two Level Multivariable Experimentation Method

Using the results of the process window verification, a multivariable experiment can be set up which facilitates the comparison of several variables and can help visualise their interactions. A matrix approach provides an efficient method to reduce the number of tests required to make these comparisons. A measurement of line width was used as the measured response, as the ultimate objective of the body of work is to jet the material into channels which will change the profile and spattering characteristics.

Table G1: Design of Experiment Boundary Conditions

Parameter	Lower Limit	Upper Limit
Sheath gas	30 sccm	40 sccm
Atomiser gas	20 sccm	25 sccm
Scanning speed	70 mm/min	90 mm/min
z stand-off	2.5 mm	3.5 mm

Hypotheses

Table G2: Design of Experiments Hypotheses

Subject	Null Hypothesis	Alternate Hypothesis
Sheath gas	Increasing sheath gas has no effect on line width	Increasing sheath gas reduces line width (H _a) ₁ : $\mu_{s30} > \mu_{s40}$ (H ₀) ₁ : $\mu_{s30} = \mu_{s40}$
Atomiser gas	Decreasing atomiser gas has no effect on line width	Decreasing atomiser gas reduces line width (H _a) ₂ : $\mu_{a20} < \mu_{a25}$ (H ₀) ₂ : $\mu_{a20} = \mu_{a25}$

Scanning speed	Increasing the scanning speed has no effect on line width $(H_0)_3: \mu_{f70} = \mu_{f90}$	Increasing the scanning speed reduces line width $(H_a)_3: \mu_{f70} > \mu_{f90}$
z stand-off	Decreasing the z stand-off has no affect on line width $(H_0)_4: \mu_{z2.5} = \mu_{z3.5}$	Increasing the z stand-off changes the line width $(H_a)_4: \mu_{z2.5} \neq \mu_{z3.5}$
Sheath gas/ atomiser gas interaction	There is no interaction between sheath gas and atomiser gas $(H_0)_5: \mu_{sa \text{ interaction}}=0$	There is an interaction between atomiser gas and sheath gas $(H_a)_5: \mu_{sa \text{ interaction}} > 0$
Sheath gas/ scanning speed interaction	There is no interaction between sheath gas and scanning speed $(H_0)_6: \mu_{sf \text{ interaction}}=0$	There is an interaction between atomiser gas and scanning speed $(H_a)_6: \mu_{sf \text{ interaction}} > 0$
Sheath gas/ z stand-off interaction	There is no interaction between sheath gas and z stand-off $(H_0)_7: \mu_{sz \text{ interaction}}=0$	There is an interaction between atomiser gas and z stand-off $(H_a)_7: \mu_{sz \text{ interaction}} > 0$
Atomiser gas/ scanning speed Interaction	There is no interaction between atomiser gas and scanning speed $(H_0)_8: \mu_{af \text{ interaction}}=0$	There is an interaction between atomiser gas and z stand-off $(H_a)_8: \mu_{af \text{ interaction}} > 0$

Atomiser gas/ z stand-off interaction	There is no interaction between atomiser gas and z stand-off	There is an interaction between atomiser gas and z stand-off
	(H ₀) ₉ : $\mu_{az \text{ interaction}}=0$	(H _a) ₉ : $ \mu_{az \text{ interaction}} > 0$
Scanning speed/ z stand-off interaction	There is no interaction between scanning speed and z stand-off	There is an interaction between scanning speed and z stand-off
	(H ₀) ₁₀ : $\mu_{fz \text{ interaction}}=0$	(H _a) ₁₀ : $ \mu_{fz \text{ interaction}} > 0$
Sheath gas/atomiser gas/ scanning speed interaction	There is no interaction between sheath gas, atomiser gas and scanning speed	There is an interaction between sheath gas, atomiser gas and scanning speed
	(H ₀) ₁₁ : $\mu_{saf \text{ interaction}}=0$	(H _a) ₁₁ : $ \mu_{saf \text{ interaction}} > 0$
Sheath gas/atomiser gas/ z stand-off interaction	There is no interaction between sheath gas, atomiser gas and scanning speed	There is an interaction between sheath gas, atomiser gas and scanning speed
	(H ₀) ₁₂ : $\mu_{saz \text{ interaction}}=0$	(H _a) ₁₂ : $ \mu_{saz \text{ interaction}} > 0$
Sheath gas/ scanning speed/ z stand-off interaction	There is no interaction between sheath gas, scanning speed and z stand-off	There is an interaction between sheath gas, scanning speed and z stand-off
	(H ₀) ₁₃ : $\mu_{sfz \text{ interaction}}=0$	(H _a) ₁₃ : $ \mu_{sfz \text{ interaction}} > 0$
Atomiser gas/scanning speed/ z stand-off interaction	There is no interaction between atomiser gas,	There is an interaction between atomiser gas,

	scanning speed and z stand-off	scanning speed and z stand-off
	(H ₀) ₁₄ : $\mu_{afz \text{ interaction}}=0$	(H _a) ₁₄ : $ \mu_{afz \text{ interaction}} > 0$
Sheath gas/ atomiser gas/ scanning speed/ z stand-off interaction	There is no interaction between sheath gas, atomiser gas, scanning speed and z stand-off	There is an interaction between sheath gas, atomiser gas, scanning speed and z stand-off
	(H ₀) ₁₅ : $\mu_{safz \text{ interaction}}=0$	(H ₀) ₁₅ : $ \mu_{safz \text{ interaction}} > 0$

Determination of Parameters

For this experimentation alpha and beta errors are 5%. A significant result is two standard deviations (~12µm).

$$N_a=N_b=2(U_\alpha + U_\beta)^2 \left(\frac{\sigma}{\delta}\right)^2 = \frac{2(U_\alpha+U_\beta)^2}{4} = 0.5 * (1.960 + 1.645)^2 = 6.50$$

Therefore 7 comparisons are necessary when creating the matrix for them to be significant with a tolerable error of 5%. The 16X16 Hadamard matrix will allow 8 comparisons of both individual parameters and interactions. The Hadamard matrix is simply a list of the 16 trials. The columns allow the analysis of different characteristics of the experiment. The first column (0) is a mathematical phenomenon and is not useful in the analysis of data. Each subsequent column is used to analyse the results of the 6 trials. The columns requires some processing depending on if it is analysing a single variable (Columns 1-4), a two way interaction (columns 5-7,9,10,15), a three way interaction (8,11,12,14), a four way interaction (13) or the variance of the experiment (not used in this analysis). The four variables were assigned as in Table G3.

Table G3: Variable Assignment for Hadamard Matrix

Variable	'High' value notation	Assigned to
A	a	Sheath Gas
B	b	Atomiser Gas
C	c	Scanning Speed
D	d	z stand-off

Variable interactions are denoted by columns with more than one variable name. By default, the variables are set to the low value in the experiments. The treatment combination column defines the variables which will have a 'high' value in each specific trial. The + and – cells in each column will be used in the analysis to compare the effect of the variable or the interaction. For example if one wanted to find the effect of the Sheath gas (variable A). Trials where A is high (1-4, 6, 8, 9, 12) can be compared to the remaining trials where A is low (5,7,10,11,13-15). This can be done manually (for example trial 1 compared with trial 16, trial 2 compared with trial 13 and so forth) or can be done quickly using the mathematical analysis used later in the method. The method to analyse interactions is similar but requires the additional post processing to ensure the data is as valid. For example, for the two way interactions it can be noted that in column 5, a + is when the combination 'ab' is not present in the trial. Therefore it is multiplied by -1 in the analysis to give the true value of the interaction.

Table G4: A 16x16 Hadamard matrix set up to measure four variables at two levels

	A	B	C	D	A	B	C	A	A	B	A	B	AB	A	A	Treatment
					B	C	D	B	C	D	B	C	CD	C	D	Combination
								D			C	D		D		

Tr ial	0	1	2	3	4	5	6	7	8	9	10	11	12	13	14	15		
1	+	+	-	-	-	+	-	-	+	+	-	+	-	+	+	+	a	
2	+	+	+	-	-	-	+	-	-	+	+	-	+	-	+	+	ab	
3	+	+	+	+	-	-	-	+	-	-	+	+	-	+	-	+	abc	
4	+	+	+	+	+	-	-	-	+	-	-	+	+	-	+	-	abcd	
5	+	-	+	+	+	+	-	-	-	+	-	-	+	+	-	+	bcd	
6	+	+	-	+	+	+	+	-	-	-	+	-	-	+	+	-	acd	
7	+	-	+	-	+	+	+	+	-	-	-	+	-	-	+	+	bd	
8	+	+	-	+	-	+	+	+	+	-	-	-	+	-	-	+	ac	
9	+	+	+	-	+	-	+	+	+	+	-	-	-	+	-	-	abd	
10	1	+	-	+	+	-	+	-	+	+	+	+	-	-	-	+	-	bc
11	1	+	-	-	+	+	-	+	-	+	+	+	+	-	-	-	+	cd
12	1	+	+	-	-	+	+	-	+	-	+	+	+	-	-	-	ad	
13	1	+	-	+	-	-	+	+	-	+	-	+	+	+	-	-	b	
14	1	+	-	-	+	-	-	+	+	-	+	-	+	+	+	-	c	
15	1	+	-	-	-	+	-	-	+	+	-	+	-	+	+	+	d	
16	1	+	-	-	-	-	-	-	-	-	-	-	-	-	-	-	None	

The treatment combinations defined above give the following process parameters to be analysed.

Table G5: Trial Conditions

Trial	Sheath Flow (SCCM)	Atomiser Flow (SCCM)	Scanning (mm/min)	Speed	Nozzle Height (mm)
1	40	20	70		2.5
2	40	25	70		2.5
3	40	25	90		2.5
4	40	25	90		3.5
5	30	25	90		3.5
6	40	20	90		3.5
7	30	25	70		3.5
8	40	20	90		2.5
9	40	25	70		3.5
10	30	25	90		2.5
11	30	20	90		3.5
12	40	20	70		3.5
13	30	25	70		2.5
14	30	20	90		2.5
15	30	20	70		3.5
16	30	20	70		2.5

Results

The initial experimental parameters were run three times, on three separate days with a disassembly and clean of the functional end of the machine after each run. The machine was re-assembled prior to each experiment. This improved the reliability of the results as they were not specific to a particular experimental run. The data was analysed by white light interferometry as described in the main text, and the results are shown in Table G6.

Table G6: White light interferometry data. (a) = day 1, (b) = day 2 (c) = day 3.

Trial	Step Height (nm)				WHM (μm)				Area (μm) ²			
	Sample 1	Sample 2	Sample 3		Sample 1	Sample 2	Sample 3		Sample 1	Sample 2	Sample 3	
1a	259	273	231		23.8	23.9	22.3		6.08	6.04	4.83	
1b	274	294	294		22.7	25.8	25.4		6.49	5.97	6.45	
1c	307	222	209		28.1	28.8	20.8		4.97	8.00	4.71	
	Mean	263	SD	34.846	Mean	24.6	SD	2.7	Mean	5.95	SD	1.03
2a	315	322	291		31.4	31.8	31.3		8.99	9.85	9.90	
2b	295	359	288		33.7	33.5	30.2		8.25	11.15	10.45	
2c	249	365	284		35.8	31.5	28.5		10.16	6.72	12.28	
	Mean	308	SD	37	Mean	32.0	SD	2.1	Mean	9.75	SD	1.62
3a	265	258	313		23.3	26.4	27.1		7.56	6.46	8.85	
3b	340	256	302		26.9	30.0	32.9		9.02	7.61	12.54	
3c	288	329	321		29.1	27.8	27.9		7.66	9.16	9.02	
	Mean	297	SD	32	Mean	27.9	SD	2.6	Mean	8.65	SD	1.72
4a	298	350	303		28.1	25.9	28.6		7.54	9.78	7.81	
4b	304	259	221		24.0	27.1	30.2		9.48	6.72	5.48	
4c	295	347	299		28.8	26.0	30.8		7.91	10.11	7.71	
	Mean	297	SD	40	Mean	27.7	SD	2.2	Mean	8.06	SD	1.50
5a	182	246	262		23.4	28.3	36.8		5.60	8.19	9.56	
5b	249	292	250		35.4	42.3	30.5		8.90	13.40	11.21	
5c	226	302	215		43.1	28.5	35.9		9.09	10.34	5.64	

	Mean	247	SD	37	Mean	33.8	SD	6.6	Mean	9.10	SD	2.50
6a	239	270	253		24.3	24.1	25.1		6.09	6.57	6.29	
6b	252	248	264		23.8	24.1	27.3		6.63	5.99	6.47	
6c	243	264	269		24.8	25.2	24.1		6.64	5.96	6.72	
	Mean	256	SD	11	Mean	24.8	SD	1.1	Mean	6.37	SD	0.30
7a	328	300	277		44.6	41.8	43.5		13.24	11.72	10.38	
7b	347	329	304		38.1	35.1	42.2		13.46	12.44	12.98	
7c	335	293	305		32.7	37.9	36.8		12.47	11.15	11.09	
	Mean	313	SD	23	Mean	39.2	SD	4.0	Mean	12.10	SD	1.07
8a	235	245	236		20.0	21.2	20.4		5.78	6.10	5.70	
8b	215	251	210		25.1	19.2	21.0		4.78	5.97	4.67	
8c	249	256	192		24.0	18.2	23.1		6.31	6.21	3.61	
	Mean	232	SD	22	Mean	21.4	SD	2.3	Mean	5.46	SD	0.91
9a	220	266	338		25.4	30.7	22.8		6.15	7.27	10.39	
9b	306	328	267		26.6	28.0	28.4		9.62	9.30	8.05	
9c	313	269	328		24.8	26.6	25.3		7.95	7.69	9.55	
	Mean	293	SD	39	Mean	26.5	SD	2.3	Mean	8.44	SD	1.36
10a	247	293	271		33.1	34.9	35.7		9.19	9.64	10.85	
10b	254	274	263		36.5	33.8	39.8		9.94	9.90	8.90	
10c	259	273	285		36.5	33.2	35.1		8.56	9.97	10.39	
	Mean	269	SD	15	Mean	35.4	SD	2.1	Mean	9.71	SD	0.72
11a	238	229	242		26.6	26.4	26.9		6.89	6.22	6.27	

11b	238	212	228		23.5	26.5	26.1		7.03	5.90	6.57	
11c	231	224	229		28.9	28.0	30.4		6.34	6.21	5.25	
	Mean	230	SD	9	Mean	27.0	SD	1.9	Mean	6.30	SD	0.53
12a	275	259	248		23	21.6	24.8		7.04	7.03	6.68	
12b	223	250	237		22.8	24.8	22.6		5.21	6.92	6.46	
12c	255	255	267		24.9	26.9	24.7		7.15	6.88	7.04	
	Mean	252	SD	15	Mean	24.0	SD	1.6	Mean	6.71	SD	0.60
13a	337	248	352		39.7	46	40.8		12.98	8.35	14.64	
13b	299	285	237		41.7	40.2	35.7		12.27	12.24	8.16	
13c	310	361	312		38.5	38.4	36.8		13.06	15.10	10.60	
	Mean	305	SD	43	Mean	39.8	SD	3.0	Mean	11.93	SD	2.47
14a	225	257	250		28.9	26.9	25.7		6.87	7.80	6.90	
14b	218	219	210		24.3	23.6	24.8		5.04	6.64	5.80	
14c	240	252	235		27.9	28.4	26.6		7.59	7.29	6.91	
	Mean	234	SD	17	Mean	26.3	SD	1.9	Mean	6.76	SD	0.86
15a	266	278	253		30.9	27.6	29.4		7.99	9.56	8.14	
15b	294	278	264		29.1	31.5	30.7		9.25	8.21	8.31	
15c	269	263	286		31.0	32.9	29.0		8.26	8.00	8.87	
	Mean	272	SD	13	Mean	30.2	SD	1.6	Mean	8.51	SD	0.57
16a	284	290	312		28.5	27.5	29		8.10	8.12	8.67	
16b	281	307	291		27.4	26.1	26.9		7.55	9.06	7.49	
16c	313	290	314		26.7	25.5	27.3		9.00	8.06	8.55	
	Mean	298	SD	13	Mean	27.2	SD	1.1	Mean	8.29	SD	0.57

The mean values of these analysis were taken forward for analysis using the matrix approach, and are summarised for clarity in Table

Table G7: Mean values of the data for each trial.

Trial	1	2	3	4	5	6	7	8	9	10	11	12	13	14	15	16
Area	5.9	9.7	8.7	8.1	9.1	6.4	12.1	5.5	8.4	9.7	6.3	6.7	11.9	6.8	8.5	8.3
WHM (μm)	25	32	28	28	34	25	39	21	27	35	27	24	40	26	30	27
Step Height (nm)	25	32	28	28	34	25	39	21	27	35	27	24	40	26	30	27

Calculation of Deviation and Objective Criterion

These three data sets were separately applied to the Hadamard matrix. The columns were each summed, averaged (by dividing by eight) and the results are shown in the main text.

The variance and objective criterion for each case was calculated using column one in the subsequent sections. Any column can be used to calculate an estimation of these values and this was verified by further analysis (not shown).

Cross Sectional Area

Table G8: First three columns of are data applied to Hadamard Matrix

Trial	Measured value of area (μm) ²	Colum 'A' when applied to Hadamard matrix
1	5.9	5.9
2	9.7	9.7
3	8.7	8.7
4	8.1	8.1
5	9.1	-9.1
6	6.4	6.4
7	12.1	-12.1
8	5.5	5.5
9	8.4	8.4
10	9.7	-9.7
11	6.3	-6.3
12	6.7	6.7
13	11.9	-11.9
14	6.8	-6.8
15	8.5	-8.5
16	8.3	-8.3

$$\text{Mean of positive values} = \bar{X}_{High} = 7.4$$

$$\text{Mean of negative values} = \bar{X}_{Low} = -9.1$$

$$\text{Variance of positive values} = S_{High}^2 = 2.3$$

$$\text{Variance of negative values} = S_{Low}^2 = 4.5$$

$$\text{Deviation} = S = \sqrt{\frac{S_{High}^2 + S_{Low}^2}{2}} = 1.84$$

And the objective criterion was calculated by:

$$\text{Objective Criterion} = \sqrt{2 \times \frac{S}{8} \times 1.44} = 0.98 \mu\text{m}^2$$

Width at Half Maximum

Table G9: First three columns of are data applied to Hadamard Matrix

Trial	Measured value of WHM (μm)	Column 'A' when applied to Hadamard matrix
1	25	25
2	32	32
3	28	28
4	28	28
5	34	-34
6	25	25
7	39	-39
8	21	21
9	27	27
10	35	-35
11	27	-27
12	24	24
13	40	-40
14	26	-26
15	30	-30
16	27	-27

$$\text{Mean of positive values} = \bar{X}_{High} = 26.1$$

$$\text{Mean of negative values} = \bar{X}_{Low} = -32.4$$

$$\text{Variance of positive values} = S_{High}^2 = 10.2$$

$$\text{Variance of negative values} = S_{Low}^2 = 29.7$$

$$Deviation = S = \sqrt{\frac{S_{High}^2 + S_{Low}^2}{2}} = 4.49$$

And the objective criterion was calculated by:

$$Objective\ Criterion = \sqrt{2 \times \frac{S}{8} \times 1.44} = 1.52\mu m$$

Step Height

Table G10: First three columns of are data applied to Hadamard Matrix

Tri al	Measured value of step height (nm)	Column 'A' when applied to Hadamard matrix
1	263	263
2	308	308
3	297	297
4	297	297
5	247	-247
6	256	256
7	313	-313
8	232	232
9	293	293
10	269	-269
11	230	-230
12	252	252
13	305	-305
14	234	-234
15	272	-272
16	298	-298

$$Mean\ of\ positive\ values = \bar{X}_{High} = 274.6$$

$$Mean\ of\ negative\ values = \bar{X}_{Low} = -271.0$$

$$Variance\ of\ positive\ values = S_{High}^2 = 748.6$$

$$Variance\ of\ negative\ values = S_{Low}^2 = 1035.2$$

$$Deviation = S = \sqrt{\frac{S_{High}^2 + S_{Low}^2}{2}} = 29.86$$

And the objective criterion was calculated by:

$$Objective\ Criterion = \sqrt{2 \times \frac{S}{8} \times 1.44} = 3.93nm$$

Finally, each column of the Hadamard matrix was summed, and divided by 8 to provide the mean value of the 8 comparisons (as described in the main text). Each value is compared against its objective criterion to determine significant processing parameters and interactions. If the value is over the objective criterion, the alternate hypothesis is accepted (i.e a significant change is observed, directly due to the variable or interaction). If the objective criterion is not accepted, the null hypotheses is accepted (that is, no significant change is observed due to the variable or interaction).

Appendix H: Additional Images of Cells Responding to Printed Features

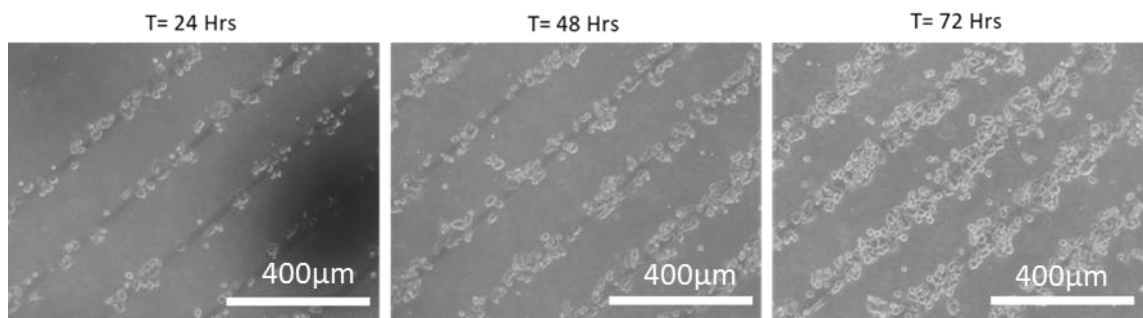


Figure I1: HCT-116 cells growing to lines.

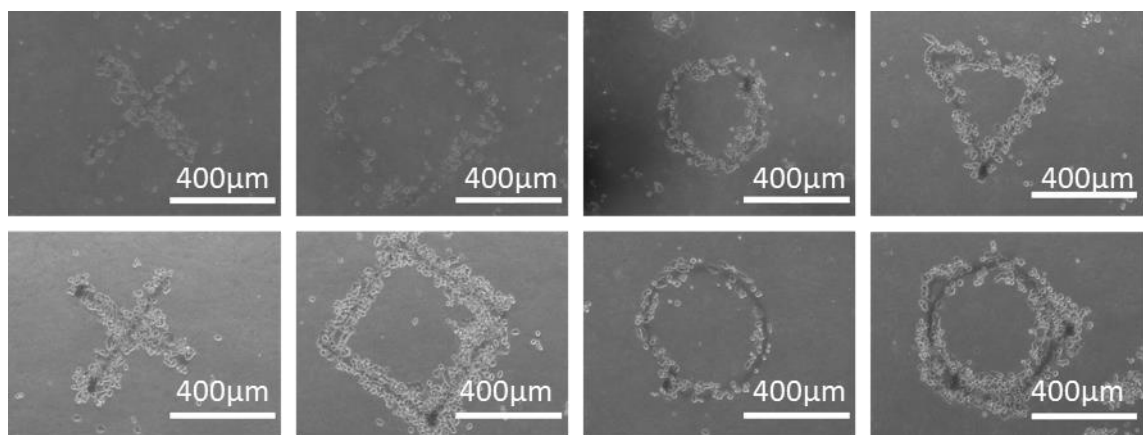


Figure I2: HCT-116 cells conforming to shapes as soon as 24 hours after seeding.

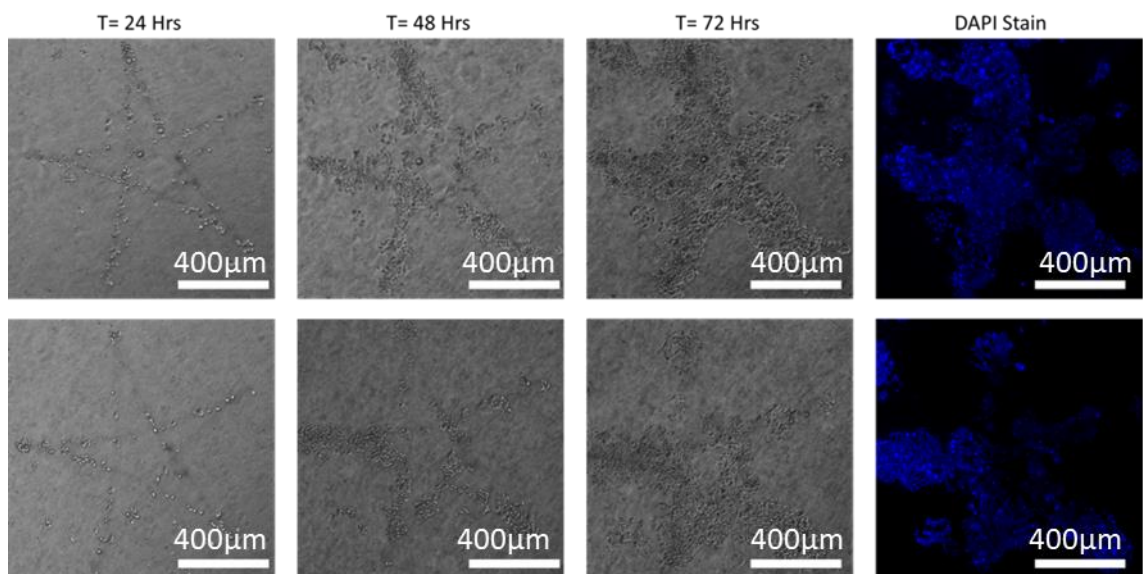


Figure I3: HCT-116 cells growing on a star over time.

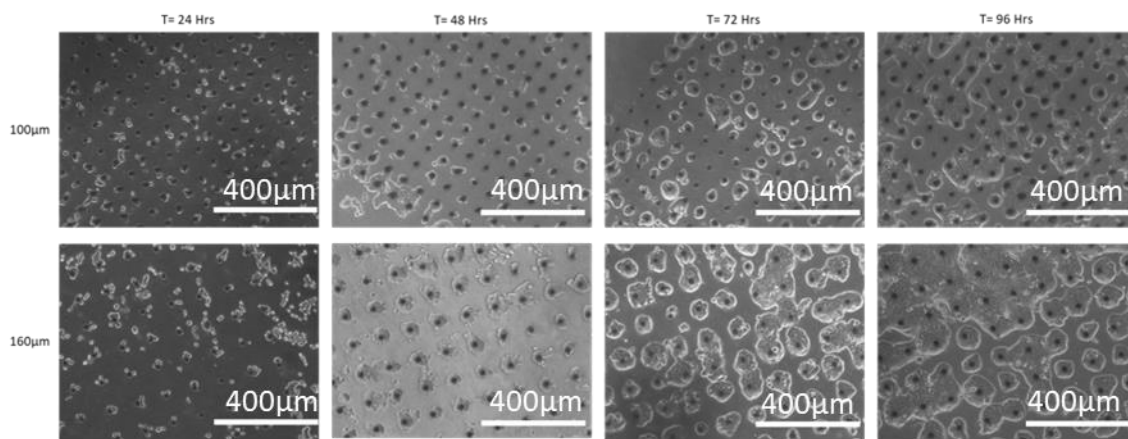


Figure 14: HT-29 cells growing to dot arrays.

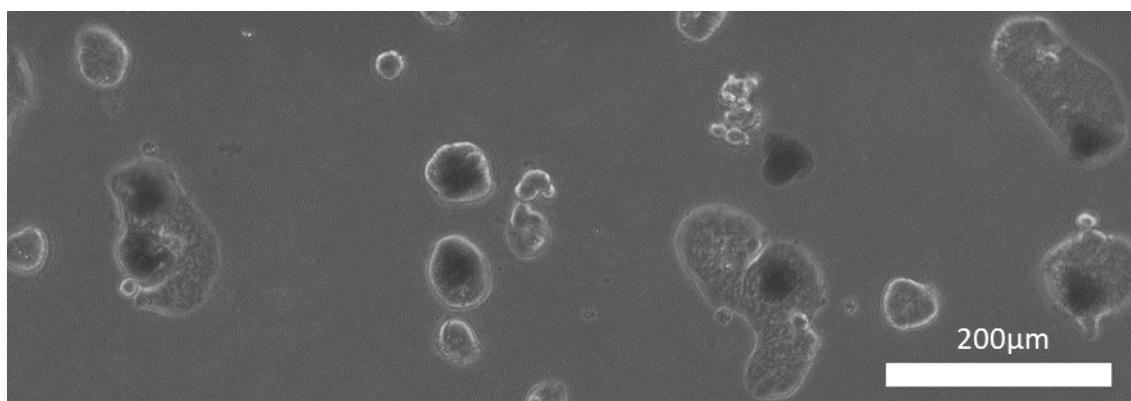


Figure 15: HT-29 cells growing on a motility test after 72 hours.

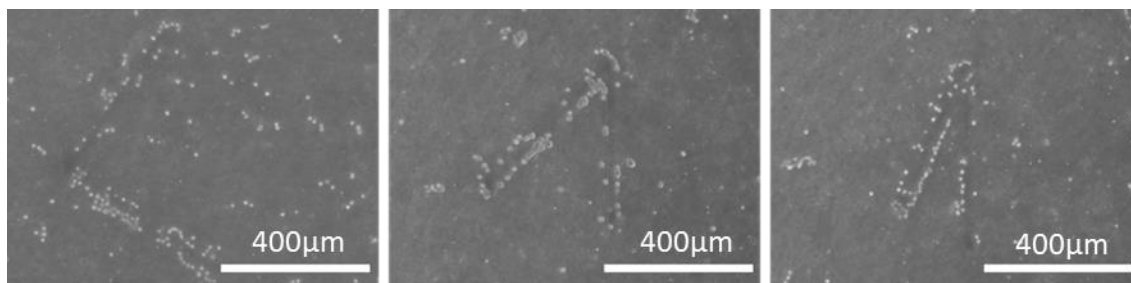


Figure 16: HT-29 cells tether to angles after 24 hours.

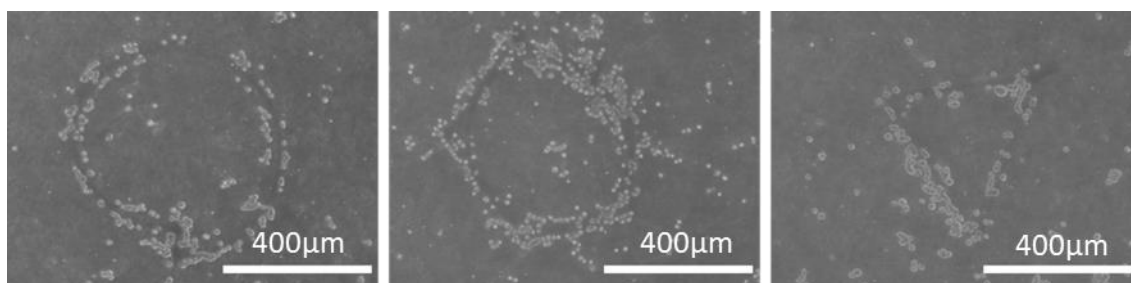


Figure 17: HT-29 cells tether to shapes after 24 hours.

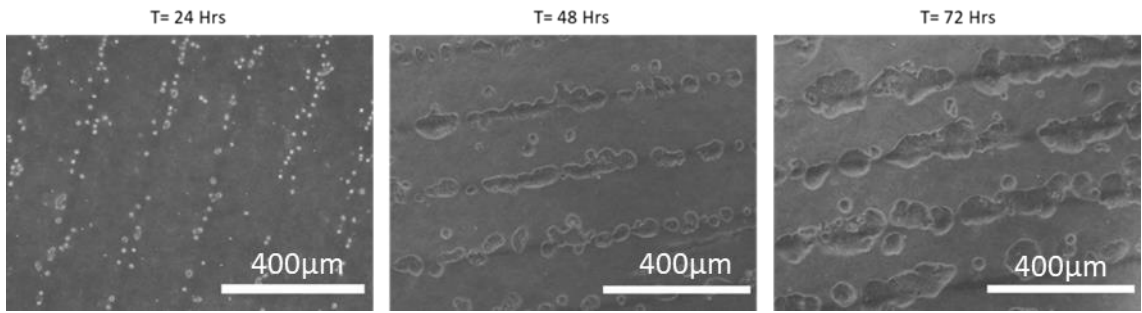


Figure I8: HT-29 cell growth on lines over time.

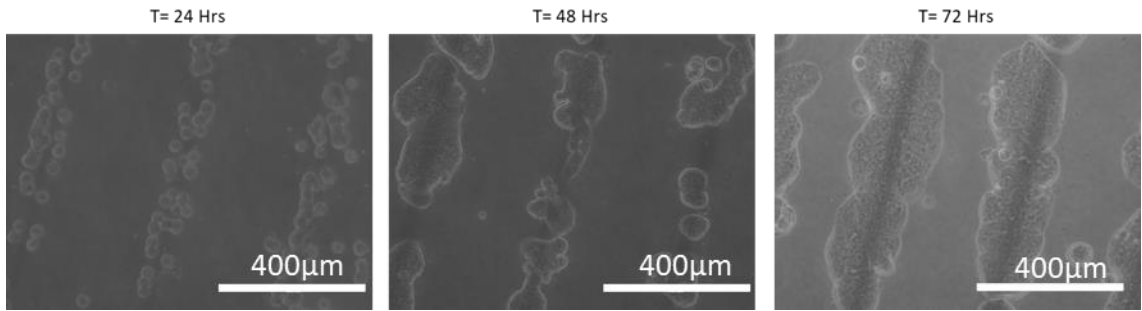


Figure I9: HT-29 cell growth on lines over time.

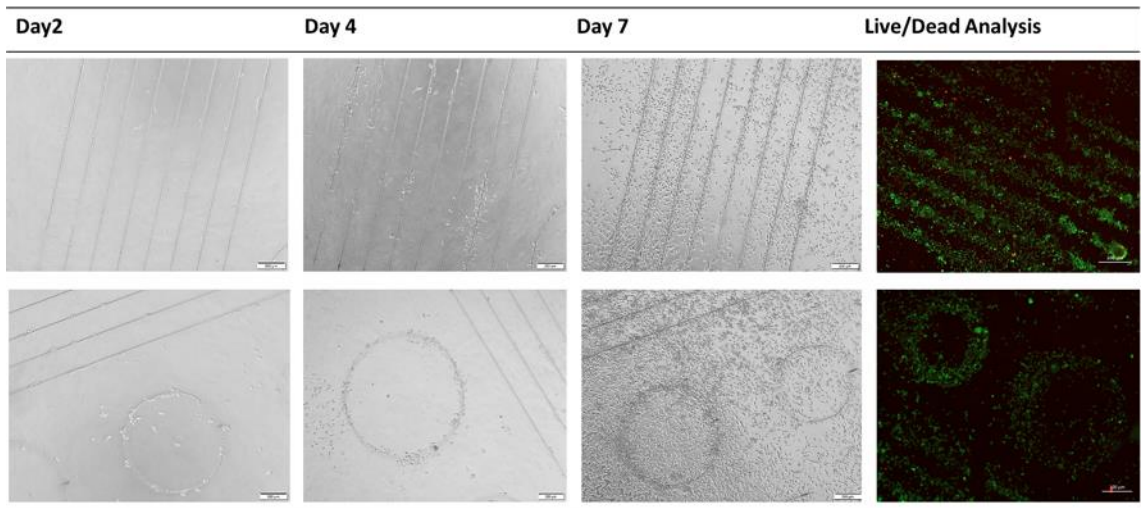


Figure IJ0: BHK Cells

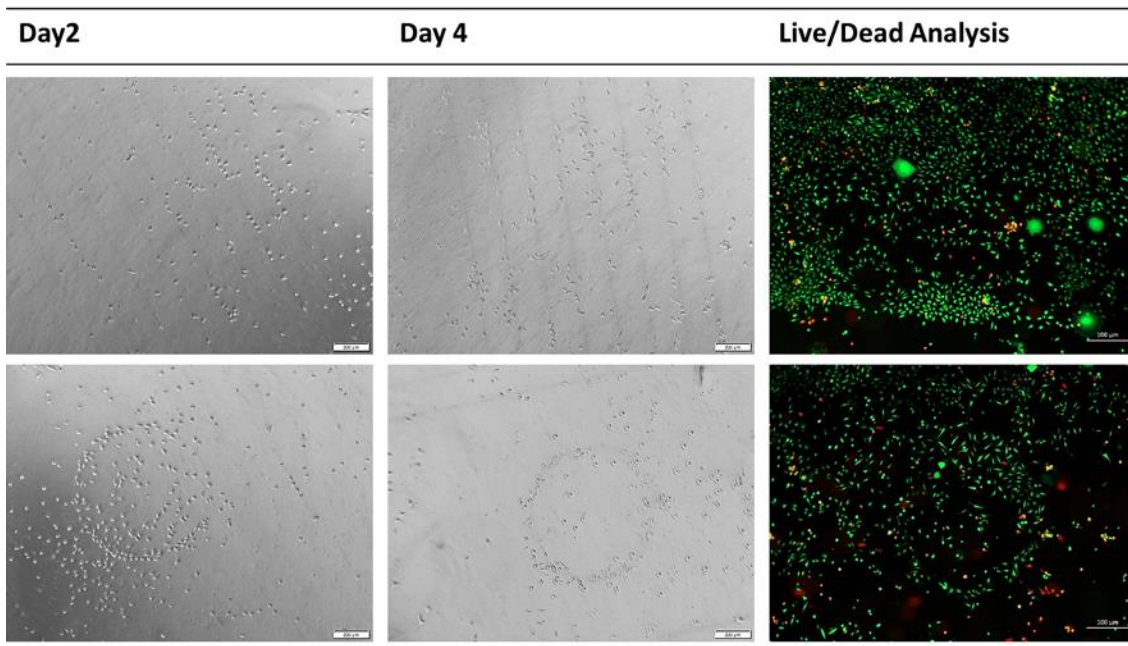


Figure I11: L929 Cells

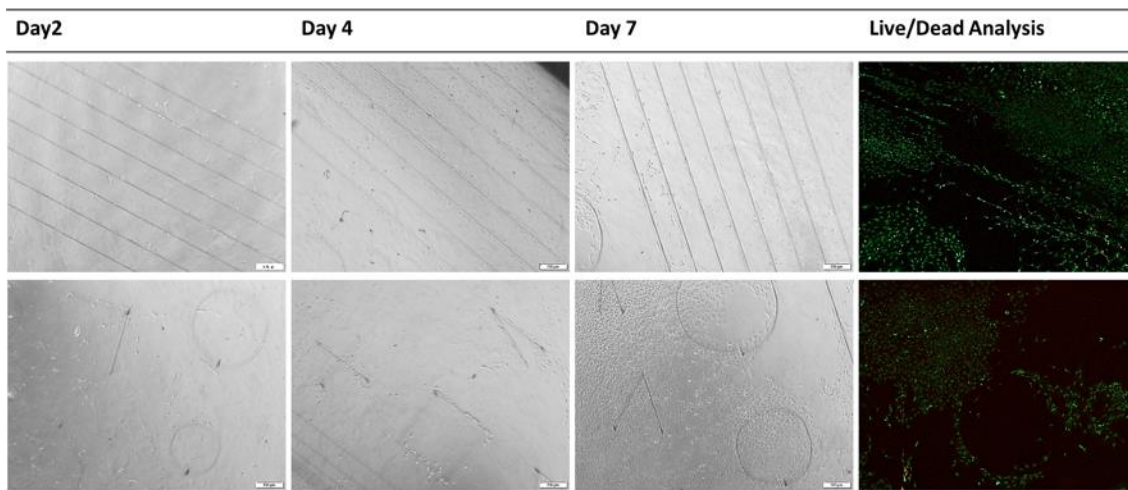


Figure I12: C6 Cells

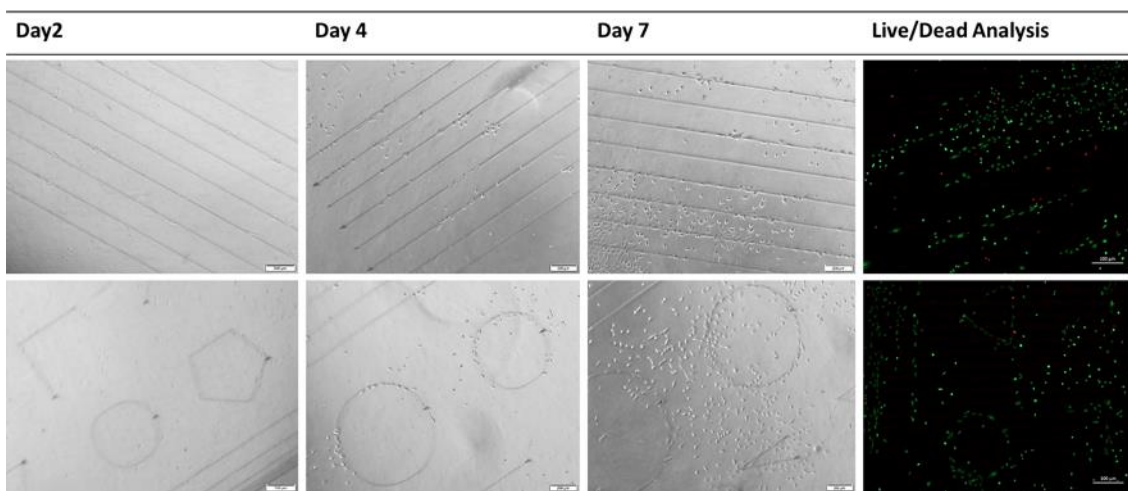


Figure I13: pHDF Cells

RAW 3D

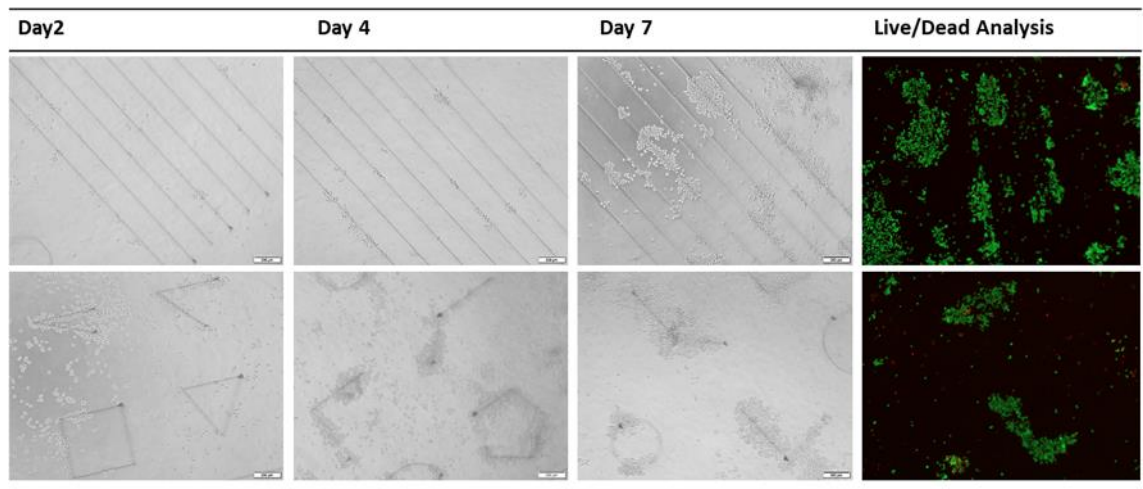


Figure I14: RAW 3D Cells

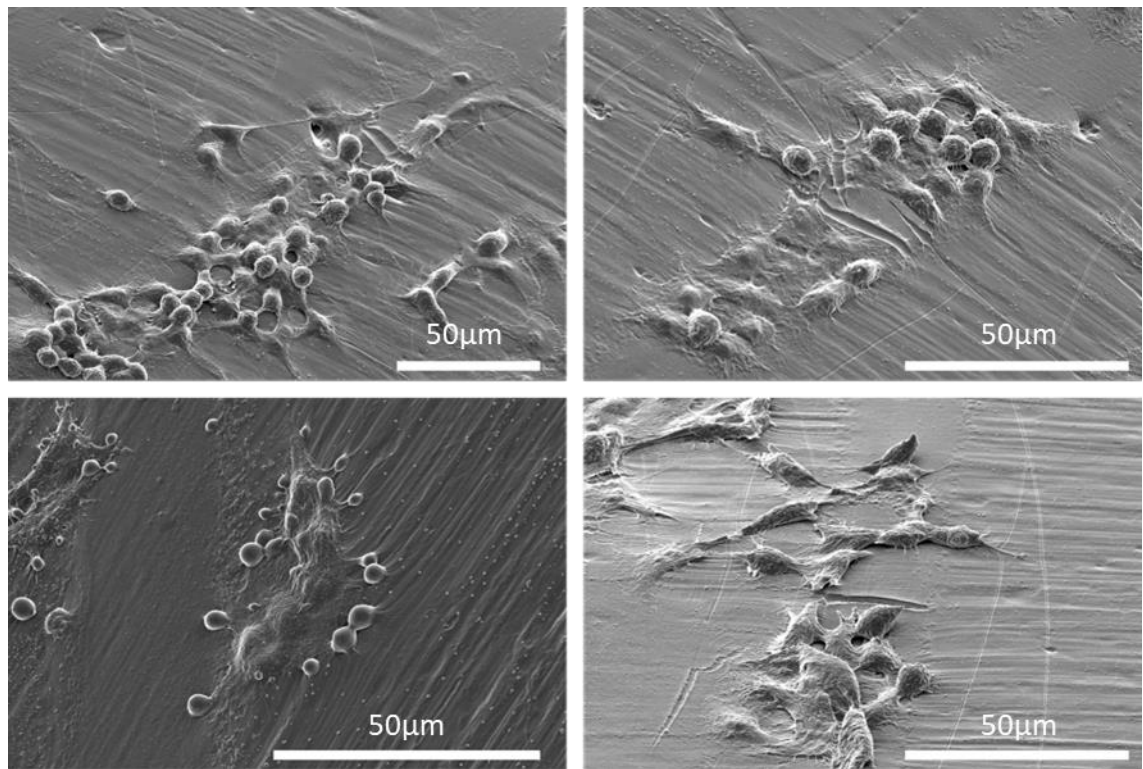


Figure I15: SEM Images of HCT-116 cells growing on a PEDOT:PSS track on a double curved substrate.